

Spectroscopy Applied to Engineering Materials

Guest Editors: Ming-Guo Ma, Wen Zeng, Shao-Wen Cao, Zhong-Chang Wang, and Jie-Fang Zhu





Spectroscopy Applied to Engineering Materials

Journal of Spectroscopy

Spectroscopy Applied to Engineering Materials

Guest Editors: Ming-Guo Ma, Wen Zeng, Shao-Wen Cao,
Zhong-Chang Wang, and Jie-Fang Zhu



Copyright © 2015 Hindawi Publishing Corporation. All rights reserved.

This is a special issue published in "Journal of Spectroscopy." All articles are open access articles distributed under the Creative Commons Attribution License, which permits unrestricted use, distribution, and reproduction in any medium, provided the original work is properly cited.

Editorial Board

- J. Abrantes, Portugal
Khalique Ahmed, USA
Faisal M. Alamgir, USA
Wolfgang Anwand, Germany
Gabriele Arnold, Germany
Naoki Asakawa, Japan
Luciano Bachmann, Brazil
Mark A. Baker, UK
Adam G. Balogh, Germany
M. Baranska, Poland
Lahcen Bih, Morocco
Dhananjay Bodas, India
L. H. Böttger, Germany
Damien Boyer, France
Stefano Caldarelli, France
Jose S. Camara, Portugal
Brian Cannon, USA
E. A. Carter, Australia
J. Castillo-Chara, USA
Wee Chew, Singapore
Jau-Wern Chiou, Taiwan
Daniel O. Cicero, Italy
Malcolm R. Clench, UK
Stephen Cooke, USA
Mircea Cotlet, USA
Daniel Cozzolino, Australia
Vincenza Crupi, Italy
Arnaud Cuisset, France
Eugen Culea, Romania
Eric Da Silva, Canada
Lesley Davenport, USA
A. De Giacomo, Italy
Marcella Dell'aglio, Italy
Renata Diniz, Brazil
Ana Dominguez-Vidal, Spain
C. Dujardin, France
Thomas R. Eykyn, UK
Michele Fedel, Italy
Davide Ferri, Switzerland
- Roberto Flammini, Italy
Anatoly Frenkel, USA
Nives Galicfh, Croatia
Javier Garcia-Guinea, Spain
Martin Giera, The Netherlands
Gianfranco Giubileo, Italy
Andras Gorzsas, Sweden
S. P. Hernandez-Rivera, Puerto Rico
Tino Hofmann, USA
Shuchen Hsieh, Taiwan
Xinyang Huang, China
H. Ikeura-Sekiguchi, Japan
Fumiyuki Ito, Japan
Rodolphe Jaffiol, France
C. K. Jankowski, Canada
ZhiLiang Jiang, China
Dale Keefe, Canada
Rizwan Hasan Khan, India
J. Kim, Republic of Korea
Scott J. Kirkby, USA
Piotr Koczon, Poland
Nikolaos Kourkoumelis, Greece
Christoph Krafft, Germany
N. Krstulović, Croatia
Violeta Lazic, Italy
Young Jong Lee, USA
Adam F. Lee, UK
Nicolae Leopold, Romania
Min Soo Lim, USA
Alessandro Longo, Italy
Paola Luches, Italy
Burkhard Luy, Germany
Mahmoud A. Mahmoud, USA
Petre Makreski, Macedonia
Dmitriy Malinovsky, UK
Djordje Mandrino, Slovenia
Artem E. Masunov, USA
T. G. Mayerhofer, Germany
Yehia Mechref, USA
- Gellert Mezei, USA
Shinichi Morita, Japan
Kouichi Nakagawa, Japan
Austin Nevin, Italy
Masaki Oura, Japan
Giancarlo Pace, Portugal
Carlos A. Palacio, Belgium
Jisheng Pan, Singapore
Jose M. Pedrosa, Spain
Simona C. Pinzaru, Romania
Piotr Przybylski, Poland
Maria Ramil, Spain
K. Krishna Rao, India
Ihtesham ur Rehman, UK
Tomasz Ruman, Poland
Davidson Sajan, India
Alan C. Samuels, USA
Stephane Schilt, Switzerland
Feride Severcan, Turkey
Zhifeng Shao, USA
Masanori Shinohara, Japan
Maciej Sitarz, Poland
Rafal Sitko, Poland
Massimo Tallarida, Germany
Riadh Ternane, Tunisia
Kong-Thon Tsen, USA
Pedro D. Vaz, Portugal
S. Viel, France
Annemarie Wagner, Sweden
Thomas Walther, UK
Chuji Wang, USA
Chih-Che Wu, Taiwan
Lu Yang, Canada
M. C. Yebra-Biurrun, Spain
Guoqiang Yu, USA
Kassym Zhumadilov, Japan
Zoran D. Zujovic, New Zealand
M. Gizdavic-Nikolaidis, New Zealand

Contents

Spectroscopy Applied to Engineering Materials, Ming-Guo Ma, Wen Zeng, Shao-Wen Cao, Zhong-Chang Wang, and Jie-Fang Zhu
Volume 2015, Article ID 693276, 2 pages

The Improvement Effect of Dispersant in Fluorite Flotation: Determination by the Analysis of XRD and FESEM-EDX, Y. J. Li, F. Y. Sun, Y. Zhou, and L. Zeng
Volume 2015, Article ID 859365, 5 pages

Atomic Force Microscopy for Understanding Solvent Cointercalation into Graphite Electrode in Lithium Secondary Batteries, Yang-Soo Kim and Soon-Ki Jeong
Volume 2015, Article ID 462140, 6 pages

Detection of Dissolved Carbon Monoxide in Transformer Oil Using 1.567 μm Diode Laser-Based Photoacoustic Spectroscopy, Qu Zhou, Chao Tang, Shiping Zhu, Weigen Chen, and Xiaojuan Peng
Volume 2015, Article ID 737635, 7 pages

Hydrothermal Synthesis and Structural Characterization of NiO/SnO₂ Composites and Hydrogen Sensing Properties, Chao Wei, Bin Bo, Fengbo Tao, Yuncai Lu, Shudi Peng, Wei Song, and Qu Zhou
Volume 2015, Article ID 450485, 6 pages

Orientation Mapping of Extruded Polymeric Composites by Polarized Micro-Raman Spectroscopy, Xiaoyun Chen, M. Anne Leugers, Tim Kirch, and Jamie Stanley
Volume 2015, Article ID 518054, 7 pages

Evaluation of Salmon Adhesion on PET-Metal Interface by ATR, FT-IR, and Raman Spectroscopy, E. Zumelzu, M. J. Wehrhahn, F. Rull, H. Pesenti, O. Muñoz, and R. Ugarte
Volume 2015, Article ID 835798, 7 pages

Monitoring of Spectral Map Changes from Normal State to Superconducting State in High- T_C Superconductor Films Using Raman Imaging, J. L. González-Solís, R. Sánchez-Ruiz, I. A. Arana-Zamora, J. C. Martínez-Espinosa, M. L. Pérez-Arrieta, and C. Falcony-Guajardo
Volume 2015, Article ID 276537, 6 pages

Research on Fluorescence Spectroscopy Characteristics of Dissolved Organic Matter of Landfill Leachate in the Rear Part of Three Gorges Reservoir, Zhigang Xie and Wei Guan
Volume 2015, Article ID 785406, 9 pages

NIRS Characterization of Paper Pulps to Predict Kappa Number, Ana Moral, Elena Cabeza, Roberto Aguado, and Antonio Tijero
Volume 2015, Article ID 104609, 6 pages

Binding Cellulose and Chitosan via Intermolecular Inclusion Interaction: Synthesis and Characterisation of Gel, Jiufang Duan, Chunrui Han, Liujun Liu, Jianxin Jiang, Jianzhang Li, Yiqiang Li, and Chao Guan
Volume 2015, Article ID 179258, 6 pages

Preparation and Aromatic Hydrocarbon Removal Performance of Potassium Ferrate, Wei Guan,
Zhigang Xie, and Jia Zhang
Volume 2014, Article ID 171484, 8 pages

Influence of Zn/Fe Molar Ratio on Optical and Magnetic Properties of ZnO and ZnFe₂O₄ Nanocrystal as Calcined Products of Layered Double Hydroxides, Abdullah Ahmed Ali Ahmed, Zainal Abidin Talib, Mohd Zobir Hussein, Moayad Husein Flaifel, and Naif Mohammed Al-Hada
Volume 2014, Article ID 732163, 6 pages

Structural Characterization of Carbon Nanomaterial Film *In Situ* Synthesized on Various Bulk Metals, J. Y. Xu, R. Yang, Z. Z. Fan, and X. C. Lei
Volume 2014, Article ID 467185, 6 pages

Fabrication and Characterization of Regenerated Cellulose Films Using Different Ionic Liquids, Jin-Hui Pang, Xin Liu, Miao Wu, Yu-Ying Wu, Xue-Ming Zhang, and Run-Cang Sun
Volume 2014, Article ID 214057, 8 pages

Editorial

Spectroscopy Applied to Engineering Materials

Ming-Guo Ma,¹ Wen Zeng,² Shao-Wen Cao,³ Zhong-Chang Wang,⁴ and Jie-Fang Zhu⁵

¹Beijing Key Laboratory of Lignocellulosic Chemistry, College of Materials Science and Technology, Beijing Forestry University, Beijing 100083, China

²College of Materials Science and Engineering, Chongqing University, Chongqing 400040, China

³School of Materials Science and Engineering, Nanyang Technological University, Singapore 639798

⁴WPI Research Center, Advanced Institute for Materials Research, Tohoku University, Sendai 980-8577, Japan

⁵Department of Materials Chemistry, Ångström Laboratory, Uppsala University, 75121 Uppsala, Sweden

Correspondence should be addressed to Ming-Guo Ma; mg_ma@bjfu.edu.cn

Received 15 December 2014; Accepted 15 December 2014

Copyright © 2015 Ming-Guo Ma et al. This is an open access article distributed under the Creative Commons Attribution License, which permits unrestricted use, distribution, and reproduction in any medium, provided the original work is properly cited.

For this special issue, we received 29 papers. Finally, 14 papers were selected for publication and more than 50% of the papers were rejected.

It is well known that engineering materials were always important tools in the technological development mainly due to their physical/chemical and mechanical properties in a wide range of applications such as machinery, vehicles, ships, construction, energy instrumentation, and aerospace. It is necessary to use spectroscopes analysis to study structure in engineering materials.

Within the published papers, various engineering materials were introduced such as lithium secondary batteries, hydrogen sensing materials, polymeric composites, high-TC superconductor, cellulose film, carbon nanomaterial, and chitosan. In particular, most spectroscopes analysis methods were applied for the characterization of engineering materials including fluorescence spectroscopy, atomic force microscopy, diode laser-based photoacoustic spectroscopy, polarized micro-Raman spectroscopy, and Raman imaging.

Z. Xie and W. Guan reported three-dimensional fluorescence and infrared spectroscopy analysis of the leachate dissolved organic matter (DOM) of the Three Gorges in spring, summer, and autumn seasons, respectively. Experimental results indicated that three-dimensional fluorescence spectra of the landfill leachate varied with rubbish stacking time. They also reported that the longer the waste stacking

time, the lower the protein in leachate concentration and the higher the fulvic-like acid concentration.

Y.-S. Kim and S.-K. Jeong investigated the electrochemical processes occurring at the surface of a highly ordered pyrolytic graphite electrode by *in situ* atomic force microscopy (AFM). Their results provided the direct and obvious evidence that solvent cointercalation reaction occurred at the initial stage of the surface film formation.

X. Chen et al. used polarized micro-Raman spectroscopy as a powerful tool to map out the molecular orientation of a uniaxially oriented polypropylene-based composite material. Micro-Raman analysis at the surface region was found to demonstrate the surface orientation relaxation and provide an effective way to correlate the extent of relaxation and process conditions. J. L. González-Solís et al. also explored the chemical structure of $TlBa_2Ca_2Cu_3O_9$ high-TC superconductor films with Tl-1223 phase to monitor spectral map changes from normal state to superconducting state using the technique of Raman imaging, which provided the spatial distribution of the various molecular species within a sample. They reported that this is the first report of preliminary results evaluating the usefulness of Raman imaging in the determination of transition temperature of $TlBa_2Ca_2Cu_3O_9$ high-TC superconductor films with Tl-1223 phase.

This issue provided the recent development of advanced spectroscopic characterizations for engineering materials.

Our expectation is that more attentions will be paid to the research of engineering materials.

Acknowledgments

The editors would like to take advantage of this opportunity to express their sincere thanks to the authors. They would like to thank them for submitting their best papers to this issue. Then, they also apologize for the long time of the review process. For example, it took 115 days to review E. Zumelzu et al.'s paper. Finally, the lead guest editor expresses his/her sincere gratitude to the editor team as it is not easy for them to assign the article to a reviewer.

*Ming-Guo Ma
Wen Zeng
Shao-Wen Cao
Zhong-Chang Wang
Jie-Fang Zhu*

Research Article

The Improvement Effect of Dispersant in Fluorite Flotation: Determination by the Analysis of XRD and FESEM-EDX

Y. J. Li,¹ F. Y. Sun,¹ Y. Zhou,¹ and L. Zeng²

¹College of Earth Sciences, Jilin University, Changchun 130000, China

²College of Materials Science and Engineering, Chongqing University, Chongqing 400030, China

Correspondence should be addressed to L. Zeng; zool@foxmail.com

Received 29 July 2014; Accepted 26 August 2014

Academic Editor: Wen Zeng

Copyright © 2015 Y. J. Li et al. This is an open access article distributed under the Creative Commons Attribution License, which permits unrestricted use, distribution, and reproduction in any medium, provided the original work is properly cited.

Different dispersants were added in the dispersion process to improve the efficiency of fluorite flotation. The types and dosage of dispersant on the improvement of fluorite flotation were investigated; when the sodium polyacrylate (SPA) was used as the dispersant and its addition is 0.5%, the concentrate grade of CaF_2 increased from 90% to 98% and the fluorite recovery increased from 81% to 85%. Methods of X-ray powder diffraction (XRD), field emission scanning electron microscopy (FESEM), and Energy dispersive X-ray spectrometer (EDX) were used to characterize the sample. According to the analysis of results, the optimal sample consisted of CaF_2 and very little CaCO_3 in the size range of 0–5 μm . It could be concluded that the mechanism of improvement for the concentrate grade and recovery of CaF_2 was attributed to the change of potential energy barrier which caused the separation of particles with different charge. All results indicate that SPA has a great potential to be an efficient and cost-effective dispersant for the improvement of fluorite flotation.

1. Introduction

Fluorite, which is a kind of mineral with the highest level of fluoride content, derives its name from the Latin word “flurum.” The main chemical component of fluorite is CaF_2 , and fluorite also contains traces of impurity elements such as silicon, aluminum, magnesium, strontium, yttrium, cerium, and uranium and other foreign matters like asphalt, ferric oxide, and so forth [1]. Fluorite is a kind of equiaxial crystal, often featuring in a cube and octahedron, and it also shapes into a monocrystalline of rhombic dodecahedron or irregular granular aggregate. Fluorite is characterized by the vitreous luster, crispness, shell-shaped fractures, and complete cleavages along the octahedron. With its relative density of 3.18 and melting point of 1360°C, it is insoluble in water or acid [2]. It has been a long time since humans began to make use of fluorite. Early in the 15th century, Agricola found the features of “Flares” in fluorites and employed them as a metallurgical flux [3]. Fluorite is the most important industrial mineral containing fluorine. It not only is widely used in the industrial sectors such as metallurgy, chemicals, ceramics, building

materials, machinery, electrical machinery, aviation, agriculture, medicine, and precise instruments, but also serves as the important energetic materials in the cutting-edge science and emerging industries such as atomic energy, the rockets, and aerospace. Fluorite ore can produce products of different specifications through mineral processing [4]. With the development of industrial technology, there is a growing demand for high-quality fluorite ore (with the contents of CaF_2 more than 93%) [5]. However, there is less rich ore and poorer ore in terms of the fluorite ore resources in China, with the contents of CaF_2 in fluorite ore about 35 to 40% on average [6]. Therefore, we must adopt efficient mineral processing ways so as to improve the contents of CaF_2 .

At present, we commonly adopt the flotation method to remove the mineral impurities except fluorite in the fluorite ore to improve the content of CaF_2 , among which the dispersion process is a very important technique and the selection of dispersants will have a direct impact on the contents of CaF_2 of the final products [7]. In this work, we chose four types of dispersants, studying the dispersion effect of them on the fluorite purification to produce a high-grade

TABLE 1: The effect of dispersants on the concentrate grade and recovery of CaF_2 .

Samples	Dispersant	Grade (%)	Recovery (%)
FR	—	90	81
FSS	SS	92	82
FPAM	PAM	95	82
FHPMC	HPMC	92	83
FSPA	SPA	98	85

concentrate of fluorite. The objective of this study is to explore the best dispersant in increasing the concentrate grade and recovery of CaF_2 .

2. Experimental

2.1. Materials. The fluorite ore used in this work was mined from Inner Mongolia, which mainly consists of 77.12% CaF_2 , 11.35% CaCO_3 , 9.71% SiO_2 , and a little clay. The sample was dried at 95°C to constant mass and then milled to less than $45\ \mu\text{m}$. The dispersants supplied from Aladdin Co. Ltd. are all analytical reagents, including silica sol (SS), polyacrylamide (PAM), hydroxypropyl methyl cellulose (HPMC), and sodium polyacrylate (SPA), and the corresponding samples with different dispersants are FSS, FPAM, FHPMC, and FSPA, respectively.

2.2. Experimental Methods. For the preparation of high-grade fluorite concentrate, the slurry with 200 g fluorite ore and 700 mL water was ground in a ball mill for 20 min while the dispersant was added in this dispersion process, and then, by the process of rougher flotation and cleaner flotation, the final fluorite concentrate was obtained. The fluorite concentrate was dried at 95°C to constant mass and weighed, of which the composition was analyzed. From the procedure, the concentrate grade and recovery of fluorite were calculated to choose the best dispersant in increasing the concentrate grade and recovery. The sample prepared with the best dispersant was characterized by different methods, including X-ray powder diffraction (XRD), field emission scanning electron microscopy (FESEM), and energy dispersive X-ray spectrometer (EDX). XRD was performed on a Rigaku D/max-3Bx diffractometer with $\text{Cu K}\alpha$ radiation, in the range of 30° – 65° 2θ and at a step size of 0.02° . FESEM micrographs were performed by the Hitachi SU8010 operating at the accelerating voltage of 15 kV and FESEM images were taken at different magnifications. The instrument was equipped with the energy dispersion X-ray spectroscopy.

3. Results and Discussion

3.1. Effects of Dispersants. Table 1 shows the effect of dispersants (0.5% addition) on the concentrate grade and recovery of CaF_2 . As can be seen from Table 1, without the addition of dispersant, the concentrate grade and recovery of CaF_2 were 90% and 81%, and, with the addition of dispersant, it could increase the concentrate grade and recovery of CaF_2

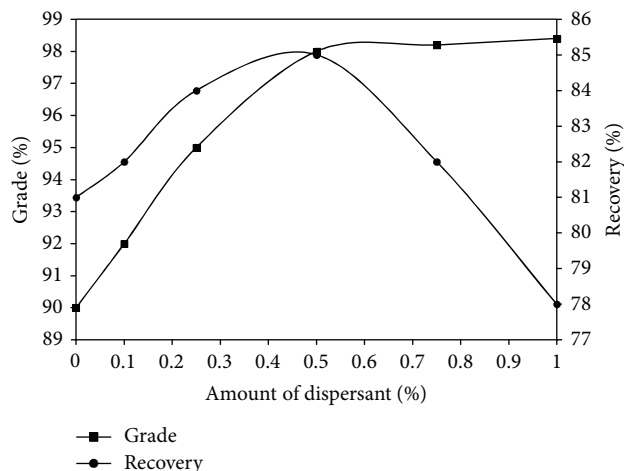


FIGURE 1: The effect of SPA amount on the concentrate grade and recovery of CaF_2 .

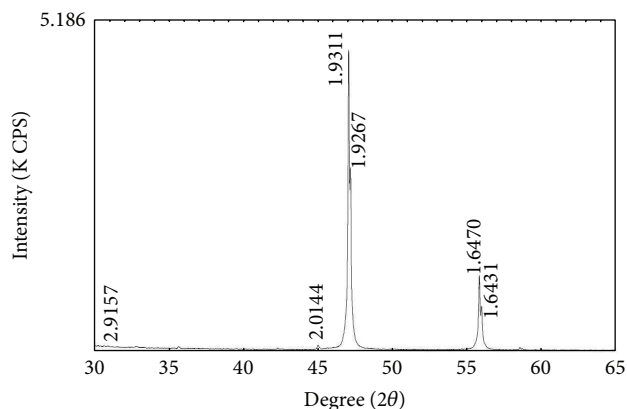


FIGURE 2: XRD pattern of FSPA.

but with a different effect. The concentrate grade of CaF_2 was in the range of 92~98% and the recovery was in the range of 82~85% with the addition of dispersant. In particular, with the addition of SPA, the concentrate grade and recovery of FSPA were 98% and 85%, which increased about 8% and 4% compared with FR. It can be attributed to the dispersion effect which dispersed the mineral particles equably in the solution and thus prevented other minerals such as calcite and quartz from being entered into the concentrate [8]. Hence, the addition of dispersant has great influences on the concentrate grade and recovery of CaF_2 .

3.2. The Effect of Dispersant Amount. The amount of dispersant is an important parameter determining the concentrate to grade and recovery of CaF_2 . The effect of SPA amount on the concentrate grade and recovery is shown in Figure 1, which indicates that the dispersant amount has great influence on both of concentrate grade and recovery. It is observed that the concentrate grade of CaF_2 increases obviously with the increase of SPA addition all the while, and the increases are much stronger in the low SPA addition than in the high

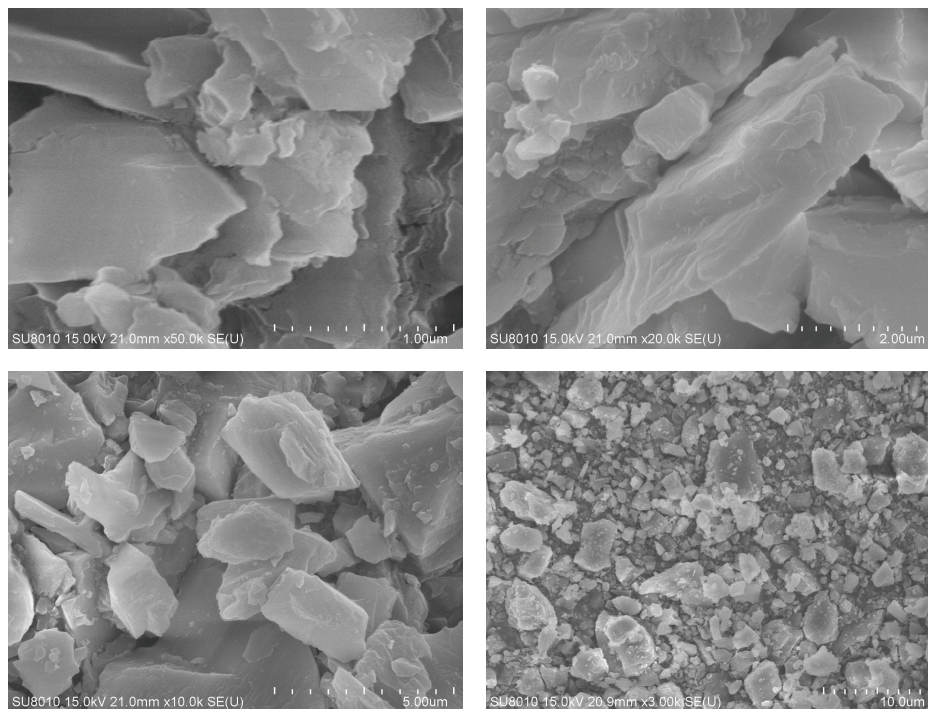


FIGURE 3: FESEM micrographs of FSPA.

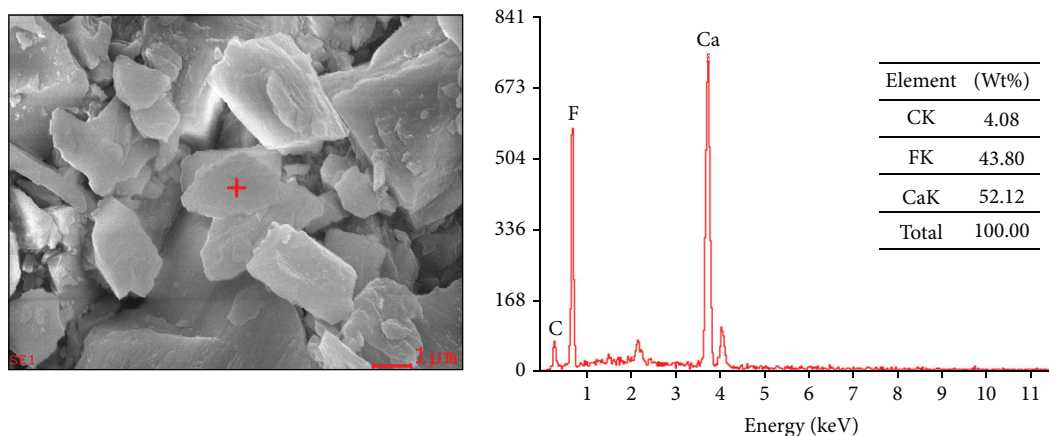


FIGURE 4: FESEM-EDX analysis of FSPA.

addition, which can be attributed to the dispersion effect [9]. As the dispersibility of raw ore is poor, the impurity is hard to separate. With the addition of SPA, the dispersibility is improved and causes the increase of concentrate grade. However, the recovery of CaF_2 increases with the increase of dispersant at first but reaches the maximum value when the dispersant addition is 0.5% and then declines. It shows that too much dispersant addition makes a bad effect on the recovery of CaF_2 and the best amount of SPA addition is about 0.5%.

3.3. XRD Characterization. XRD pattern reveals the microstructure and composition of sample. The XRD pattern of FSPA is presented in Figure 2. As can be seen, the FSPA

consists of fluorite (CaF_2) with peaks at 1.9311, 1.9267, 1.6470, and 1.6431 Å (corresponding to 46.1, 47.2, 55.7, and 56.3° 2θ, resp.). The peaks are strong and sharp, reflecting an ordered and high-crystallinity structure, which show that the disposal of floatation does not change the crystallinity structure of fluorite [10, 11]. Meanwhile, the peaks of calcite, quartz, and other minerals are almost not observed, which indicate the high concentrate grade of CaF_2 . As already introduced, fluorite, calcite, and quartz are the main minerals in the fluorite ore; the result suggests that, with the SPA addition, the other minerals such as calcite and quartz can be removed drastically from the concentrate and a high concentrate grade of CaF_2 can be obtained.

3.4. FESEM-EDX Characterization. The FESEM micrographs of FSPA are presented in Figure 3. As it can be seen in Figure 3, the microappearance of FSPA is irregular platelet and pile on each other, and its size is in the range of 0–5 μm , and its appearance is consistent with the typical characteristics of fluorite [12]. The particle size of FSPA is very fine due to the addition of dispersant, which is beneficial for the floatation. As the main minerals in the fluorite ore are fluorite, calcite, and quartz which have their isoelectric point (IEP) at different pH, the addition of dispersant changes the pH of slurry and endows the minerals with different charges, which are beneficial for the separation of the minerals and getting the high concentrate grade of CaF_2 [13, 14]. It can be explained that the existence of potential energy barrier between particles keeps from the approach of particles, which causes the aggregative stability of colloidal suspensions, but the interaction energies of electrical double layer and van der Waals cause the potential energy barrier to arise and the particles with different charge to separate [15–17]. Meanwhile, the sample was characterized by the method of EDX in order to analyze the composition of the sample. Figure 4 shows the results of FESEM-EDX analysis of FSPA. As it can be seen in Figure 4, the EDX spectra reveal the presence of calcium, fluorine, and carbon (Ca = 52.12 wt%, F = 43.80 wt%, and C = 4.08 wt%), which indicate that the sample consists of CaF_2 , and little of CaCO_3 may be residual [18]. In addition, Si is not detected in the sample which suggests the quartz had been removed completely. The result shows the high concentrate grade of CaF_2 , and in this system the quartz, compared with calcite, is easier to be removed with the addition of dispersant.

4. Conclusion

The final results presented in this paper demonstrated the influence of dispersants in the floatation of fluorite. It was shown that all the dispersants exhibited certain effects in increasing the concentrate grade and recovery of CaF_2 and SPA presented high improvement in the purification of fluorite ores by floatation. With the addition of SPA in the slurry, the sample with high concentrate grade and recovery of CaF_2 was prepared, and when the addition of SPA is 0.5%, FSPA obtained the highest concentrate grade (98%) and recovery (85%). FSPA were characterized by several methods, including XRD, FESEM, and EDX. According to the analysis of results, the optimal sample consisted of CaF_2 and very little CaCO_3 in the size range of 0–5 μm . It can be concluded that the mechanism of improvement for the concentrate grade and recovery of CaF_2 could be attributed to the change of potential energy barrier which caused the separation of particles with different charges.

Generally speaking, in the practical application, the addition of dispersant is technically and economically reliable for the floatation of fluorite, including (a) the high concentrate grade of CaF_2 , (b) the increasing recovery of ore fluorite, and (c) the finer particles. Meanwhile, the addition of dispersant is cost-effective and has a high recovery for CaF_2 from the slurry. Furthermore, the dispersion disposal with SPA as the dispersant in the fluorite floatation could increase the concentrate grade from 90% to 98% while the fluorite

recovery was increased from 81% to 85%. Hence, in order to increase the concentrate grade and recovery of CaF_2 , the SPA can be used as the potential dispersant in the fluorite floatation.

Conflict of Interests

The authors declare no conflict of interests regarding the publication of this paper.

Acknowledgments

The study was supported by the Research Funds for the Comprehensive Test Technology: The Mineralization Elements and Components of Associated Fluorite (12120113014300). The authors are also grateful for the support of Siziwang Banner Land and Resources Bureau.

References

- [1] J. S. Laskowski and R. J. Pugh, "Dispersions stability and dispersing agents," in *Colloid Chemistry in Mineral Processing*, J. S. Laskowski and J. Ralston, Eds., pp. 151–166, Elsevier, Amsterdam, The Netherlands, 1992.
- [2] M. A. Elrashidi and W. L. Lindsay, "Chemical equilibria of fluorine in soils: a theoretical development," *Soil Science*, vol. 141, no. 4, pp. 274–280, 1986.
- [3] C. E. Manning and D. K. Bird, "Fluorian garnets from the host rocks of the Skaergaard intrusion: implications for metamorphic fluid composition," *American Mineralogist*, vol. 75, no. 7–8, pp. 859–873, 1990.
- [4] G. Bhaskar Raju and S. Prabhakar, "Beneficiation of fluorspar by column floatation," *Minerals and Metallurgical Processing*, vol. 17, no. 3, pp. 167–172, 2000.
- [5] G. Ateşok, F. Boylu, and M. S. Çelik, "Carrier floatation for desulfurization and deashing of difficult-to-float coals," *Minerals Engineering*, vol. 14, no. 6, pp. 661–670, 2001.
- [6] X. Zhou, J. Liu, Y. Wang, D. Tao, and C. Zhao, "Pilot-scale study of fluorite beneficiation using a cyclonic static microbubble floatation column," *Minerals and Metallurgical Processing*, vol. 24, no. 4, pp. 271–274, 2007.
- [7] S. Song, A. Lopez-Valdivieso, C. Martinez-Martinez, and R. Torres-Armenta, "Improving fluorite floatation from ores by dispersion processing," *Minerals Engineering*, vol. 19, no. 9, pp. 912–917, 2006.
- [8] R. A. Grau, J. S. Laskowski, and K. Heiskanen, "Effect of frothers on bubble size," *International Journal of Mineral Processing*, vol. 76, no. 4, pp. 225–233, 2005.
- [9] R. P. Garibay, P. M. Gallegos, S. A. Uribe, and A. F. Nava, "Effect of collection zone height and operating variables on recovery of overload floatation columns," *Minerals Engineering*, vol. 15, no. 5, pp. 325–331, 2002.
- [10] L. A. Kienko and O. V. Voronova, "Performance evaluation of comprehensive processing of zinc-fluorite ore in the Voznesensky mining area," *Journal of Mining Science*, vol. 48, no. 5, pp. 928–933, 2012.
- [11] W. Aliaga, C. H. Sampaio, I. A. S. Brum, K. R. S. Ferreira, and M. A. Batistella, "Flotation of high-grade fluorite in a short column under negative bias regime," *Minerals Engineering*, vol. 19, no. 13, pp. 1393–1396, 2006.

- [12] J. Zawala, J. Drzymala, and K. Malysa, "An investigation into the mechanism of the three-phase contact formation at fluorite surface by colliding bubble," *International Journal of Mineral Processing*, vol. 88, no. 3-4, pp. 72-79, 2008.
- [13] J. D. Miller, K. Fa, J. V. Calara, and V. K. Paruchuri, "The surface charge of fluorite in the absence of surface carbonation," *Colloids and Surfaces A: Physicochemical and Engineering Aspects*, vol. 238, no. 1-3, pp. 91-97, 2004.
- [14] Z. Xu, J. Liu, J. W. Choung, and Z. Zhou, "Electrokinetic study of clay interactions with coal in flotation," *International Journal of Mineral Processing*, vol. 68, no. 1-4, pp. 183-196, 2003.
- [15] Q. Wang, "A study on shear coagulation and heterocoagulation," *Journal of Colloid And Interface Science*, vol. 150, no. 2, pp. 418-427, 1992.
- [16] Y. Zhang and S. Song, "Beneficiation of fluorite by flotation in a new chemical scheme," *Minerals Engineering*, vol. 16, no. 7, pp. 597-600, 2003.
- [17] A. A. Abramov and D. V. Magazanik, "Theoretical basis for optimal collector concentrations and pulp pH values during flotation of sulfide-free minerals," *Journal of Mining Science*, vol. 42, no. 2, pp. 178-188, 2006.
- [18] W. Zhou, J. Moreno, R. Torres, H. Valle, and S. Song, "Flotation of fluorite from ores by using acidized water glass as depressant," *Minerals Engineering*, vol. 45, pp. 142-145, 2013.

Research Article

Atomic Force Microscopy for Understanding Solvent Cointercalation into Graphite Electrode in Lithium Secondary Batteries

Yang-Soo Kim¹ and Soon-Ki Jeong²

¹ Suncheon Center, Korea Basic Science Institute, Suncheon 540-742, Republic of Korea

² Department of Chemical Engineering, Soonchunhyang University, Asan, Chungnam 336-745, Republic of Korea

Correspondence should be addressed to Soon-Ki Jeong; hamin611@sch.ac.kr

Received 8 August 2014; Accepted 30 November 2014

Academic Editor: Zhong-Chang Wang

Copyright © 2015 Y.-S. Kim and S.-K. Jeong. This is an open access article distributed under the Creative Commons Attribution License, which permits unrestricted use, distribution, and reproduction in any medium, provided the original work is properly cited.

The electrochemical processes occurring at the surface of a highly ordered pyrolytic graphite (HOPG) electrode were investigated by *in situ* atomic force microscopy (AFM) to understand the solvent cointercalation involved in the formation of a surface film. AFM images were recorded under the conditions that AFM probe does not affect the electrode reaction. The AFM images show the morphological changes occurring at the electrode surface, indicating that two different types of reactions occurred in the film formation at the surface of the electrode. The formation of a blister structure was observed on the graphite surface, because of the decomposition of solvated lithium ions produced in the electrolyte solution and intercalation between the graphite layer and particulate materials. The solvent cointercalation reaction leading to the blister structure was more pronounced for the HOPG electrode with a higher value of mosaic spread.

1. Introduction

Graphite is one of the most important negatively charged electrode materials in commercially available lithium secondary batteries. During the charge-discharge processes in negatively charged graphite electrode, the intercalation and deintercalation reactions of lithium ions occur in the potential range 0–0.25 V (versus Li^+/Li) [1–4]. However, as such potentials produce very strong reducing environments from the thermodynamic perspective, chemically stable electrolytes are unlikely to exist in such situations, thereby reducing and/or decomposing during the electrode reactions. Nevertheless, because a film is formed on the graphite surface by the decomposition of electrolyte, stable intercalation and deintercalation reactions occur at the graphite electrode, before the intercalation of lithium ions into graphite [5]. This surface film, often called the solid electrolyte interface, allows lithium ions to pass through, whereas it blocks the transfer of electrons [5, 6]. Thus, the surface film formation suppresses the decomposition of electrolyte that occurs because of the electron transfer between electrode and electrolyte and allows

selective intercalation and deintercalation of lithium ions. The formation of surface films strongly depends on the type of electrolyte used. Surface films with excellent properties are formed when an ethylene carbonate- (EC-) based electrolyte solution is used [7]. With the EC-based electrolytes, the intercalated lithium ions can be extracted with very high efficiency, after their electrochemical intercalation into the graphite. Surface films significantly affect the battery performance; therefore, identifying their physicochemical characteristics is crucial. Even though surface films have been studied in detail [8–20], many issues still need to be investigated.

The solvent cointercalation reaction occurring at the initial stage of surface film formation also needs to be investigated. This phenomenon, first reported by the Besenhard group [10], refers to the intercalation of not only lithium ions but also the solvent in electrolytes into the graphite at the initial film-forming stage. This solvent cointercalation reaction is fundamental in ascertaining the formation and properties of the surface films. The Besenhard group investigated the expansion/contraction of electrodes associated with the electrochemical intercalation and deintercalation of lithium

ions by dilatometry using highly ordered pyrolytic graphite (HOPG) as a negative electrode [10, 11]. The results confirmed that the electrode width increased ~ 1.5 times at ~ 0.8 V in a vertical direction to the basal plane prior to reaching the potential range 0.0–0.25 V, in which only lithium ions were intercalated. The data were considered to result from the intercalation of the solvated lithium ions. This solvent cointercalation phenomenon cannot be investigated by X-ray diffraction (XRD) analysis [2]. When the molecular space in graphite is enlarged because of the intercalation of different chemical species, the position of the XRD peaks is expected to shift toward the low angle side according to the Bragg theory. However, because this explanation was not obtained experimentally, the results of the Besenhard's group study were initially not widely accepted. Later studies using scanning tunneling microscopy (STM) and atomic force microscopy (AFM) by the Ogumi group and Raman spectroscopic study by the Huang group confirmed the solvent cointercalation phenomenon [12–20], and the study results of the Besenhard group started to receive support. Nevertheless, definite experimental evidence for the solvent cointercalation reaction is still necessary.

The solvent cointercalation phenomenon was confirmed by the previously mentioned studies; however, we contend that the inferences from their data are in contrast with the explanations provided. In the case of the investigation by the Besenhard group by dilatometry, considering the structure of the experimental apparatus, a minute amount of electrolyte could possibly penetrate into the contact surface between the electrode and electrical leads of dilatometer. The penetrated electrolyte might get reduced and decomposed at ~ 0.8 V, thereby detecting the expansion by dilatometry. Studies by the Ogumi group involving STM [12, 13] reported the formation of a hill structure on the electrode surface at 1.1 V by gradually lowering the potential of the HOPG electrodes from the open circuit potential, probably because of the cointercalation. In this study, because the STM analysis can be applied to conducting materials, a possibility of breakdown on the thin surface component with insulating components probably occurred by the decomposition of electrolyte before the appearance of the hill structure as a result of the intercalation of the solvated lithium ions into the damaged surface. In the analysis using AFM [14–17] in the contact modes of the probe and electrode, a possible breakdown (of both the insulating and conductive properties) of the surface films similar to the case of the STM experiments exists, thereby intercalating the solvated lithium ions on the damaged surface. Moreover, the Huang group analyzed the Raman band at a wavelength of 1598 cm^{-1} during the first lithium intercalation process to understand the solvent cointercalation. However, this band was not observed by other research groups using similar analysis techniques [4, 21, 22].

Based on such reasoning, we considered that more definite experimental evidence is required to explain the solvent cointercalation phenomenon. In this study, we used AFM similar to that used by the Ogumi group and ensured that the surface films were not damaged by the probes. As a result, direct experimental evidence strongly supporting the solvent cointercalation phenomenon was obtained.

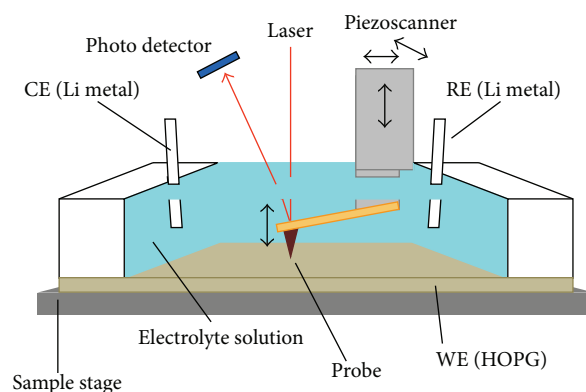


FIGURE 1: Schematic of electrochemical cell for *in situ* AFM observation.

2. Experimental

The electrolyte solutions were prepared by dissolving LiClO_4 in a 1:1 (by volume) mixture of EC and diethyl carbonate (DEC). All the electrolytes were purchased from Kishida Chemical Co. and were used as received. The water content in the electrolyte solution was <30 ppm, as measured using a Karl-Fischer moisture titrator (Kyoto Electronics Manufacturing Co., MKC-210).

HOPG blocks (Advanced Ceramics, ZYH grade, Mosaic spread: $3.5 \pm 1.5^\circ$; ZYA grade, Mosaic spread: $0.4 \pm 0.1^\circ$) were used for AFM observations. A flat surface was easily prepared by cleaving the HOPG with tape. *In situ* electrochemical AFM observations were performed in a conventional contact mode using an AFM system (Molecular Imaging, PicoSPM) equipped with a potentiostat (Molecular Imaging, PicoStat) and a laboratory-made electrochemical cell as shown in Figure 1. Freshly cleaved HOPG was mounted on the bottom of the cell. Only the basal plane was brought into contact with the electrolyte solution using an O-ring. The geometrical surface area was 1.2 cm^2 . Lithium foil was used as the counter and reference electrodes. Pyramidal silicon nitride tips were used for AFM measurements. Cyclic voltammetry (CV) was performed between 2.9 and 0.0 V at a sweep rate of 5 or 0.5 mV s^{-1} .

All the electrochemical measurements including AFM were performed in an argon-filled glovebox (Three-Shine, SK-G1200) with a dew point below -60°C . All the potentials are referred to as volts versus Li^+/Li .

3. Results and Discussion

The main objective of the study was to investigate the solvent cointercalation reaction on the graphite electrode surfaces in the absence of physical forces applied by the AFM probes. Prior to the relevant explanation, the Ogumi group's conclusion on the mechanism of the surface film generation, verified from different aspects, is mentioned. Figure 2 shows the surface film formation measured by *in situ* AFM during the HOPG electrode reaction by CV. In Figure 2(a), three

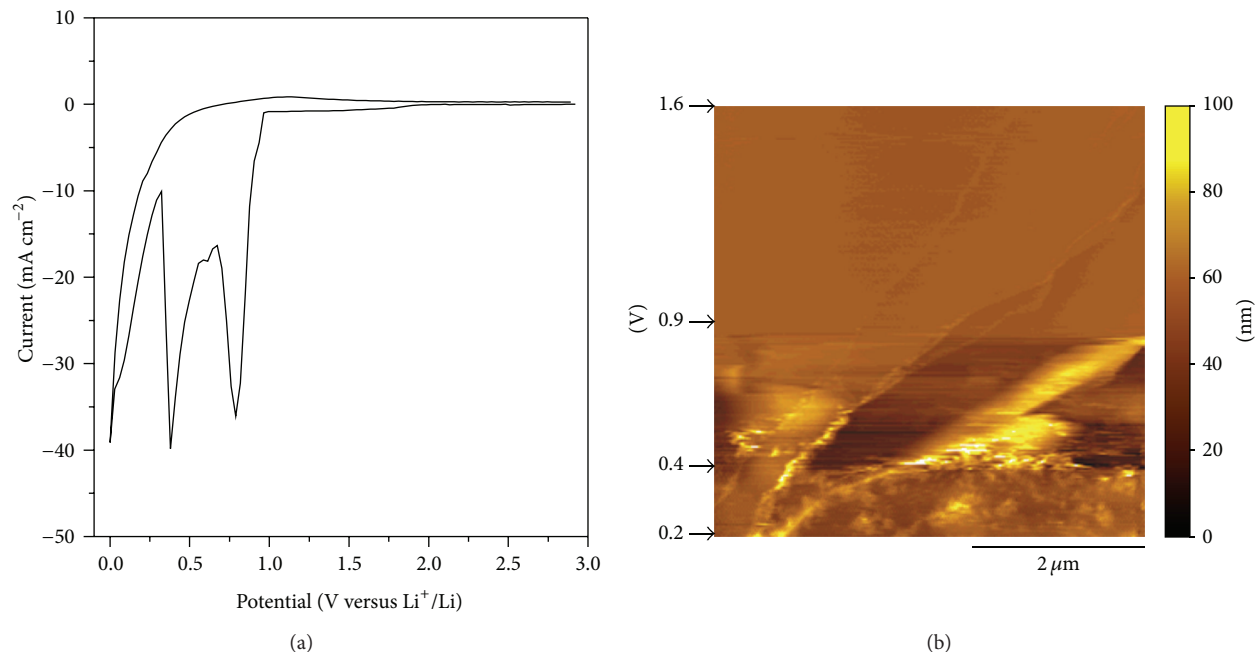


FIGURE 2: (a) The first cyclic voltammogram of the HOPG basal plane at 5 mV s^{-1} in $1 \text{ M LiClO}_4/\text{EC} + \text{DEC}$ and (b) *in situ* AFM image ($5 \times 5 \mu\text{m}^2$) of the HOPG basal plane surface obtained at 2.9 V between 1.6 and 0.2 V in (a).

large peaks are observed at ~ 0.8 , 0.35 , and 0 V . The corresponding changes on the electrode surfaces in response to the peaks measured by CV were confirmed from the AFM image in Figure 2(b), which shows the *in situ* AFM image observed in the potential range 1.6 – 0.2 V during the electrode reactions by CV. The AFM image was scanned from 1.6 V , progressing in the negative direction until a potential of 0.2 V . The surface configurations of the electrode showed significant changes at 0.9 and 0.4 V , confirming a two-step reaction. These results are consistent with the report by the Ogumi group [14].

The Ogumi group reported that the formation of surface films involves two different types of reactions: the decomposition reaction of the intercalated solvated lithium ions into graphite and accompanying solvent coinsertion and direct decomposition reaction of the electrolyte solution on the graphite surface. The results obtained from Figure 2 are consistent with those reported by the Ogumi group, and the AFM measurement was performed in the contact mode under similar conditions. However, Figure 2 also shows that the two different types of reactions involved at the surface films as described earlier were confirmed in one single image obtained by one time measurement. Figure 2(b) shows the first situation where two different reactions are confirmed by a one-time measurement. The studies performed until now in relation to the formation of surface films involved either single observations or single measurements of one reaction even though two reactions occurred, leading some researchers to doubt the involvement of two different reactions in surface film formation. The results in Figure 2(b) provide unambiguous evidence, supporting the existence of two different reactions without considering the effects of the contact mode.

Figure 2(b) shows that the results obtained in the contact mode and the solvent coinsertion phenomenon initiated at 0.9 V may be caused by the physical force of the AFM probe, as mentioned in the Introduction. To prevent this, the AFM observations were not performed until the completion of surface film formation reactions, and Figure 3(a) shows the surface configuration before the start of the electrode reaction. The height of the largest step edge in the image was $\sim 10 \text{ nm}$. Figure 3(b) shows the results of the observation at 2.9 V after one cycle of CV at the same location as shown in Figure 3(a). The reasons for the measurement at 2.9 V are as follows: electrode reactions do not occur at this potential, allowing observations on the surface films generated on the electrode by CV without transformation into other physicochemical states by electrochemical reactions. Moreover, Figure 3(b) shows the results obtained in the contact mode similar to that shown in Figure 2(b), and the lack of physical contact between the electrode surface and AFM probes during surface film formation rules out any possible effect of the contact mode on the surface film generation. Undoubtedly, the observations in Figure 3(b) result from the formation of surface films after one cycle.

To discover any solvent coinsertion in graphite in any situation independent of any effect produced from the AFM probes, the film material formed on the surface of the electrode was physically removed using probes. AFM measurements were performed in both the contact mode and non-contact mode between the probe and sample. Accordingly, by appropriately controlling the force applied between the probe and sample while performing AFM in the contact mode, the film covering the graphite surface was partially removed.

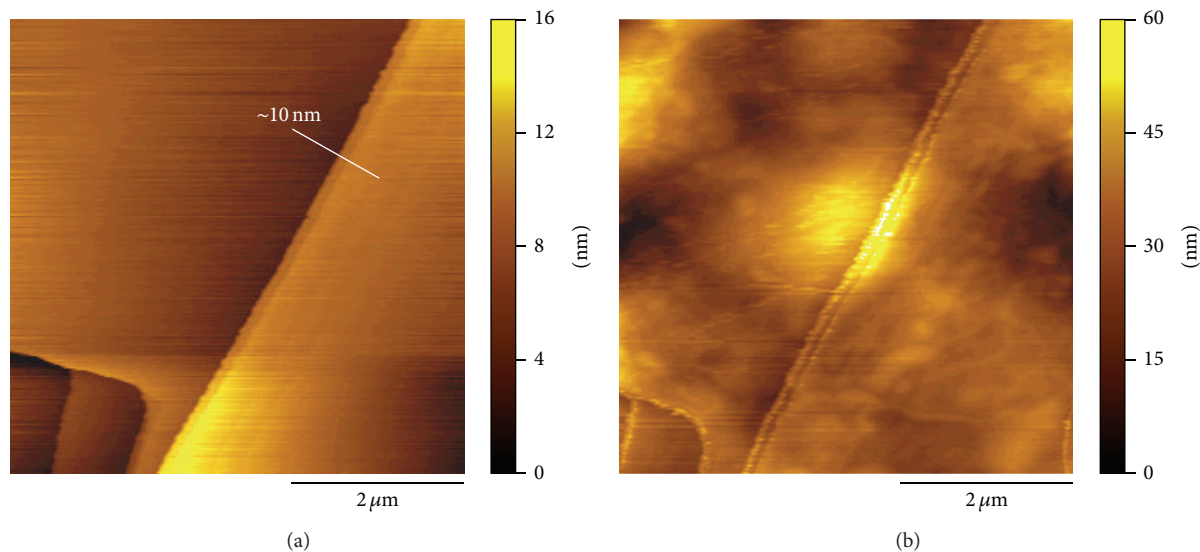


FIGURE 3: *In situ* AFM images ($5 \times 5 \mu\text{m}^2$) of the HOPG basal plane surface obtained at 2.9 V (a) before and (b) after the first cycle CV at 5 mV s^{-1} in 1 M $\text{LiClO}_4/\text{EC} + \text{DEC}$.

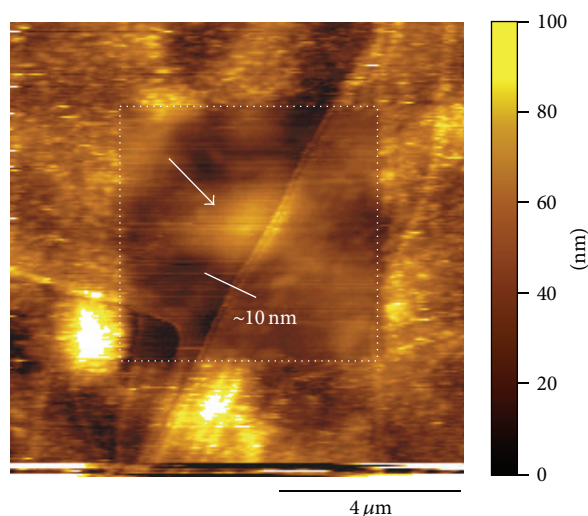


FIGURE 4: *In situ* AFM image of an expanded area ($10 \times 10 \mu\text{m}^2$) of the HOPG basal plane surface obtained at 2.9 V after the first cycle of CV. The dotted square shows the area observed after the first cycle in Figure 2(b).

This method was also used by the Ogumi group [14–16]. The results after the removal of the film obtained in Figure 3(b) are shown in Figure 4. The area indicated by the dotted line square in Figure 4 is identical to the area shown by $5 \times 5 \mu\text{m}^2$ in Figure 3(b) and is the region where the surface films are removed by the AFM probe. The surrounding area still shows the remaining film, indicating the selected removal of the film from the central area of $5 \times 5 \mu\text{m}^2$. Several blisters were noticed on the graphite surface from which the film was removed. These blisters were very similar to that reported by the Ogumi group [14, 16] and can be regarded as structures resulting from the decomposition of the solvent intercalated inside graphite, proving the solvent cointercalation.

Figure 3(a) also shows that the step edge on the electrode surface before the occurrence of electrode reaction is situated over the blister, indicated by the white arrow at the center of Figure 4. In other words, the blister structure is not caused by the decomposed electrolyte attached to the top of the graphite surface but rather is a result of the swollen decomposed product of solvated lithium ions intercalated between the graphite layers.

The results from the CV and AFM analyses indicate that the electrochemical reactions occurred during the solvent cointercalation in the potential range 0.9–0.4 V. However, since AFM is an analytical method presenting information only on a localized area, the localized reaction cannot be assumed to occur over the entire electrode surface. Thus, more investigations considering other aspects are required. Other electrodes with similar areas but with a different number of step edges where intercalation and deintercalation of lithium ion occur were used. The reason for using different electrodes during the investigation was the expectation of similar electrolyte decomposition reactions on the electrodes, even though a large difference may be observed in the solvent cointercalation phenomenon. With a similar intention, the CV behavior was investigated using two different HOPG electrodes with very different mosaic spread values, as shown in Figure 4. Mosaic spread is a factor indicating the crystallinity of HOPG. A higher value indicates inferior crystalline properties (higher number of step edges on the electrode surface). The ZYH electrode has a mosaic spread approximately nine times greater than that of the ZYA electrode and significantly higher current flow at $\sim 0.8 \text{ V}$ range related to the solvent cointercalation reaction as shown in Figure 5. This result is consistent with the expectation that the solvent cointercalation is much more pronounced at the electrode containing a higher number of step edges. Therefore, it can be assumed to be actively involved in the graphite surface film formation reactions.

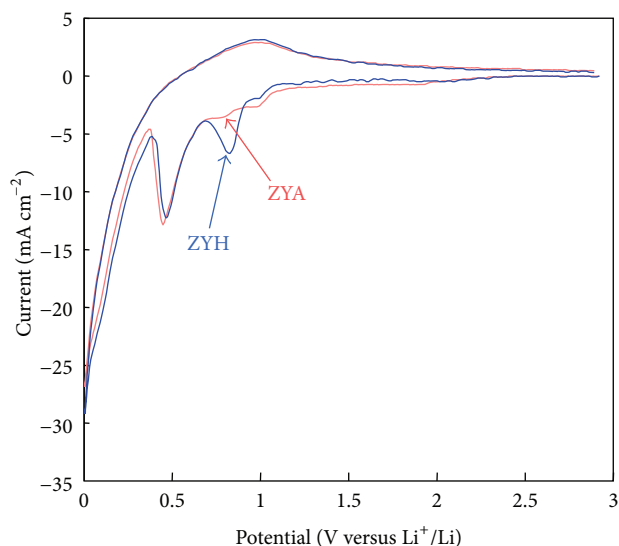


FIGURE 5: Cyclic voltammograms in the first cycle of ZYA and ZYH samples in 1 M $\text{LiClO}_4/\text{EC} + \text{DEC}$. Sweep rate: 0.5 mV s^{-1} .

4. Conclusions

In this study, the surface film formation reactions occurring at the interface between the negatively charged graphite electrode and electrolyte in lithium secondary batteries were investigated. The direct and obvious evidence shows that solvent cointercalation reaction occurred at the initial stage of the surface film formation as indicated by the *in situ* AFM analysis. The formation of blisters was also confirmed after the decomposition of lithium ions. These blisters were presumed to suppress the continued intercalation of the solvent in the graphite layer. In contrast, this may also be one of the reasons for the decrease in capacity of the graphite electrode by obstructing the movement of the lithium ions and reducing the number of sites for lithium ions intercalation, as a result of the existence of decomposed solvent products within the graphite. Another possibility of the decreased electrode capacity may be the stress resulting during the intercalation and decomposition of the solvent, thereby detaching the graphite layer and decreasing the number of active materials used. To minimize these negative effects, further studies on the physicochemical properties of the blisters are required.

Conflict of Interests

The authors declare that there is no conflict of interests regarding the publication of this paper.

Acknowledgments

This research was financially supported by the Ministry of Education (MOE) and National Research Foundation of Korea (NRF) through the Human Resource Training Project for Regional Innovation (no. 2014H1C1A1060729). This research was supported by Soonchunhyang University Research Fund.

References

- [1] J. R. Dahn, "Phase diagram of Li_xC_6 ," *Physical Review B*, vol. 44, no. 17, pp. 9170–9177, 1991.
- [2] T. Ohzuku, Y. Iwakoshi, and K. Sawai, "Formation of lithium-graphite intercalation compounds in nonaqueous electrolytes and their application as a negative electrode for a lithium ion (shuttlecock) cell," *Journal of the Electrochemical Society*, vol. 140, no. 9, pp. 2490–2497, 1993.
- [3] Z. Jiang, M. Alamgir, and K. M. Abraham, "Electrochemical intercalation of Li into graphite in Li/polymer electrolyte/graphite cells," *Journal of the Electrochemical Society*, vol. 142, no. 2, pp. 333–340, 1995.
- [4] M. Inaba, H. Yoshida, Z. Ogumi, T. Abe, Y. Mizutani, and M. Asano, "In situ Raman study on electrochemical Li intercalation into graphite," *Journal of the Electrochemical Society*, vol. 142, no. 1, pp. 20–26, 1995.
- [5] R. Yazami and D. Guerard, "Some aspects on the preparation, structure and physical and electrochemical properties of Li_xC_6 ," *Journal of Power Sources*, vol. 43, no. 1–3, pp. 39–46, 1993.
- [6] E. Peled, "The electrochemical behavior of alkali and alkaline earth metals in nonaqueous battery systems? The solid electrolyte interphase model," *Journal of the Electrochemical Society*, vol. 126, no. 12, pp. 2047–2051, 1979.
- [7] R. Fong, U. von Sacken, and J. R. Dahn, "Studies of lithium intercalation into carbons using nonaqueous electrochemical cells," *Journal of the Electrochemical Society*, vol. 137, no. 7, pp. 2009–2013, 1990.
- [8] S. Malmgren, K. Ciosek, R. Lindblad et al., "Consequences of air exposure on the lithiated graphite SEI," *Electrochimica Acta*, vol. 105, pp. 83–91, 2013.
- [9] P. Verma, P. Maire, and P. Novák, "A review of the features and analyses of the solid electrolyte interphase in Li-ion batteries," *Electrochimica Acta*, vol. 55, no. 22, pp. 6332–6341, 2010.
- [10] J. O. Besenhard, M. Winter, J. Yang, and W. Biberacher, "Filming mechanism of lithium-carbon anodes in organic and inorganic electrolytes," *Journal of Power Sources*, vol. 54, no. 2, pp. 228–231, 1995.
- [11] M. Winter, G. H. Wrodnigg, J. O. Besenhard, W. Biberacher, and P. Novák, "Dilatometric investigations of graphite electrodes in nonaqueous lithium battery electrolytes," *Journal of the Electrochemical Society*, vol. 147, no. 7, pp. 2427–2431, 2000.
- [12] M. Inaba, Z. Siroma, A. Funabiki et al., "Electrochemical scanning tunneling microscopy observation of highly oriented pyrolytic graphite surface reactions in an ethylene carbonate-based electrolyte solution," *Langmuir*, vol. 12, no. 6, pp. 1535–1540, 1996.
- [13] M. Inaba, Z. Siroma, Y. Kawatate, A. Funabiki, and Z. Ogumi, "Electrochemical scanning tunneling microscopy analysis of the surface reactions on graphite basal plane in ethylene carbonate-based solvents and propylene carbonate," *Journal of Power Sources*, vol. 68, no. 2, pp. 221–226, 1997.
- [14] S.-K. Jeong, M. Inaba, T. Abe, and Z. Ogumi, "Surface Film Formation on Graphite Negative Electrode in Lithium-Ion Batteries: AFM Study in an Ethylene Carbonate-Based Solution," *Journal of the Electrochemical Society*, vol. 148, no. 9, pp. A989–A993, 2001.
- [15] S.-K. Jeong, M. Inaba, R. Mogi, Y. Iriyama, T. Abe, and Z. Ogumi, "Surface film formation on a graphite negative electrode in lithium-ion batteries: Atomic force microscopy study on the effects of film-forming additives in propylene carbonate solutions," *Langmuir*, vol. 17, no. 26, pp. 8281–8286, 2001.

- [16] S.-K. Jeong, M. Inaba, Y. Iriyama, T. Abe, and Z. Ogumi, "Surface film formation on a graphite negative electrode in lithium-ion batteries: AFM study on the effects of co-solvents in ethylene carbonate-based solutions," *Electrochimica Acta*, vol. 47, no. 12, pp. 1975–1982, 2002.
- [17] S.-K. Jeong, M. Inaba, Y. Iriyama, T. Abe, and Z. Ogumi, "AFM study of surface film formation on a composite graphite electrode in lithium-ion batteries," *Journal of Power Sources*, vol. 119–121, pp. 555–560, 2003.
- [18] W. Huang and R. Frech, "In situ Raman studies of graphite surface structures during lithium electrochemical intercalation," *Journal of the Electrochemical Society*, vol. 145, no. 3, pp. 765–770, 1998.
- [19] S. Tsubouchi, Y. Domi, T. Doi et al., "Spectroscopic analysis of surface layers in close contact with edge plane graphite negative-electrodes," *Journal of the Electrochemical Society*, vol. 160, no. 4, pp. A575–A580, 2013.
- [20] Y. Domi, M. Ochida, S. Tsubouchi et al., "Electrochemical AFM observation of the HOPG edge plane in ethylene carbonate-based electrolytes containing film-forming additives," *Journal of the Electrochemical Society*, vol. 159, no. 8, pp. A1292–A1297, 2012.
- [21] P. Novák, D. Goers, L. Hardwick et al., "Advanced in situ characterization methods applied to carbonaceous materials," *Journal of Power Sources*, vol. 146, no. 1-2, pp. 15–20, 2005.
- [22] H. Nakagawa, Y. Domi, T. Doi et al., "In situ Raman study on the structural degradation of a graphite composite negative-electrode and the influence of the salt in the electrolyte solution," *Journal of Power Sources*, vol. 236, pp. 138–144, 2013.

Research Article

Detection of Dissolved Carbon Monoxide in Transformer Oil Using 1.567 μm Diode Laser-Based Photoacoustic Spectroscopy

Qu Zhou,^{1,2} Chao Tang,¹ Shiping Zhu,¹ Weigen Chen,² and Xiaojuan Peng²

¹College of Engineering and Technology, Southwest University, Chongqing 400715, China

²State Key Laboratory of Power Transmission Equipment & System Security and New Technology, Chongqing University, Chongqing 400030, China

Correspondence should be addressed to Qu Zhou; zhouqu@swu.edu.cn and Weigen Chen; 15541342@qq.com

Received 6 August 2014; Revised 10 October 2014; Accepted 11 October 2014

Academic Editor: Wen Zeng

Copyright © 2015 Qu Zhou et al. This is an open access article distributed under the Creative Commons Attribution License, which permits unrestricted use, distribution, and reproduction in any medium, provided the original work is properly cited.

Carbon monoxide (CO) is one of the most important fault characteristic gases dissolved in power transformer oil. With the advantages of high sensitivity and accuracy, long-term stability, and short detection time, photoacoustic spectroscopy (PAS) has been proven to be one promising sensing technology for trace gas recognition. In this investigation, a tunable PAS experimental system based on a distributed-feedback (DFB) diode laser was proposed for recognizing dissolved CO in transformer oil. The molecular spectral line of CO gas detection was selected at 1.567 μm in the whole experiment. Relationships between the photoacoustic (PA) signal and gas pressure, temperature, laser power, and CO gas concentration were measured and discussed in detail, respectively. Finally, based on the least square regression theory, a novel quantitative identification method for CO gas detection with the PAS experimental system was proposed. And a comparative research about the gas detection performances performed by the PAS system and gas chromatography (GC) measurement was presented. All results lay a solid foundation for exploring a portable and tunable CO gas PAS detection device for practical application in future.

1. Introduction

Large power transformers are costly and essential apparatus in power transmission and distribution system [1, 2], and their running conditions have important influence on the safety and reliability of the whole power system [3, 4]. Carbon monoxide is a critical fault characteristic gas dissolved in oil-filled power transformers, which can timely and effectively reflect the insulation performance of transformer insulating paper and paperboard [5]. And it has been widely used in assessing the insulation state of running transformers. Online monitoring and analyzing the gas concentration and generation rate of dissolved CO gas in transformer oil plays a quite significant role in transformer condition assessment and fault diagnosis [6]. In recent years, interest in CO gas detection has been extremely simulated and many researchers have been immersed into this field [5–9]. And metal oxide semiconductors, palladium gate field effect transistors, catalytic combustion sensors, and fuel cell sensors are the main

conventional methods used to detect and analyze dissolved gases in transformer oil [5, 7].

As a novel gas sensing technology, photoacoustic spectrometry (PAS) has obtained great development and reported effectively for recognition of both reducing and oxidizing gases [10, 11]. For instance, Spagnolo et al. [10] reported a NO trace gas sensor based on quartz-enhanced photoacoustic spectroscopy and external cavity quantum cascade laser. Lewicki et al. [11] designed a 2 μm diode laser-based quartz-enhanced photoacoustic spectroscopy system for carbon dioxide and ammonia detection. Due to the advantages of high sensitivity and accuracy, rapid detection speed, long-term stability, and no gas separation and consumption [12, 13], PAS would be a promising detection technology for dissolved fault characteristic gases in transformer oil, such as hydrogen, carbon monoxide, methane, ethane, ethylene, and acetylene [3].

And with the advantages of narrow line width, tunable wavelength, and so forth, diode laser has developed as

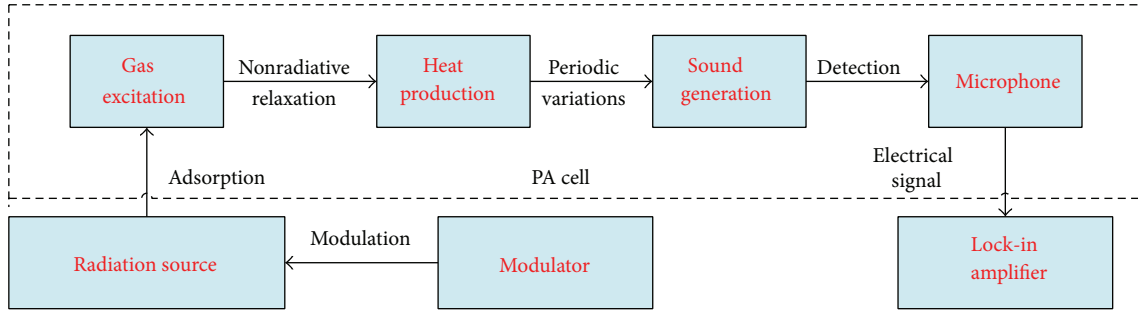


FIGURE 1: The principle of gas photoacoustic effect.

an ideal light source, which can be used to analyze molecular absorption lines and obtain good selectivity, large dynamic range, excellent portability, and adjustability [14]. In this study, a distributed-feedback (DFB) diode laser-based PAS experimental system was proposed, and the molecular spectral line was selected at $1.567 \mu\text{m}$ for CO detection. CO response characteristics between the PA signals and gas pressure, temperature, laser power, and gas concentration were performed and discussed. Furthermore, the least square regression method was applied to quantitatively recognize the gas concentrations from the measured PA signals.

2. Experimental Setup

2.1. The Principle of Gas Photoacoustic Spectroscopy. Photoacoustic spectrometry is a kind of calorimetric spectroscopy technique with high sensitive and dynamic range based on the gas photoacoustic effect [6]. The basic principle of gas photoacoustic effect is represented in Figure 1. Generation and detection of photoacoustic signal is a complex energy conversion process, which combines with light, heat, sound, and electricity.

Firstly, light generated from the radiation source is modulated by a modulator and passes into a PA cell container. Some gas molecules will absorb certain wavelengths of modulated light and excite to the upper energy state from its ground states. Then the absorbed energy is released to the PA cell and heats the gas molecule periodically to generate the same frequency thermoacoustic waves with the modulation light. Finally, the generated acoustic waves are sensed by high sensitivity of microphone and translated into electrical signals.

On the basis of the fluid mechanism and thermodynamics law, the gas PA signal S_{PA} can be expressed as follows [6, 15]:

$$S_{\text{PA}} = C_{\text{cell}} \alpha P_0. \quad (1)$$

As shown in (1) S_{PA} , C_{cell} , α , and P_0 denote the gas PA signal, the PA cell constant, the gas absorption coefficient, and the incident laser power, respectively, where the gas PA signal, S_{PA} , is proportional to the product of gas absorption coefficient and incident laser power. And the PA cell constant C_{cell} reflects the conversion from light energy to acoustic energy.

2.2. The Photoacoustic Spectroscopy Experimental Setup. In this investigation, a tunable PAS experimental setup for gas

recognition with a DFB diode laser was proposed [15] and the structure diagram of the gas PAS detection system was shown in Figure 2. It can be clearly seen in Figure 2 that the main experimental platform consists of several components including laser controller, laser source, lock-in amplifier, frequency modulator, modulating chopper, pressure sensor, temperature sensor, microphone, and laser power meter.

As shown in Figure 2 a certain wavelength of infrared radiation light generated by the diode laser is modulated to a particular frequency of intermittent beams by a modulating chopper firstly and then is injected into the PA cell to excite the PA effect. Finally, the excited acoustic waves are detected by a microphone for gas recognition. For the purpose of minimizing the acoustic noise generated by wall absorption, a collimator is installed at the end of the laser so that the beams could be aligned with the longitudinal axis of the PA cell.

A butterfly shape DFB diode laser (NLK1L5GAAA, NEL Corporation, Japan) was selected as the laser source, which was mainly fabricated with InGaAsP material. The central wavelength of the DFB diode laser is $1.567 \mu\text{m}$ with a maximum power output of 20 mW, a narrow linewidth of 2 MHz, and a side-mode suppression ratio of 43 dB. The deviation of its radiation wavelength is not bigger than 1 nm under room temperature. The diode laser is operated at an amplitude-modulation mode, and its working temperature and injection current are controlled by a laser controller (ITC502, THORLABS Corporation, USA) to tune the emission wavelength. A mechanical modulating chopper (SR540, Stanford Research System Inc., Sunnyvale, CA, USA) was applied to obtain a particular frequency of intermittent beams and a microphone (EK-3024, Knowles Corporation, USA) was used to acquire the PA signal with a sensitivity of 22 mV/Pa. Finally the PA signal was measured using a lock-in amplifier (SR830, Stanford Research System Inc., Sunnyvale, CA, USA).

The PA cell is the core of the gas PAS detection system, and its performance has a significant influence on the sensitivity and stability of the experimental system [16]. In our test the PA cell is made of stainless steel which has a high heat conduction coefficient. And it is designed as a first longitudinal resonant mode and the physical figure and the longitudinal section drawing of the PA cell are shown in Figures 3 and 4. One can clearly see from Figures 3 and 4 that the PA cell mainly contains five departments: a cylindrical resonator cavity, two Brewster windows, and two buffer volumes.

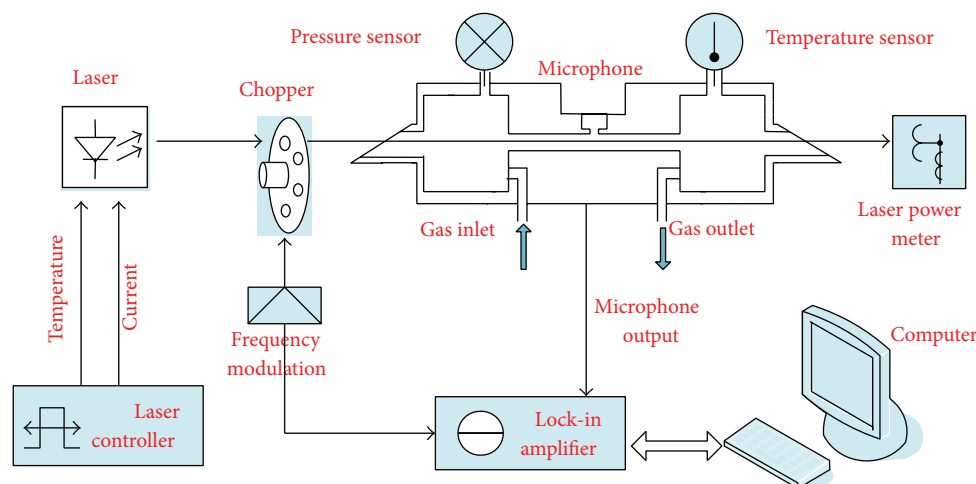


FIGURE 2: The structure diagram of the gas PAS detection system.

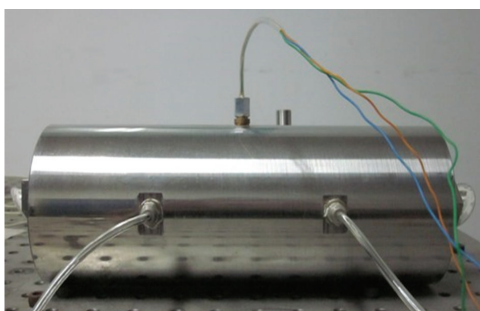


FIGURE 3: The physical figure of the fabricated PA cell.

The length and width of the resonator cavity are 120 mm and 6 mm, respectively, and 60 mm and 30 mm for the length and radius of the buffer volume, separately. The theoretical resonance frequency, quality factor, and cell constant of the PA cell in our experiment are calculated to be about 1395.7 Hz, 32.8, and 3775.35 Pa-cm/W.

3. Results and Discussion

3.1. The Molecular Spectral Line of Carbon Monoxide. Gas detection with the PAS system mainly depends on the wavelength of the radiation light source; thus the radiation wavelength of the DFB diode laser should be well-matched with the characteristic spectrum line of the target gas [6]. The basic principles [14] for choosing the characteristic wavelengths of CO gas are as follows.

All characteristic wavelengths should be covered in the spectrum output range of the radiation source. Cross-interference between CO gas and the potential interface gases (other characteristic fault gases dissolved in transformer oil and impurity gases) should be avoided or decreased as much as possible. And the characteristic wavelength should be chosen at a stronger adsorption place.

Combined with the HITRAN 2008 molecular spectroscopic database [17], we calculated the near infrared spectra of

CO gas using the line-by-line integral method. Figure 5 shows the calculating result of CO gas with the temperature of 300 K, the pressure of 0.1 MPa, and concentration of 1000 $\mu\text{L/L}$.

According to the selecting guidelines of gas characteristic absorption lines, the line at 6380.3012 cm^{-1} ($1.567\text{ }\mu\text{m}$) with an intensity of $2.138 \times 10^{-23}\text{ cm}^{-1}$ ($\text{molecule}\cdot\text{cm}^{-2}$) was chosen as the characteristic absorption line of CO gas in the following experiments. Meanwhile, no obvious spectral absorption has been observed at $1.567\text{ }\mu\text{m}$ for other fault gases dissolved in transformer oil, implying an excellent selection absorption line for CO detection.

3.2. The PAS Performances of Carbon Monoxide. Since the PA cell is sealed during the whole measurement, a variation of the CO gas pressure will directly change the gas PA signal immediately. The influence of gas pressure to PA signal is mainly by means of the change of gas molecular absorption coefficient. Figure 6 shows the PA signal of CO gas as a function of gas pressure ranging from 0.03 MPa to 0.12 MPa, where the power of the DFB diode laser was operated at 13.7 mW with a radiation wavelength of $1.567\text{ }\mu\text{m}$, atmospheric temperature of 300 K, and CO gas concentration of 10000 $\mu\text{L/L}$. As shown in Figure 6, the PA signal increases rapidly first in linearity with increasing the gas pressure below 0.08 MPa and nearly reaches saturation at 0.10 MPa. This is mainly due to the variation of the gas molecular absorption spectrum broadening under different pressure. Therefore, if the gas pressure could be controlled and maintained equal to and higher than 0.1 MPa, the influence of the gas pressure to PA signal will be eliminated nearly. The saturated PA signal to 10000 $\mu\text{L/L}$ of CO gas under the current condition is about 28.56 μV .

Temperature is another significance influence factor to the PA signal. A standard concentration of CO gas was injected into the PA cell slowly in a dynamic flow way under various operating temperature to investigate the PA signal versus operating temperature. In the whole test period, the gas pressure was kept at 0.1 MPa, the integration time of the lock-in amplifier was set as 1 s, and the power of the DFB diode laser was maintained at 13.7 mW. As shown in

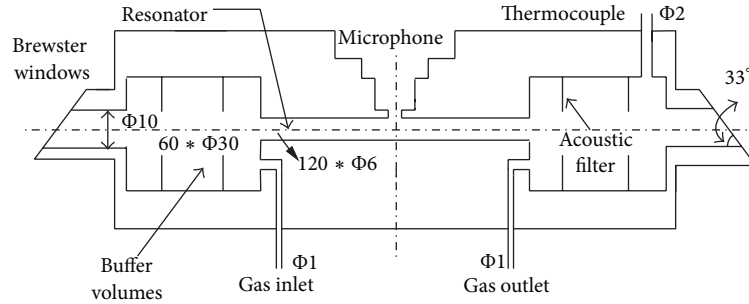


FIGURE 4: The longitudinal section drawing of the PA cell.

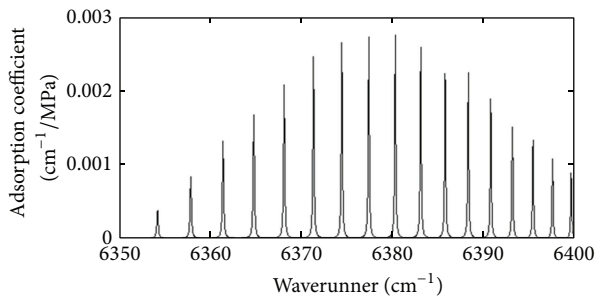


FIGURE 5: The characteristic absorption lines of CO in the spectral range of 6350~6400 cm^{-1} .

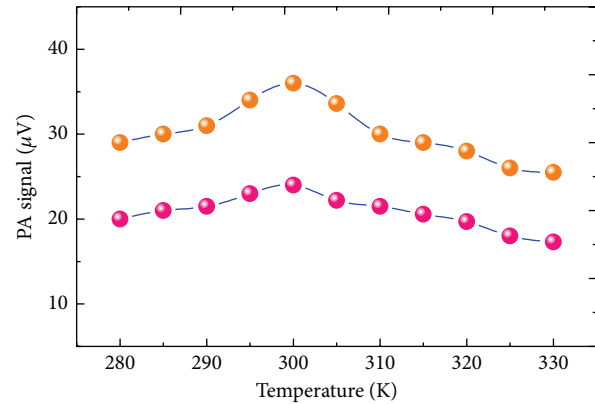


FIGURE 7: The PA signal versus operating temperature ranging from 280 to 330 K.

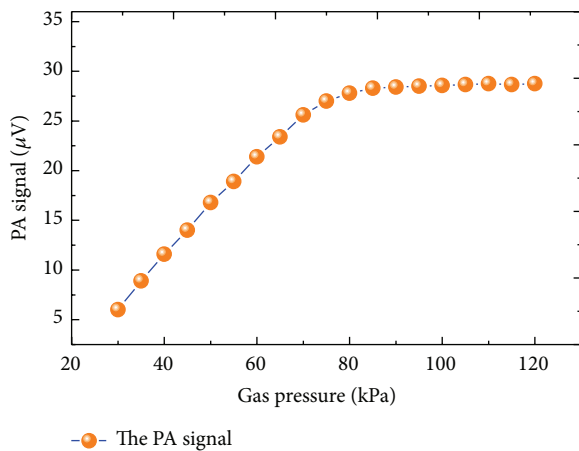


FIGURE 6: The PA signal versus CO gas pressure ranging from 0.03 to 0.12 MPa.

Figure 7, the PA signal increases firstly and reaches its maximum value and then decreases rapidly with the further increasing operating temperature. These results indicate that the chopping frequency should be adjusted timely according to operating temperature during the PAS experiment to obtain the maximum PA signal.

A standard concentration of 5000 $\mu\text{L/L}$ of CO gas was injected into the PA cell slowly. The chopping frequency at 1305 Hz referred to the measured first-order longitudinal resonance frequency was regulated and maintained. The PA response of CO gas versus different levels of laser power

ranging from 3 to 14 mW was investigated through adjusting the laser output power. It is noted that when adjusting the laser output power, there would exist an inevitable migration between the laser radiation wavelength and the characteristic absorption line of CO gas at 1.567 μm . Therefore, a reasonable calibration of the laser radiation wavelength is necessary and should be employed immediately. In this study an effective calibration method was performed as follows. The laser output power was set at the expected value first and then fine-tuned the laser temperature until the PA signal reached its maximum, where the laser radiation wavelength could be supposed to adjust back to the characteristic absorption line of CO gas.

Figure 8 shows the PA signal and linear fit curve of CO gas to laser power ranging from 3 to 14 mW, where the gas pressure was maintained at 0.1 MPa, the integration time of the lock-in amplifier was set as 1 s, and the operating temperature was 300 K. As shown in Figure 8, a good quasilinear relationship between the laser power and the PA signal has been measured, which is well consistent with (1). That is to say the number of the excited gas molecules increases with an increasing laser output power at a certain concentration of target gas, and it should be pointed out that the PA signal

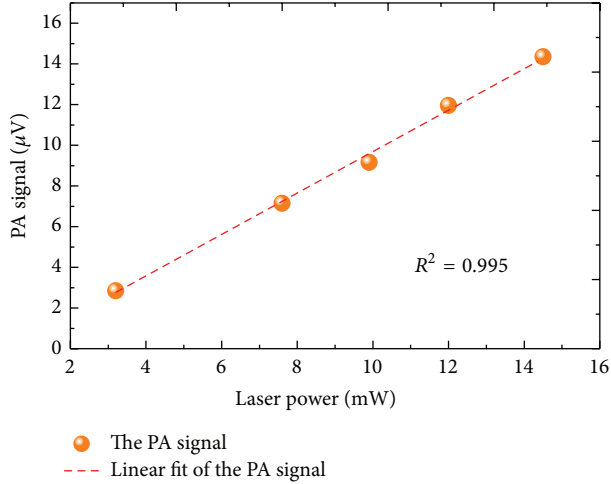


FIGURE 8: The PA signal versus laser power in the range of 3 to 14 mW.

will not increase consistently and turn to be saturated at a threshold power.

The gas responses of the PAS detection system to various concentrations of CO gas were measured and represented in Figure 9. In our experiment different concentrations of CO gas were obtained using a RCS2000-A computer controlled automatic gas distribution system with high purity nitrogen as the carrier gas. The measurement was performed under the optimum condition, namely, a gas pressure of 0.1 MPa, a laser output power of 13.7 mW, an integration time of 1 s, a laser radiation wavelength of 1.567 μm , a chopping frequency of 1305 Hz, and an operating temperature of 300 K. It can be seen clearly in Figure 10 that a good linearity between the PA signal and CO gas concentration was found, well consistent with (1) as well, and the linear regression coefficient R^2 is as high as 0.997. Similarly with the relationship between the PA signal and the laser power, it should be pointed out that the PA signal will not increase unceasingly, and a saturation phenomenon would appear at the corresponding threshold concentration.

3.3. The PAS Quantitative Analysis of Carbon Monoxide.

Based on the least square regression principle [15, 18], a novel quantitative identification method was proposed for CO gas recognition with the PAS experimental system. The relationship between the measured PA signal and the known CO concentration is established using the least square regression method first. Then according to the established regression relationship, the concentration value of an unknown CO gas can be derived from the PA signal value measured by the PAS detection system. This proposed method can effectively avoid the measurement errors introduced by the PA cell constant, gas absorption coefficient, laser power, and so on. Various concentrations of CO ranging from 1000 to 10000 $\mu\text{L/L}$ have been obtained with the RCS2000-A gas distribution system and measured by our experimental device.

As shows in Figure 10 the PA signal exhibits a good linear relationship with CO gas in the whole concentration range.

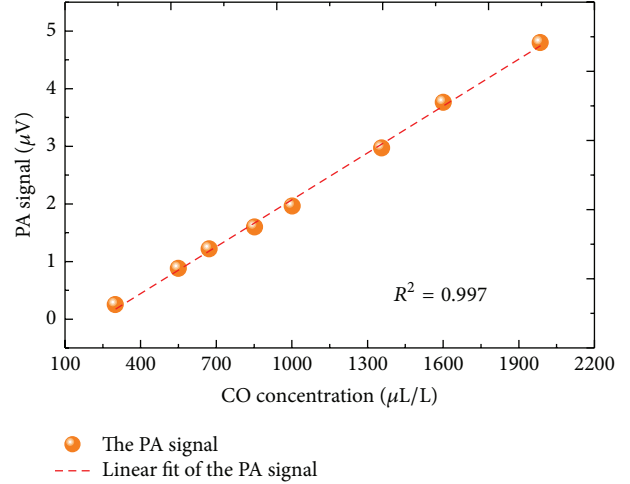


FIGURE 9: The PA signal versus CO concentration ranging from 300 to 2000 $\mu\text{L/L}$.

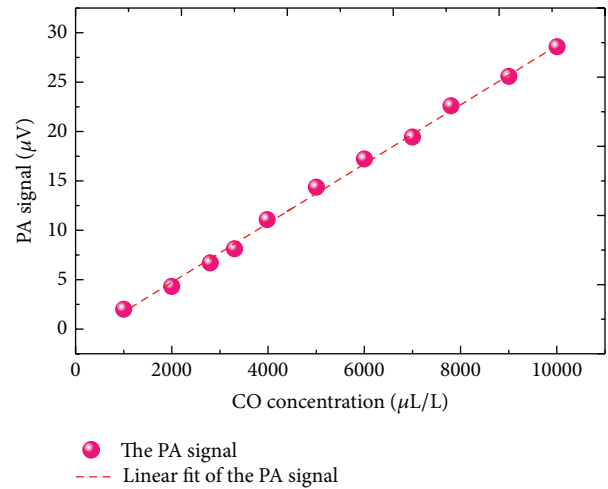


FIGURE 10: The regression relationship between CO concentration and PA signal with the least square regression method.

The regression relationship is

$$y_{\text{CO}} = 0.003x_{\text{CO}} - 1.3241. \quad (2)$$

A comparison study about the PAS detection results with the gas chromatography (GC) test results was performed to investigate the detection accuracy of PAS system. Detection error (e) is defined as the deviation percentage of C_{PAS} compared with C_{GC} , where C_{PAS} and C_{GC} denote the PAS detection value and the GC detection value, respectively:

$$e = \frac{|C_{\text{PAS}} - C_{\text{GC}}|}{C_{\text{GC}}} \times 100\%. \quad (3)$$

One can clearly see in Table 1 that detection error from the PAS measurement result compared with the GC method is quite small, that is, not greater than 2%. Considering

TABLE 1: Measurement results detected by PAS and GA.

CO concentration	PAS ($\mu\text{L/L}$)	GA ($\mu\text{L/L}$)	Detection error (%)
Sample 1	5019.4	5003.8	0.31
Sample 2	2012.7	2000.6	0.61
Sample 3	1011.5	1002.3	0.92
Sample 4	860.9	851.7	1.08
Sample 5	682.1	673.9	1.22
Sample 6	559.8	550.2	1.75

the error induced by gas chromatograph, gas distribution system, and other laboratory equipment and human factors, the regression results are acceptable. All results indicate that the proposed gas analysis method based on the DFB diode laser PAS system and combined with the least square regression approach is feasible and effective.

4. Conclusion

In this investigation, we proposed a tunable distributed-feedback (DFB) diode laser-based PAS system for the purpose of recognizing dissolved CO in transformer oil. According to the HITRAN 2008 molecular spectroscopic database, the characteristic absorption line at 6380.3012 cm^{-1} ($1.567\text{ }\mu\text{m}$) was selected as the molecular spectral line of CO gas. Gas response characteristics were measured with the proposed PAS system, and relationships between the sensing performances and gas pressure, temperature, laser power, and gas concentration were investigated in detail. Moreover, the least square regression approach was applied to quantitatively recognize the CO gas concentration from the measured PA signal. Compared with the GC measurement, error from the PAS system is not bigger than 2%. All results indicate the proposed method is an effective and feasible way for CO gas recognition, laying a solid foundation for exploring PAS online monitoring device for practical application.

Conflict of Interests

The authors declare that there is no conflict of interests regarding the publication of this paper.

Acknowledgments

This work has been supported in part by Fundamental Research Funds for the Central Universities (nos. SWU-114051 and XDJK2014B031) and National Special Funds for Major Research Instrumentation Development (no. 2012YQ-160007).

References

- [1] M. Duval, "A review of faults detectable by gas-in-oil analysis in transformers," *IEEE Electrical Insulation Magazine*, vol. 18, no. 3, pp. 8–17, 2002.
- [2] M. Wang, A. J. Vandermaar, and K. D. Srivastava, "Review of condition assessment of power transformers in service," *IEEE Electrical Insulation Magazine*, vol. 18, no. 6, pp. 12–25, 2002.
- [3] W. Fu, Q. Zhou, J. Zou, Z. Gu, W. Chen, and C. Wang, "Using a sensitive optical system to analyze gases dissolved in samples extracted from transformer oil," *IEEE Electrical Insulation Magazine*, vol. 30, no. 5, pp. 15–22, 2014.
- [4] M. Duval and J. J. Dukarm, "Improving the reliability of transformer gas-in-oil diagnosis," *IEEE Electrical Insulation Magazine*, vol. 21, no. 4, pp. 21–27, 2005.
- [5] W. Chen, Q. Zhou, F. Wan, and T. Gao, "Gas sensing properties and mechanism of Nano-SnO₂-based sensor for hydrogen and carbon monoxide," *Journal of Nanomaterials*, vol. 2012, Article ID 612420, 9 pages, 2012.
- [6] Y. Yun, W. Chen, Y. Wang, and C. Pan, "Photoacoustic detection of dissolved gases in transformer oil," *European Transactions on Electrical Power*, vol. 18, no. 6, pp. 562–576, 2008.
- [7] W. Chen, Q. Zhou, and S. Peng, "Hydrothermal synthesis of Pt-, Fe-, and Zn-doped SnO₂ nanospheres and carbon monoxide sensing properties," *Advances in Materials Science and Engineering*, vol. 2013, Article ID 578460, 8 pages, 2013.
- [8] H. Teichert, T. Fernholz, and V. Ebert, "Simultaneous in situ measurement of CO, H₂O, and gas temperatures in a full-sized coal-fired power plant by near-infrared diode lasers," *Applied Optics*, vol. 42, no. 12, pp. 2043–2051, 2003.
- [9] R. Wang, D. Zhang, W. Sun, Z. Han, and C. Liu, "A novel aluminum-doped carbon nanotubes sensor for carbon monoxide," *Journal of Molecular Structure: THEOCHEM*, vol. 806, no. 1–3, pp. 93–97, 2007.
- [10] V. Spagnolo, A. A. Kosterev, L. Dong, R. Lewicki, and F. K. Tittel, "NO trace gas sensor based on quartz-enhanced photoacoustic spectroscopy and external cavity quantum cascade laser," *Applied Physics B: Lasers and Optics*, vol. 100, no. 1, pp. 125–130, 2010.
- [11] R. Lewicki, G. Wysocki, A. A. Kosterev, and F. K. Tittel, "Carbon dioxide and ammonia detection using 2 μm diode laser based quartz-enhanced photoacoustic spectroscopy," *Applied Physics B*, vol. 87, no. 1, pp. 157–162, 2007.
- [12] C. Popa, M. Patachia, S. Banita, and D. C. Dumitras, "Exertion in kangoo jumps aerobic: evaluation and interpretation using spectroscopic technique determinations," *Journal of Spectroscopy*, vol. 2013, Article ID 602434, 6 pages, 2013.
- [13] M. A. Gondal, A. Dastageer, and M. H. Shwehdi, "Photoacoustic spectrometry for trace gas analysis and leak detection using different cell geometries," *Talanta*, vol. 62, no. 1, pp. 131–141, 2004.
- [14] T. Laurila, H. Cattaneo, V. Koskinen, J. Kauppinen, and R. Hernberg, "Diode laser-based photoacoustic spectroscopy with interferometrically-enhanced cantilever detection," *Optics Express*, vol. 13, no. 7, pp. 2453–2458, 2005.
- [15] W. Chen, B. Liu, H. Zhou, Y. Wang, and C. Wang, "Diode laser-based photoacoustic spectroscopy detection of acetylene gas and its quantitative analysis," *European Transactions on Electrical Power*, vol. 22, no. 2, pp. 226–234, 2012.
- [16] V. A. Kapitanov, V. Zeninari, B. Parvitte, D. Courtois, and Y. N. Ponomarev, "Optimisation of photoacoustic resonant cells with commercial microphones for diode laser gas detection," *Spectrochimica Acta A: Molecular and Biomolecular Spectroscopy*, vol. 58, no. 11, pp. 2397–2404, 2002.

- [17] L. S. Rothman, I. E. Gordon, A. Barbe et al., "The HITRAN 2008 molecular spectroscopic database," *Journal of Quantitative Spectroscopy and Radiative Transfer*, vol. 110, no. 9-10, pp. 533-572, 2009.
- [18] H. Sun and Q. Wu, "Least square regression with indefinite kernels and coefficient regularization," *Applied and Computational Harmonic Analysis*, vol. 30, no. 1, pp. 96-109, 2011.

Research Article

Hydrothermal Synthesis and Structural Characterization of NiO/SnO₂ Composites and Hydrogen Sensing Properties

Chao Wei,¹ Bin Bo,¹ Fengbo Tao,¹ Yuncai Lu,¹ Shudi Peng,² Wei Song,² and Qu Zhou³

¹ Jiangsu Electric Power Company Research Institute, Nanjing 211103, China

² Chongqing Electric Power Research Institute, Chongqing 401123, China

³ College of Engineering and Technology, Southwest University, Chongqing 400715, China

Correspondence should be addressed to Qu Zhou; zhouqu@swu.edu.cn

Received 6 August 2014; Revised 10 October 2014; Accepted 11 October 2014

Academic Editor: Wen Zeng

Copyright © 2015 Chao Wei et al. This is an open access article distributed under the Creative Commons Attribution License, which permits unrestricted use, distribution, and reproduction in any medium, provided the original work is properly cited.

Pure SnO₂ and NiO doped SnO₂ nanostructures were successfully synthesized via a simple and environment-friendly hydrothermal method. X-ray powder diffraction (XRD), scanning electron microscopy (SEM), energy dispersive X-ray spectroscopy (EDS), and X-ray photoelectron spectra (XPS) were used to investigate the crystalline structures, surface morphologies and microstructures, and element components and their valences of the as-synthesized samples. Furthermore, planar chemical gas sensors based on the synthesized pure SnO₂ and NiO/SnO₂ composites were fabricated and their sensing performances to hydrogen, an important fault characteristic gas dissolved in power transformer oil, were investigated in detail. Gas sensing experiments indicate that the NiO/SnO₂ composites showed much higher gas response and lower working temperature than those of pure SnO₂, which could be ascribed to the formation of p-n heterojunctions between p-type NiO and n-type SnO₂. These results demonstrate that the as-synthesized NiO/SnO₂ composites a promising hydrogen sensing material.

1. Introduction

Larger oil-immersed power transformers are costly and important electrical apparatus in power supply system. Once faults happened on transformers, the safety and reliability of the power system would be affected and cause great damage to the national economy [1, 2]. As hydrogen gas (H₂) is one of the most important fault characteristic gases dissolved in oil-filled power transformers, we can timely and effectively acquire the running condition of power transformer through recognition and analysis of dissolved H₂ gas in oil [3, 4]. In recent years, interest in recognition of dissolved H₂ in transformer oil has been extremely simulated and a great deal of effort has been devoted to this field [5].

Currently, metal oxide semiconductor (MOS) [6], carbon nanotube [7], grapheme [8], infrared spectroscopy, and photoacoustic spectroscopy [9] have been reported for gas detection. And due to the remarkable advantages of simple fabrication technology, rapid response and recovery speed, and low maintenance cost and long service life, metal oxide

SnO₂ has been proved to be the most promising sensing material for H₂ recognition [10–12]. However, there still exist some limitations needed to be further improved, for instance, higher operating temperature, lower gas response, and poor selectivity and stability. Thus, many scientific and technological efforts have been done to perfect SnO₂ sensing performances [5].

Among them three kinds of doping strategies are developed and reported, doping noble metals [6] or rare earth elements, using other n-type semiconductors such as ZnO and TiO₂ to form composites [11, 13], and forming p-n composites with p-type semiconductors [14] such as CuO and NiO. For example, Zeng et al. [6] synthesized Pd²⁺ doped SnO₂ nanostructures by the sol-gel method and investigated their gas sensing performances to hydrogen and its sensing mechanism by the first principles calculation. Tang et al. [15] prepared hollow hierarchical SnO₂-ZnO composite nanofibers by an electrospinning method and reported the SnO₂-ZnO composite nanofibers exhibited excellent methanol selectivity in the presence of ethanol, acetone, formaldehyde, ammonia,

toluene, and benzene at an operating temperature of 350°C. Hieu et al. [16] synthesized p-type NiO nanoparticles decorated n-type SnO₂ nanowires through thermal evaporation and reported that NiO-decorated SnO₂ NW sensors exhibit a significantly enhanced H₂S response with good improved response and recovery times. Shen et al. [17] synthesized NiO-SnO₂ nanofibers via electrospinning and investigated their sensing performances to ethanol with three types of sensor structures.

To the best of our knowledge, reports on the synthesis of p-NiO/n-SnO₂ composites through a simple and environment-friendly hydrothermal method and researches on their sensing properties for recognition of dissolved H₂ in transformer oil have been rare. Herein, in this study, we present sensitive H₂ sensors fabricated from p-NiO and n-SnO₂ nanostructures and measure their gas sensing performances toward H₂. Firstly, pure SnO₂ nanostructures and NiO/SnO₂ composites were synthesized by a hydrothermal method. And then the surface morphologies and structural features of the samples were characterized by X-ray powder diffraction (XRD), scanning electron microscopy (SEM), energy dispersive X-ray spectroscopy (EDS), and X-ray photoelectron spectra (XPS), respectively. Finally, chemical gas sensors were fabricated and their sensing performances toward H₂ were measured. We interestingly find that the NiO/SnO₂ composites sensor exhibits excellent H₂ sensing properties in comparison to the pure SnO₂ based sensor.

2. Experimental

2.1. Preparation of Pure SnO₂ and NiO/SnO₂ Composites. The sensing materials in this study, that is, pure SnO₂ and NiO/SnO₂ composites, were synthesized with a simple, facile, and environment-friendly hydrothermal method. All chemicals were analytical-grade reagents purchased from Beijing Chemical Reagent Co., Ltd. and used as received without any further purification. The detailed synthesis processes were represented as follows.

In a typical synthesis process of NiO/SnO₂ composites, firstly 2.0 mmol SnCl₄·5H₂O, 0.10 mmol Ni(CH₃COOH)₂·4H₂O, 3 mmol ammonium carbonate ((NH₄)₂CO₃), 0.1 g of citric acid, 30 mL absolute ethanol, and 30 mL distilled water were mixed together with intense magnetic stirring in a 100 mL capacity beaker. Then the mixed solution was transferred into a 100 mL Teflon autoclave, sealed, and heated at 180°C for 24 h in an electric furnace. After reaction, the autoclave was cooled to room temperature naturally, and the product was harvested by centrifugation, washed with distilled water and absolute ethanol four times, respectively, and dried at 80°C in air for further use [6, 18]. For comparison, pure SnO₂ nanomaterials were prepared in a similar synthesis process mentioned above except that no Ni(CH₃COOH)₂·4H₂O was added to the precursor solution.

2.2. Structural Characterization of Pure SnO₂ and NiO/SnO₂ Composites. The crystalline structures of the as-prepared samples were performed by X-ray powder diffraction (XRD, Rigaku D/Max-1200X, Japan) with Cu K α radiation operated at 40 kV and 200 mA and a scanning rate of 0.02° s⁻¹ from

20° to 80°. Surface morphologies and microstructures of the as-prepared nanostructures were observed with a Nova 400 Nano field emission scanning electron microscope (FE-SEM, FEI, Hillsboro, OR, USA) equipped with an energy dispersive X-ray spectroscopy (EDS). Element components and their valences of the powders were investigated by the X-ray photoelectron spectra (XPS) performed on an ESCLAB MKII using Al as the exciting source.

2.3. Fabrication and Measurement of Pure SnO₂ and NiO/SnO₂ Based Sensors. Planar chemical gas sensors were fabricated with screen-printing technique and the planar ceramic substrates were purchased from Beijing Elite Tech Co., Ltd., China. The planar chemical gas sensor was made up of three main components: the sensing material, the Ag-Pd interdigital electrode, and the ceramic substrate [2, 19]. The length, width, and thickness of the planar ceramic substrate were 13.4, 7, and 1 mm, respectively. And five pairs of Ag-Pd interdigital electrodes have been preplaced on the planar ceramic substrate with a width of 0.2 mm. Firstly, the as-synthesized sensing materials were mixed with absolute ethanol and distilled water in a weight ratio of 8 : 1 : 1 to form a paste, which was subsequently screen-printed onto the planar ceramic substrate to form a sensing film, and its thickness is about 50 μ m [2, 19]. Then the sensing film was dried in air to remove the unwanted impurities, and a certain amount of antipollution solution was coated onto the surface of the sensing film as a protective layer. Finally, the fabricated sensor was aged in an aging test chamber at 80°C for 48 h.

Gas sensor properties of the fabricated sensors to H₂ were performed on a CGS-ITP (Chemical Gas Sensor-1 Temperature Pressure) intelligent gas sensing analysis system (Beijing Elite Tech Co., Ltd.) [2]. This gas sensing analysis system can automatically record the electrical resistance, sensitivity, and working temperature of the gas sensor as well as the humidity and temperature of environment. The gas response value of the sensor was designated as the ratio of sensor resistance in air to that in a mixture of H₂ gas and air [19, 20]. The response and recovery times were defined as the time taken by the sensor to achieve 90% of the total resistance change in the case of adsorption and desorption, respectively [21, 22]. All measurements were repeated several times to ensure the repeatability and stability of the sensor [23].

3. Results and Discussion

3.1. Structural and Morphological Characterizations. Figure 1 shows the typical XRD patterns of pure SnO₂ and NiO/SnO₂ composites. As shown in Figure 1 both the as-synthesized pure SnO₂ and NiO/SnO₂ composites samples are polycrystalline in nature. It can be clearly seen in Figure 1(a) that the prominent peaks at 26.6°, 33.9°, and 51.8°, which can be well indexed as (110), (101), and (211), respectively, and other smaller peaks well correspond to the standard spectrum of rutile SnO₂ given in the standard data file (JCPDS File number 41-1445). Similar XRD patterns are observed for the as-prepared NiO/SnO₂ composites samples as shown in Figure 1(b), and (111), (200), (220), and (311) peaks could

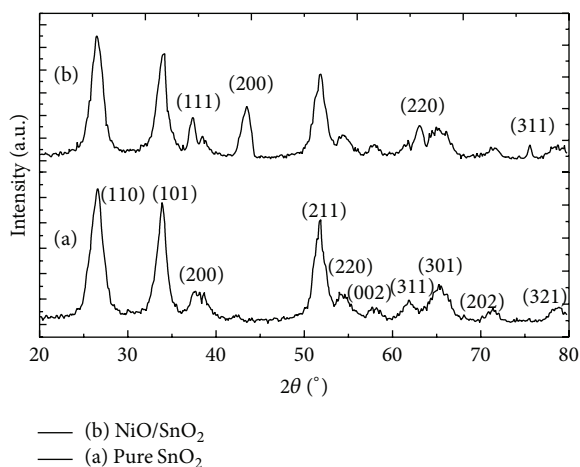


FIGURE 1: XRD patterns of (a) pure SnO_2 and (b) NiO/SnO_2 composites.

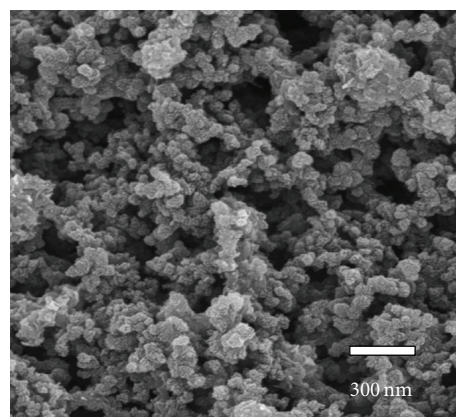
be attributed to nickel oxide. These results are consistent with other XRD characterizations reported in some similar publications [16, 17].

The surface structure and morphology characteristics of the as-synthesized samples were performed by field emission scanning electron microscopy and shown in Figure 2. As shown in Figure 2 the overview images of pure SnO_2 and NiO/SnO_2 composites nanostructures are uniform in size and shape with spherical structure. The diameters of pure SnO_2 nanostructures are ranging from 40 to 50 nm and from 38 to 46 nm for NiO/SnO_2 samples. These results indicate that in this study NiO dopant only has a slight influence on the structures and morphologies of pure SnO_2 nanostructures except for an evidently inhibitory effect on its crystalline growth.

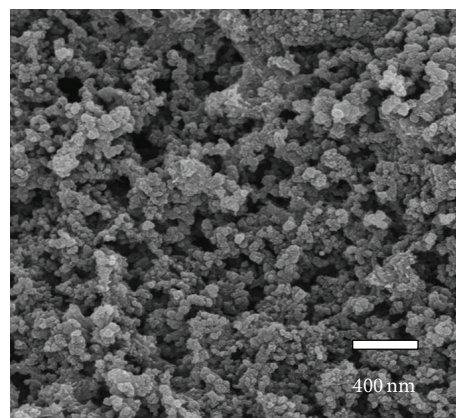
Energy dispersive X-ray spectroscopy measurement was performed to make clear the element components of the as-synthesized samples and check whether Ni element has been successfully doped into the prepared SnO_2 nanostructures. Figure 3 is the EDS spectrum of the synthesized NiO/SnO_2 composites nanostructures, where Sn , Ni , and O element peaks are observed and the atomic ratio of Ni element to Sn element is calculated to be about 8.9 at%. Therefore, we could draw a conclusion that Ni element has been successfully incorporated into the SnO_2 nanostructures.

X-ray photoelectron spectra measurement was further conducted to investigate the compositions and chemical states of the elements existed in the as-prepared products. Figure 4 shows the survey spectrum of pure SnO_2 and NiO/SnO_2 composites nanostructures. As shown in Figure 4(a) only Sn and O spectra are observed and no spectrum from Ni element has been measured, while in Figure 4(b) spectra for Sn , O , and Ni element are found.

Figure 5 shows the high-resolution spectrum of Sn 3d, O 1s, and Ni 2p for the synthesized NiO/SnO_2 composites. As shown in Figures 5(a) and 5(b) the spin orbit components of the Sn 3d_{5/2} and Sn 3d_{3/2} peaks are measured at 487.1 eV and 495.4 eV, and the peak of O 1s is located at 531.9 eV, which



(a)



(b)

FIGURE 2: SEM images of (a) pure SnO_2 and (b) NiO/SnO_2 composites.

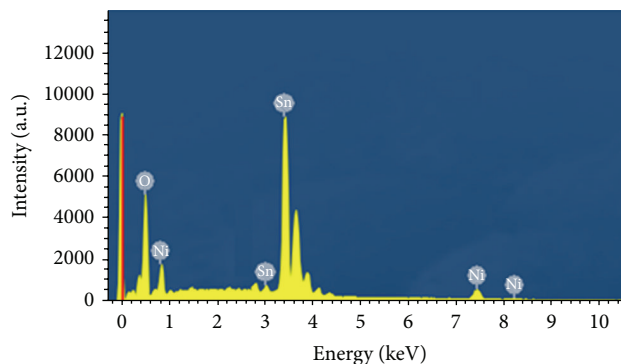


FIGURE 3: EDS spectrum of NiO/SnO_2 composites.

are both well indexed to Sn^{4+} and O^{2-} in a tetragonal rutile SnO_2 structure. And in Figure 5(c) the peaks at 850.1 eV and 861.7 eV are defined as Ni 2p_{3/2} and Ni 2p_{1/2}, which could be assigned to Ni^{2+} ions in the synthesized samples. Meanwhile these Ni 2p_{3/2} and Ni 2p_{1/2} peaks ruled out the existence of Ni and Ni_2O_3 in the as-prepared NiO/SnO_2 composites [24]. Based on these results, we could draw a conclusion

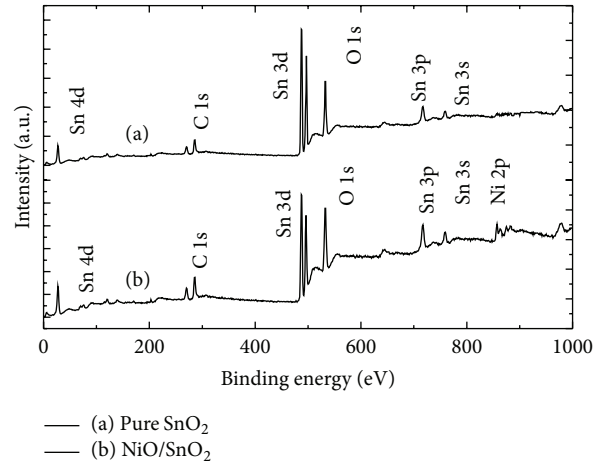


FIGURE 4: XPS patterns of full spectrum of (a) pure SnO_2 and (b) NiO/SnO_2 composites.

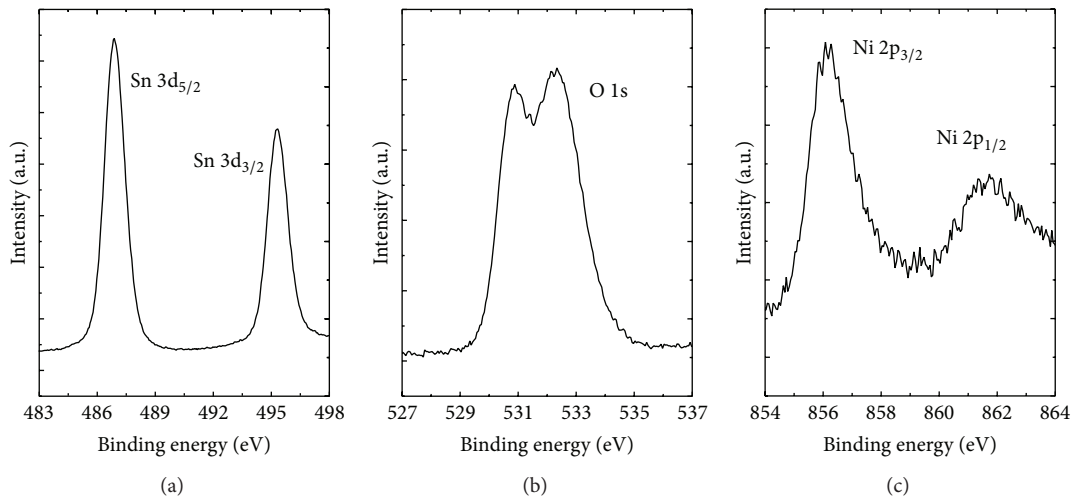


FIGURE 5: High-resolution spectrum of (a) Sn 3d, (b) O 1s, and (c) Ni 2p peaks.

that the synthesized samples are composed of NiO and SnO_2 nanostructures.

3.2. Gas Sensing Properties. Firstly, the sensors fabricated from the synthesized pure SnO_2 and NiO/SnO_2 composites were exposed to a certain concentration of H_2 gas at various working conditions to find out the optimum operating temperature. Figure 6 shows the gas responses of the prepared sensors to $100 \mu\text{L/L}$ of H_2 gas as a function of operating temperature ranging from 150 to 450°C . For each sensor, its gas response increases quickly firstly and obtains its maximum gas response value and then decreases rapidly with further increasing temperature. As shown in Figure 6 the optimum operating temperature of NiO/SnO_2 composites was suggested to be 325°C and 375°C for pure SnO_2 samples, where the sensor exhibits the maximum gas response value at this condition. Simultaneously, at the optimum working condition, the corresponding H_2 gas response is 45.23 for NiO/SnO_2 composites and 13.12 for pure SnO_2 samples.

Figure 7 represents the gas responses of the NiO/SnO_2 composites as a function of H_2 gas concentration with sensor working at its own optimum working condition mentioned above. Compared with pure SnO_2 samples, the NiO/SnO_2 composites sensor exhibits an obvious H_2 sensing enhancement in the whole range of concentrations. Furthermore, the gas response curve of the NiO/SnO_2 composites based sensor demonstrates a quasilinear relationship with H_2 gas concentration in the range of $1\text{--}50 \mu\text{L/L}$. These results imply that the NiO dopant can not only increase the gas response of pure SnO_2 nanostructures but also lower its working temperature with a high linearity of 0.991 in the range of $1\text{--}50 \mu\text{L/L}$.

A possible sensing mechanism is depicted as follows to understand the sensing behaviors of fabricated SnO_2 based gas sensors toward H_2 and get an insight into how the NiO particles improve the sensing properties of SnO_2 based sensor. As we know SnO_2 is a typical n-type semiconducting sensing material and a large number of oxygen vacancies

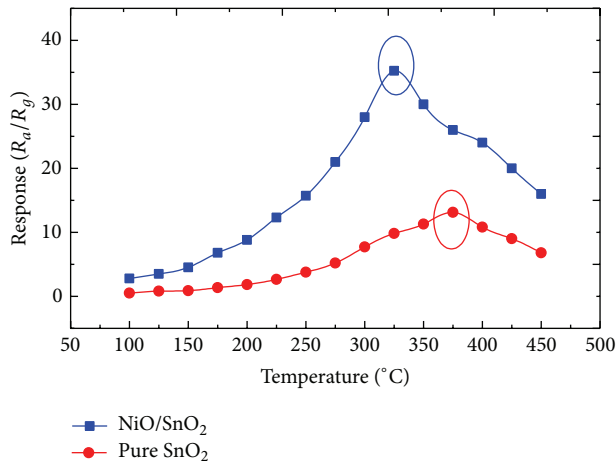


FIGURE 6: Gas responses of pure SnO_2 and NiO/SnO_2 composites based sensor to $100 \mu\text{L}/\text{L}$ of H_2 at different working temperature from 150 to 450°C .

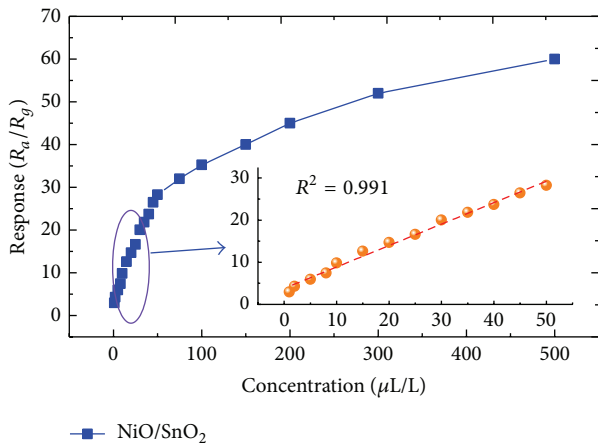


FIGURE 7: Gas responses of NiO/SnO_2 composites based sensor versus different concentration of H_2 . The inset one is the linear fitting curve in the range of 1 to $50 \mu\text{L}/\text{L}$.

exist in its crystal lattices, and its sensing behaviors are predominantly controlled by the surface resistance of sensing materials [5]. In ambient air, free oxygen molecules are absorbed on SnO_2 surface and capture electrons from the conduction band of SnO_2 to form chemisorbed oxygen ions, such as O_2^- , O^{2-} , and O^- [6]. When exposed to a reducing gas ambient (H_2 in this study), H_2 gas molecules react with chemisorbed oxygen ions. The trapped electrons are released back to the conduction band of SnO_2 , resulting in an increase of the carrier concentration and electron mobility; thus a decreased resistance is measured.

The enhanced H_2 gas response and decreased working temperature of NiO/SnO_2 based sensor in the present investigation may be attributed to a p-n heterojunction effect between NiO and SnO_2 surface. A similar p-n heterojunction system has been proposed to explain the enhanced gas sensitivity of $\text{CuO}-\text{SnO}_2$ heterostructures to hydrogen sulfide [17, 25]. Figure 8 depicts the energy band structure

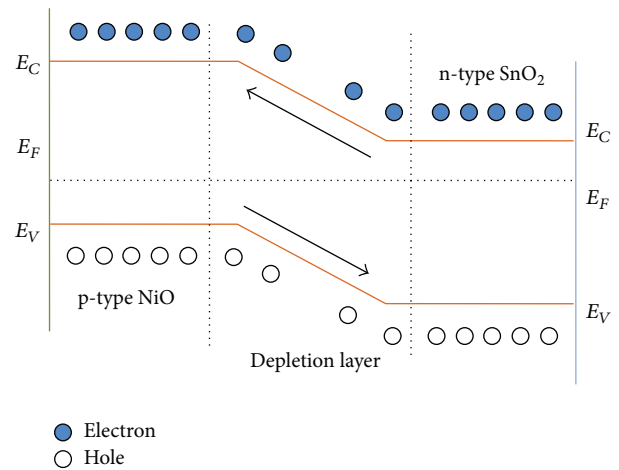


FIGURE 8: Energy band structure diagram of NiO/SnO_2 p-n heterojunction (E_C : lower level of conduction band, E_F : Fermi level, and E_V : upper level of valence band).

diagram of NiO/SnO_2 p-n heterojunction. As NiO and SnO_2 have different electron affinities and work functions, a p-n heterojunction structure emerges at the surface between NiO and SnO_2 , which leads to a band bending in the depletion. Then the holes transfer from oxygen-excess NiO to oxygen-deficient SnO_2 and the electrons transfer from oxygen-deficient SnO_2 to oxygen-excess NiO until the system obtains an equalization in the Fermi levels between NiO and SnO_2 [16, 17]. This process will lead to a wider depletion layer, and more chemisorbed oxygen ions are absorbed on NiO/SnO_2 heterojunction system. Thus more electrons are released back into the conduction band of NiO/SnO_2 composites in H_2 sensing reaction, and lower optimum working temperature and higher gas response are measured for NiO/SnO_2 composites to H_2 .

4. Conclusion

A simple and environment-friendly hydrothermal method was employed to prepare pure SnO_2 and NiO -doped SnO_2 nanostructures. The crystalline structures, surface and morphology characteristics, and compositions and chemical states were characterized by XRD, SEM, EDS, and XPS measurement, respectively. Chemical gas sensors were fabricated based on the synthesized samples and their sensing performances to H_2 were performed on a CGS-1TP intelligent gas sensing analysis system. The NiO/SnO_2 composites based sensor demonstrates a lower optimum operating temperature of 325°C and higher gas response than those of pure SnO_2 , which could be ascribed to the formation of p-n heterojunctions between p-type NiO and n-type SnO_2 . Furthermore, the NiO/SnO_2 composites based sensor exhibits a quasilinear relationship to H_2 gas with concentration ranging 1– $50 \mu\text{L}/\text{L}$. All results indicate that the prepared NiO/SnO_2 composites a promising sensing material for recognition and analysis of dissolved H_2 gas in transformer oil.

Conflict of Interests

The authors declare that there is no conflict of interests regarding the publication of this paper.

Acknowledgment

This work has been supported in part by Fundamental Research Funds for the Central Universities (nos. SWU114051, XDJK2014B031).

References

- [1] M. Duval and J. J. Dukarm, "Improving the reliability of transformer gas-in-oil diagnosis," *IEEE Electrical Insulation Magazine*, vol. 21, no. 4, pp. 21–27, 2005.
- [2] Q. Zhou, W. Chen, L. Xu, and S. Peng, "Hydrothermal synthesis of various hierarchical ZnO nanostructures and their methane sensing properties," *Sensors*, vol. 13, no. 5, pp. 6171–6182, 2013.
- [3] M. Duval, "The duval triangle for load tap changers, non-mineral oils and low temperature faults in transformers," *IEEE Electrical Insulation Magazine*, vol. 24, no. 6, pp. 22–29, 2008.
- [4] S. Singh and M. Bandyopadhyay, "Dissolved gas analysis technique for incipient fault diagnosis in power transformers: a bibliographic survey," *IEEE Electrical Insulation Magazine*, vol. 26, no. 6, pp. 41–46, 2010.
- [5] W. Chen, Q. Zhou, F. Wan, and T. Gao, "Gas sensing properties and mechanism of Nano-SnO₂-based sensor for hydrogen and carbon monoxide," *Journal of Nanomaterials*, vol. 2012, Article ID 612420, 9 pages, 2012.
- [6] W. Zeng, T. Liu, D. Liu, and E. Han, "Hydrogen sensing and mechanism of M-doped SnO₂ (M = Cr³⁺, Cu²⁺ and Pd²⁺) nanocomposite," *Sensors and Actuators B: Chemical*, vol. 160, no. 1, pp. 455–462, 2011.
- [7] M. Yang, D. H. Kim, W. S. Kim et al., "H₂ sensing characteristics of SnO₂ coated single wall carbon nanotube network sensors," *Nanotechnology*, vol. 21, Article ID 215501, 8 pages, 2010.
- [8] S. Rumyantsev, G. Liu, R. A. Potyrailo, A. A. Balandin, and M. S. Shur, "Selective sensing of individual gases using graphene devices," *IEEE Sensors Journal*, vol. 13, no. 8, pp. 2818–2822, 2013.
- [9] P. Patimisco, S. Borri, A. Sampaolo et al., "A quartz enhanced photo-acoustic gas sensor based on a custom tuning fork and a terahertz quantum cascade laser," *Analyst*, vol. 139, no. 9, pp. 2079–2087, 2014.
- [10] C.-H. Han, S.-D. Han, and S. P. Khatkar, "Enhancement of H₂-sensing properties of F-doped SnO₂ sensor by surface modification with SiO₂," *Sensors*, vol. 6, no. 5, pp. 492–502, 2006.
- [11] I.-C. Yao, P. Lin, and T.-Y. Tseng, "Hydrogen gas sensors using ZnO-SnO₂ core-shell nanostructure," *Advanced Science Letters*, vol. 3, no. 4, pp. 548–553, 2010.
- [12] Z. J. Wang, Z. Y. Li, T. T. Jiang, X. R. Xu, and C. Wang, "Ultrasensitive hydrogen sensor based on Pd⁰-Loaded SnO₂ electrospun nanofibers at room temperature," *ACS Applied Materials and Interfaces*, vol. 5, no. 6, pp. 2013–2021, 2013.
- [13] W. Wang, Y. Tian, X. Li et al., "Enhanced ethanol sensing properties of Zn-doped SnO₂ porous hollow microspheres," *Applied Surface Science*, vol. 261, pp. 890–895, 2012.
- [14] L. He, Y. Jia, F. Meng, M. Li, and J. Liu, "Development of sensors based on CuO-doped SnO₂ hollow spheres for ppb level H₂S gas sensing," *Journal of Materials Science*, vol. 44, no. 16, pp. 4326–4333, 2009.
- [15] W. Tang, J. Wang, P. J. Yao, and X. J. Li, "Hollow hierarchical SnO₂-ZnO composite nanofibers with heterostructure based on electrospinning method for detecting methanol," *Sensors and Actuators B: Chemical*, vol. 192, no. 1, pp. 543–549, 2014.
- [16] N. van Hieu, P. Thi Hong Van, L. Tien Nhan, N. van Duy, and N. Duc Hoa, "Giant enhancement of H₂S gas response by decorating n-type SnO₂ nanowires with p-type NiO nanoparticles," *Applied Physics Letters*, vol. 101, no. 25, Article ID 253106, 2012.
- [17] R. S. Shen, X. P. Li, X. C. Xia et al., "Comparative investigation of three types of ethanol sensor based on NiO-SnO₂ composite nanofibers," *Chinese Science Bulletin*, vol. 57, no. 17, pp. 2087–2093, 2012.
- [18] W. Chen, Q. Zhou, and S. Peng, "Hydrothermal synthesis of Pt-, Fe-, and Zn-doped SnO₂ nanospheres and carbon monoxide sensing properties," *Advances in Materials Science and Engineering*, vol. 2013, Article ID 578460, 9 pages, 2013.
- [19] Q. Qi, P.-P. Wang, J. Zhao et al., "SnO₂ nanoparticle-coated In₂O₃ nanofibers with improved NH₃ sensing properties," *Sensors and Actuators B: Chemical*, vol. 194, no. 4, pp. 440–446, 2014.
- [20] W. Zeng, T. Liu, and Z. Wang, "Enhanced gas sensing properties by SnO₂ nanosphere functionalized TiO₂ nanobelts," *Journal of Materials Chemistry*, vol. 22, no. 8, pp. 3544–3548, 2012.
- [21] W. Chen, Q. Zhou, F. Wan, S. Peng, and W. Zeng, "Synthesis and enhanced ethane sensing properties of pt-doped nio nanofibers via electrospinning," *Nanoscience and Nanotechnology Letters*, vol. 5, no. 12, pp. 1231–1236, 2013.
- [22] Q. Qi, T. Zhang, X. Zheng et al., "Electrical response of Sm₂O₃-doped SnO₂ to C₂H₂ and effect of humidity interference," *Sensors and Actuators B: Chemical*, vol. 134, no. 1, pp. 36–42, 2008.
- [23] Q. Zhou, W. G. Chen, S. D. Peng, and W. Zeng, "Hydrothermal synthesis and acetylene sensing properties of variety low dimensional zinc oxide nanostructures," *The Scientific World Journal*, vol. 2014, Article ID 489170, 8 pages, 2014.
- [24] I. Preda, R. J. O. Mossaneck, M. Abbate et al., "Surface contributions to the XPS spectra of nanostructured NiO deposited on HOPG," *Surface Science*, vol. 606, no. 17-18, pp. 1426–1430, 2012.
- [25] X. Xue, L. Xing, Y. Chen, S. Shi, Y. Wang, and T. Wang, "Synthesis and H₂S sensing properties of CuO-SnO₂ core/shell PN-junction nanorods," *The Journal of Physical Chemistry C*, vol. 112, no. 32, pp. 12157–12160, 2008.

Research Article

Orientation Mapping of Extruded Polymeric Composites by Polarized Micro-Raman Spectroscopy

Xiaoyun Chen,¹ M. Anne Leugers,¹ Tim Kirch,² and Jamie Stanley¹

¹Analytical Sciences, Core R&D, The Dow Chemical Company, Midland, MI 48667, USA

²Dow Building Solutions, The Dow Chemical Company, 200 Larkin 1605 Joseph Drive, Midland, MI 48674, USA

Correspondence should be addressed to Xiaoyun Chen; xchen4@dow.com

Received 5 August 2014; Accepted 8 September 2014

Academic Editor: Jie-Fang Zhu

Copyright © 2015 Xiaoyun Chen et al. This is an open access article distributed under the Creative Commons Attribution License, which permits unrestricted use, distribution, and reproduction in any medium, provided the original work is properly cited.

Molecular orientation has a strong influence on polymeric composite materials' mechanical properties. In this paper we describe the use of polarized micro-Raman spectroscopy as a powerful tool to map out the molecular orientation of a uniaxially oriented polypropylene- (PP-) based composite material. Initial samples exhibited a high degree of surface fibrillation upon cutting. Raman spectroscopy was used to characterize the degree of orientation in the skin and guide the development of the posttreatment process to optimize the skin relaxation while maintaining the high degree of orientation in the rest of the board. The PP oriented polymer composite (OPC) was oriented through an extrusion process and its surface was then treated to achieve relaxation. Micro-Raman analysis at the surface region demonstrated the surface orientation relaxation, and the results provide an effective way to correlate the extent of relaxation and process conditions. Larger scale orientation mapping was also carried out over the entire cross-section (12.7 cm × 2.54 cm). The results agree well with prior expectation of the molecular orientation based on the extrusion and subsequent quenching process. The methodologies described here can be readily applied to other polymeric systems.

1. Introduction

Polymer composites are gaining market share in construction markets and offer several advantages over the traditional wood materials. A variety of plastic composite manufacturers are offering products for the decking, window and door, and other specialty markets. A recent development is an oriented polymer composite (OPC). Using a temperature controlled proprietary orientation process, products can be fabricated with a unique combination of low density, high stiffness, good processability with traditional wood-working tools, and weatherability compared to traditional plastic composite structures. Unlike wood boards, where the orientation of the fibrils and microfibrils is aligned by nature to maintain stiffness, semicrystalline polymeric materials must be oriented during processing to align the polymer chains to achieve the desired stiffness.

A high degree of orientation of amorphous regions and crystalline regions is quite desirable for modulus and stiffness under load; however the orientation can present issues with the shaping and cutting of the composites to form the final

part. Initial products showed a high degree of orientation on the surface of the product that extended toward the center of the parts dimensions. These products exhibited highly undesirable fibrillation during surface wear evaluation and cutting. Efforts were initiated to understand and improve both wear and cutting performance.

Extensive studies have been previously carried out to characterize molecular orientation of a wide range of systems such as liquid crystals, polymers, proteins, and peptides using vibrational spectroscopic tools. For example, polarized infrared spectroscopy (IR) can be used to obtain order parameter defined as $S_{\theta} = (3\langle \cos^2\theta \rangle - 1)/2$, where θ is the angle of the functional group's dipole moment relative to the symmetry axis and the bracket denotes ensemble average [1]. However, the requirement of thin samples sections for transmission mode or a good contact with attenuated total reflectance (ATR) crystals in the ATR mode limits the application of IR for molecular orientation study in an industrial environment. Polarized Raman spectroscopy offers more flexibility as signals can be generated from any surface or cross-section in a contact-free fashion and, in theory, yields

more information. For example, the second and fourth terms of the orientation distribution function, characterized by Legendre polynomial $\langle P_2(\cos\theta) \rangle$ and $\langle P_4(\cos\theta) \rangle$, can be calculated for vibrational modes whose Raman tensor is known [2, 3]. Other higher order spectroscopy techniques such as second harmonic generation (SHG) [4, 5] and sum frequency generation vibrational spectroscopy (SFG) [6–8] have also been shown to provide insights into molecular orientation, especially when combined with linear spectroscopy techniques such as IR or Raman. Their complex instrumentation and data analysis and surface/interface-specific nature have limited their applications mostly to academic settings.

Here we describe an industrial application of polarized Raman spectroscopy to characterize the molecular orientation of polymers within an oriented composite material with uniaxial orientation. It is demonstrated that through the use of orientation ratio (O.R. (1)), the molecular orientation of OPC can be effectively characterized on length scale spanning from μm scale to macroscopic scale, thus enabling the mapping of orientation across the entire cross-section of an OPC sample. O.R. is defined in (1), where I_1 stands for the intensity of a band that is sensitive to polarization while I_2 stands for the intensity of another band that is insensitive to polarization or shows the opposite trend. The ZZ and YY in the subscript denote whether the spectrum is collected with the electric field of the excitation/collection beam parallel or perpendicular to the extrusion direction of the sample (see Figure 1):

$$\text{O.R.} = \frac{I_{1,ZZ}/I_{2,ZZ}}{I_{1,YY}/I_{2,YY}}. \quad (1)$$

Although this approach does not yield detailed quantitative orientation distribution functions, as the more elaborate polarized Raman methods previously developed, its simplicity and robustness make it suitable for industrial applications where most samples have many nonpolymer components such as additives, fillers, and pigments. Voyiatzis and Andrikopoulos showed that despite the use of calibration curve, the O.R. can potentially be correlated to the various terms of the orientation distribution function [9]. This was not necessary for the applications investigated herein. Voyiatzis and Andrikopoulos also demonstrated that, for well-behaved systems such as a dye dissolved in polymeric matrix, the orientation of the dye molecules can be effectively characterized by a simple ratio of $I_{1,zz}/I_{2,zz}$, which enables fast monitoring of orientation during a drawing process. The assumptions behind this approach may not always be satisfied by many industrial OPC samples. For example, difference in crystallinity may be another factor that may cause a change in the $I_{1,zz}/I_{2,zz}$ ratio [10, 11]. The $I_{1,yy}/I_{2,yy}$ term in the denominator of the O.R. equation can effectively account for the variation of other factors such as crystallinity and concentration.

2. Materials and Methods

2.1. OPC Board Production. The details on the OPC extrusion and processing can be found in previous patents [12].

An appropriate formulation, consisting of both miscible and nonmiscible components, is extruded into a profile using standard material feeding and extruding technology. The extruded profile is then uniaxially drawn using a drawing die in a temperature controlled environment. The ratio of the product dimensions before and after drawing is known as the drawing ratio. As the drawing ratio is increased towards its optimum value, density tends to decrease while product stiffness, defined by flexural modulus and elasticity, tends to increase.

Use of high draw ratios tends to produce products with high degrees of surface orientation. While the level of orientation generates many useful properties for the oriented polymer composite, high surface orientation causes issues when the product's surface undergoes surface wear or the product is cut to specific lengths or shapes. As noted earlier, the high degree of orientation tends to generate fibrils on the worn surface or along the fabricated edges of the product. Experimentation indicated that controlled surface deorientation would eliminate these issues. An analytical technique was required that could determine the level of orientation in multiple axis to allow identification of an effective heat-treating method to achieve surface deorientation as well as develop control parameters for processing equipment that could be applied during the commercial manufacturing process.

2.2. Sample Preparation for Micro-Raman Spectroscopy. An OPC board was cut with a saw along the extrusion direction to expose the cross-section that was perpendicular to the heat-treated surface as shown in Figure 1. The cutting direction shown in Figure 1 is vertical but can also be horizontal as long as it is parallel to the extrusion direction. The exposed cross-section was then ground to a smooth flat surface using grinding papers of 320, 800, 1200, 2400, and 4000 grit on a Struers Pedemat Rotopol-V polisher with water cooling. Control experiments using different orientation of samples relative to polishing direction were carried out to ensure that such sample preparation method does not alter or introduce orientation to OPC board cross-sections. Polarized Raman spectra were then collected at various depths as indicated by the red dots on the polished cross-section as shown in Figure 1.

2.3. Polarized Micro-Raman Analysis. A Kaiser Raman RXN1 microscope with 785 nm laser excitation was used. A schematic of the Raman optical pathway is shown in Figure 1. Multimode optical fibers were used to deliver the laser to the microscope and the signal back to the spectrometer. Two independent linear polarizers were used to control the polarization state of the excitation laser and the Raman signals.

Raman signals were collected in the backscattering geometry using a 20x long-working-distance objective. The laser spot size was approximately 20 μm in diameter. Typical laser power used was in the range of 30 to 100 mW, depending on the pigment loading in a sample. It should be noted that laser heating could cause molecular relaxation and even melting. The exact power used for each spectrum was generally half of

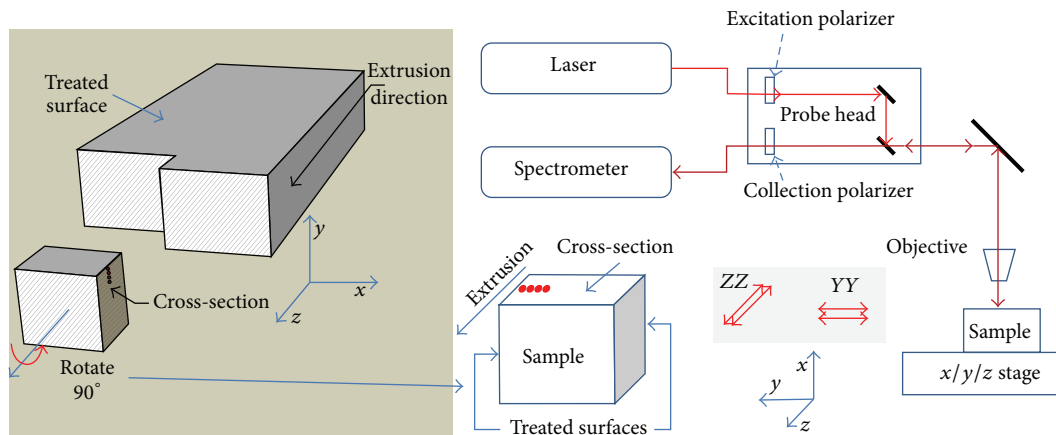


FIGURE 1: Schematic illustration of how a board was cut and analyzed by micro-Raman analysis.

the power that would cause specimen surface melting. One minute collection time was used to acquire sufficient signal-to-noise ratio.

At each point of a sample two spectra were collected, the parallel and the perpendicular. The parallel (perpendicular) spectrum is collected with the two polarizers oriented so that the electric field of the incoming laser beam and the outgoing signal beam are both parallel (perpendicular) to the extrusion direction. It should be noted that there are many more geometries that can be used (e.g., one polarizer parallel to and one polarizer perpendicular to the extrusion direction, or with the sample oriented differently), but the parallel and perpendicular spectra collected in the manner described above can best reflect the orientation differences in a sample.

3. Results and Discussion

3.1. Control Samples. Figure 3 compares the parallel and perpendicular spectra collected from a plastic pellet of the same material used in the composite formulation (top panel) and from an oriented fiber of the same material (bottom panel). For this specific sample, polypropylene was used as the plastic component of the composite. Details in the peak assignments for PP have previously been reported and will not be repeated here [13, 14]. It is obvious that while the parallel and perpendicular spectra are almost indistinguishable for the PP pellet sample (note all spectra are normalized to the strongest peak within each panel), dramatic differences can be found for the parallel and perpendicular spectra of PP fibers.

Such differences in the spectra collected with different polarizers are commonly observed for most oriented polymers and several examples are shown in Figure 3. The extent of differences exhibited by the parallel and perpendicular spectra depends on several factors, such as the level of orientation within the macromolecular chain, the orientation of a functional group relative to its polymer backbone, and the Raman tensor of the functional group. As can be observed in Figure 3, spectral differences present between

the parallel and perpendicular spectra range from dramatic for polyethylene and poly(vinylidene fluoride-co-polyester) fibers, to intermediate for polybutene-1 fibers, and to quite subtle for poly(styrene-co-acrylonitrile) fibers. O.R. should not be used to directly compare the level of orientation across different polymers and rather should only be used as a relative measure to evaluate molecular orientation level for uniaxially oriented samples of the same polymer. Discussion below will be focused on the PP orientation in OPC boards.

According to (1), two bands need to be selected for the calculation of O.R. for each phase. For the PP investigated here, both the crystalline and the amorphous phases are present in significant amount and therefore two sets of bands should be used, one set for each phase [15]. Below we will focus on the orientation characterization of the crystalline phase because a similar trend was observed for the amorphous phase. The baseline-corrected peak height of the 809 cm^{-1} peak and the 841 cm^{-1} peak is used as I_1 and I_2 , respectively, as used in several previous studies [16–18]. In the next sections line maps, small-area mapping and large-area mapping will be shown for the PP OPC samples with and without surface treatment.

3.2. Line Maps. For consistency, PP OPC cross-section samples are always oriented the same way in reference to the lab coordinate system with the extrusion direction parallel to the microscope stage as shown in Figure 1. Two line maps were collected: one parallel and one perpendicular. A stable stage is critical to ensure that the corresponding parallel and perpendicular spectra in the two line maps are from the same spot. Spectra in these line maps were collected from evenly spaced points on an OPC cross-section spanning from the surface into the core. The O.R. profiles from three representative samples are shown in Figure 4. Samples (a), (b), and (c) were from similar OPC boards, but after different level of surface treatments aimed to cause orientation relaxation, with (a) receiving no surface treatment, (b) an intermediate level, and (c) the highest level of surface treatment. Before we compare the O.R. profiles in Figure 4, it is worth noting that the O.R. for the PP fiber shown in Figure 2 is calculated to be 7.7

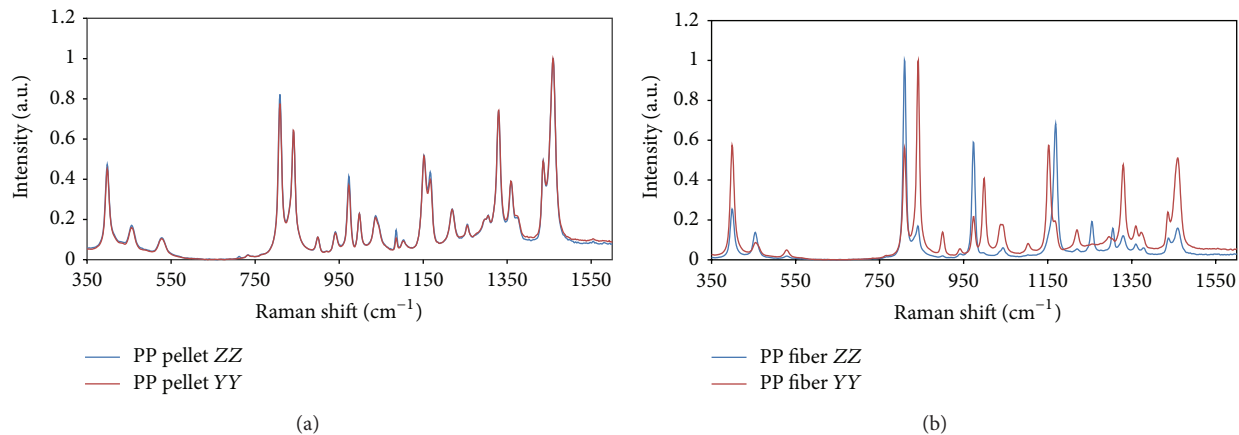


FIGURE 2: (a) ZZ and YY spectra of a PP pellet; (b) ZZ and YY spectra of a PP fiber.

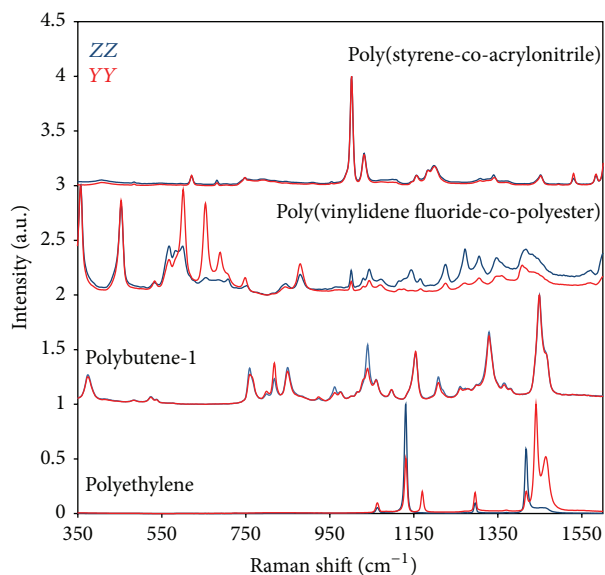


FIGURE 3: Comparison of ZZ to YY spectra of (from top to bottom) poly(styrene-co-acrylonitrile), poly(vinylidene fluoride-co-polyester), poly(1-butene), and polyethylene.

and about 1 for the PP pellet. The values of 7.7 and 1 are specific for the particular bands selected (841 and 809 cm^{-1}) and other choices of bands may also be valid but will have different O.R. values. The O.R. ratio calculated using the same pair of bands for PP in OPC can be compared. It is unlikely for the O.R. value for PP in an extrusion oriented sample to reach as high as 7.7 as very high draw ratio is needed; for completely relaxed PP samples its O.R. will be close to 1 as the polarization should not affect the Raman spectra of isotropic materials. If somehow the PP chain has a preferred orientation in the transverse direction, then an O.R. smaller than 1 will be observed. Samples with O.R. value of x and $1/x$ should have the same level of orientation, but with the orientation direction orthogonal to each other.

Given the above information, it is clear from Figure 4 that while the inner region of all three samples is relatively

orientated with O.R. ranging from 2.5 to 4, their surface orientation exhibited dramatic differences. Sample (a) showed no relaxed orientation at the surface because it did not receive any surface treatment. Samples (b) and (c) both showed partially relaxed surface region with O.R. ranging between 1 and 1.6, but the relaxed surface layer is only about $110\text{ }\mu\text{m}$ for Sample (b), much thinner than the $380\text{ }\mu\text{m}$ thick relaxed skin of Sample (c). Such observations are in good agreement with the sample treatment history and provided an effective way to understand how efficient the treatment is in relaxing polymer orientation.

3.3. Small-Area Maps. The above line map methods can be readily applied to acquire an area map of PP orientation if the area of interest can fit within the range of the microscope stage. It is critical for the OPC cross-section surface to be horizontal and parallel to the stage to ensure that all the spots in the map are in focus. The results shown in Figure 5 were from a surface-treated OPC cross-section with its surface on the right edge of the map. Spectra were collected in a raster-scan fashion from an area of $600\text{ }\mu\text{m}$ (along the depth direction) \times $1000\text{ }\mu\text{m}$ (along the extrusion direction). The red dots in Figure 5 right panel represent the spectral collection spots, which formed a 26×8 grid, with 26 evenly spaced lines distributed along the depth direction and 8 evenly spaced lines distributed along the extrusion direction. Such a form of grid was chosen in order to capture the sharp transition between the skin and core region and because less dramatic change in O.R. was expected along the extrusion direction. The map in Figure 5 indeed confirms this expectation and clearly shows that the skin layer was relatively uniform with a thickness on the order of 200 to $250\text{ }\mu\text{m}$. The false-color map in the left panel of Figure 5 was generated by interpolating the O.R. over the 26×8 grid.

3.4. Large-Area Mapping. While the results above clearly demonstrate the power of polarized micro-Raman analysis to characterize the surface relaxation, the orientation distribution across the entire OPC product cross-section is what determines the overall mechanical strength of an OPC

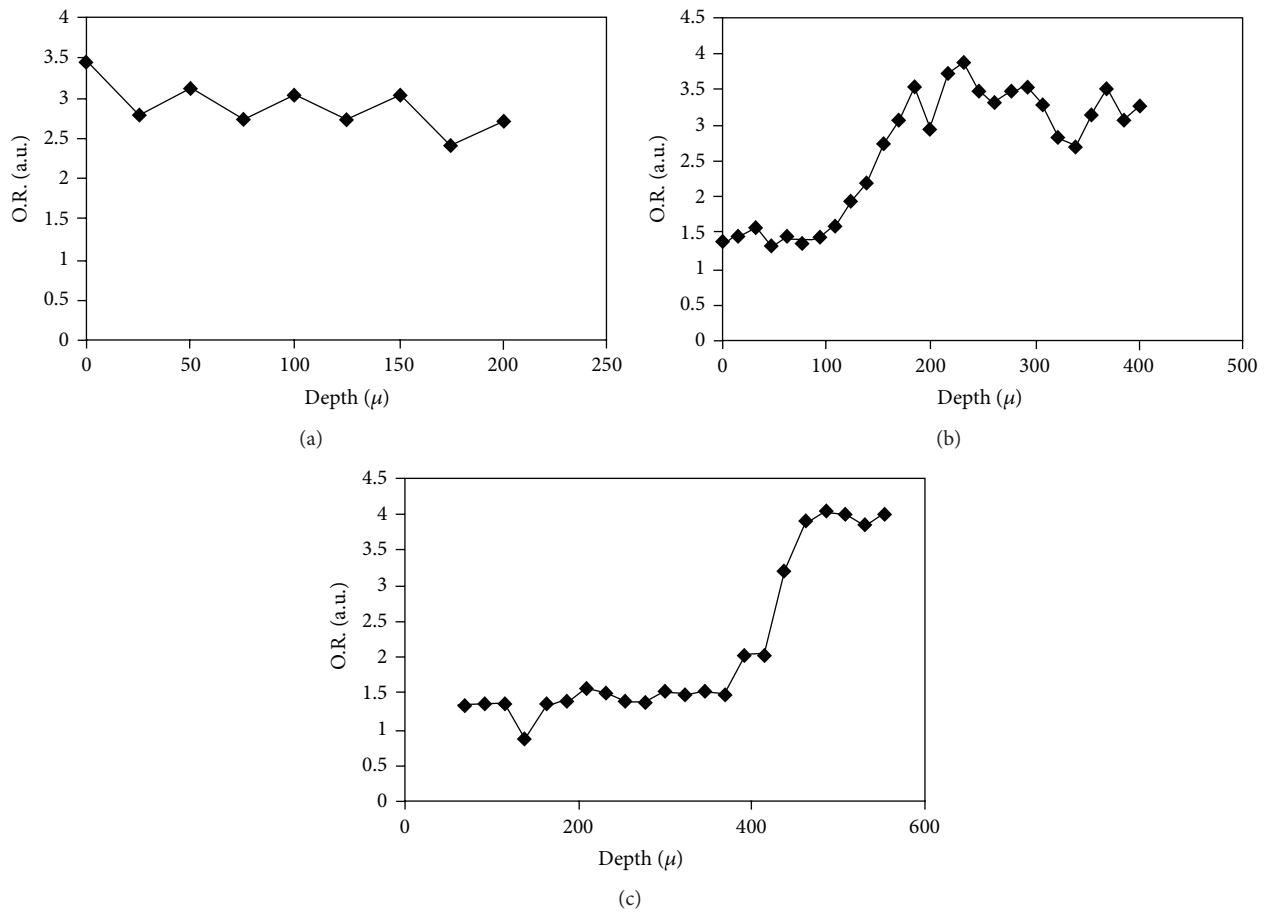


FIGURE 4: Line maps of O.R. profiles collected from the surface region of three different samples with (a) no, (b) medium level, and (c) high level of surface treatment.

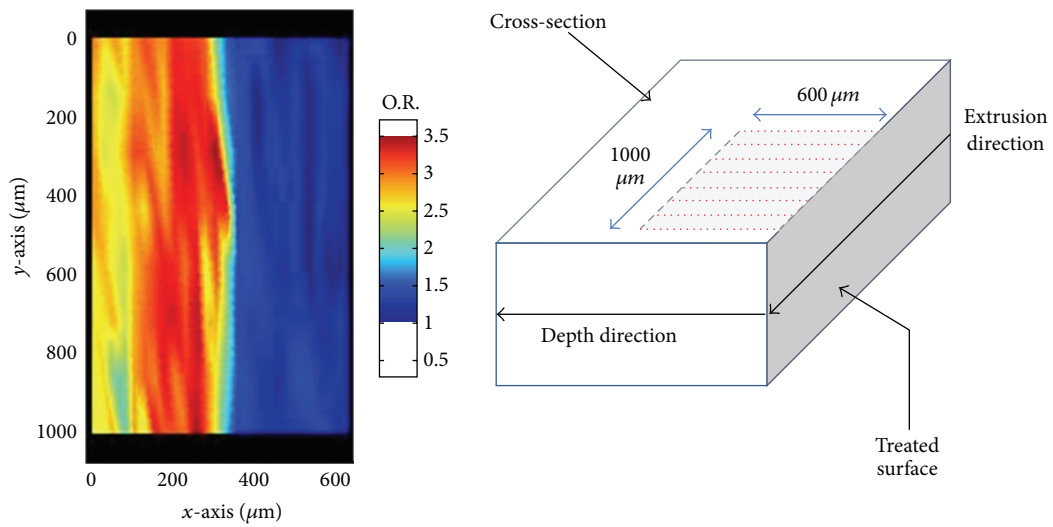


FIGURE 5: Mapping of orientation for a $600 \times 1000 \mu\text{m}$ area as marked by the shaded area with red dots representing the spectral collection spots.

structure. Many interdependent factors can influence the final strength of an OPC product such as the die design, temperature, feed rate, cooling rate, and fillers and it is often difficult to understand how these various factors can lead to final product performance without first understanding how they influence the molecular orientation.

Figure 6 illustrates how the large-area orientation mapping was carried out. An OPC sample was cut into 11 vertical sections and line maps were carried out on each section as represented by the red dots. The sample can also be cut into horizontal sections. However, due to the sample geometry, horizontal sections are thin and thus more prone to deformations.

The orientation mapping results from two representative samples are shown in the bottom panel of Figure 6. OPC sample 1 was a regular product while a side slot was built into OPC sample 2 according to its design. The orientation mapping yields a direct and visual way to understand the level of orientation at various regions within an OPC product. Both samples showed similar general patterns: a surface skin region on the top and bottom of the product that underwent relaxation during surface treatment, a relatively oriented region beyond the skin, and a relaxed core region.

For OPC sample 1 the entire orientation map shows remarkable symmetry along both the horizontal and vertical middle line, with the oriented outer layer about 2.5 cm or 1 inch thick (excluding the relaxed surface which was oriented prior to surface treatment) surrounding the core region and with the core region showing a gradient of O.R. which can be further used to define an inner and outer core region. Such a distribution of orientation supports the hypothesis that the core region, due to insulation by the outer layer, has more time to relax than the material in the outer layer. In contrast the outer region cools down faster and thus effectively locks the molecular orientation once the sample temperature drops below T_m or T_g . Analysis using micro-Raman technology provides an improved understanding of how process conditions can be related to molecular orientation and ultimately to product performance which is thus achieved. OPC sample 2 shows an orientation map that is rather different from OPC sample 1. This sample appeared to be less oriented overall. The exact reasons behind such differences are of great interest to engineers and material scientists but are beyond the scope of this study.

4. Conclusions

In this study we used polarized micro-Raman spectroscopy to study PP morphology and orientation in uniaxially oriented OPC products in order to guide the posttreatment of PP composite products. We applied this method to analyze PP OPC and the results from the surface region enable us to correlate the surface treatment parameters to the level of skin orientation relaxation and skin thickness, and the results from the large scale mapping show in a visual way how process conditions can influence the molecular orientation across the entire cross-section of an OPC material.

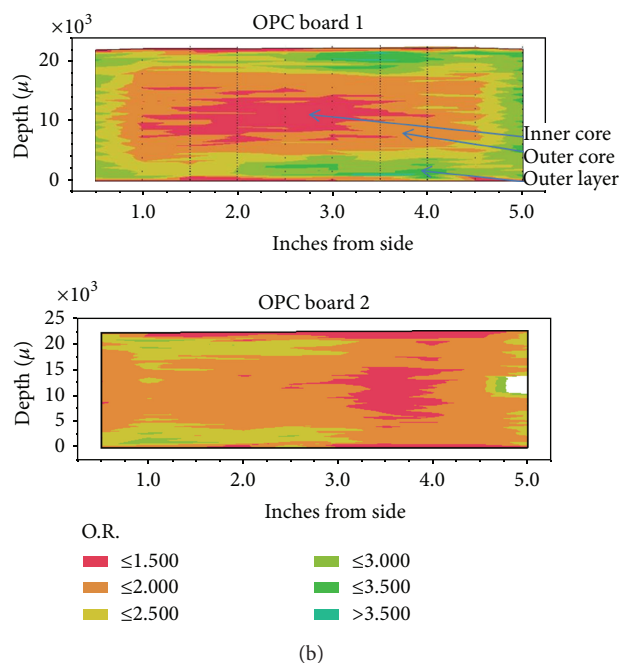
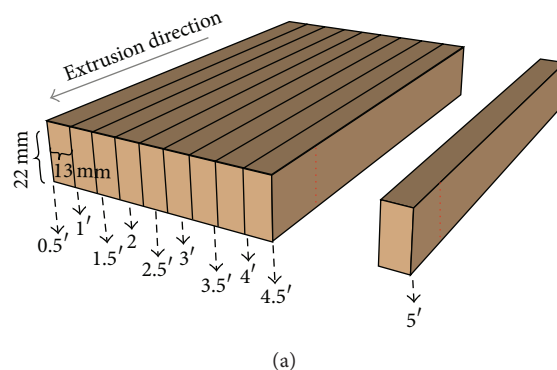


FIGURE 6: (a) A schematic illustration of how an OPC board is cut into sections. (b) Orientation map of two OPC boards. O.R. is color-coded.

The methodologies described here can be readily applied to other polymeric systems.

Conflict of Interests

The authors declare that there is no conflict of interests regarding the publication of this paper.

Acknowledgments

The authors would like to thank the Dow Chemical Company and Eovations, LLC, for permission to publish this work. Help in sample preparation from Robbie Samson is gratefully acknowledged. They also appreciate the inspiring discussions with Robert Cieslinski and Kevin Nichols.

References

- [1] L. K. Tamm and S. A. Tatulian, "Infrared spectroscopy of proteins and peptides in lipid bilayers," *Quarterly Reviews of Biophysics*, vol. 30, no. 4, pp. 365–429, 1997.
- [2] M. Tanaka and R. J. Young, "Review Polarised Raman spectroscopy for the study of molecular orientation distributions in polymers," *Journal of Materials Science*, vol. 41, no. 3, pp. 963–991, 2006.
- [3] R. Ikeda, B. Chase, and N. J. Everall, "Basics of orientation measurements in Infrared and Raman spectroscopy," in *Handbook of Vibrational Spectroscopy*, John Wiley & Sons, 2006.
- [4] T. G. Zhang, C. H. Zhang, and G. K. Wong, "Determination of molecular orientation in molecular monolayers by second-harmonic generation," *Journal of the Optical Society of America B*, vol. 7, no. 6, pp. 902–907, 1990.
- [5] M. B. Feller, W. Chen, and Y. R. Shen, "Investigation of surface-induced alignment of liquid-crystal molecules by optical second-harmonic generation," *Physical Review A*, vol. 43, no. 12, pp. 6778–6792, 1991.
- [6] X. Chen, M. L. Clarke, J. Wang, and Z. Chen, "Sum frequency generation vibrational spectroscopy studies on molecular conformation and orientation of biological molecules at interfaces," *International Journal of Modern Physics B*, vol. 19, no. 4, pp. 691–713, 2005.
- [7] Z. Chen, Y. R. Shen, and G. A. Somorjai, "Studies of polymer surfaces by sum frequency generation vibrational spectroscopy," *Annual Review of Physical Chemistry*, vol. 53, pp. 437–465, 2002.
- [8] X. Chen, J. Wang, A. P. Boughton, C. B. Kristalyn, and Z. Chen, "Multiple orientation of melittin inside a single lipid bilayer determined by combined vibrational spectroscopic studies," *Journal of the American Chemical Society*, vol. 129, no. 5, pp. 1420–1427, 2007.
- [9] G. A. Voyatzis and K. S. Andrikopoulos, "Fast monitoring of the molecular orientation in drawn polymers using micro-Raman spectroscopy," *Applied Spectroscopy*, vol. 56, no. 4, pp. 528–535, 2002.
- [10] C. Minogianni, K. G. Gatos, and C. Galiotis, "Estimation of crystallinity in isotropic isotactic polypropylene with Raman spectroscopy," *Applied Spectroscopy*, vol. 59, no. 9, pp. 1141–1147, 2005.
- [11] R. M. Khafagy, "In situ FT-Raman spectroscopic study of the conformational changes occurring in isotactic polypropylene during its melting and crystallization processes," *Journal of Polymer Science, Part B: Polymer Physics*, vol. 44, no. 15, pp. 2173–2182, 2006.
- [12] J. J. O'Brien, T. O. Kirch, K. L. Nichols, and B. M. Birchmeier, "Oriented polymer composition with a deoriented surface layer," US8475700 B2, 2010.
- [13] M. C. Tobin, "The infrared spectra of polymers. III. The infrared and Raman spectra of isotactic polypropylene," *The Journal of Physical Chemistry*, vol. 64, no. 2, pp. 216–219, 1960.
- [14] P. D. Vasko and J. L. Koenig, "Raman scattering and polarization measurements of isotactic polypropylene," *Macromolecules*, vol. 3, no. 5, pp. 597–601, 1970.
- [15] R. P. Paradkar, A. Leugers, R. Patel, X. Chen, G. Meyers, and E. Lipp, "Raman spectroscopy of polymers," in *Encyclopedia of Analytical Chemistry*, John Wiley & Sons, New York, NY, USA, 2006.
- [16] D. García-López, J. C. Merino, I. Gobernado-Mitre, and J. M. Pastor, "Polarized confocal Raman microspectroscopy studies of chain orientation on injected poly(propylene)/montmorillonite nanocomposites," *Journal of Applied Polymer Science*, vol. 96, no. 6, pp. 2377–2382, 2005.
- [17] X. Wang and S. Michielsen, "Isotactic polypropylene morphology-Raman spectra correlations," *Journal of Applied Polymer Science*, vol. 82, no. 6, pp. 1330–1338, 2001.
- [18] K. Aratake, M. Taniguchi, and H. Ito, "Polyolefin fiber and non-woven fabric produced by using the same," Patent: US5910362 A, 1999.

Research Article

Evaluation of Salmon Adhesion on PET-Metal Interface by ATR, FT-IR, and Raman Spectroscopy

E. Zumelzu,¹ M. J. Wehrhahn,¹ F. Rull,² H. Pesenti,¹ O. Muñoz,¹ and R. Ugarte¹

¹*Institute of Materials, Chemistry and Food Science, University Austral of Chile, P.O. Box 567, 5111187 Valdivia, Chile*

²*Department of Condensed Matter Physics, University of Valladolid, 47002 Valladolid, Spain*

Correspondence should be addressed to E. Zumelzu; ezumelzu@uach.cl

Received 8 August 2014; Accepted 1 December 2014

Academic Editor: Ming-Guo Ma

Copyright © 2015 E. Zumelzu et al. This is an open access article distributed under the Creative Commons Attribution License, which permits unrestricted use, distribution, and reproduction in any medium, provided the original work is properly cited.

The material employed in this study is an ecoefficient, environmentally friendly, chromium (VI)-free (noncarcinogenic) metal polymer. The originality of the research lies in the study of the effect of new production procedures of salmon on metal packaging with multilayer polyethylene terephthalate (PET) polymer coatings. Our hypothesis states that the adhesion of postmortem salmon muscles to the PET polymer coating produces surface and structural changes that affect the functionality and limit the useful life of metal containers, compromising therefore their recycling capacity as ecomaterials. This work is focused on studying the effects of the biochemical changes of postmortem salmon on the PET coating and how muscle degradation favors adhesion to the container. The experimental design considered a series of laboratory tests of containers simulating the conditions of canned salmon, chemical and physical tests of food-contact canning to evaluate the adhesion, and characterization of changes in the multilayer PET polymer by electron microscopy, ATR, FT-IR, and Raman spectroscopy analyses. The analyses determined the effect of heat treatment of containers on the loss of freshness of canned fish and the increased adhesion to the container wall, and the limited capability of the urea treatment to remove salmon muscle from the container for recycling purposes.

1. Introduction

There is currently a dispute regarding biosafety in the salmon farming industry due to the loss of freshness of canned fish, as evidenced by changes in pH and *K* index value, and the adhesion of small muscle portions to the protective polymer coating of the container walls. Spoilage has eventually an impact on polymer coatings regarding their ecomaterial capabilities for recycling due to the surface changes undergone by the polymer [1–5].

This work evaluated the effect of the salmon farming processes on the performance of metal-polymer composites coated with low-permeability, homogeneous polymers employed in salmon canning.

The release of ammonia compounds, hydrogen sulfide, and mercaptans (indole, skatole, and other sulfur-containing chemical compounds) is indicative of the microbiological spoilage of fish and depends on the storage temperature [6–10].

Such release generally tends to produce chemical changes on the industrial molecules and is strongly related to the crystallinity of polymers; thus, polyethylene terephthalate (PET) polymer coatings may degrade under extreme conditions [11–14].

This study addresses the impact of the new aquaculture production practices on polyethylene terephthalate (PET) coatings protecting electrolytic chromium coated steel (ECCS) plates, employed as canning materials, resulting from the biochemical changes undergone by the postmortem salmon and its adherence to the can walls; therefore, it is essential to determine the freshness degree of canned salmon fish and its influence as a factor of adhesion.

These are fundamental topics focused on the basic understanding of the mechanics and physics of structural and functional materials at different length scales to accurately determine their properties in relation to the underlying multimaterial microstructures.

To ensure sufficient shelf life, canned food is heat-treated by steam, steam-air mixtures, water, or spraying water. The coldest spot in the can is used as the reference point to determine whether the cans have received an adequate heat treatment. The heat treatment should ensure the inactivation of microorganisms that cause food poisoning and spoilage. The amount of heating needed in the coldest spot of the packaged food is in the range 4–12 min at 121°C for some typical canned food products [11, 15, 16]. As a consequence of this heat treatment, some packed food products can partly adhere to the can wall.

An important aspect to consider is the production of energy in the postmortem muscle, where the oxygen supply to the muscle tissue is interrupted and then the energy production is restricted. The glycogen (storage carbohydrate) or fats are oxidized in a series of reactions which finally produce carbon dioxide (CO₂), water, and adenosine triphosphate (ATP). This type of respiration occurs in two stages: anaerobic and aerobic. The latter depends on the continuous presence of oxygen (O₂), only available in the circulatory system [17]. Postmortem glycolysis results in the accumulation of lactic acid with the concomitant decrease in muscular pH.

Bistac et al. [18] found several factors that affect mackerel adhesion to lacquered can walls. The reported effects clearly indicate that proteins are the major cause of this adhesion. Proteins consist of chains of covalently bound amino acids. Four types of bonds can be formed between the amino acids residues: covalent, electrostatic, hydrogen, and hydrophobic bonds [19]. These bonds are responsible for the structure of the native protein. During the heat processes, these interactions, especially the noncovalent bonds, are partly broken and hence they become available for interaction with, for instance, the surface of a can wall.

This study is focused on an integral view of the problems and considers recent new researches to integrate every necessary aspect for the optimization of multilayer materials used in salmon containers, which are subject to changes due to the canning processes employed to improve their commercialization, enhance sustainable recycling, and reduce energy consumption [20].

2. Methodology

The standard manufacturing protocol was employed to determine the salmon adhesion to the PET coating of the container and the morphological and chemical changes in the multilayers. Food cans were manufactured employing 50 mL of 2.5% NaCl solution, sterilized at 120°C for 60 minutes, immersed in warm water bath ranging from 50°C to 80°C prior to sterilization, and stored for one week at 20°C before opening. The adhesion of salmon was determined by subtracting the weight of the can after cleaning with detergent and water from the weight of the can with portions of flesh attached to the polymer after emptying the container. The protein denaturation step or removal of muscle material from the PET surface was performed by soaking the emptied cans in 6 M urea solution, since urea is well known for its capacity to form hydrogen bonds and is therefore used to unfold proteins.

A number of parameters typical of the analysis of fish spoilage were considered to estimate the freshness of canned salmon. These parameters were referred to as *K* value and pH.

The *K* value is an important index for assessing the freshness quality of postmortem salmon. Nucleotide degradation analysis can be used to determine the degree of fish freshness before spoilage commences. This value can be obtained by calculating the concentration of nucleotides, inosine and hypoxanthine, in the muscle. Homogenized samples of salmon muscle were prepared with trichloroacetic acid. The homogenized sample was centrifuged and the supernatant was neutralized with 1 M potassium hydroxide. Later, the *K* value was determined by high-performance liquid chromatography (HPCL); the nucleotide concentration in the samples was assessed using a C8 reversed-phase column with phosphate buffer at pH 3.0 as the mobile phase. The flow was maintained at 1 mL/min and measured at a wavelength of 254 nm.

The variations in the acidity of the solution resulting from the loss of freshness of canned salmon were measured in situ by the Unisense pH microelectrode.

The morphology of the composite's constituting layers was characterized by SEM to assess the level of degradation, intending to determine the relationships between surface structure and adhesion of salmon to the PET.

The changes in the multilayers were characterized by vibrational spectroscopy: ATR, FT-IR, and Raman. These techniques have proven extremely reliable and useful in the chemical fingerprinting of a wide range of materials employed in several applications [21–24]. The Raman analyses considered the employment of two back-illuminated fiber-coupled spectrometers featuring 633 nm and 785 nm wavelengths. The experiment considered mainly the data gathered with the 785 nm spectrometer. This device consisted of a multimode fiber laser BWTEK BRM-OEM-785 (785 nm), a Raman head BWTEK BAC100-785E, and an objective lens Zeiss Epiplan 50X/0.50 infinite/0 44 28 50 (focal length). The maximum output of the laser through this lens was approximately 165 mW; the laser spot diameter measured on the samples was 48 microns. The spectrometer employed was a BWTEK Prime T BTC661E-785CUST, covering a spectral range 0–3000 cm⁻¹, with a spectral resolution of 5 cm⁻¹, and the detection was performed by a CCD Hamamatsu S10141-1107S operating at -10°C. Several analyses were made to determine the chemical and orientation changes of the molecular chains and/or atomic rearrangements; in addition, atomic absorption measurements in the PET polymer were also performed.

3. Results and Discussion

3.1. Evaluation and Characterization of the Loss of Salmon Freshness and Adhesion to the PET Surface. Variations in canned salmon pH affect the PET surface and adhesion to the container wall in time. Figure 1 shows the pH gradient measurements of preserved salmon using Unisense pH microelectrode.

The in situ measurements reflected the acidity of the solution in the food container with changes from the head

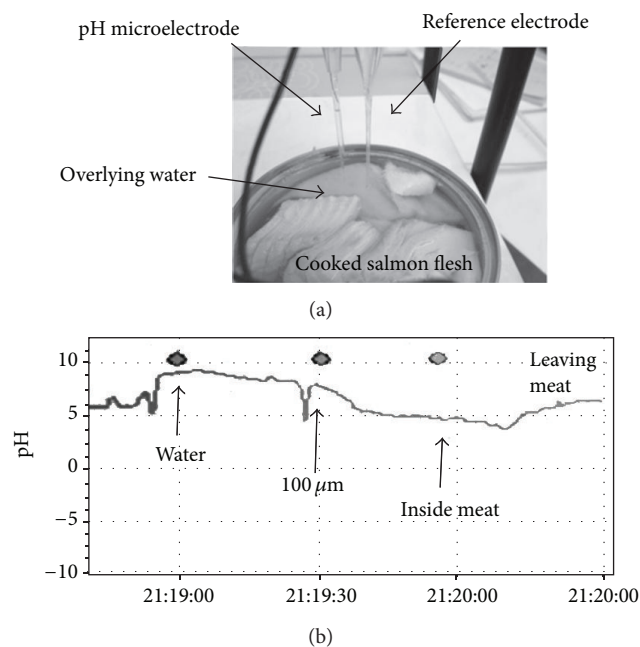


FIGURE 1: (a) Unisense pH microelectrode measurements performed in canned salmon samples; (b) there was a pH gradient from water overlying fluid towards the surface of the salmon meat. The gradient started at neutral pH 6-7 and ended at 4-5 inside the flesh.

space of the container to the bottom thereof, with evident variations from neutral to acid in areas of adhesion and around the PET polymer surface.

The following results were obtained after emptying the container, when determining adhesion of salmon to polymer-coated can walls: a slight increase in the percentage of salmon muscle adhering to the PET-coated can wall was observed with longer storage times. The percentage of adhesion for the samples analyzed was in the range 2.5–4%. The batch of cans stored for a period of 11 months showed the greatest adhesion. Possibly, this adhesion may have been enhanced by higher canning or storage temperatures. The lowest amount of adhesion was observed in cans opened after 4 months of storage. These results indicate that the major cause of salmon adhesion was mainly related to physical flaws on the PET surface, such as bends and micropores, as evidenced by electron microscopy observations. These surface defects may have favored a major role of the chemical interactions between the polymer coating and the proteins of salmon (Figure 2).

The following interaction has been suggested for the adhesion of proteins to PET: the carbonyl group in the ester bond of the PET coating is engaged to form hydrogen links with the amino group of the protein, which would explain the adhesion of salmon to the food container (Figure 3).

According to Fletcher et al., the *K* value ranges from approximately 36% for fresh salmon to 73% for spoiled raw material. The results obtained indicated that canned salmon samples were within acceptable levels (Figure 4); however, those values were close to the maximum limit where loss of freshness occurs.

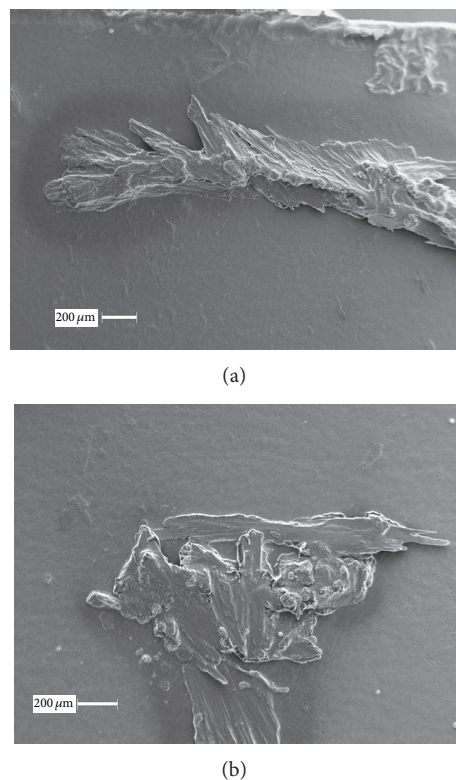


FIGURE 2: (a) The filiform and bifurcated muscle edges increase physical adhesion to the PET polymer coating; (b) salmon flesh not removed by the urea treatment and adhered to the container wall surface.

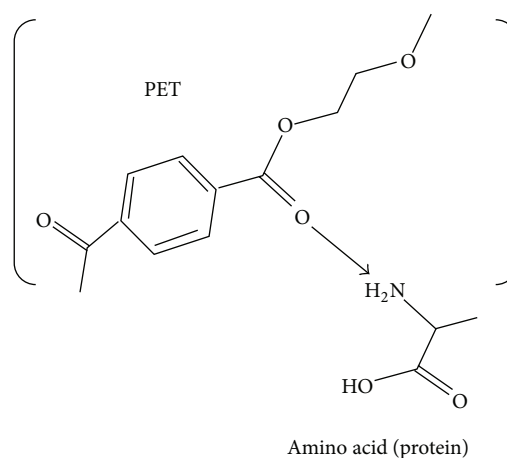


FIGURE 3: PET-protein chemical interaction.

The morphological characterization of salmon tissue adhered to the polymer showed not only the adhesion of physical portions of raw material related to the surface roughness and flaws of the coating but stronger long-lasting bonds.

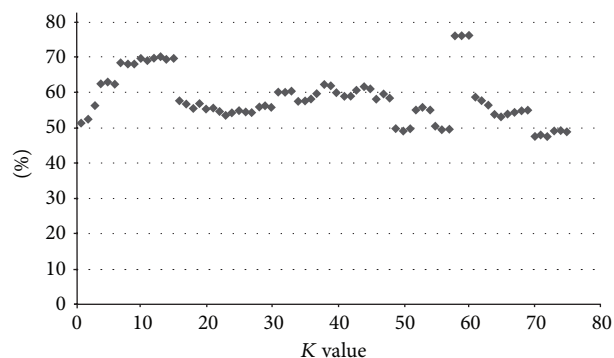


FIGURE 4: K value, freshness quality index of canned salmon.

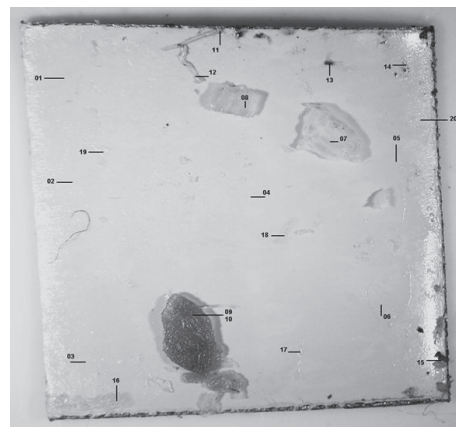
3.2. Evaluation of Chemical and Structural Changes of the PET Coating by Vibrational Spectroscopy: ATR, FT-IR, and Raman. In this work we intended to identify any changes occurring on the polymer in contact with the salmon tissues and also explore the possibility of contamination. Sample M1 is from salmon tissue adhered to the container wall and sample M2 is from muscle treated with urea. Figure 5 shows the spectroscopy results of samples M1 and M2; the last digit refers to their position on the images.

3.2.1. FT-IR. FT-IR spectra were measured on different points of the sample with a PerkinElmer Spectrum 100 spectrometer equipped with a universal ATR accessory. These points were very similar to those employed in the Raman spectroscopy analyses in order to determine differences and similarities between the results of both methods. The nomenclature of the spectra followed that established in Figure 5 and, in general, spectra were taken from areas without remains of salmon, areas with stains arising from the contact with salmon, and areas with small portions of salmon adhered to the surface. In the case of sample M2, no appreciable areas of the latter type were found.

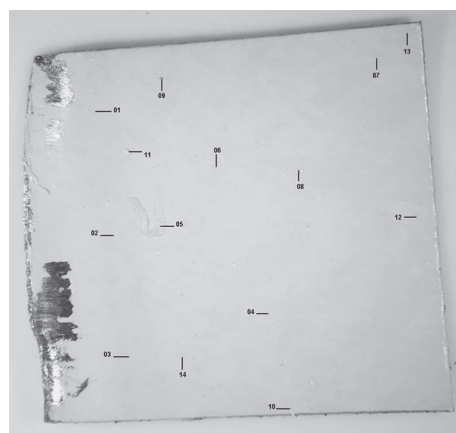
Figure 6 shows some of the differences observed between the spectra of M1, corresponding to muscle naturally adhered to the can wall, and M2 belonging to the urea-treated container to detach the salmon flesh and where no appreciable remains of salmon can be seen.

These differences were clearly associated with the presence of urea in the sample M2 with residues easily noticeable: bands $\nu(\text{NH})$ at 3220 and 3360 cm^{-1} , the $\nu(\text{C}=\text{O})$ band at 1676 cm^{-1} , and deformation bands $\delta(\text{NH}_2)$ at 1630 and 1595 cm^{-1} , respectively. That is, the protective polymer allowed for the adhesion of salmon on certain given areas depending on the heterogeneity of the surface, defects, and pores. The urea solution treatment was not able to detach all of the material adhered to the polymer surface and small residues remained attached as indicated by the FT-IR analyses.

Even though the spectra are fairly homogeneous within each sample, the spectroscopy analyses are capable of characterizing them for quality control purposes of the canning processes. Thus, Figure 7 shows the spectra taken at points where salmon muscle adhesion was clearly visible (points 8



(a)



(b)

FIGURE 5: (a) Sample M1 of PET-coated ECCS plate showing zones of salmon muscle adhesion; numbers indicate points of spectral analyses. (b) Layout of points for spectral analyses in urea-treated sample M2.

and 9 in Figure 5) and hardly noticeable (point 6 in Figure 5) in sample M1, demonstrating the sensitivity of the spectral analyses performed. The spectrum of PET in points 8 and 9 remains largely concealed; however, the $\text{C}=\text{O}$ band of the protein at 1743 cm^{-1} can be easily seen. In point 6, this band appears as a shoulder of the $\text{C}=\text{O}$ band of PET.

3.2.2. Micro-Raman Spectroscopy. Figure 8 shows the micro-Raman spectral measurements made in nondegraded areas of samples M1 and M2, respectively, whose references to points in Figure 5 can be seen in the upper right side. In some spots, such as point 5 in sample M2 (M2-P5), the concentration of urea was very high as indicated by the most intense band observed at 1013 cm^{-1} . Also the bands at 136 , 548 , and 1541 cm^{-1} were also detected. In other spots the intense band of urea was observed as a shoulder of the 1003 cm^{-1} band of PET. These results showed that the distribution of the residual urea on the PET surface was not homogeneous. No bands from urea were detected in sample M1 and, in general, the spectra observed were quite homogeneous and represented the structure of PET.

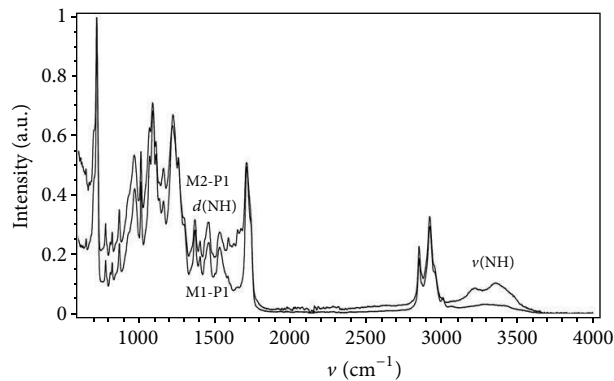


FIGURE 6: ATR spectra from samples M1 (bottom) and M2 (top) measured in areas of reduced contamination (point 1 in Figure 5).

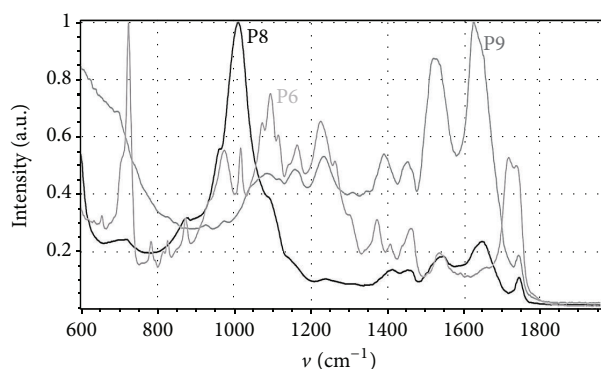


FIGURE 7: ATR spectra taken on sample M1 at positions where remains of adhered salmon were observed. Points 6, 8, and 9 from Figure 5.

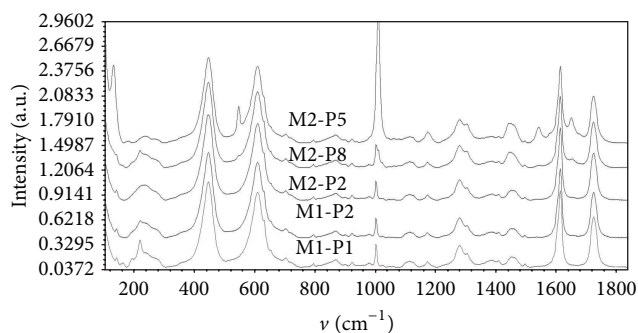


FIGURE 8: Raman spectra from nondegraded areas of samples M1 and M2. The spectrum for point 5 in sample M2 is dominated by urea bands.

Figure 9 shows the micro-Raman spectra from areas degraded by salmon adhesion in sample M1 and compares them with the spectrum taken at a nondegraded spot (point P1). Even though the spectra are similar, those bands corresponding to adhered salmon muscle can be easily distinguished. These bands can be seen at 960 cm^{-1} , 1260 cm^{-1} , 1300 cm^{-1} , 1440 cm^{-1} , and 1657 cm^{-1} . The spectral plot shows the correlation between bands and adhered muscle and can

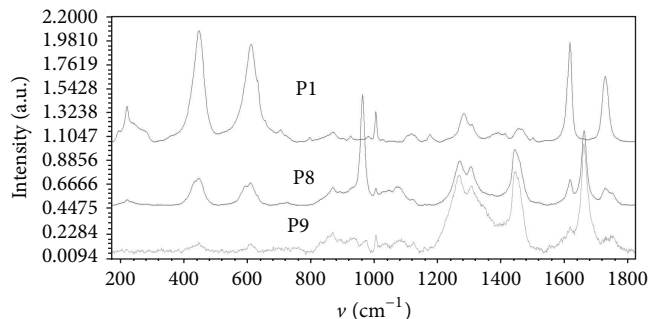


FIGURE 9: Micro-Raman spectra from areas of salmon adhesion in sample M1; points 01, 08, and 09 in Figure 5.

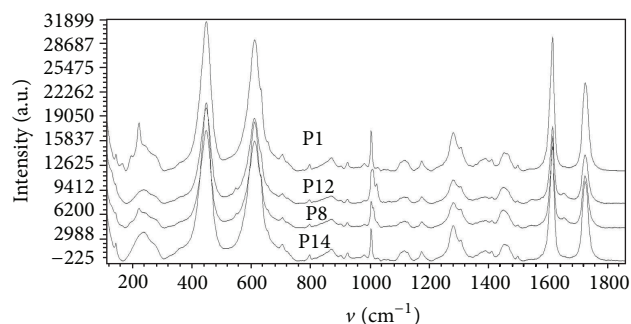


FIGURE 10: Micro-Raman spectra at grey areas of sample M2 where salmon adhesion was observed. Spectral plots P1, P8, P12, and P14 correspond to points 01, 08, 12, and 14 in Figure 5.

therefore determine if the polymer surface has undergone any damage. The above values indicated no significant effects on the polymer surface structure; however, it was possible to characterize the different areas of the samples. Nevertheless, band 960 cm^{-1} can be attributed to the symmetrical vibration of the phosphate group, possibly resulting from the contamination of salmon during the canning process; therefore, Raman spectroscopy becomes a useful tool by showing the presence of elements potentially threatening the human health or affecting the PET surface and the recycling capabilities. Work is in progress to identify the spectral characteristics of different parts of salmon.

Figure 10 shows a similar analysis that was performed on sample M2, comparing grey areas where visual remains of salmon were observed with clear areas (P1). No evidence of Raman bands was observed as a consequence of the urea treatment. The urea band at 1013 cm^{-1} was observed as a shoulder of the 1003 cm^{-1} band of PET, as previously mentioned.

The most outstanding of these results was the presence of urea in almost all the spots of sample M2, with the characteristic band $\nu(\text{CN})$ at 1003 cm^{-1} and variable intensity. Even though salmon residues were persistent after the urea treatment, no bands were seen for salmon muscle; however, the urea employed to remove the salmon residues could be identified on the PET surface.

The degradation of PET coatings by salmon muscle is time dependent and it can be further monitored using local techniques with higher spatial resolution. In this sense, electron probe microanalyses (EPMA) can be used to collect qualitative and quantitative elemental information to establish the composition of small areas on specimens at a nanoscale level. In addition, Kelvin probe force microscopy (KPFM) can be a useful tool to study the composition and electronic state at the surface of materials.

4. Conclusions

This study evaluated the adhesion of salmon to PET polymer coatings employed in canning processes in order to understand this physicochemical phenomenon and hence minimize adhesion for the benefit of consumers.

Thermal treatment of containers is directly related to the loss of freshness, understood as the lack of ability to meet sensory and chemical requirements for a long shelf life, as indicated by pH and *K* index values. Fish spoilage facilitates adhesion of salmon tissue to the container wall; proteins are responsible for the formation of bonds between the PET coating and salmon muscle, and the application of urea makes evident the presence of noncovalent bonds due to the easy removal of the remaining tissue.

The morphology characterization of the PET polymer in areas of salmon adhesion by scanning electron microscopy (SEM) showed a homogeneous contact surface; however, surface pores, roughness, or polymer microfolds favored adhesion of muscle proteins to the container.

Spectroscopy analyses showed the presence of PET and rutile, as well as salmon tissue adhered to the polymer surface. Areas with salmon adhesion or surface degraded showed small microstructural changes; the PET polymer with small traces of urea did not show the same crystallinity, as indicated by the low Raman frequencies. This would prove that the urea solution activity causes changes on the polymer, compromising its functionality in degraded areas.

Finally, the vibrational techniques allowed the understanding of the adhesion mechanisms of salmon to polymer-coated can walls and discerning the changes undergone after the urea treatments employed to minimize the amount of salmon adhering in salmon canning processes.

Conflict of Interests

The authors declare that there is no conflict of interests regarding the publication of this paper.

Acknowledgments

The authors gratefully acknowledge Fondecyt Program of Conicyt Chile for the financial support through Grant no. 1130634 and the special contribution of University Austral of Chile.

References

- [1] Z. Jiang, H. Neetoo, and H. Chen, "Control of *Listeria monocytogenes* on cold-smoked salmon using chitosan-based antimicrobial coatings and films," *Journal of Food Science*, vol. 76, no. 1, pp. 22–26, 2011.
- [2] F. Lu, D. Liu, X. Ye, Y. Wei, and F. Liu, "Alginate-calcium coating incorporating nisin and EDTA maintains the quality of fresh northern snakehead (*Channa argus*) fillets stored at 4°C," *Journal of the Science of Food and Agriculture*, vol. 89, no. 5, pp. 848–854, 2009.
- [3] M. Mariscal-Arcas, A. Rivas, A. Granada, C. Monteagudo, M. A. Murcia, and F. Olea-Serrano, "Dietary exposure assessment of pregnant women to bisphenol-A from cans and microwave containers in Southern Spain," *Food and Chemical Toxicology*, vol. 47, no. 2, pp. 506–510, 2009.
- [4] U. Rafique, S. Iqbal, S. Faiz, and A. Hashmi, "Analysis of variation in concentration of essential and non essential elements in canned and fresh food," *Journal of Food Processing and Preservation*, vol. 33, no. 2, pp. 186–203, 2009.
- [5] A. Rodríguez, N. Carriles, J. M. Gallardo, and S. P. Aubourg, "Chemical changes during farmed coho salmon (*Oncorhynchus kisutch*) canning: effect of a preliminary chilled storage," *Food Chemistry*, vol. 112, no. 2, pp. 362–368, 2009.
- [6] M. Mastromatteo, A. Danza, A. Conte, G. Muratore, and M. A. del Nobile, "Shelf life of ready to use peeled shrimps as affected by thymol essential oil and modified atmosphere packaging," *International Journal of Food Microbiology*, vol. 144, no. 2, pp. 250–256, 2010.
- [7] Y. Byun, H. J. Bae, K. Cooksey, and S. Whiteside, "Comparison of the quality and storage stability of salmon packaged in various retort pouches," *LWT—Food Science and Technology*, vol. 43, no. 3, pp. 551–555, 2010.
- [8] G. Choubert, F. Brisbarre, D. Parfouru, and M. Baccaunaud, "Argon modified atmosphere packaging for fillets of rainbow trout (*Oncorhynchus mykiss*) fed astaxanthin or canthaxanthin," *Journal of Aquatic Food Product Technology*, vol. 17, no. 2, pp. 117–136, 2008.
- [9] G. C. Fletcher, V. K. Corrigan, G. Summers, M. J. Leonard, A. R. Jerrett, and S. E. Black, "Spoilage of rested harvested king Salmon (*Oncorhynchus tshawytscha*)," *Journal of Food Science*, vol. 68, no. 9, pp. 2810–2816, 2003.
- [10] T. Geens, L. Goeyens, and A. Covaci, "Are potential sources for human exposure to bisphenol-a overlooked?" *International Journal of Hygiene and Environmental Health*, vol. 214, no. 5, pp. 339–347, 2011.
- [11] E. Zumelzu, F. Rull, C. Ortega, and C. Cabezas, "Effect of temperature on polyethylene terephthalate coated ECCS plates in acetic-acetate medium," *Journal of Applied Polymer Science*, vol. 113, no. 3, pp. 1853–1859, 2009.
- [12] E. Zumelzu, F. Rull, and C. Ortega, "Titanium dioxide performance in polyethylene terephthalate protective coatings on electrolytic chromium coated steels," *Surface Engineering*, vol. 25, no. 2, pp. 111–115, 2009.
- [13] C. Schick, A. Wurm, and A. Mohammed, "Formation and disappearance of the rigid amorphous fraction in semicrystalline polymers revealed from frequency dependent heat capacity," *Thermochimica Acta*, vol. 396, no. 1–2, pp. 119–132, 2003.
- [14] E. Zumelzu, C. Cabezas, and R. Alvarado, "Evaluation of the degradation of traditional and ECCS canning tins in acetic-acetate medium," *Science and Engineering of Composite Materials*, vol. 13, no. 1, pp. 13–20, 2006.

- [15] X. D. Chen, L. Zhang, and D. Li, "The combined effects of heat transfer coefficient and thermal diffusivity on heating rates of solid materials—a simple analysis," *International Journal of Food Engineering*, vol. 4, no. 5, article 2, 2008.
- [16] X. D. Chen, "Simultaneous heat and mass transfer," in *Handbook of Food and Bioprocess Modeling Techniques*, S. S. Sablani, A. K. Datta, M. S. Rahman, and A. S. Mujumdar, Eds., Chapter 6, CRC Press, 2007.
- [17] O. Fennema, *Quimic a de los Alimentos*, Acribia S.A., Zaragoza, Spain, 2000.
- [18] S. Bistac, M. F. Vallat, and J. Schultz, "Durability of steel/polymer adhesion in an aqueous environment," *International Journal of Adhesion and Adhesives*, vol. 18, no. 5, pp. 365–369, 1998.
- [19] H. D. Belitz and W. Grosch, *Food Chemistry*, Springer, Berlin, Germany, 2nd edition, 1999.
- [20] G. Curtzwiler, K. Vorst, J. E. Danes, R. Auras, and J. Singh, "Effect of recycled poly(ethylene terephthalate) content on properties of extruded poly(ethylene terephthalate) sheets," *Journal of Plastic Film and Sheeting*, vol. 27, no. 1-2, pp. 65–86, 2011.
- [21] A. L. Galo and M. F. Colombo, "Singular value decomposition and ligand binding analysis," *Journal of Spectroscopy*, vol. 2013, Article ID 372596, 7 pages, 2013.
- [22] R. A. Sayed, W. S. Hassan, M. Y. El-Mammli, and A. Shalaby, "New spectrophotometric and conductometric methods for macrolide antibiotics determination in pure and pharmaceutical dosage forms using rose Bengal," *Journal of Spectroscopy*, vol. 2013, Article ID 214270, 13 pages, 2013.
- [23] E. Zumelzu, I. Asomavich, F. Rull, and C. Cabezas, "Evaluation of NaCl effect on vibration-delaminated metal-polymer composites by improved micro-raman methodology," *Journal of Spectroscopy*, vol. 2013, Article ID 742681, 6 pages, 2013.
- [24] N. N. Brandt, A. Y. Chikishev, A. A. Mankova, M. M. Nazarov, I. K. Sakodynskaya, and A. P. Shkurinov, "THz and IR spectroscopy of molecular systems that simulate function-related structural changes of proteins," *Journal of Spectroscopy*, vol. 27, no. 5-6, pp. 429–432, 2012.

Research Article

Monitoring of Spectral Map Changes from Normal State to Superconducting State in High- T_C Superconductor Films Using Raman Imaging

J. L. González-Solís,¹ R. Sánchez-Ruiz,¹ I. A. Arana-Zamora,¹ J. C. Martínez-Espinosa,² M. L. Pérez-Arrieta,³ and C. Falcony-Guajardo⁴

¹*Biophysics and Biomedical Sciences Laboratory, Centro Universitario de Lagos, Universidad de Guadalajara, Enrique Díaz de León S/N, Paseo de la Montaña, 47460 Lagos de Moreno, JAL, Mexico*

²*Mathematics and Biotechnology Academy, Instituto Politécnico Nacional-UPIIG, 36275 Silao de la Victoria, GTO, Mexico*

³*Unidad Académica de Física, Universidad Autónoma de Zacatecas, Calzada Solidaridad Esq. Paseo, La Bufa s/n, 98060 Zacatecas, ZAC, Mexico*

⁴*Departamento de Física, Centro de Investigación y Estudios Avanzados-IPN, Apdo., Postal 14-470, Del. Gustavo A. Madero, 07000 México, DF, Mexico*

Correspondence should be addressed to J. L. González-Solís; jluis0968@gmail.com

Received 16 July 2014; Revised 23 September 2014; Accepted 24 September 2014

Academic Editor: Jie-Fang Zhu

Copyright © 2015 J. L. González-Solís et al. This is an open access article distributed under the Creative Commons Attribution License, which permits unrestricted use, distribution, and reproduction in any medium, provided the original work is properly cited.

We have explored the chemical structure of $TlBa_2Ca_2Cu_3O_9$ high- T_C superconductor films with Tl-1223 phase to monitor spectral map changes from normal state to superconducting state using the technique of Raman imaging. Raman images were performed for 12 different temperatures in the 77–293 K range. At room temperature, the Raman images were characterized by a single color but as the temperature dropped a new color appeared and when the temperature of 77 K is reached and the superconducting state is assured, the Raman images were characterized by the red, green, and blue colors. Our study could suggest that the superconducting state emerged around 133 K, in full agreement with those reported in the literature. A cross-checking was done applying principal component analysis (PCA) to other sets of Raman spectra of our films measured at different temperatures. PCA result showed that the spectra can be grouped into two temperature ranges, one in the 293–153 K range and the other in the 133–77 K range suggesting that transition to the superconducting state occurred at some temperature around 133 K. This is the first report of preliminary results evaluating the usefulness of Raman imaging in determination of transition temperature of superconductor films.

1. Introduction

The scientific applications of superconductivity in commerce and industry have been broadened by the discovery of ceramic superconductors or high- T_C superconductors [1]. Creating high- T_C superconductor films with high current densities (~ 106 A/cm²) in long kilometer lengths has become the major goal to be achieved for industrial and commercial applications. The creation of high- T_C superconductor films with high current densities has been achieved in laboratories with smaller lengths of films but has not yet been achieved for longer lengths of film. Some of the superconducting films

preparation techniques used include metal organic chemical vapor deposition (MOCVD), pulsed laser deposition (PLD), sol-gel, metal-organic deposition (MOD), chemical vapor deposition (CVD), electrophoresis, electrodeposition, and aerosol/spray pyrolysis. Because only films of high quality are useful in industrial and commercial applications, several parameters of the films as crystal orientation, oxygen concentration, morphology, grain size, and layer thickness must be monitored to insure that films with high current density and transition temperature are being manufactured [2]. In order to determine the current density and transition temperature of the films, crystal orientation, oxygen concentration, and

layer thickness play major roles [2–5]. Current flow in a high- T_C superconductor film is directly related to the crystal orientation and layer thickness of the films, so that the better aligned the axes of the crystal for the appropriate layer thickness, the higher the current density in the film. Furthermore, the transition temperature is directly related to the oxygen concentration of the crystal; the higher the oxygen concentration, the higher the transition temperature. Previously published works show that these three important characteristics of these films can be monitored using Raman spectroscopy technique [6]. In addition, the temperature dependence of the Raman line shapes can indicate changes in the electronic density of states and help in the search for superconducting mechanisms. The analysis of temperature dependence of the phonon frequencies is also a means to determine which phonons could be directly associated with the superconducting transition. Almost all aspects of high- T_C superconductivity have been addressed by Raman scattering because of its experimental versatility and the coupling of the elementary excitations to electron-hole pairs. Small samples have been nondestructively investigated at low temperatures, under electric or magnetic fields, as a function of excitation energy, and under high pressure. Thus, the effects of external parameters on superconductivity can be studied [7].

Raman scattering is the inelastic scattering of photons creating or annihilating an elementary excitation (phonons, plasmons, excitons, or spin fluctuations) in the solid. All of these excitations have been observed and studied in high- T_C superconductors, which is why Raman scattering has contributed so much to their understanding [8]. Raman spectroscopy is a powerful analytical investigation technique for studying phonons in solid with relatively simple instrumentation [9]. Therefore, Raman spectroscopy is an excellent tool for acquiring information on properties of high- T_C superconductor films in situ; however, the technique of Raman spectroscopy could be even more powerful if it allows us to know the spatial distribution of the chemical composition in high- T_C films. In a Raman image, each pixel is assigned the Raman spectrum recorded in the same position obtaining a spatial distribution of colors (red, green, or blue) where each color indicates a specific chemical component [10].

Furthermore of the Raman imaging, recently multivariate analysis has been applied to Raman spectroscopy to classify a wide variety of biological samples becoming a very promising tool to be used in biomedical research. In particular, PCA has been used to differentiate between epithelial precancers and cancers [11] and leukemia, cervical cancer, and control samples [12, 13]. PCA is a way of identifying patterns in data and expressing the data in such a way as to highlight differences. When the principal component loadings are plotted as a function of different variables, they reveal which variable accounts for the greatest difference. Other techniques widely used in data analysis are linear discriminant analysis (LDA) and hierarchical clustering analysis (HCA), allowing identifying in a natural way the classes present in data and depicted by a tree diagram or dendrogram. These techniques have been used in a large variety of engineering and

scientific disciplines such as gene expression [14, 15], stock indices [16], and astrophysics [17].

In this work, we characterized the chemical structure of $TlBa_2Ca_2Cu_3O_9$ high- T_C superconductor films with Tl-1223 phase and monitored spectral map changes from normal state to superconducting state by using the technique of Raman imaging. A cross-checking was done applying PCA to other sets of Raman spectra measured at different temperature of the films obtaining the same Raman imaging result. The transition temperature reported for these films using the standard technique of the strong fall in the electrical resistance is 133.5 K [18]. It is the first report of preliminary results evaluating the usefulness of Raman imaging and PCA in the determination of transition temperature of $TlBa_2Ca_2Cu_3O_9$ high- T_C superconductor films with Tl-1223 phase.

2. Experiment

In this work, we explored three $TlBa_2Ca_2Cu_3O_9$ high- T_C superconductor films with Tl-1223 phase processed by Pérez-Arrieta et al. through a two-step novel synthesis [19]. The films of average size of about 0.5 cm^2 and a thickness of $\sim 3\text{ }\mu\text{m}$ were labeled as M74, M89A, and M98A. Raman images were obtained using a Horiba Jobin-Yvon LabRAM HR800 Raman system, constituted by an Olympus confocal microscope which focuses with a 50X Leica long-range objective, a laser of 830 nm, and 17 mW power irradiation (spot size of approximately $1\text{ }\mu\text{m}$ diameter) on the surface of the superconductor film and collects the Raman backscattered radiation.

The control of the Raman system, spectra recording, and images processing were performed with the LabSpec 5.0 software. We used the Raman peak at 520 cm^{-1} of a silicon semiconductor for instrument calibration. In order to measure temperature-dependent Raman spectra, each superconductor film covered by a pair of quartz sheets was placed inside a Linkam THMS600 heating and cooling microscope stage coupled to Raman system. Microscope stage or cryostat allows that the Raman measurements can be performed within the 77 to 900 K temperature range. The cryostat is attached to a Linkam TMS94 temperature programmer whereby the desired temperature and laser exposure were programmed. Temperature programmer and the cryostat are connected to a tank, which supplies liquid nitrogen to cryostat. The cryostat is placed on the X-Y stage of microscope and its window positioned under the microscope objective allowing point to point automatic mapping of the interest region on the film.

All Raman spectra were recorded with spectral resolution of 0.6 cm^{-1} . By using LabSpec software, a region of $100 \times 100\text{ }\mu\text{m}^2$ was selected to characterize the films. Once desired temperature is reached, X-Y stage automatically moves across the selected region in step of $1\text{ }\mu\text{m}$ with laser exposure of 0.5 seconds. For each temperature, the data acquisition time for a single Raman image of a superconductor film was 90 minutes, on average.

Raman images of the three superconductor films were obtained for 12 different temperatures within 77–293 K range. The resolution for each Raman image was 100×100 pixels by containing a total of 10,000 Raman spectra.

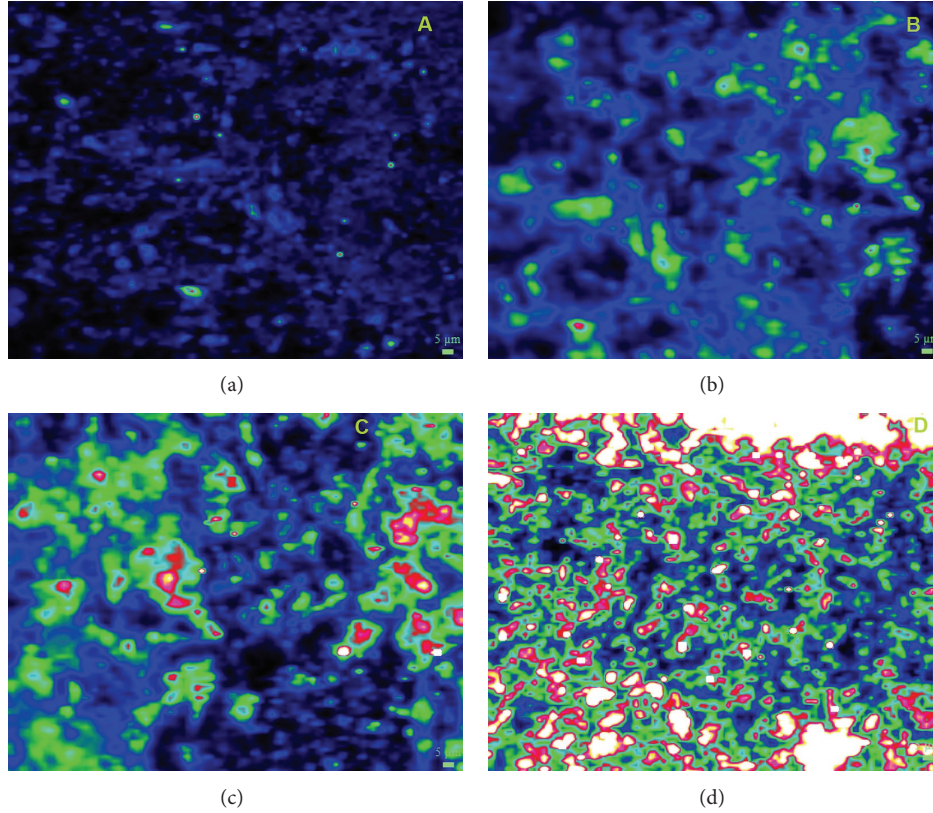


FIGURE 1: Raman images of M74 $\text{TlBa}_2\text{Ca}_2\text{Cu}_3\text{O}_9$ high- T_C superconductor films with Tl-1223 phase. (a) Raman image at 293 K. (b) Raman image at 153 K. (c) Raman image at 133 K. (d) Raman image at 77 K.

For the PCA, we measured an average of 2.5 spectra for each of the 12 temperatures within 77–293 K temperature range using the same Raman system. PCA and all the algorithms for data analysis were implemented in MatLab commercial software.

3. Results and Discussion

We analyzed three $\text{TlBa}_2\text{Ca}_2\text{Cu}_3\text{O}_9$ high- T_C superconductor films with Tl-1223 phase. These superconductor films have a tetragonal ($D4h$) unit cell with $a = 0.38429$ and $c = 15.871$ Å and belong to the $P4/mmm$ space group. They have one insulating TlO layer, two spacing BaO layers, two separating Ca layers, and three conducting CuO_2 planes making them “1223” type. The transition temperature measured in these films using standard techniques is about 133.5 K [3, 4, 18, 20].

Raman images were constructed by plotting spectral intensities of superconductor films versus the coordinates of points from where spectra were recorded and, according to this, the red, green, or blue colors are assigned. Each film was analyzed according to the methodology described in the previous section.

In order to obtain the Raman images, we measured a large number of spectra in a programmed manner. Figure 1 shows four of twelve Raman images of M74 superconductor film measured at 293, 153, 133, and 77 K. Raman image measured at 293 K (see Figure 1(a)) is characterized only by

TABLE 1: Experimental Raman bands for $\text{TlBa}_2\text{Ca}_2\text{Cu}_3\text{O}_9$ high- T_C superconductor films with Tl-1223 phase.

Banda (cm^{-1})	Symmetry	Atoms mainly involved
104	A_{1g}	Tl, Ba, Cu
152	A_{1g}	Cu, Ba
238	B_{1g}	O(1) CuO_2 plane-O(4)
260	A_{1g}	Ca-Ca
526	A_{1g}	Bridge O(3), O(4)

the blue color and its representative spectrum is given in Figure 2(a). At room temperature, the blue color dominates and as temperature drops and approaches the transition temperature, T_C , new green regions appear and increase considerably (see Figures 1(b) and 2(b) and Table 1). Figures 1(c) and 1(d) show Raman images of M74 superconductor film measured at 133 and 77 K, respectively. At 133 K, we observed that the red color started to appear inside green regions and its Raman spectrum is shown in Figure 2(c) (see Table 1). At 77 K, where it is known that the superconducting state is already expressed in our type of films, the Raman image is characterized by the red color showing that its appearance shows us the emergence of the superconducting state, determining T_C . This monitoring of spectral map changes from normal state to superconducting state in $\text{TlBa}_2\text{Ca}_2\text{Cu}_3\text{O}_9$ high- T_C superconductor films with Tl-1223

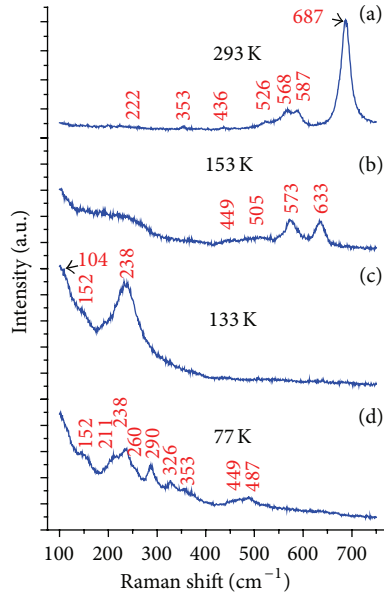


FIGURE 2: Raman spectra of the $\text{TlBa}_2\text{Ca}_2\text{Cu}_3\text{O}_9$ high- T_C superconductor films with Tl-1223 phase measured at different temperatures.

phase using Raman imaging could allow us to suggest that the emergence of the superconducting state occurred around $T_C = 133$ K. In Raman spectra at 133 and 77 K (Figures 2(c) and 2(d)), we observe that the strong band at 238 cm^{-1} (B_{1g} modes) is the one that best characterizes this red region of the Raman images and it is assigned to O(1) in CuO_2 planes, where the superconducting charge carriers are thought to be localized.

In Table 1, we observe that the A_{1g} modes of Tl-1223 involve motion of Ca, Ba, Cu(2), O(2), and O(3) atoms along the c -axis [21–25]. Other Raman bands, whose origin is not clear, are shown in the Raman spectra; however, some of the bands at 293 and 449 cm^{-1} could be assigned Cu planes O(1,2) and O(2,3) [25] and the bands at 587 and 633 cm^{-1} could be a B_{1g} O(4) motion (oxygen atom of TlO plane) [26].

Raman images and spectra obtained for superconductor films, M89A and M98A, showed the same behavior as the Raman images and spectra for M74 film.

In this paper, we present the spatial distribution of the high- T_C superconductor film's major chemical components during the transition to the superconducting state.

We have reported in this paper the first spectral maps of superconductor films during superconducting transition. Raman imaging could provide us with information about which phonons could be directly associated with the superconducting transition and the regions on superconductor films where there is a greater concentration of oxygen as temperature approaches the transition temperature.

The exact sequence of events during superconducting transition is, of course, well understood from studies of fall in the electrical resistance of the superconductor films. Unlike this method, highly limited by the grain boundaries, spectral imaging methodology affords the advantage of monitoring the distribution of chemical components using only their inherent vibrational fingerprints and therefore without these

limitations of granular type. Furthermore, spectral recognition of $\text{TlBa}_2\text{Ca}_2\text{Cu}_3\text{O}_9$ high- T_C superconductor films is necessary for an application of vibrational imaging methodology to aid in the detection of the superconducting phase in high- T_C films.

The main advantages of Raman imaging over other techniques include the high spatial resolution achievable, which is in the same order as visible microscopy, and the compositional sensitivity of vibrational spectroscopic methods.

As a cross-checking, we applied PCA to other sets of spectra from each film. The average of Raman spectra taken per temperature was 3 obtaining a total of 30 spectra for each film. Raw spectra were processed by carrying baseline correction, smoothing, and normalization to remove noise, sample fluorescence, and shot noise from cosmic rays. This spectral processing was performed through a filter based on the Baseline Correction with Asymmetric Least Squares Smoothing algorithm [27]. Unlike other algorithms, it is fast and simple (even for large signals) and asymmetric weighting applies everywhere. Each acquired spectrum was normalized to the highest peak. Upon processing the spectra, PCA was implemented, where the main information is described by the first principal components.

PCA was implemented based on the temperature dependence of Raman spectra. The PCA results for the M74, M89A, and M98A films are shown in Figure 3. In PCA plots, each point represents a Raman spectrum measured to a given temperature.

In each plot, clearly, the 30 points can be grouped into two temperature ranges, one in the range of 293 – 153 K (black points and normal state of films) and the other in the range of 133 – 77 K (red points and superconducting state of films) suggesting that the transition to the superconducting state occurred at some temperature around 133 K. Our result of the transition temperature using the Raman imaging technique is strongly supported by a cross-checking applying PCA. PCA was able to distinguish between spectra of the normal state and superconducting state of high- T_C superconductor films with 100% sensitivity and 100% specificity allowing us to obtain a highly reliable value for the transition temperature, T_C . This temperature value, around $T_C = 133$ K, obtained using PCA agrees perfectly with the value obtained using the technique of Raman imaging.

In this paper, we demonstrate that the recognition of the superconducting transition using methods of vibrational spectral imaging is possible, although the instrumentation utilized may not have been optimal for this purpose. In Raman spectroscopy, the high spatial resolution reveals details of the spatial distribution of chemical components in high- T_C superconductor films. The use of somewhat higher laser power and more efficient optical components will reduce the data acquisition time and improve the signal quality to such an extent that this methodology may be useful for screening applications of all types of thin films.

4. Conclusions

In this paper, we presented the first spectral maps of the distribution of the high- T_C superconductor film's major chemical

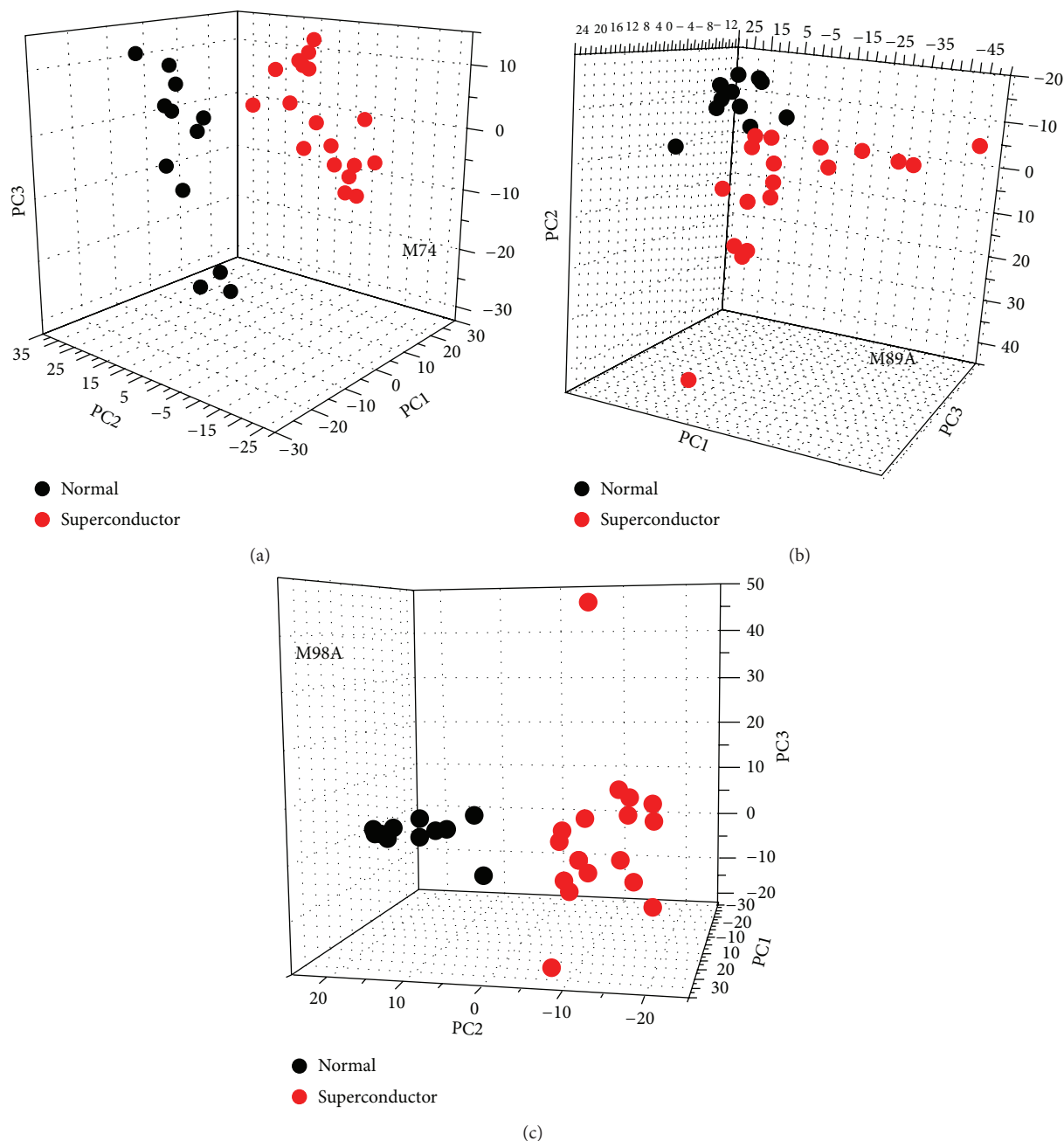


FIGURE 3: Scatter plot of all temperature-dependent Raman spectra for three $\text{TlBa}_2\text{Ca}_2\text{Cu}_3\text{O}_9$ high- T_C superconductor films with Tl-1223 phase.

components during the transition to the superconducting state allowing us to determine the transition temperature, T_C . Raman imaging showed that the transition temperature to superconducting state for $\text{TlBa}_2\text{Ca}_2\text{Cu}_3\text{O}_9$ superconductor films occurred at some temperature around $T_C = 133$ K in full agreement with those reported in the literature. A cross-checking was done applying principal component analysis to other sets of spectra of the superconductor films measured at different temperatures and obtaining same value for the transition temperature. Unlike other methods to measure this critical temperature in high- T_C superconductor films, highly limited by the grain boundaries, Raman imaging technique

affords the advantage of monitoring the distribution of chemical components using only their inherent vibrational fingerprints and therefore without these limitations of granular type. This is the first report of preliminary results evaluating the usefulness of Raman imaging and PCA in the determination of transition temperature of $\text{TlBa}_2\text{Ca}_2\text{Cu}_3\text{O}_9$ high- T_C superconductor films with Tl-1223 phase.

Conflict of Interests

The authors declare that there is no conflict of interests regarding the publication of this paper.

Acknowledgments

The authors wish to thank CONACYT for financial support under Grant no. 45488. Also, they are thankful to Intercovamex Company in Mexico for the financial aid to show this work in XXII International Material Research Congress, IMRC 2013.

References

- [1] T. P. Sheahen, *Introduction to High-Temperature Superconductivity*, Plenum Press, New York, NY, USA, 1994.
- [2] A. Goyal, D. P. Norton, J. D. Budai et al., "High critical current density superconducting tapes by epitaxial deposition of $\text{YBa}_2\text{Cu}_3\text{O}_x$ thick films on biaxially textured metals," *Applied Physics Letters*, vol. 69, no. 12, pp. 1795–1797, 1996.
- [3] N. Dieckmann, A. Bock, and U. Merkt, "Spatially resolved analyses of epitaxial and electrical properties of $\text{YBa}_2\text{Cu}_3\text{O}_7$ devices," *Applied Physics Letters*, vol. 68, no. 25, pp. 3626–3628, 1996.
- [4] A. Bock, R. Kürsten, M. Brühl, N. Dieckmann, and U. Merkt, "Desorption of oxygen from $\text{YBa}_2\text{Cu}_3\text{O}_{6+x}$ films studied by Raman spectroscopy," *Physical Review B - Condensed Matter and Materials Physics*, vol. 54, no. 6, pp. 4300–4309, 1996.
- [5] C. Thomsen, R. Liu, M. Bauer et al., "Systematic Raman and infrared studies of the superconductor $\text{YBa}_2\text{Cu}_3\text{O}_{7-x}$ as a function of oxygen concentration ($0 \leq x \leq 1$)," *Solid State Communications*, vol. 65, no. 1, pp. 55–58, 1988.
- [6] R. Feile, U. Schmitt, and P. Leiderer, "Raman experiments on YBaCuO -Superconductors," *Physica C*, vol. 153–155, no. 1, pp. 292–293, 1988.
- [7] S. B. Dierker, M. V. Klein, G. W. Webb, and Z. Fisk, "Electronic Raman scattering by superconducting-gap excitations in Nb_3Sn and V_3Si ," *Physical Review Letters*, vol. 50, no. 11, pp. 853–856, 1983.
- [8] C. Thomsen, "Light scattering in high- T_c superconductors," in *Light Scattering in Solids VI*, M. Cardona and G. Güntherodt, Eds., vol. 68 of *Topics in Applied Physics*, pp. 285–359, Springer, Berlin, Germany, 1991.
- [9] E. Faulques and R. E. Russo, "Characterization of high temperature superconductors with Raman spectroscopy," in *Applications of Analytical Techniques to the Characterization of Materials*, D. L. Perry, Ed., Plenum Press, New York, NY, USA, 1991.
- [10] C. Matthäus, S. Boydston-White, M. Miljković, M. Romeo, and M. Diem, "Raman and infrared microspectral imaging of mitotic cells," *Applied Spectroscopy*, vol. 60, no. 1, pp. 1–8, 2006.
- [11] N. Stone, C. Kendall, N. Shepherd, P. Crow, and H. Barr, "Near-infrared Raman spectroscopy for the classification of epithelial pre-cancers and cancers," *Journal of Raman Spectroscopy*, vol. 33, no. 7, pp. 564–573, 2002.
- [12] J. L. González-Solís, J. C. Martínez-Espinosa, L. A. Torres-González, A. Aguilar-Lemarroy, L. F. Jave-Suárez, and P. Palomares-Anda, "Cervical cancer detection based on serum sample Raman spectroscopy," *Lasers in Medical Science*, vol. 29, pp. 979–985, 2014.
- [13] J. L. González-Solís, J. C. Martínez-Espinosa, J. M. Salgado-Román, and P. Palomares-Anda, "Monitoring of chemotherapy leukemia treatment using Raman spectroscopy and principal component analysis," *Lasers in Medical Science*, vol. 29, no. 3, pp. 1241–1249, 2014.
- [14] Q. Zhang and Y. Zhang, "Hierarchical clustering of gene expression profiles with graphics hardware acceleration," *Pattern Recognition Letters*, vol. 27, no. 6, pp. 676–681, 2006.
- [15] P. D'Haeseleer, "How does gene expression clustering work?" *Nature Biotechnology*, vol. 23, no. 12, pp. 1499–1501, 2005.
- [16] L. Kullmann, J. Kertesz, and R. N. Mantegna, "Identification of clusters of companies in stock indices via Potts superparamagnetic transitions," *Physica A*, vol. 287, no. 3–4, pp. 412–419, 2000.
- [17] A. Dekel and M. J. West, "On percolation as a cosmological test," *The Astrophysical Journal*, vol. 288, pp. 411–417, 1985.
- [18] A. Iyo, Y. Tanaka, Y. Ishiura et al., "Study on enhancement of T_c (≥ 130 K) in $\text{TlBa}_2\text{Ca}_2\text{Cu}_3\text{O}_y$ superconductors," *Superconductor Science and Technology*, vol. 14, no. 7, pp. 504–510, 2001.
- [19] L. Pérez-Arrieta, M. Aguilar-Frutis, J. L. Rosas-Mendoza, C. Falcony, and M. Jergel, "Two step synthesis of $\text{TlBa}_2\text{Ca}_2\text{Cu}_3\text{O}_x$ films on Ag substrates by spray pyrolysis of metal-acetylacetonates," *Revista Mexicana de Fisica*, vol. 54, no. 6, pp. 446–450, 2008.
- [20] S. S. P. Parkin, V. Y. Lee, A. I. Nazzal, R. Savoy, R. Beyers, and S. J. La Placa, " $\text{Tl}_1\text{Ca}_{n-1}\text{Ba}_2\text{Cu}_n\text{O}_{2n+3}$ ($n = 1, 2, 3$): a new class of crystal structures exhibiting volume superconductivity at up to ~ 110 K," *Physical Review Letters*, vol. 61, no. 6, pp. 750–753, 1988.
- [21] C. Thomsen and G. Kaczmarczyk, "Vibrational Raman spectroscopy of high-temperature superconductors," in *Handbook of Vibrational Spectroscopy*, J. M. Chalmers and P. R. Griffiths, Eds., John Wiley & Sons, Chichester, UK, 2002.
- [22] D. L. Perry, *Applications of Analytical Techniques to the Characterization of Materials*, Springer Science+Business Media, LLC, 1990.
- [23] K. F. McCarty, B. Morosin, D. S. Ginley, and D. R. Boehme, "Raman analysis of $\text{TlCa}_2\text{Ba}_2\text{Cu}_3\text{O}_{19}$ and $\text{Tl}_2\text{Ca}_2\text{Ba}_2\text{Cu}_3\text{O}_{10}$ crystals," *Physica C: Superconductivity and Its Applications*, vol. 157, no. 1, pp. 135–143, 1989.
- [24] C. Thomsen and M. Cardona, "Light scattering in high- T_c superconductors," in *Physical Properties of High Temperature Superconductors I*, D. M. Ginsberg, Ed., p. 409, World Scientific, Singapore, 1990.
- [25] A. D. Kulkarni, F. W. de Wette, J. Prade, U. Schröder, and W. Kress, "Lattice dynamics of high- T_c superconductors: optical modes of the thallium-based compounds," *Physical Review B*, vol. 41, no. 10, pp. 6409–6417, 1990.
- [26] E. Faulques, P. Dupouy, and S. Lefrant, "Oxygen vibrations in the series $\text{Bi}_2\text{Sr}_2\text{Ca}_{n-1}\text{Cu}_n\text{O}_{4+2n+y}$," *Journal de Physique I*, vol. 1, pp. 901–916, 1991.
- [27] H. F. M. Boelens, P. H. C. Eilers, and T. Hankemeier, "Sign constraints improve the detection of differences between complex spectral data sets: LC-IR as an example," *Analytical Chemistry*, vol. 77, no. 24, pp. 7998–8007, 2005.

Research Article

Research on Fluorescence Spectroscopy Characteristics of Dissolved Organic Matter of Landfill Leachate in the Rear Part of Three Gorges Reservoir

Zhigang Xie and Wei Guan

College of Materials & Chemical Engineering, Chongqing University of Arts and Sciences, Chongqing 402160, China

Correspondence should be addressed to Wei Guan; guanwei951030@126.com

Received 8 August 2014; Revised 7 September 2014; Accepted 8 September 2014

Academic Editor: Wen Zeng

Copyright © 2015 Z. Xie and W. Guan. This is an open access article distributed under the Creative Commons Attribution License, which permits unrestricted use, distribution, and reproduction in any medium, provided the original work is properly cited.

Three-dimensional fluorescence and infrared spectroscopy analysis of the leachate dissolved organic matter (DOM) of the Three Gorges was reported in spring, summer, and autumn seasons, respectively. Studies show that, that organic matter of landfill leachate in Yongchuan, Dazu and Jiangjin is the class of fulvic-like acid and protein-like fluorescence. The study also found that the longer the time of the pile of garbage, the lower the content of class of protein-like concentration, and the higher the concentration of fulvic-like acid, indicating that the protein waste material in the humification process is easy degradation. However, the same source of DOM is similar in the functional group composition and molecular structure. Characteristic frequency area analysis showed that humic acids (HA), and fulvic acids (FA) contain more than hydrophilic organic matter (HyI) aromatic ring structure, and FA aromatic ring structure is the most. Because of Chung-amide NH deformation vibration, there are strong absorption peaks in the $1562\sim 1572\text{ cm}^{-1}$ for various components; HyI contains many organic nitrogen compounds and fatty acids.

1. Introduction

Chinese major cities' living garbage is given priority to kitchen waste, its organic matter composition is high, calorific value matter content is little, the moisture content is high, making landfill leachate water amount large, and water contained more organic pollutants [1, 2]. DOM in landfill leachate comes from landfill organic matter biodegradation, which is similar to the degradation of organic matter in the soil. DOM refers to organic matter retained in water after filtering through the $0.45\text{ }\mu\text{m}$ film. Generally, in leachate DOM can be divided into three ingredients such as HA, FA, and HyI. HA and FA in waste leachate are known as humic substances (HS).

Ultraviolet-visible spectroscopy, infrared spectroscopy, fluorescence spectroscopy, nuclear magnetic resonance (NMR), pyrolysis + GC-MS, and other analysis technology are widely used in chemistry to determine structure and functional characteristics of organic matter [3–8]. Many researchers in other disciplines at home and abroad applied these for chemical structure characteristics analysis of

hydrophilic organic matter, humic acid, and fulvic acids of natural water body or soil. At present, there are also some abroad researchers who carry out these techniques to study chemical structure and functional characteristics of dissolved organic matter in the landfill leachate [9–12]. In order to further understand the chemical properties of organic matter in leachate, the most prevalent method is ultraviolet-visible spectroscopy and infrared spectroscopy. In domestic, the related research reports about this technology used in leachate organic matter are rare. However, three-dimensional fluorescence spectrum can be used to characterize the leachate DOM and organic fluorophores specific information can be obtained; infrared spectroscopy can be further used to characterize the structure characteristics of DOM rapidly.

The reports of three-dimensional fluorescence and infrared spectrum used to study the characteristics of waste leachate quality are very rare and those combined with two kinds of spectral technology in molecular level study landfill leachate are rarely reported. In order to understand physical and chemical characteristics and their seasonal variation of landfill leachate, three-dimensional fluorescence, infrared

TABLE 1: Water quality parameters landfill leachate.

Season	Region	pH	COD	UV ₂₅₄	E4/E6
Spring	Yongchuan	8.0	5162	123.9	1.857
	Jiangjin	8.2	5225	139.5	2.667
	Dazu	8.2	5045	74.2	1.310
Summer	Yongchuan	8.3	3918	66.4	2.784
	Yongchuan	7.9	2255	28.1	1.777
Autumn	Jiangjin	8.5	2332	29.2	2.680
	Dazu	8.3	3668	46.8	1.125

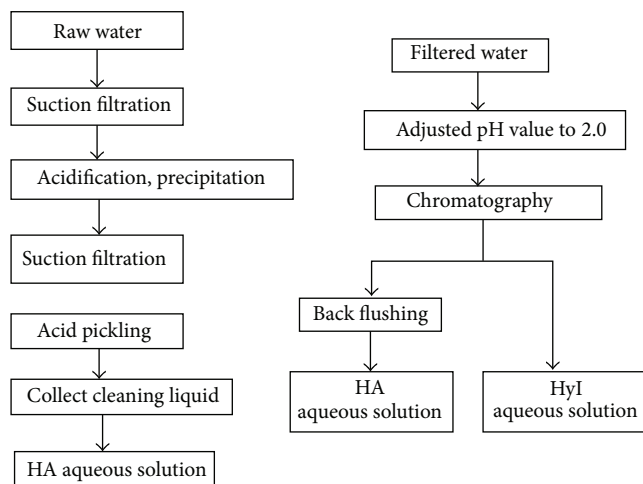


FIGURE 1: Separation procedures to fractionate DOM in leachate.

spectroscopy, UV-Vis spectra, and elemental are used to characterize rear parts of the Three Gorges for the leachate DOM. It has a positive guiding significance on developing landfill leachate treatment technology and on studying the landfill leachate influence on environment.

2. Materials and Methods

2.1. Sample Collection. Landfill leachate samples were collected from leachate equalization basin of domestic waste treatment plant in Yongchuan, Jiangjin, and Dazu. The landfill times were 4, 5, and 6 years in these three sites, respectively. When water samples is brought to the laboratory, it is immediately centrifuged under the condition of 12000 r/min for 10 min, followed by supernatant filtration with 0.45 μm microporous membrane, and the organic matter in filtrate is the DOM. The basic physical and chemical parameters of water samples are shown in Table 1.

2.2. Enrichment and Separation of the DOM. XAD-8 resins are adopted to enrich and to separate DOM in leachate, namely, HA, FA, and HyI. XAD-8 resins are widely used in the enrichment and separation of DOM in sewage and natural water [13–16]. Separation step is shown in Figure 1.

Water amount relationship is recorded before and after the enrichment and separation, and the water samples are stored separately at 4°C in refrigerator. Some water samples

are taken out to freeze and to dry. Freeze drier, manufactured at Beijing Boyikang Experimental Instrument Co., Ltd., with working condition temperature less than -50°C and pressure less than 20 Pa, was used to analyze HA, FA, and HyI after freeze drying.

2.3. Three-Dimensional Fluorescence Spectrum Analysis. Fluorescence spectrum determined by HITACHI F-7000 fluorescence spectrophotometer. Instrument light source is 150 W xenon lamp, and photomultiplier tube voltage is 700 V. Excitation and emission monochromator are diffraction grating, and excitation and emission slit width is 5 nm. Excitation light wavelength range is 200~450 nm, and emitting light wavelength range is 250~550 nm. Data are processed with Sigmaplot software and are characterized by contour line diagram, with reference to ultrapure water as blank correction on basis of the Raman scattering of water.

2.4. Infrared Spectrum Analysis. Fourier transformation infrared spectroscopy (FTIR) was adapted in infrared spectrum analysis. 1~2 mg freeze dried HA, FA, HyI, and intact samples from landfill leachate are taken and are mixed with about 300 mg KBr (spectrum pure). These samples are ground to the fine particles and are blended to the particle size of smaller than 2 μm . These are pressed to flakiness in $(5\sim 10) \times 10^7$ pa for 1 min. FTIR-8400 spectrometer scan is used in the range of 4000~1200 cm^{-1} , and the spectrum is measured and recorded.

3. Results and Analysis

3.1. Three-Dimensional Fluorescence Spectrum of Leachate DOM. Different DOM has different fluorescent groups. Our previous research [17] suggests that the three-dimensional fluorescence characteristic of wastewater DOM is shown in Table 2. Fulvic-like fluorescence (Peak A and Peak C) is relevant with carbonyl and carboxyl of humus structure [18–22]. However, protein-like fluorescence (Peak D, Peak B, Peak S, and Peak T) is relevant with amino acid structure [17, 23–26].

The position and intensity of fluorescence peak are different. Figure 2 is partial diagram of the three-dimensional fluorescence spectra of landfill leachate DOM. Table 3 shows the fluorescence and fluorescence intensity of percolate DOM.

According to Figure 2, for spring landfill leachate, the fluorescence peak type of Yongchuan includes fulvic-like acid (visible region, UV region, resp.), high excitation wavelength tryptophan-like, high excitation wavelength tyrosine-like, and humic acid. The fluorescence peak of low excitation wavelength tryptophan-like and low excitation wavelength tyrosine-like is weak. Leachate fluorescence peak type of Spring Jiangjin is visible fulvic-like acid, high excitation wavelength tryptophan-like, UV fulvic-like acid, high excitation wavelength tyrosine-like, and high excitation wavelength tryptophan-like, respectively. The leachate fluorescence peak type of Dazu and Jiangjin is similar. The UV fulvic-like acid fluorescence intensity of Dazu is stronger than that of Jiangjin, and the high excitation wavelength tryptophan-like

TABLE 2: Major fluorescence peak for DOM.

Peak	Ex/nm	Em/nm	Matter
I	350~440	430~510	Humic-like
A	240~270	370~440	UV fulvic-like
C	310~360	370~450	Vis fulvic-like
D	220~230	280~310	Low-excitation wavelength tyrosine-like
B	270~280	280~310	High-excitation wavelength tyrosine-like
S	220~230	320~350	Low-excitation wavelength tryptophan-like
T	270~280	320~350	High-excitation wavelength tryptophan-like

fluorescence intensity of Dazu is weaker than that of Jiangjin. There is no humic-like fluorescence peak in percolate of Dazu and Jiangjin; maybe it is related to longer landfill time.

We test the dissolved organic matter of summer Yongchuan landfill leachate. The fluorescence peak type includes ultraviolet fulvic-like acid, visible fulvic-like acid, high excitation wavelength tyrosine-like, and high excitation wavelength tryptophan-like.

The fluorescence peak type of autumn landfill leachate includes UV fulvic-like acid, visible fulvic-like acid, high excitation wavelength tryptophan-like, and low excitation wavelength tryptophan-like. The strongest fluorescence peak is Yongchuan infiltration fluorescence intensity of filtrate is strong, and Dazu infiltration fluorescence intensity of filtrate is weak.

Leachate fulvic-like fluorescence (including visible and ultraviolet region) is related to the carbonyl and carboxyl groups in humus structure. Protein-like fluorescence is related to aromatic amino acid structure. The study of three-dimensional fluorescence spectroscopy indicates that the dissolved organic matter of landfill leachate of Three Gorges Reservoir (Yongchuan, Jiangjin, and Dazu) mainly includes organics with aromatic amino acid structure and organics with carbonyl and carboxyl groups.

Fluorescent intensity of proteins in landfill leachate decreased with the increase of landfill time, while the trend of fulvic-like acid is opposite. This indicated that with the prolonged time of the landfill, microorganisms become more active, and degradation of organic matter is more obvious. With the increase of landfill time, there are obvious red shifts in fluorescence peak. This result indicated that, during the stacking process, except for the degradation of organic matter, microbial would break down proteins to produce small organic molecules. Thus, landfill proteins fluorescence intensity in the filtrate weakened, and fluorescence spectrum red shifted. The seasonal variations of leachate organic matter content are similar to the research of Coble [18], but the change magnitude is relatively small. However, the variation characteristics in spring and summer are inconsistent with Lou's study results [19]. Lou considered that summer leachate organic matter content should be reduced due to the dilution effect of rainfall. Yongchuan leachate organic matter content increased in summer, the reason is that the influence of landfill leachate is complex, such as landfill age, operation mode, climatic characteristics, and waste components. It is worth further studying these influencing factors.

3.2. Fluorescence Emission Spectrum of Leachate DOM. DOM is a complex mixture comprised of fluorescent groups. The band wide fluorescence peak is shown in Figure 3. Fluorescence intensity maximum at about 412 nm is obtained, and the fluorescence is made from unsaturated hydroxyl and carbonyl in the DOM. In spring, the fluorescence intensity of landfill leachate DOM at ex = 335 nm shows gradually increasing trend with landfill time, which is consistent with the result of three-dimensional fluorescence spectrum. However, the fluorescence intensity of Jiangjin leachate DOM in at ex = 335 nm is strong on the contrary. The reasons may be many, which is worthy of further exploration.

The fluorescence index $f_{450/500}$ can describe the humic acid in the water. The index $f_{450/500} = 1.4$ indicates that the humic acid generated from land, $f_{450/500} = 1.9$, indicates that the humic acid produced by organisms [20]. The index $f_{450/500}$ of Jiangjin, Yongchuan, and Dazu spring leachate is 3.0, 2.9, and 2.8, respectively. The index $f_{450/500}$ of summer Yongchuan is 2.7. The index $f_{450/500}$ of autumn of these three regions is 3.0, 2.8, and 2.8, respectively. These values (>1.9) indicate that humus leachate comes from organisms. The higher $f_{450/500}$ values reveal that humic substances aromatic is weak with less benzene ring structure. The fluorescence index increased with the decrease of landfill time. As the landfill time becomes longer, the contribution of microorganism to fluorescence increased.

3.3. Infrared Spectra of Landfill Leachate DOM. FTIR can provide more detailed organic matter information about chemical and functional group. Various kinds of compound functional group and characteristic frequency area are located in the area of 4000~1300 cm^{-1} . Vibration frequency is higher in this area, due to influence by the rest of small molecule. But different groups can form the interference, affecting the group's judgment. And 1300~400 cm^{-1} area is fingerprint region, in which a variety of functional groups do not have distinct characteristics, and it is strongly influenced by the molecular structure. Small changes of molecular structure can cause the obvious spectrum change in fingerprint region. In this study, organic constituent is relatively complex, and characteristics area is mainly used to identify the main functional groups. Each component landfill leachate infrared spectrum was shown in Figure 4, while the infrared spectrum of Yongchuan spring, summer, and autumn landfill DOM was shown Figure 5.

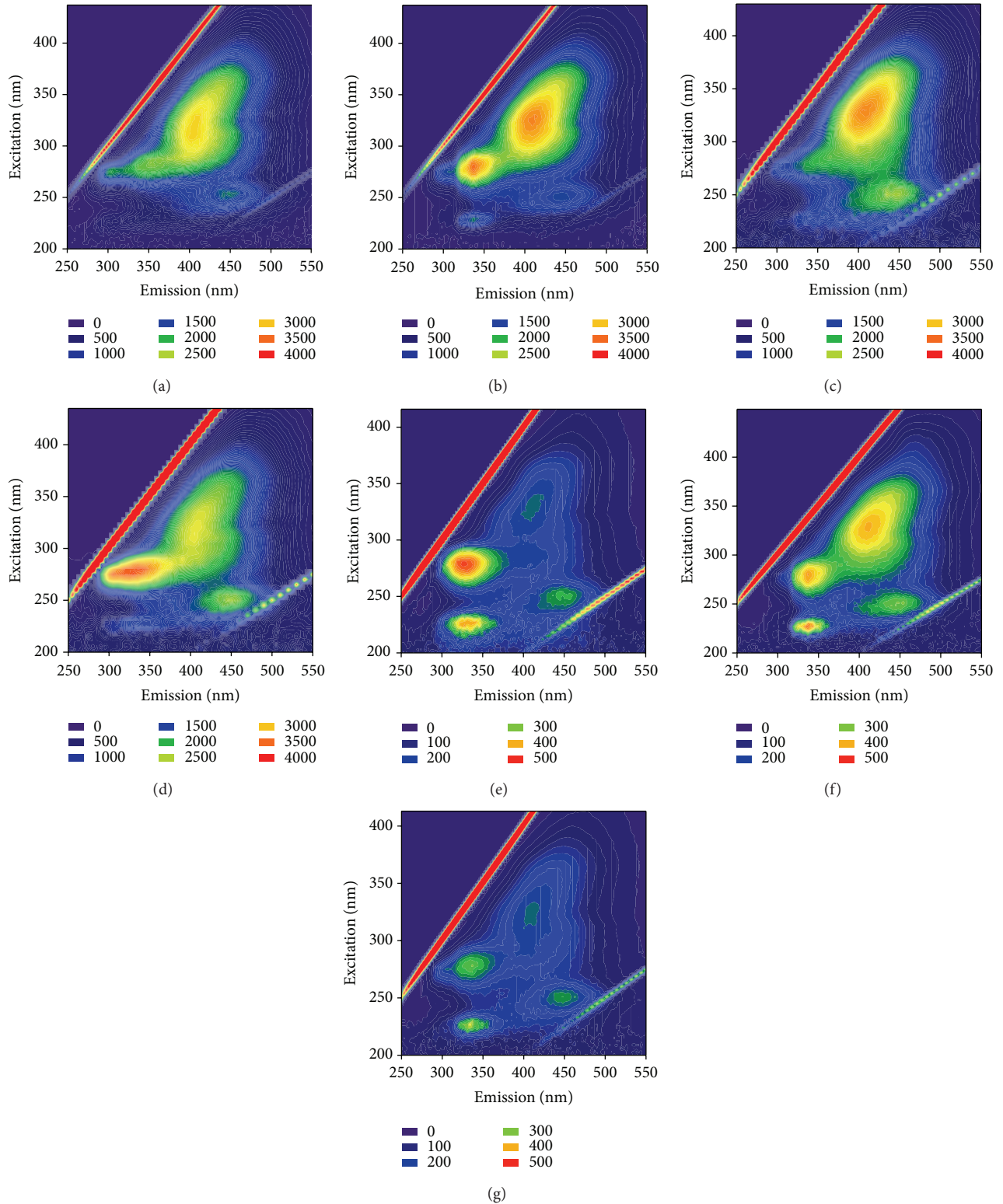


FIGURE 2: Three-dimensional fluorescence spectrum of organic matter in different landfill leachate. *Note.* Spring—(a) Yongchuan; (b) Jiangjin; (c) Dazu. Summer—(d) Yongchuan. Autumn—(e) Yongchuan; (f) Jiangjin; (g) Dazu (all 10 times diluted).

TABLE 3: Fluorescence types and intensity of dissolved organic matter.

Samples	Peak I		Peak A		Peak C		Peak D		Peak B		Peak S		Peak T	
	Ex/Em nm	$I_A/a.u.$	Ex/Em nm	$I_A/a.u.$	Ex/Em nm	$I_C/a.u.$	Ex/Em nm	$I_D/a.u.$	Ex/Em nm	$I_B/a.u.$	Ex/Em nm	$I_S/a.u.$	Ex/Em nm	$I_T/a.u.$
Yongchuan spring	356/439	2515	254/448	1806	311/403	2898	227/310	395.3	275/304	1922	230/349	689.9	284/352	2373
Yongchuan summer			250/450	2446	315/405	2671	225/305	654.3	275/305	3503	225/335	1419	275/330	3620
Yongchuan autumn			251/442	2532	323/412	2080					224/328	4032	278/328	4693
Jiangjin spring			251/436	1574	326/406	3356			275/307	1636	230/337	1758	278/337	3515
Jiangjin autumn			251/448	2875	332/412	3901					227/337	4370	281/337	4056
Dazu spring			250/435	2476	330/405	3314					230/334	1531	280/355	2104
Dazu autumn			251/448	2414	326/409	2085					227/337	3392	278/337	2871

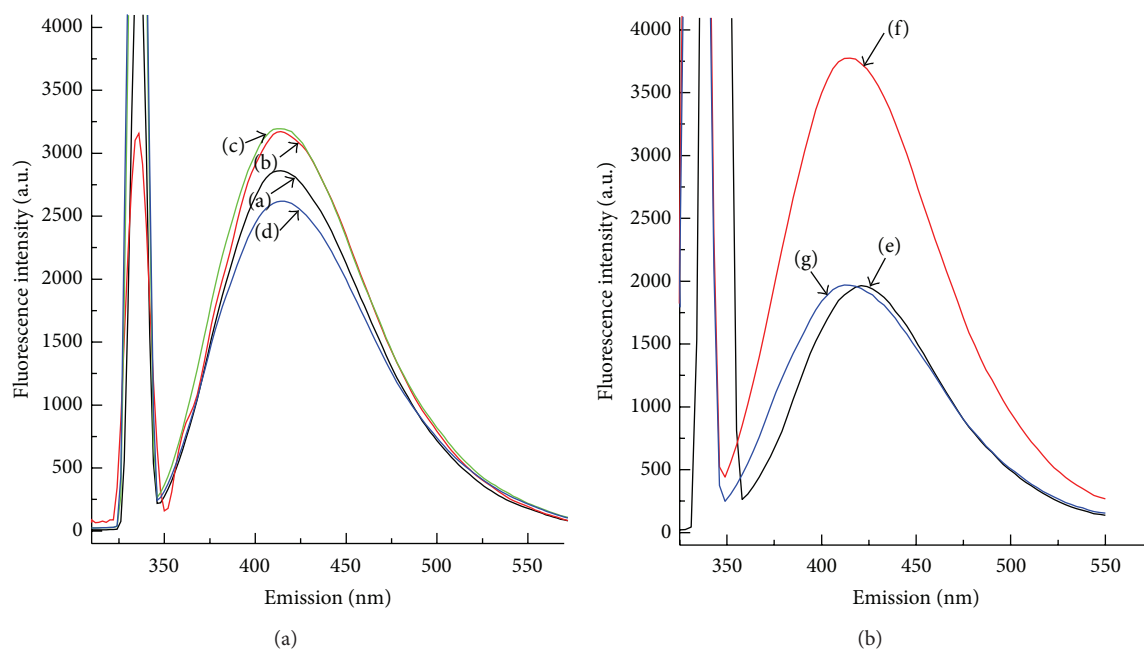


FIGURE 3: Fluorescence emission spectrum of DOM ($E_x = 335$ nm). Spring: Yongchuan (a), Jiangjin (b), and Dazu (c). Summer: Yongchuan (d). Autumn: Yongchuan (e), Jiangjin (f), and Dazu (g).

Related infrared absorption peak of humic organic matter [27–29] shows that the absorption peak in $1735\sim 1690\text{ cm}^{-1}$ is stretching vibration of carboxyl (COOH) group and the C=O of ketone compounds in organic matter. The absorption peak in $1550\sim 1515\text{ cm}^{-1}$ is deformation vibration of N–H in nitrogen compounds, namely, the characteristic band II of amide compounds. The absorption peak in $1460\sim 1450\text{ cm}^{-1}$ is shear type asymmetric deformation of carbohydrates and aliphatic compounds $-\text{CH}_2$ group and asymmetric deformation vibration of C–H in aliphatic compounds $-\text{CH}_3$ groups. The absorption peak in $1430\sim 1420\text{ cm}^{-1}$ is deformation vibration of aliphatic compounds in the double bond or $-\text{CH}_2$ connected with carbonyl.

As described in Figure 4, in different seasons and the same landfill, HA and FA have similar spectrum characteristics, showing that the same source humus is more similar in functional groups and molecular structure. Different landfill site spectrum feature has greater difference, showing that different sources of humus in have great difference in functional groups and in molecular structure, and HyI spectrum has little difference.

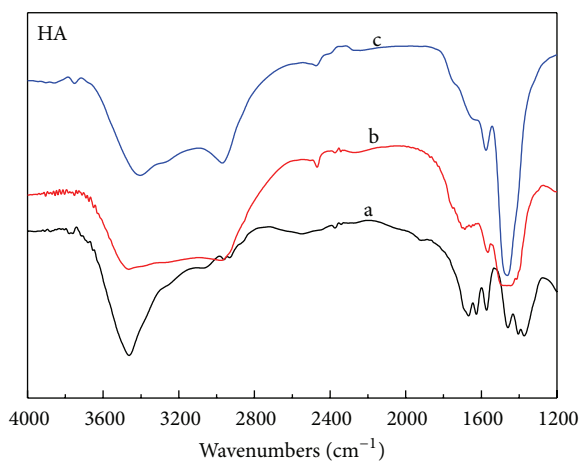
IR analysis showed that the components of different molecular weight in terms of functional group and the molecular structure are relatively similar, but the same molecular weight of each components spectrum feature has greater differences, whereas the composition of different landfills is similar. All ingredients in $1637\sim 1644\text{ cm}^{-1}$ area have a strong stretching vibration of C=C in aromatic ring skeleton, and the absorption intensity of HA and FA in this area is stronger than HyI and that of FA is larger than that of HA. It shows that HA and FA contain more aromatic ring structure. The absorption degree of HA and FA composition in Dazu and

Jiangjin is greater than that in Yongchuan. It shows that both Dazu and Jiangjin contain more aromatic ring structure. FA contains more aromatic ring structure than HA, and it is higher in autumn than in spring and in summer. In all regions, HA and FA spectrum are similar, and both in $1562\sim 1572\text{ cm}^{-1}$ area have a strong and apparent absorption peak. This should be deformation vibration of N–H in secondary amide. In addition, in the 1402 cm^{-1} area HyI also has a strong absorption peak, which is shear type asymmetric deformation of carbohydrates and aliphatic compounds $-\text{CH}_2$ group and contraction vibration of N–H in amide compounds. HyI in 1630 cm^{-1} area has strong absorption. HyI composition absorption intensity in Dazu is greater than the other two. In the organic matter, the concentration of N elements is very high; it should be shear type vibration absorption peak of a $-\text{NH}_2$ in primary amide, and this is amide characteristic peak II. In different places, HyI components in leachate at $1400\sim 1420\text{ cm}^{-1}$ area all have very strong absorption peak; this is because the C=O stretching vibration absorption.

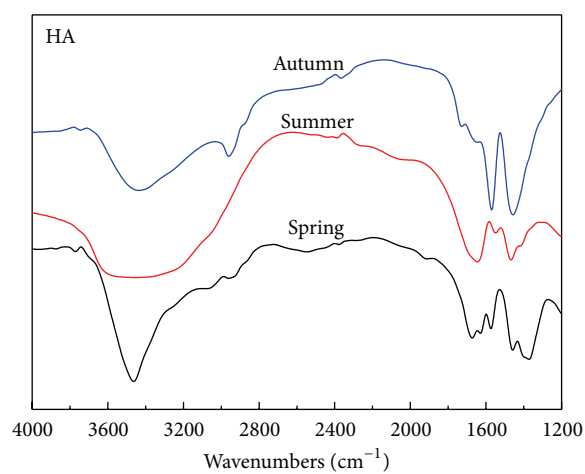
According to Figure 5, the spectroscopic characteristic of FA and HyI in same landfill with different season is similar, except for the absorption peak position. This result indicated that the functional group and molecular structure of same source of fulvic acid and hydrophilic organic matter are similar. The obvious difference of HA atlas indicated that the structure and composition of humic acid affect the degradation of humus.

4. Conclusions

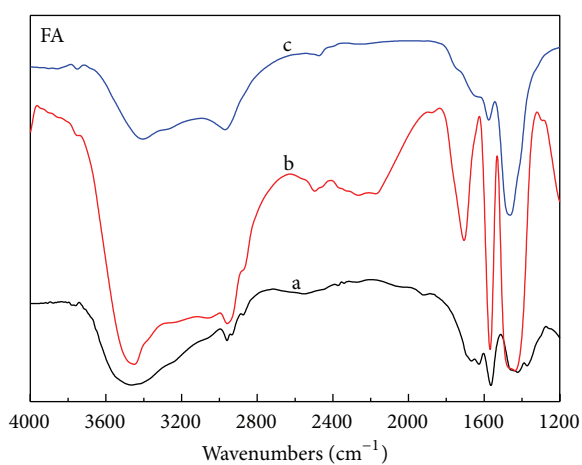
From the three-dimensional fluorescence spectrum analysis of garbage leachate, it is concluded that the characteristic



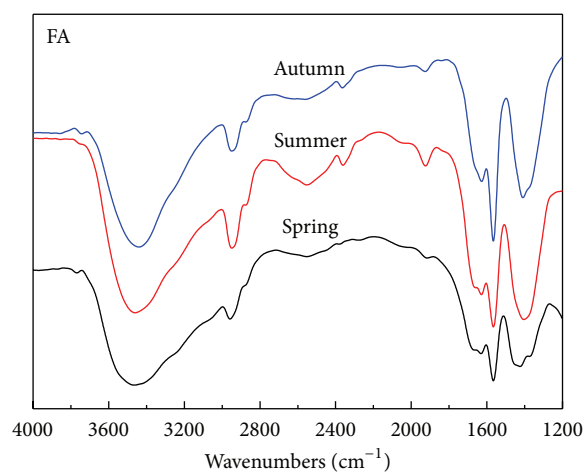
(a)



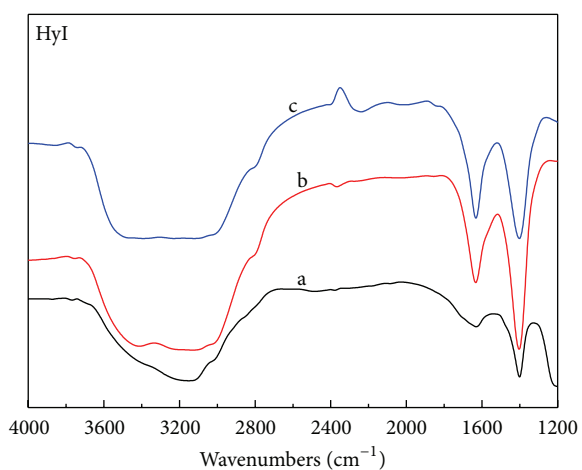
(a)



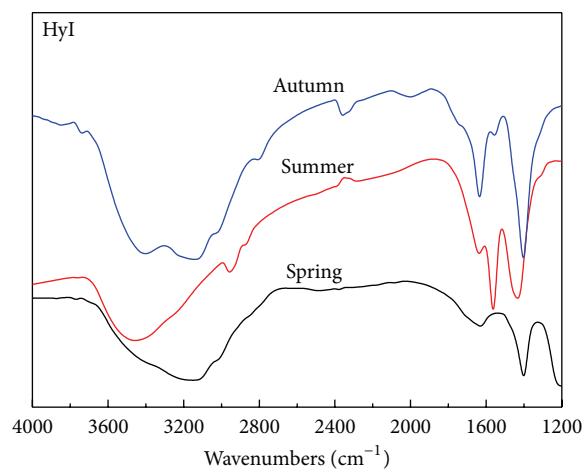
(b)



(b)



(c)



(c)

FIGURE 4: HA, FA, and HyI FTIR spectra from different landfill site. Notes: a—Yongchuan, b—Jiangjin, and c—Dazu.

FIGURE 5: HA, FA, and HyI FTIR spectra in different season site (Yongchuan).

peak type, position, and fluorescence intensity of landfill leachate organic matter in different landfill leachate are different season and different region. In different landfill, leachate DOM structure is different that is mainly embodied in leachate. HA proportion in Yongchuan is greater than that in other regions, and FA and Hyl regional difference is not large.

Three-dimensional fluorescence spectra of the landfill leachate varied with rubbish stacking time. The longer the waste stacking time, the lower the protein in leachate concentration, and the higher the fulvic-like acid concentration. It shows that the protein material in the garbage is easily degraded in the process of humification, and it humified and produced all sorts of humus. These have some guiding significance in landfill leachate treatment.

Infrared spectrum analysis shows that, in the same area among different components, they have similar spectrum characteristics. It indicates that the same source humus in terms of functional group and molecular structure is relatively similar. Characteristic frequency area analysis shows that FA contains more aromatic ring structure than HA. In autumn there is more aromatic ring structure. Due to deformation vibration of N-H in secondary amide, all the components in 1562~1572 cm^{-1} area has a very intense and obvious absorption peak. Hyl contains a lot of nitrogen compounds and fatty acid organic matter.

Conflict of Interests

The authors declare that there is no conflict of interests regarding the publication of this paper.

Acknowledgments

The present work was financially supported by Scientific Research Fund, Chongqing Municipal Education Commission (no. KJ111203), and Construction Science and Technology Project of Chongqing (2011-2-115).

References

- [1] B. Ozkaya, "Chlorophenols in leachates originating from different landfills and aerobic composting plants," *Journal of Hazardous Materials*, vol. 124, no. 1-3, pp. 107-112, 2005.
- [2] P. J. He, L. M. Shao, X. Qu, G. J. Li, and D. J. Lee, "Effects of feed solutions on refuse hydrolysis and landfill leachate characteristics," *Chemosphere*, vol. 59, no. 6, pp. 837-844, 2005.
- [3] T. Fukushima, T. Ishibashi, and A. Imai, "Chemical characterization of dissolved organic matter in Hiroshima Bay, Japan," *Estuarine, Coastal and Shelf Science*, vol. 53, no. 1, pp. 51-62, 2001.
- [4] K. Michel, E. Matzner, M. F. Dignac, and I. Kögel-Knabner, "Properties of dissolved organic matter related to soil organic matter quality and nitrogen additions in Norway spruce forest floors," *Geoderma*, vol. 130, no. 3-4, pp. 250-264, 2006.
- [5] S. Amir, M. Hafidi, G. Merlina, and J.-C. Revel, "Structural characterization of fulvic acids during composting of sewage sludge," *Process Biochemistry*, vol. 40, no. 5, pp. 1693-1700, 2005.
- [6] A. Brown, D. M. McKnight, Y. P. Chin, E. C. Roberts, and M. Uhle, "Chemical characterization of dissolved organic material in Pony Lake, a saline coastal pond in Antarctica," *Marine Chemistry*, vol. 89, no. 1-4, pp. 327-337, 2004.
- [7] K. Hautala, J. Peuravuori, and K. Pihlaja, "Measurement of aquatic humus content by spectroscopic analyses," *Water Research*, vol. 34, no. 1, pp. 246-258, 2000.
- [8] A. Baker and M. Curry, "Fluorescence of leachates from three contrasting landfills," *Water Research*, vol. 38, no. 10, pp. 2605-2613, 2004.
- [9] H. J. Fan, H. Y. Shu, H. S. Yang, and W. C. Chen, "Characteristics of landfill leachates in central Taiwan," *Science of the Total Environment*, vol. 361, no. 1-3, pp. 25-37, 2006.
- [10] H. Youssef, D. Ibrahim, S. Komarneni, and K. J. D. Mackenzie, "Synthesis of 11 Å Al-substituted tobermorite from trachyte rock by hydrothermal treatment," *Ceramics International*, vol. 36, no. 1, pp. 203-209, 2010.
- [11] M. A. Nanny and N. Ratasuk, "Characterization and comparison of hydrophobic neutral and hydrophobic acid dissolved organic carbon isolated from three municipal landfill leachates," *Water Research*, vol. 36, no. 6, pp. 1572-1584, 2002.
- [12] L. Persson, T. Alsberg, A. Ledin, and G. Odham, "Transformations of dissolved organic matter in a landfill leachate—a size exclusion chromatography/mass spectrometric approach," *Chemosphere*, vol. 64, no. 7, pp. 1093-1099, 2006.
- [13] Y.-D. Xu, D.-B. Yue, Y. Zhu, and Y.-F. Nie, "Fractionation of dissolved organic matter in mature landfill leachate and its recycling by ultrafiltration and evaporation combined processes," *Chemosphere*, vol. 64, no. 6, pp. 903-911, 2006.
- [14] J. Rodriguez, L. Castrillon, E. Maranon, H. Sastre, and E. Fernandez, "Removal of non-biodegradable organic matter from landfill leachates by adsorption," *Water Research*, vol. 38, no. 14-15, pp. 3297-3303, 2004.
- [15] E. M. Thurman and R. L. Malcolm, "Preparative isolation of aquatic humic substances," *Environmental Science and Technology*, vol. 15, no. 4, pp. 463-566, 1981.
- [16] J. B. Christensen, D. L. Jensen, C. Gron, Z. Filip, and T. H. Christensen, "Characterization of the dissolved organic carbon in landfill leachate-polluted groundwater," *Water Research*, vol. 32, no. 1, pp. 125-135, 1998.
- [17] S. Petzet, B. Peplinski, and P. Cornel, "On wet chemical phosphorus recovery from sewage sludge ash by acidic or alkaline leaching and an optimized combination of both," *Water Research*, vol. 46, no. 12, pp. 3769-3780, 2012.
- [18] P. G. Coble, "Characterization of marine and terrestrial DOM in seawater using excitation-emission matrix spectroscopy," *Marine Chemistry*, vol. 51, no. 4, pp. 325-346, 1996.
- [19] D. M. McKnight, E. W. Boyer, P. K. Westerhoff, P. T. Doran, T. Kulbe, and D. T. Andersen, "Spectrofluorometric characterization of dissolved organic matter for indication of precursor organic material and aromaticity," *Limnology and Oceanography*, vol. 46, no. 1, pp. 38-48, 2001.
- [20] F. Wu, T. Midorikawa, and E. Tanoue, "Fluorescence properties of organic ligands for copper(II) in Lake Biwa and its rivers," *Geochemical Journal*, vol. 35, no. 5, pp. 333-346, 2001.
- [21] F. Wu and E. Tanoue, "Isolation and partial characterization of dissolved copper-complexing ligands in streamwaters," *Environmental Science and Technology*, vol. 35, no. 18, pp. 3646-3652, 2001.
- [22] F. C. Wu, R. D. Evans, and P. J. Dillon, "Separation and characterization of NOM by high-performance liquid chromatography and on-line three-dimensional excitation emission matrix

- fluorescence detection," *Environmental Science and Technology*, vol. 37, no. 16, pp. 3687–3693, 2003.
- [23] F. C. Wu, E. Tanoue, and C. Q. Liu, "Fluorescence and amino acid characteristics of molecular size fractions of DOM in the waters of Lake Biwa," *Biogeochemistry*, vol. 65, no. 2, pp. 245–257, 2003.
- [24] L. Ziyang and Z. Youcai, "Size-fractionation and characterization of refuse landfill leachate by sequential filtration using membranes with varied porosity," *Journal of Hazardous Materials*, vol. 147, no. 1-2, pp. 257–264, 2007.
- [25] Z.-L. Ye, S.-H. Chen, S.-M. Wang et al., "Phosphorus recovery from synthetic swine wastewater by chemical precipitation using response surface methodology," *Journal of Hazardous Materials*, vol. 176, no. 1–3, pp. 1083–1088, 2010.
- [26] K.-H. Kang, H. S. Shin, and H. Park, "Characterization of humic substances present in landfill leachates with different landfill ages and its implications," *Water Research*, vol. 36, no. 16, pp. 4023–4032, 2002.
- [27] S. Kuwatsuka, A. Watanabe, K. Itoh, and S. Arai, "Comparison of two methods of preparation of humic and fulvic acids, IHSS method and NAGOYA method," *Soil Science and Plant Nutrition*, vol. 38, no. 1, pp. 23–30, 1992.
- [28] Y. Inbar, Y. Chen, and Y. Hadar, "Carbon12 13CPMAS NMR and FTIR spectroscopic analysis of organic matter transformations during decomposition of solid wastes from wineries," *Soil Science*, vol. 4, pp. 272–281, 1991.
- [29] D. T. Durig, J. S. Esterle, T. J. Dickson, and J. R. Durig, "Investigation of the chemical variability of woody peat by FT-IR spectroscopy," *Applied Spectroscopy*, vol. 42, no. 7, pp. 1239–1244, 1988.

Research Article

NIRS Characterization of Paper Pulps to Predict Kappa Number

Ana Moral,¹ Elena Cabeza,¹ Roberto Aguado,² and Antonio Tijero²

¹Chemical Engineering Department, Experimental Sciences Faculty, Pablo de Olavide University, Road of Utrera km 1, 41013 Seville, Spain

²Grupo de Celulosa y Papel, Chemical Engineering Department, Faculty of Chemistry, Complutense University of Madrid, Avenue Complutense s/n, 28040 Madrid, Spain

Correspondence should be addressed to Ana Moral; amoram@upo.es

Received 8 August 2014; Revised 18 October 2014; Accepted 27 October 2014

Academic Editor: Ming-Guo Ma

Copyright © 2015 Ana Moral et al. This is an open access article distributed under the Creative Commons Attribution License, which permits unrestricted use, distribution, and reproduction in any medium, provided the original work is properly cited.

Rice is one of the most abundant food crops in the world and its straw stands as an important source of fibres both from an economic and an environmental point of view. Pulp characterization is of special relevance in works involving alternative raw materials, since pulp properties are closely linked to the quality of the final product. One of the analytical techniques that can be used in pulp characterization is near-infrared spectroscopy (NIRS). The use of NIRS has economic and technical advantages over conventional techniques. This paper aims to discuss the convenience of using NIRS to predict Kappa number in rice straw pulps produced under different conditions. We found that the resulting Kappa number can be acceptably estimated by NIRS, as the errors obtained with that method are similar to those found for other techniques.

1. Introduction

The use of wood as the main raw material in the pulp and paper industry is related to some economic and environmental issues. Wood prices make up the largest part of the costs of cellulose pulp production. While most of the wood comes from plantation forests, this has raised some controversy due to some natural forests having been replaced by monocultures. These are two of the reasons that have fostered research into the use of alternative, nonwood raw materials in response to environmental and economic pressure. In fact, nonwood raw materials constitute the sole effective source of cellulose fibre in some regions of the world where wood is a scarce resource [1–4].

Rice for human consumption belongs commonly to species *Oryza sativa* or *Oryza glaberrima*; the latter, however, is much less widely used than the former and its production is restricted to West Africa [5]. Rice straw is an abundant nonwood raw material due to the large disposal of it which takes place during the harvest which poses serious problems to farmers. Traditionally, straw has been burnt on site. This practice generates heavy smoke frequently resulting in

breathing, cardiorespiratory, and allergic problems in nearby populations and also in the release of large amounts of carbon dioxide to the environment. However, rice straw can be processed differently in order to facilitate its valorisation. One way is by using it as animal feed; however, advocates and detractors of this use disagree on the actual protein value and the digestibility of the material [6]. Another way is by using straw ash or husk ash, which is similar in composition, to extract silicon [7]. This substance can also be obtained from the liquors of alkaline and acid treatments [8]. In any case, using rice straw to produce cellulose pulp [9] is the most attractive choice.

The growing concern with the preservation of the environment in developed societies must be reconciled with the increasing demand for paper and board pulp worldwide. This leads to a new focus on the use of alternative raw materials and the development of pulping processes which cause less environmental impact (soda, soda-anthraquinone) [10].

Pulps characterization has special relevance in studies related to the use of alternative raw materials through less polluting processes in the pulp and paper industry. Pulp properties are closely linked to the quality of the final product.

However, conventional techniques imply a high consumption of reagents and time for its realization. At the same time, the destruction of samples during the process hinders the execution of subsequent determinations that could favour the knowledge of other parameters of special interest [11].

From the 1950s, near-infrared spectroscopy (NIRS) began to get known, and its possibilities were foreseen. Previously, only MIR and FIR spectroscopy were considered useful, since they allowed for analysing individual components present in each sample [12]. NIRS began to be used in the characterization of organic compounds from the 60s and its use has been extended to the control of almost all processes in food, pharmaceuticals, textile, chemical, petrochemical, and medical industries [13, 14].

NIRS has a number of advantages over conventional techniques: it suits solids, liquids, and gases and does not require sample pretreatment; the spectral recording and analysis of routine are fast; it is nondestructive and allows for multicomponent analysis and in-line analysis, and it is inexpensive [15].

NIRS is a powerful and fast tool for the determination of the constituents of wood [16, 17]. There are precedents for the use of the near-infrared spectroscopy for the determination of yield [18] and Kappa number of pulps from hardwoods and softwoods [19, 20]. Absorption bands observed in the reflectance of the wood spectra arise from the emission of electromagnetic waves produced by the overtones and combinations of C–H, C–O, N–H, and O–H [18].

The difficulty of NIRS application lies in the nature of spectra combined with the existence of multiple peaks which overlap. Therefore, it is necessary to develop advanced chemometric techniques helping to decipher the wide range of information provided by the spectra. Instruments and software developments have allowed great advances in the applicability of the technique [21].

Multivariate calibration can be difficult to perform, and it generally requires quantitative and qualitative knowledge of the properties of the samples to be analysed. In order to extract valuable information, different chemometric techniques can be used: principal components analysis (PCA), partial least squares (PLS), and multivariate resolution of curves (MCR), to name a few.

In the pulp and paper industry, the determination of the Kappa number is a parameter of special significance, since it is an indirect method to estimate the content of residual lignin and an indicator of bleachability [22]. The aim of this study is to evaluate the potential of NIR technology as a substitute for conventional trials in the determination of the Kappa number. The influence of the variables involved in the cooking process of rice straw on Kappa number has been studied, and so has their relationship with the NIR spectra obtained.

2. Materials and Methods

2.1. Raw Material. The rice species used in this study are *Oryza sativa* (Asiatic) and *Oryza glaberrima* (African). Rice from both species was grown in the Southeast of Spain and its straw was harvested.

2.2. Pulping. Pulps were obtained by cooking rice straw in a 15 L batch cylindrical reactor that was heated by means of electrical resistances. Rice straw was placed in the reactor together with soda and anthraquinone and pulped by using a reagent concentration, temperature, cooking time, and a liquid/solid ratio as shown in Table 1. The operating conditions have been chosen based on previous works [2]. The reactor was linked through an axle to a control unit, which included a motor actuating the reactor and instruments for measurement and control of pressure and temperature. Afterwards, the cooked material was unloaded into a washer in order to remove residual cooking liquor and then fiberized in a disintegrator at 1200 rpm for 30 min. The washed pulp was beaten in a Sprout-Bauer refiner and the fiberized material passed through a screen of 0.16 mm mesh size in order to remove uncooked particles.

2.3. Experimental Design. Pulping processes have been modelled in various ways for the estimation of Kappa number in terms of process variables, in order to optimize the operating conditions accordingly.

Most of the existing models are kinetic equations. However, to the best of our knowledge, few researchers have used a factorial design that allows for the development of empirical models with several independent variables, to examine the Kappa number. These empirical models are preferable to the mechanistic ones, since the latter are too complex when they contain more than two independent variables.

In this work, we chose a factorial design consisting of a series of points (tests) around a central composition point (central test).

The total number of tests required for the five independent variables studied (namely, temperature (T), time (t), soda concentration (S), anthraquinone concentration (A), and liquid/solid ratio (H)) was found to be 27.

The values of the independent variables were normalized:

$$X_n = 2 \frac{X - \bar{X}}{X_{\max} - X_{\min}}, \quad (1)$$

where X_n is the normalized value of temperature (T), time (t), or liquid/solid ratio (S); X is the absolute experimental value of the variable concerned; \bar{X} is the mean of the extreme values of X , and X_{\max} and X_{\min} are its maximum and minimum value, respectively. Experimental conditions and normalized values are shown in Table 1.

The experimental data were fitted to the following second order polynomial model:

$$Y = a_0 + \sum_{i=1}^n b_i X_{n,i} + \sum_{i=1}^n c_i X_{n,i}^2 + \sum_{i=1}^n b_i X_{n,i} X_{n,j}, \quad (2)$$

where $i < j$. X_n represent the normalized values of the process variables (time, temperature, concentration of reagents, etc.). The coefficients a_0 , b_i , c_i , and d_{ij} are constants to be estimated from the experimental data.

2.4. Determination of Kappa Number. Kappa number was determined in accordance with ISO 302:2004, applicable for

TABLE 1: Values of operating variables used in the design of experiments.

Experiment	T , °C	t , min	Soda, %	Anthraquinone, %	Liquid/solid ratio	X_T	X_t	X_S	X_A	X_H
1	170	60	15	0.5	6	0	0	0	0	0
2	155	30	10	1	4	-1	-1	-1	1	-1
3	155	30	10	0	8	-1	-1	-1	-1	1
4	155	30	20	1	8	-1	-1	1	1	1
5	185	60	15	0.5	6	1	0	0	0	0
6	170	60	15	1	6	0	0	0	1	0
7	170	30	15	0.5	6	0	-1	0	0	0
8	170	60	10	0.5	6	0	0	-1	0	0
9	185	30	10	1	8	1	-1	-1	1	1
10	185	30	20	1	4	1	-1	1	1	-1
11	170	60	20	0.5	6	0	0	1	0	0
12	170	90	15	0.5	6	0	1	0	0	0
13	185	30	20	0	8	1	-1	1	-1	1
14	170	60	15	0.5	8	0	0	0	0	1
15	155	60	15	0.5	6	-1	0	0	0	0
16	185	90	10	0	8	1	1	-1	-1	1
17	170	60	15	0	6	0	0	0	-1	0
18	155	90	20	0	8	-1	1	1	-1	1
19	185	90	20	0	4	1	1	1	-1	-1
20	155	90	20	1	4	-1	1	1	1	-1
21	185	90	20	1	8	1	1	1	1	1
22	155	90	10	1	8	-1	1	-1	1	1
23	185	90	10	1	4	1	1	-1	1	-1
24	155	30	20	0	4	-1	-1	1	-1	-1
25	155	90	10	0	4	-1	1	-1	-1	-1
26	170	60	15	0.5	4	0	0	0	0	-1
27	185	30	10	0	4	1	-1	-1	-1	-1

X_T , X_t , X_S , X_A , and X_H = normalized values of temperature (T), time (t), soda concentration (S), anthraquinone concentration (A), and liquid/solid ratio (H), respectively.

a wide range of values, from 1 to 100. It aims to determine the degree of delignification of pulp. It is defined as the volume (in mL) of a 0.1 N solution of potassium permanganate that is consumed per gram of dry pulp. Iodometric titration was performed to measure permanganate consumption. Three repetitions were made for each test.

2.5. NIR Spectroscopy Analysis. All samples were scanned by duplicate with a Foss NIRSystems 6500 monochromator (Foss NIRSystems, Silver Spring, MD, USA) using the WinISI II 1.5 software (Infrasoft International, Port Matilda, PA, USA). This software was also used for the treatment of the spectral data obtained. The visible and NIR (VNIR) spectra (400 to 2500 nm) were collected at 2 nm intervals. Samples were placed in a rectangular cell with a $4.5 \times 5.5 \text{ cm}^2$ quartz window.

2.6. Spectral Data Analysis. Spectral data analysis and calibration equations were performed with WinISI II 1.5 software (Infrasoft International, Port Matilda, PA, USA). Data of calibration sets were subjected to spectral pretreatments combined with mathematical pretreatments. Standard normal

variate (SNV) and Multiplicative scatter correction (MSC) were used as spectral pretreatments [23].

SNV is often used on spectra where baseline and path length changes cause differences between otherwise identical spectra. Mathematically, it is identical to an autoscaling of the rows instead of the columns of the matrix.

Multiplicative scatter correction (MSC) is achieved by regressing a measured spectrum against a reference spectrum and then correcting the measured spectrum using the slope and intercept of this linear fit. This pretreatment method has proven to be effective in minimizing baseline offsets and multiplicative effect.

As for mathematical pretreatments, first and second derivatives were used to reduce baseline variation and enhance spectral features. Two preprocessing methods were evaluated: (1,4,4,1) and (2,5,5,1). The numbers in parentheses, respectively, designate the order of the derivative, the gap, the first smoothing, and the second smoothing [24].

Calibration in all cases was based on full cross-validation. Modified partial least square regression (MPLSR) [22] was used to relate spectra with the measured values of dependent variables. Multivariate regression was carried out using the partial least squares (PLS) algorithm.

The residuals obtained after the calculation of each regression term in the modified partial least squares (MPLS) regression were standardized dividing by the standard deviation before the calculation of the next regression term. According to Shenk and Westerhaus [25], the number of terms was fixed when the SECV presented a minimum value before overfitting.

The different pretreatments were characterised by calculating the standard error of cross-validation (SECV) and the coefficient of determination of cross-validation (1-VR). Two measurements of each sample were used to estimate the standard error of the reference method (ETL):

$$ETL = \sqrt{\frac{\sum (y_1 - y_2)^2}{2N}}, \quad (3)$$

where y_1 and y_2 are the values obtained for a sample and its repetition and N is the number of data pairs used to calculate the ETL.

3. Results and Discussion

Table 2 gives the results of the tests (Kappa number) as the averages of three determinations for each set of independent variables. Relative standard deviation was never higher than 5%.

We dealt with experimental data by using nonlinear regression to fit them to a polynomial model of second degree described in the experimental part (see (2)). This regression analysis is conducted considering five independent variables, these same variables to the square and its products two to two, thus neglecting higher order terms.

The statistically significant terms of the polynomial model were selected with the double standard of having a value of Snedecor's F greater than 4 and a Student's t greater than 2.0. Also, coefficients whose 95% confidence interval included 0 were discarded.

We found the following equation:

$$KN = 10.9 + 1.7X_A X_H - 2.0X_t - 2.2X_S - 2.6X_T. \quad (4)$$

As expected, time, soda concentration, and temperature were found to be the most influencing independent variables. Equation (4) also shows that there is a significant interaction between anthraquinone concentration and the liquor-to-solid ratio.

Statistical parameters of the model are shown in Table 3. This model provides a good fit of the experimental data to the polynomial model, as indicated by the values of R -multiple, R^2 , R^2 -adjusted, Student's t (given for a 95% confidence level), and Snedecor's F of the terms of (4).

According to the model, the lowest value of Kappa number that can be obtained, as long as the values of independent variables fall into the intervals considered, is 2.40. The values needed to achieve that local optimum are temperature of 185°C, time of 90 min, 20 grams of soda per 100 grams of dry pulp, 1 gram of anthraquinone per 100 grams of dry pulp, and a liquid-to-solid ratio of 4. If a brighter pulp with a lower Kappa number is desired, operating under more severe conditions is necessary.

TABLE 2: Kappa number values obtained by iodometric titration for the different operating variables of the experimental design.

X_T	X_t	X_S	X_A	X_H	Kappa number
0	0	0	0	0	9.4
-1	-1	-1	1	-1	16.5
-1	-1	-1	-1	1	16.8
-1	-1	1	1	1	16.0
1	0	0	0	0	8.8
0	0	0	1	0	9.3
0	-1	0	0	0	11.6
0	0	-1	0	0	11.7
1	-1	-1	1	1	14.8
1	-1	1	1	-1	6.7
0	0	1	0	0	8.9
0	1	0	0	0	9.2
1	-1	1	-1	1	7.1
0	0	0	0	1	9.3
-1	0	0	0	0	14.5
1	1	-1	-1	1	7.8
0	0	0	-1	0	9.5
-1	1	1	-1	1	8.1
1	1	1	-1	-1	6.4
-1	1	1	1	-1	8.0
1	1	1	1	1	6.5
-1	1	-1	1	1	15.3
1	1	-1	1	-1	7.2
-1	-1	1	-1	-1	15.1
-1	1	-1	-1	-1	16.2
0	0	0	0	-1	9.4
1	-1	-1	-1	-1	15.2

TABLE 3: Values of statistical parameters for the fitting of experimental data (Kappa number) to (4).

Fitting parameter	R -multiple	R^2	R^2 -adjusted	$t >$
Value	0.96	0.93	0.92	6.69
Equation term	$X_A X_H$	X_t	X_S	X_T
Snedecor's F	44.71	65.48	80.23	112.55

As can be seen from Figure 1, all spectral data were summarized in a few variables (PLS terms of multivariate regression) with good correlation with reference values. In the graph, the predicted values (x -axis) do not deviate in more than 8% from the reference values (y -axis).

In order to determine the relevance of the simultaneous analysis of visible and NIR (VNIR) spectroscopy with the aim to perform forecasting based only with NIRS, a set of trials were carried out using both analytic methods. The VNIR trials were carried out in a spectral region between 400 and 2500 nm and the NIR samples were processed in a spectral region between 1100 and 2500 nm, as Figure 2 shows. Figure 2(a) shows the whole near-infrared spectrum with no mathematical pretreatment, while Figure 2(b) focuses on the

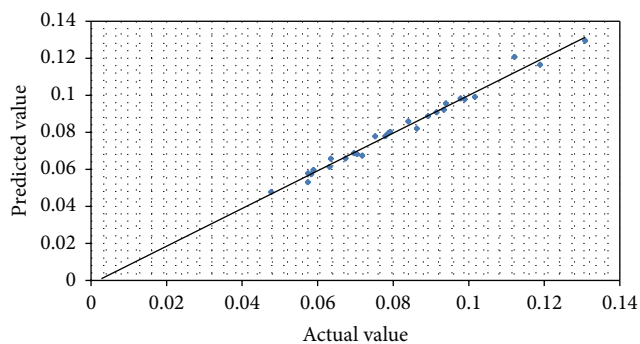
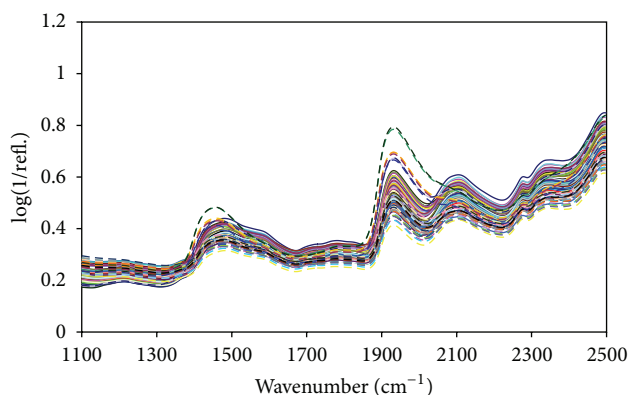
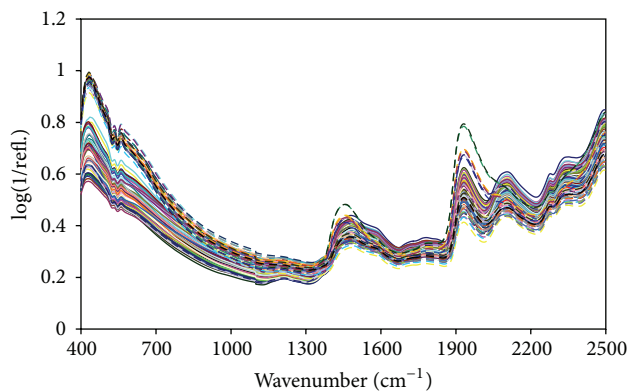


FIGURE 1: Correlation of the PLS terms with spectral data.



(a)



(b)

FIGURE 2: Near-infrared (NIR) and visible NIR (VNIR) spectra for the samples.

visible part. The whole NIR spectrum shows a peak outside of the visible region, at 450 cm^{-1} .

As it is shown in Table 4, the reference error (ETL) used in the calculation of Kappa number was 0.11. The error (as SECV) obtained by the mathematical method (1,4,4,1) in the trials carried out for NIR was lower than that obtained by the mathematical methods (2,5,5,1) for NIR. The coefficients of determination of cross-validation (measurement of the expected explained variation) obtained support the use of the NIR prediction method for the determination of Kappa index

TABLE 4: Comparison between the errors obtained by VNIR, NIR, and the standard error of the reference method (Kappa number).

Treatment	SECV	1-VR	ETL	CV (%)
1, 4, 4, 1_VNIR	0.13	0.92		
2, 5, 5, 1_VNIR	0.12	0.87	0,11	7,8
1, 4, 4, 1_NIR	0.15	0.89		
2, 5, 5, 1_NIR	0.18	0.85		

present in the raw matter studied. CV (%), the coefficient of variation, is acceptably low.

These results show that the Kappa number obtained after different cooking processes can be predicted by means of a direct measurement of rice straw pulp, using near-infrared spectroscopy.

4. Conclusions

The errors (SECV) obtained in the measurements carried out for VNIR and NIR were similar. The results obtained using a spectral scanning of VNIR and NIR do not show a significant variation between both of the systems used.

The use of NIR technology can be seen as a viable alternative method to predict Kappa number in rice straw pulp subjected to different treatments. The NIR technology also has the additional advantage of being a fast, nondestructive technique that does not need any sample pretreatment. Therefore, the cost and the environmental impact are diminished by removing the chemical reagents needed for other ways to measure Kappa number.

Conflict of Interests

The authors declare that there is no conflict of interests regarding the publication of this paper.

References

- [1] S. Navaee-Ardeh, J. M. Rovshandeh, A. A. Khodadadi, and M. Pourjoozi, "Pulp and paper characterization of rice straw produced from aqueous ethanol pulping," *Cellulose Chemistry and Technology*, vol. 37, no. 5-6, pp. 405-413, 2003.
- [2] A. Rodríguez, A. Moral, R. Sánchez, A. Requejo, and L. Jiménez, "Influence of variables in the hydrothermal treatment of rice straw on the composition of the resulting fractions," *Bioresource Technology*, vol. 100, no. 20, pp. 4863-4866, 2009.
- [3] H. Roliadi, R. M. Siagian, A. Fauzi Mas'ud, and A. N. Gintings, "The possible utilization of old newsprint, sludge waste, and abaca fibers as raw material for pulp/paper manufacture with satisfactory qualities/results: an attempt to reduce heavy dependency on the conventional wood," in *Proceedings of the 57th Appita Annual General Conference and Exhibit*, pp. 75-81, May 2003.
- [4] L. Jiménez, *Pastas celulósicas de materias primas alternativas a las convencionales*, Gráficas Sol, Écija, Spain, 2005.
- [5] Y. Agnoun, S. S. H. Biao, M. Sié, R. S. Vodouhè, and A. Ahanchède, "The African rice *Oryza glaberrima* Steud: knowledge distribution and prospects," *International Journal of Biology*, vol. 4, no. 3, pp. 158-180, 2012.

- [6] D. K. Misra, "Pulp and Paper Manufacture Volume 3: Secondary Fibers and Nonwood Pulping," in *The Joint Textbook Committee of the Paper Industry*, F. Hamilton and B. Leopold, Eds., TAPPI CPPA, Montreal, Canada, 3rd edition, 1993.
- [7] M. F. Souza, P. S. Batista, I. Regiani, J. B. L. Liborio, and D. P. F. de Souza, "Rice hull-derived silica: applications in Portland cement and mullize whiskers," *Journal of Material Research*, vol. 3, no. 2, pp. 25–30, 2000.
- [8] H. Q. Lam, Y. L. Bigot, M. Delmas, and G. Avignon, "Formic acid pulping of rice straw," *Industrial Crops and Products*, vol. 14, no. 1, pp. 65–71, 2001.
- [9] M. S. Jahan, Z. Z. Lee, and Y. Jin, "Organic acid pulping of rice straw. II. Bleaching and beating," *Cellulose Chemistry and Technology*, vol. 39, no. 1-2, pp. 85–94, 2005.
- [10] S. Navaee-Ardeh, J. Mohammadi-Rovshandeh, and M. Pourjoozi, "Influence of rice straw cooking conditions in the soda-ethanol-water pulping on the mechanical properties of produced paper sheets," *Bioresource Technology*, vol. 92, no. 1, pp. 65–69, 2004.
- [11] A. Van Heiningen, "Converting a kraft pulp mill into an integrated forest biorefinery," *Pulp and Paper Canada*, vol. 107, no. 6, pp. 38–43, 2006.
- [12] T. Davies, "The history of near infrared spectroscopic analysis: past, present and future "from sleeping technique to the morning star of spectroscopy"," *Analisis*, vol. 26, no. 4, pp. 17–19, 1998.
- [13] W. Abney and E. R. Festing, "On the influence of the atomic grouping in the molecules of organic bodies on their absorption in the infra-red region of the spectrum," *Philosophical Transactions of the Royal Society*, vol. 172, pp. 887–918, 1881.
- [14] L. Zhou, Z. Wu, X. Shi et al., "Rapid discrimination of chlorpheniramine maleate and assessment of its surface content uniformity in a pharmaceutical formulation by NIR-CI coupled with statistical measurement," *Journal of Spectroscopy*, vol. 2014, Article ID 741246, 9 pages, 2014.
- [15] E. N. M. van Sprang, H.-J. Ramaker, J. A. Westerhuis, A. K. Smilde, S. P. Gurden, and D. Wienke, "Near-infrared spectroscopic monitoring of a series of industrial batch processes using a bilinear grey model," *Applied Spectroscopy*, vol. 57, no. 8, pp. 1007–1019, 2003.
- [16] D. B. Easty, S. A. Berben, F. A. DeThomas, and P. J. Brimmer, "Near-infrared spectroscopy for the analysis of wood pulp: quantifying hardwood-softwood mixtures and estimating lignin content," *Tappi Journal*, vol. 73, pp. 257–261, 1990.
- [17] L. Wallbacks, U. Edlund, B. Norden, and T. Iversen, "Multivariate characterization of pulp. Part I: spectroscopic characterization of physical and chemical differences between pulps using ¹³C CP/MAS NMR, FT-IR, NIR and multivariate data analysis," *Nordic Pulp & Paper Research Journal*, vol. 2, pp. 74–80, 1991.
- [18] L. R. Schimleck, P. Payne, and R. H. Wearne, "Determination of important pulp properties of hybrid poplar by near infrared spectroscopy," *Wood and Fiber Science*, vol. 37, no. 3, pp. 462–471, 2005.
- [19] A. Terdwongworakul, V. Punsuwan, W. Thanapase, and S. Tsuchikawa, "Rapid assessment of wood chemical properties and pulp yield of *Eucalyptus camaldulensis* in Thailand tree plantations by near infrared spectroscopy for improving wood selection for high quality pulp," *Journal of Wood Science*, vol. 51, no. 2, pp. 167–171, 2005.
- [20] P. Malkavaara and R. Alén, "A spectroscopic method for determining lignin content of softwood and hardwood kraft pulps," *Chemometrics and Intelligent Laboratory Systems*, vol. 44, no. 1-2, pp. 287–292, 1998.
- [21] A. J. Michell, "Pulpwood quality estimation by near-infrared spectroscopic measurements on eucalypt woods," *Appita Journal*, vol. 48, pp. 425–428, 1995.
- [22] J. S. Shenk and M. O. Westerhaus, "Population definition, sample, selection and calibration procedures for near infrared reflectance," *Crop Science*, vol. 31, pp. 469–474, 1991.
- [23] H. Buddenbaum and M. Steffens, "The effects of spectral pretreatments on chemometric analyses of soil profiles using laboratory imaging spectroscopy," *Applied and Environmental Soil Science*, vol. 2012, Article ID 274903, 12 pages, 2012.
- [24] H. W. Siesler, Y. Ozaki, S. Kawata, and H. M. Heise, *Near-Infrared Spectroscopy Principles, Instruments, Applications*, Wiley-VCH, Weinheim, Germany, 2002.
- [25] J. S. Shenk and M. O. Westerhaus, "Population structuring of near infrared spectra and modified partial least squares regression," *Crop Science*, vol. 31, pp. 1548–1555, 1991.

Research Article

Binding Cellulose and Chitosan via Intermolecular Inclusion Interaction: Synthesis and Characterisation of Gel

Jiufang Duan,¹ Chunrui Han,¹ Liujun Liu,¹ Jianxin Jiang,¹ Jianzhang Li,¹ Yiqiang Li,² and Chao Guan²

¹Institute of Material Science and Technology, Beijing Forestry University, Beijing 100083, China

²Beijing Shoufa Tianren Ecological Landscape Co., Ltd., Beijing 102600, China

Correspondence should be addressed to Jiufang Duan; duanjiu99@163.com

Received 28 April 2014; Revised 29 September 2014; Accepted 30 September 2014

Academic Editor: Wen Zeng

Copyright © 2015 Jiufang Duan et al. This is an open access article distributed under the Creative Commons Attribution License, which permits unrestricted use, distribution, and reproduction in any medium, provided the original work is properly cited.

A novel cellulose-chitosan gel was successfully prepared in three steps: (1) ferrocene- (Fc-) cellulose with degrees of substitution (DS) of 0.5 wt% was synthesised by ferrocenecarboxylic acid and cellulose within dimethylacetamide/lithium chloride (DMAc/LiCl); (2) the β -cyclodextrin (β -CD) groups were introduced onto the chitosan chains by reacting chitosan with epichlorohydrin in dimethyl sulphoxide and a DS of 0.35 wt%; (3) thus, the cellulose-chitosan gel was obtained via an intermolecular inclusion interaction of Fc-cellulose and β -CD-chitosan in DMA/LiCl, that is, by an intermolecular inclusion interaction, between the Fc groups of cellulose and the β -CD groups on the chitosan backbone at room temperature. The successful synthesis of Fc-cellulose and β -CD-chitosan was characterised by ¹³C-NMR spectroscopy. The gel based on β -CD-chitosan and Fc-cellulose was formed under mild conditions which can engender autonomous healing between cut surfaces after 24 hours: the gel cannot self-heal while the cut surfaces were coated with a solution of a competitive guest (adamantane acid). The cellulose-chitosan complex made by this method underwent self-healing. Therefore, this study provided a novel method of expanding the application of chitosan by binding it with another polymer.

1. Introduction

Chitosan is a partially deacetylated polymer of N-acetyl glucosamine. It is essentially a natural, water-soluble derivative of cellulose with unique properties [1]. Chitosan is usually prepared from chitin and chitin has been found in a wide range of natural sources [2] (crustaceans, fungi, insects, annelids, molluscs, coelenterate, etc.) [1, 2]. Chitosan is used in many applications (flocculant [3, 4], clarifier [5–7], fibre [8, 9], film [10–12], and wound healing promoting agent [13, 14]). Cellulose and chitosan have similar molecular structures, with the same β -glycoside linkages. The main difference is the presence of primary amino groups at the C-2 positions in chitosan, where cellulose has hydroxyl groups. The presence of active groups in chitosan's molecular structure allows for easy chemical modification. Cellulose and chitosan are both biocompatible, nontoxic, and naturally occurring biopolymers that have been used extensively for biomedical applications.

In recent years, many studies of the different applications of chitosan and especially of chitosan blends with cellulose have been undertaken [3–24]. The complex based on cellulose and chitosan is to be studied as a fibre [8, 9], a film [3, 8, 10–12], hydrogen [7, 15], and microspheres [5, 16, 17] and be used as a drug carrier [17, 18], wound healing promoting agent [14, 15], a medical material [17], a food packaging material [11], an adsorbent [3–7], and as a range of other functional materials [15, 20–23]. The preparation of cellulose-chitosan composite materials has involved two main strategies: physical mixing [6, 8, 13] and covalent bonding [24, 25], whereas cellulose-chitosan hydrogel binding with host-guest interactions has never been reported before. This method differed with physical mixing in that it incorporated a “lock” formed by the Fc and β -CD groups between cellulose and chitosan molecules: the gel prepared by this method with Fc-cellulose and β -CD-chitosan by self-assembled Fc and β -CD groups in the absence of chemical cross-links was also novel. The incorporation of “locks” ensured a uniform mixing system and the

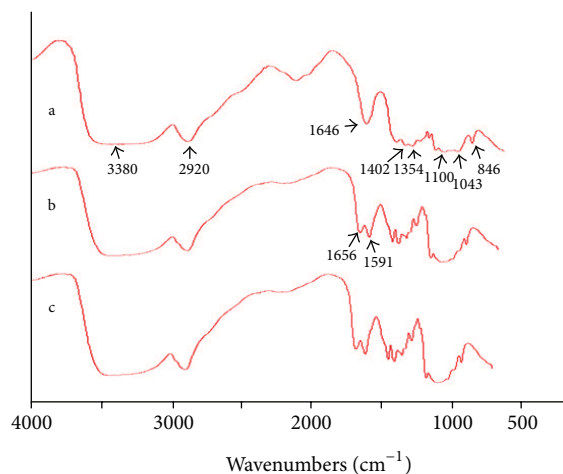


FIGURE 1: Infrared spectra of cellulose-Fc (a), chitosan-CDs (b), and the inclusion compound (c).

“locks” in this Fc- β -CD system made the materials smart in such a manner as to allow them to respond by their “locking” and “unlocking” behaviour [26–29]. The potential responsive properties present this kind of gel with a wider range of applications. The aim of this research was to modify the cellulose and chitosan and to prepare an Fc-cellulose/ β -CD-chitosan gel.

2. Experimental

2.1. Materials. Cellulose (DP380), chitosan (DP465), β -cyclodextrin, epichlorohydrin, sodium hydroxide, lithium chloride, N,N-dimethyl acetamide, methylene chloride, ferrocene carboxylic acid, oxalyl chloride, sodium hypochlorite, and glutathione were commercially available and used as received. IR spectra were recorded by FTIR (Nicolet iN10 Thermo Fisher Scientific, China) in the region of 400 to 4000 cm^{-1} . Compressive strengths were measured using an Instron 3365 Universal Testing Machine (Norwood, MA, USA) with the following parameters: sampling rate, 10.000 points/s; beam speed, 1.0000 mm/min; full-scale load range, 0.1000 kN; humidity, 25%; and temperature, 23°C. The gel samples were formed using a 10 mm diameter cylindrical die.

2.2. Preparation of Cellulose-Chitosan Gel

2.2.1. Preparation of Chitosan-CDs. β -CD and isopropanol were dissolved in dimethyl sulphoxide (DMSO). To this solution, epichlorohydrin and solution (1 mol/L) were added. After stirring for 5 h, chitosan was added and the solution was stirred for another 12 h at room temperature. The polymer product was reprecipitated from distilled water and washed with distilled water. The cyclodextrin grafting efficiency was 0.35% wt, which was detected by the phenolphthalein probe method [30].

2.2.2. Synthesis of Fc-COCl. Ferrocenecarboxylic acid was suspended in dichloromethane (DCM). Then oxalyl chloride

was added dropwise, and the suspension was stirred for 3 h at room temperature. The orange suspension turned into a red solution. After evaporating the solvent, the solid product was collected.

2.2.3. Synthesis of Cellulose-Fc. Cellulose was dissolved in lithium chloride/dimethylacetamide (LiCl/DMAc). The chlorocarbonyl ferrocene solution was added dropwise. After stirring overnight at room temperature, the solution was washed with distilled water. The orange solid was washed with lithium chloride; the solid product was collected by centrifugation and dried for 4 days at 50°C to obtain the cellulose-Fc as a yellow powder. The ferrocene grafting rate was 0.5% wt, which was detected by weighing before and after the cellulose reaction.

2.2.4. Synthesis of Cellulose-Chitosan Gel. The ferrocene-cellulose (0.017 mM) and cyclodextrin-chitosan (0.017 mM) were dissolved in N,N-dimethylformamide (DMF)/lithium chloride solution. The solution was poured into a glass mould in a humid box until the gel had stabilised.

3. Results and Discussion

Figure 1 shows the infrared spectra of the cellulose-Fc (a) and chitosan-CDs (b). According to the curves in (a), absorption was observed at 3380 cm^{-1} (hydroxyl stretch influenced by hydrogen bonding), 1646 cm^{-1} and 1354 cm^{-1} (carbonyl stretch), 1043 cm^{-1} (carboxyl in ethers), and 2920 cm^{-1} (methylene). The characteristic peaks of ferrocene could be found at 1402 cm^{-1} , 1100 cm^{-1} VC-C (cyclopentadienyl ring), and 856 cm^{-1} DC-H (cyclopentadienyl ring). As seen from the curves in (b), the characteristic absorption peaks of chitosan-CDs structures were observed at 1656 cm^{-1} (the stretching vibration of C=O) and at 1591 cm^{-1} (the bending vibration of N-H). The characteristic peaks of ferrocene disappeared from the infrared spectra of the envelope of the

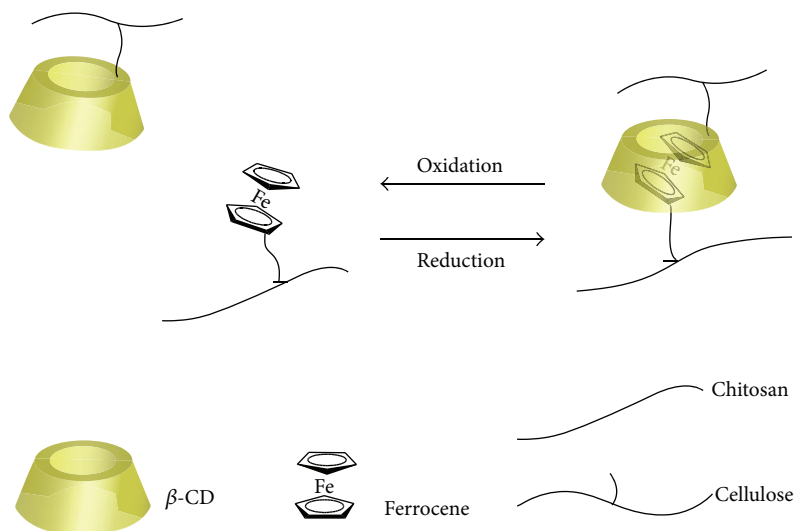


FIGURE 4: Intermolecular inclusion interaction of cellulose-chitosan hydrogel.

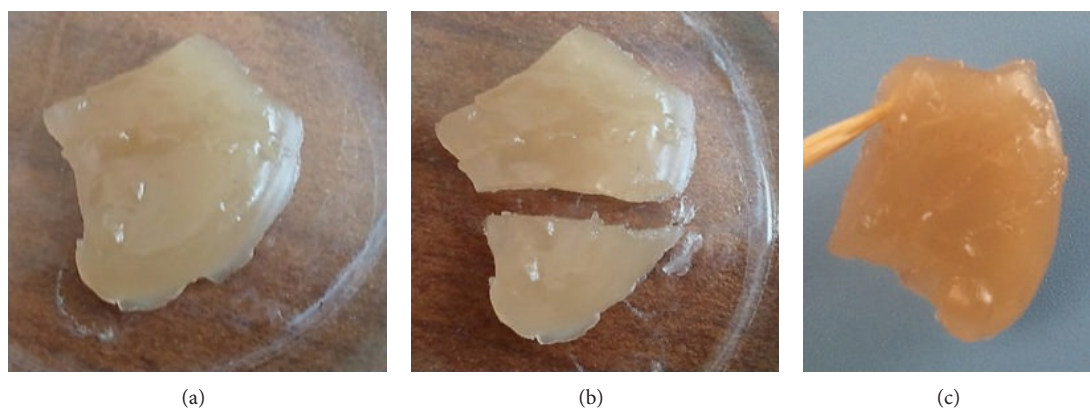


FIGURE 5: Self-healing experiments.

inclusion compound (curves in (c)). This indicated that the cellulose-Fc and chitosan-CDs have been formed in the inclusion complex. Similar findings were reported in the literature [26–28].

Figures 2 and 3 show the solid-state ^{13}C -NMR spectra of the chitin-CDs and cellulose-Fc. As can be seen in Figure 2, the C1 of the glucose units was assigned to 104.3 and 103.7 ppm, their C4 was assigned to 88.2 ppm, C2, C3, and C5 were assigned to 74.4 ppm, and C6 was assigned to 61.8 ppm. Fc could be found at carbon sites in regions between 124.4 and 123.0 ppm and 82.8 and 81.7 ppm; this suggested that ferrocene was successfully grafted to the cellulose by the proposed experimental method. A detailed assignment of different carbons of chitin-CDs was shown in Figure 3: the C1 site of the glucose units was assigned to 104.6 ppm, C4 to 85.4 ppm, C2, C3, and C5 to 74.9 ppm, C6 to 60.5 ppm and 57.0 ppm, carbonyl carbon C7 (connected acetyl group) to 173.0 ppm, and C8 to 23.5 ppm. The carbon atoms connecting cellulose and cyclodextrin were assigned to 80.9 ppm; this indicated that cyclodextrins had been successfully grafted onto chitosan.

Cellulose-chitosan gel was prepared from the solution of ferrocene-cellulose and cyclodextrin-chitosan at room temperature. The schematic diagram of the binding of cellulose and chitosan by an intermolecular inclusion interaction was shown in Figure 4. The gel based on β -CD-chitosan and Fc-cellulose was formed under mild conditions which can engender autonomous healing between cut surfaces after 24 hours (Figure 5). To clarify the intermolecular inclusion interaction between the β -CD and Fc groups on cellulose and chitosan, a competitive guest molecule was coated onto the cut surfaces. Adamantine acid was used as a competitive guest, because the association constant for β -CD ($K_a = 35 \times 10^3 \text{ M}^{-1}$) is higher than that of Fc. A β -CD-chitosan/Fc-cellulose gel was cut in half, and the cut surfaces were coated with a solution of adamantane acid (3 Mm). After 24 h, healing was not observed. These results indicated the formation of an inclusion complex between the β -CD unit of β -CD-chitosan and the Fc unit of Fc-cellulose. The compressive strength (Instron 3365 Universal Testing Machine (Norwood, MA, USA)) of Fc-cellulose/ β -CD-chitosan hydrogel (3 wt%) without cracking was 4.70 kPa, and the compressive strength

of the sample healed after standing for 24 h was 3.42 kPa. Thereafter, the compressive strength of the healed gel can recover 72.77% of its original compressive strength.

4. Conclusion

β -CD-chitosan/Fc-cellulose gel was prepared at room temperature, the β -CD unit of the β -CD-chitosan and the Fc unit of the Fc-cellulose can form inclusion complexes. The cellulose and chitosan can bind by intermolecular inclusion interaction. This research reports the resulting self-healing properties arising from host-guest interactions. The healed gel can recover 72.77% of its original compressive strength. The β -CD-chitosan/Fc-cellulose gel hydrogels have a wide potential for industrial applications including medicine, textiles, sports, cosmetics, and hygiene product manufacture.

Conflict of Interests

The authors declare that there is no conflict of interests regarding the publication of this paper.

Acknowledgment

This paper is supported by the Fundamental Research Funds for the Central Universities.

References

- [1] R. Shepherd, S. Reader, and A. Falshaw, "Chitosan functional properties," *Glycoconjugate Journal*, vol. 14, no. 4, pp. 535–542, 1997.
- [2] M. Rinaudo, "Chitin and chitosan: properties and applications," *Progress in Polymer Science*, vol. 31, no. 7, pp. 603–632, 2006.
- [3] S. Duri and C. D. Tran, "Supramolecular composite materials from cellulose, chitosan, and cyclodextrin: facile preparation and their selective inclusion complex formation with endocrine disruptors," *Langmuir*, vol. 29, no. 16, pp. 5037–5049, 2013.
- [4] Z. Liu, H. Wang, C. Liu et al., "Magnetic cellulose-chitosan hydrogels prepared from ionic liquids as reusable adsorbent for removal of heavy metal ions," *Chemical Communications*, vol. 48, no. 59, pp. 7350–7352, 2012.
- [5] N. Li and R. B. Bai, "Copper adsorption on chitosan-cellulose hydrogel beads: behaviors and mechanisms," *Separation and Purification Technology*, vol. 42, no. 3, pp. 237–247, 2005.
- [6] C. D. Tran, S. Duri, A. Delneri, and M. Franko, "Chitosan-cellulose composite materials: preparation, characterization and application for removal of microcystin," *Journal of Hazardous Materials*, vol. 252–253, pp. 355–366, 2013.
- [7] M. M. Naim and H. E. M. Abdel Razek, "Chelation and permeation of heavy metals using affinity membranes from cellulose acetate-chitosan blends," *Desalination and Water Treatment*, vol. 51, no. 1–3, pp. 644–657, 2013.
- [8] W. Xiao, T. Wu, J. Peng et al., "Preparation, structure, and properties of chitosan/cellulose/multiwalled carbon nanotube composite membranes and fibers," *Journal of Applied Polymer Science*, vol. 128, no. 2, pp. 1193–1199, 2013.
- [9] B. Ma, M. Zhang, C. He, and J. Sun, "New binary ionic liquid system for the preparation of chitosan/cellulose composite fibers," *Carbohydrate Polymers*, vol. 88, no. 1, pp. 347–351, 2012.
- [10] S. Zhang, W. Liu, J. Liang et al., "Buildup mechanism of carboxymethyl cellulose and chitosan self-assembled films," *Cellulose*, vol. 20, no. 3, pp. 1135–1143, 2013.
- [11] F. Li, P. Biagioni, M. Finazzi, S. Tavazzi, and L. Piergiorganni, "Tunable green oxygen barrier through layer-by-layer self-assembly of chitosan and cellulose nanocrystals," *Carbohydrate Polymers*, vol. 92, no. 2, pp. 2128–2134, 2013.
- [12] C. Stefanescu, W. H. Daly, and I. I. Negulescu, "Biocomposite films prepared from ionic liquid solutions of chitosan and cellulose," *Carbohydrate Polymers*, vol. 87, no. 1, pp. 435–443, 2012.
- [13] W.-C. Lin, C.-C. Lien, H.-J. Yeh, C.-M. Yu, and S.-H. Hsu, "Bacterial cellulose and bacterial cellulose-chitosan membranes for wound dressing applications," *Carbohydrate Polymers*, vol. 94, no. 1, pp. 603–611, 2013.
- [14] Y.-B. Wu, S.-H. Yu, F.-L. Mi et al., "Preparation and characterization on mechanical and antibacterial properties of chitosan/cellulose blends," *Carbohydrate Polymers*, vol. 57, no. 4, pp. 435–440, 2004.
- [15] S. Lin, L. H. Chen, L. L. Huang et al., "Preparation and characterization of chitosan/cellulose blend films using $\text{ZnCl}_2 \cdot 3\text{H}_2\text{O}$ as a solvent," *Bioresources*, vol. 7, no. 4, pp. 5488–5499, 2012.
- [16] J. Duan, Y. Wang, Y. Wang, and X. Xiong, "Preparation and characterization of cellulose-coated chitosan beads with improved strength and acid resistivity," *Journal of Applied Polymer Science*, vol. 126, no. 1, pp. E173–E179, 2012.
- [17] S.-H. Yu, H.-Y. Hsieh, J.-C. Pang et al., "Active films from water-soluble chitosan/cellulose composites incorporating releasable caffeic acid for inhibition of lipid oxidation in fish oil emulsions," *Food Hydrocolloids*, vol. 32, no. 1, pp. 9–19, 2013.
- [18] H. Feng, L. Zhang, and C. Zhu, "Genipin crosslinked ethyl cellulose-chitosan complex microspheres for anti-tuberculosis delivery," *Colloids and Surfaces B: Biointerfaces*, vol. 103, pp. 530–537, 2013.
- [19] E. P. Azevedo, R. Raghavan, M. L. Raghavan, and V. Kumar, "Mechanical properties of cellulose: chitosan blends for potential use as a coronary artery bypass graft," *Journal of Biomaterials Science: Polymer*, vol. 24, no. 3, pp. 239–252, 2013.
- [20] Z. Liu, H. Wang, B. Li et al., "Biocompatible magnetic cellulose-chitosan hybrid gel microspheres reconstituted from ionic liquids for enzyme immobilization," *Journal of Materials Chemistry*, vol. 22, no. 30, pp. 15085–15091, 2012.
- [21] Y. G. Baklagina, S. V. Kononova, V. A. Petrova et al., "Study of polyelectrolyte complexes of chitosan and sulfoethyl cellulose," *Crystallography Reports*, vol. 58, no. 2, pp. 287–294, 2013.
- [22] Z. Su, Y. Yu, C. Liang, L. Li, and S. Yu, "Properties of chitosan-immobilized cellulase in ionic liquid," *Biotechnology and Applied Biochemistry*, vol. 60, no. 2, pp. 231–235, 2013.
- [23] U. Vrabčić Brodnjak and D. Gregor-Sveteć, "Preparation and characterization of chitosan coatings onto regular cellulose fibers with ultrasound technique," *Journal of Coatings Technology Research*, vol. 10, no. 2, pp. 247–254, 2013.
- [24] P. Peng, X. Cao, F. Peng, J. Bian, F. Xu, and R. Sun, "Binding cellulose and chitosan via click chemistry: synthesis, characterization, and formation of some hollow tubes," *Journal of Polymer Science Part A: Polymer Chemistry*, vol. 50, no. 24, pp. 5201–5210, 2012.
- [25] J. P. de Mesquita, C. L. Donnici, I. F. Teixeira, and F. V. Pereira, "Bio-based nanocomposites obtained through covalent linkage between chitosan and cellulose nanocrystals," *Carbohydrate Polymers*, vol. 90, no. 1, pp. 210–217, 2012.

- [26] E. Kosecka-Judin, M. Wesolowski, and D. Paukszta, "Pattern recognition methods as supplementary techniques for identification of salicylamide—cyclodextrins inclusion complexes," *Central European Journal of Chemistry*, vol. 10, no. 5, pp. 1534–1546, 2012.
- [27] C. Volobuef, C. M. Moraes, L. A. S. Nunes et al., "Sufentanil-2-hydroxypropyl- β -cyclodextrin inclusion complex for pain treatment: physicochemical, cytotoxicity, and pharmacological evaluation," *Journal of Pharmaceutical Sciences*, vol. 101, no. 10, pp. 3698–3707, 2012.
- [28] J. Duan, X. Zhang, J. Jiang et al., "The synthesis of a novel cellulose physical gel," *Journal of Nanomaterials*, vol. 2014, Article ID 312696, 7 pages, 2014.
- [29] J. F. Duan, J. Jiang, C. Han, J. Yang, L. Liu, and J. Li, "The study of intermolecular inclusion in cellulose physical gels," *BioResources*, vol. 9, no. 3, pp. 4006–4013, 2014.
- [30] J. Wan, Z. Hu, W. Chen, H. Chen, and Z. Yu, "Synthesis and application on enrichment of metal ions of cellulose fibre grafted β -cyclodextrin," *Acta Polymerica Sinica*, vol. 2004, no. 4, pp. 566–572, 2004.

Research Article

Preparation and Aromatic Hydrocarbon Removal Performance of Potassium Ferrate

Wei Guan, Zhigang Xie, and Jia Zhang

Chongqing Key Laboratory of Environmental Materials & Remediation Technologies, Chongqing University of Arts and Sciences, Chongqing 402160, China

Correspondence should be addressed to Zhigang Xie; xinghu2200@163.com

Received 22 July 2014; Accepted 9 August 2014; Published 2 September 2014

Academic Editor: Wen Zeng

Copyright © 2014 Wei Guan et al. This is an open access article distributed under the Creative Commons Attribution License, which permits unrestricted use, distribution, and reproduction in any medium, provided the original work is properly cited.

This experiment adopts the hypochlorite oxidation method to constantly synthesize potassium ferrate. Under the condition of micropolluted source water pH and on the basis of naphthalene, phenanthrene, and pyrene as research objects, the effects of different systems to remove aromatic hydrocarbons were studied. Various oxidation systems to remove phenanthrene intermediate are analyzed and the detailed mechanisms for removal of phenanthrene are discussed. The study found that the main intermediate of potassium ferrate system to transform phenanthrene is 9,10-phenanthraquinone and its area percentage reached 82.66%; that is, 9,10-phenanthraquinone is the key entity to remove phenanthrene.

1. Introduction

Ferrate is an ideal water treatment reagent. In acidic medium, ferrate redox potential is very high; in a wide pH range, its oxidation is strong, and it has strong deactivating effect on microorganisms. Ferrate in sewage purification shows excellent oxidation, adsorption, and flocculation to remove contaminants, and it has stronger sterilization effect than chlorine department oxidant [1–3]. Ferrate is the best oxidant replacement for chlorine source as water purification agent. In addition, ferrate as the positive active material of the green power supply has high electrode potential and capacitance [4–6]. This unique feature makes ferrates environmentally friendly green oxidation reagents with dual function.

The ferrate crystal belongs to orthogonal crystal system. For potassium ferrate (K_2FeO_4), ferrate has regular tetrahedron structure. Fe atom is at the center of the tetrahedron, with four oxygen atoms in the four corners of tetrahedron, presenting a slightly distorted tetrahedron structure. Ferrate is a deep purple solid, its solution has specific purple color, and maximum absorption wavelength is 510 nm. At the same time, ferrate ion has an absorption peak at 786 nm, which is also its characteristic absorption peak. The main compound in ferrate is potassium ferrate and in solid state it is dark

purple powder, and melting point is 198°C. When ferrate is in dry conditions, it starts to break down at 230°C [7–9].

Iron (VI) ions in potassium ferrate, located in the highest valence state of iron, have strong oxidativity; also they have selectivity. They can oxidize plenty of organics. Their oxidativity is significantly stronger than conventional water treatment oxidant, such as potassium permanganate, ozone, and hypochlorite. Under acid medium their standard electrode potential is 2.20 V; however, it is 0.72 V in alkaline condition. We can modify the ferrate cations' structure and adjust pH value to control the oxidation activity, so as to achieve high selectivity [10–14].

Heavy metal pollutants in the micropolluted water, such as cadmium and manganese, can be removed by potassium ferrate, and the removal rate reached 80%. In addition, potassium ferrate has good ability to remove organic compounds, such as phenols, alcohols, phenols, organic acid, organic nitrogen, and amino acid, lipid compounds containing sulfur and benzene, and some refractory compounds.

At present, much domestic and foreign source water is polluted by aromatic hydrocarbon. The concentration of aromatic hydrocarbon in water is very low, but the removal efficiency of conventional water treatment technology is not ideal. Due to the special stability of the benzene ring

TABLE 1: Main reagents and their specifications.

Number	Name	Chemical level	Manufacturer
1	Caustic potash	AR	ACROS
2	Calcium hypochlorite	AR	ACROS
3	Potassium nitrate	AR	ACROS
4	Sodium sulfite	AR	ACROS
5	Cyanoacrylate	AR	ACROS
6	Butanol	AR	ACROS
7	Glacial acetic acid	AR	ACROS
8	Anhydrous ethanol	AR	ACROS
9	Cupric nitrate	AR	ACROS
10	Naphthalene	AR	ACROS
11	Phenanthrene	AR	ACROS
12	Pyrene	AR	ACROS

structure, aromatic hydrocarbon in oxidation might generate series of intermediates. There are some potential environmental risks; it is difficult to guarantee the safety of drinking water. This paper completes the transformation and removal of aromatic hydrocarbons in micropolluted water, in view of the refractory aromatic hydrocarbon in micropolluted source water and in view of potassium ferrate treatment technology.

2. Experiment Methods

2.1. Experiment Materials and Reagents. The main reagents and specifications used in the experiment are shown in Table 1.

2.2. Instruments and Equipment. The main instruments and related information used in the experiment are shown in Table 2. The infrared spectrum of potassium ferrate by Fourier infrared spectrometer (FTIR) is drawn, and the infrared characteristic peaks of potassium ferrate crystal are measured. Fluorescence spectrophotometer determines the degradation rate of the sample. Gas chromatography-mass spectrometry instrument determines the intermediate of sample transformation and removal.

Some small instruments used in experiments consist of the beaker, 1000 W long arc xenon lamp, magnetic stirrer, electronic balance, separatory funnel, vacuum pump, the suction filter device, and so forth.

2.3. The Preparation of Potassium Ferrate. Proper 3 mol/L and 13 mol/L saturated potassium hydroxide solutions, cooling to room temperature, are prepared, respectively, for subsequent experiments. 15 g calcium hypochlorite is weighed in a small beaker; 25 mL of 13 mol/L potassium hydroxide solution is added in slight agitation with a glass rod. The resulting solution is sucked with 800-mesh filter cloth to leach impurities such as potassium chloride, collecting the yellow-green filtrate. 20 mL cooling saturated potassium hydroxide solution is added with batch into the yellow-green filtrate. Impurities are removed by careful control of temperature, sufficient mixing, and air pump filtration, and then alkaline

saturated potassium hypochlorite solution is obtained. 8 g $\text{Fe}(\text{NO}_3)_3 \cdot 9\text{H}_2\text{O}$ is weighed and is ground to powder and then is added slowly into the alkaline saturated potassium hypochlorite solution in batch with vigorous agitation. This reaction is exothermic with the ice-bath to control reaction temperature and stirring. The oxidation reaction is fast; soon the solution turns into purple. After 1-hour sufficient reaction, 90 mL cooling saturated potassium hydroxide solution was added into purple-black solution. The mixture is continuously stirred for 5 min and then is allowed to stand to cool in ice-bath for 30–40 min, followed by quickly sucking filtration with air pump. The liquor is abandoned and the resulting filtered cake, a crude potassium ferrate product, survives. The crude potassium ferrate product is washed 3 times with 3 mol/L potassium hydroxide solution, 5 mL for each washing. The resulting potassium ferrate is redissolved, and filtration is done with air pump sucking. Filter cake is withdrawn, whereas the liquor is retained. The liquor is poured into distillation flask in ice-water bath, with addition of 40 mL cooling saturated potassium hydroxide solution. Recrystallization for 20~30 minutes is done, followed by sucking filtration with air pump. The resulting filter cake is the potassium ferrate, leached with n-hexane (4×25 mL), with pentane (4×25 mL), with methanol (4×10 mL), and with ether (2×10 mL), respectively. The final product potassium ferrate crystal (purple-black), dried at 65°C for 2 hours, weighed, and kept in the drier, is prepared for subsequent use.

2.4. The Experiment of Potassium Ferrate to Remove Aromatic Hydrocarbon. Self-made potassium ferrate transforms aromatic hydrocarbon. In the micropolluted water medium (pH = 7.1) with naphthalene, phenanthrene, and pyrene, the ability of potassium ferrate to transform aromatic hydrocarbons is explored on the basis of reaction time, potassium ferrate amounts, and removal of aromatic hydrocarbon.

On account of water quality of Chongqing Water Plant, polluted water by aromatic hydrocarbon is simulated by artificial addition of 200 $\mu\text{g/L}$ aromatic hydrocarbon. The pH of the water is 7.1. 1000 mL of the polluted water is taken into a beaker with addition of different quantity of potassium ferrate, carrying out oxidation reaction with magnetic stirrer. At a specified time point 20 mL of the said solution is taken out of reaction system, followed by addition of sodium sulfite as termination agent. The content of aromatics remaining in the solution is determined by fluorescence spectrophotometer.

2.5. The Main Testing Index and Method. The removal of aromatic hydrocarbon is quantitatively determined by fluorescence spectrophotometer. The exciting wavelength and emission wavelength of three materials are as follows: naphthalene EX/EM is 218/332 nm, phenanthrene EX/EM is 250/362 nm, and pyrene EX/EM is 238/372 nm, respectively. Excitation and emission slit are 5 nm; scanning speed is 2400 nm/min.

The properties of phenanthrene oxidation intermediate are determined by gas chromatography-mass spectrometry. After 30 min reaction to attain constant state, 200 mL solution is taken out from phenanthrene reaction system, followed

TABLE 2: Main equipment and the respective specifications.

Number	Instrument name	Instrument model	Manufacturer
1	X-ray diffractometer	XD-2	SHIMADZU, Japan
2	UV spectrometer	UV-3010	SHIMADZU, Japan
3	Fourier transform infrared spectrometer	IRPrestige-21	SHIMADZU, Japan
4	Fluorescence spectrophotometer	F-7000	SHIMADZU, Japan
5	Gas chromatograph-mass spectrometer (GC-MS)	6890N GC/5973 MS	SHIMADZU, Japan

by introduction into 400 mL separatory funnel. 6 g NaCl is added into the filtered solution. When completely dissolved, 10 mL CH_2Cl_2 is poured. The said solution is shaken for 10 min, and then it was allowed to stand for 5 min. CH_2Cl_2 layer is transferred to the pear-shaped flask. Additional 10 mL CH_2Cl_2 is put into the separative funnel twice, 5 mL for each. The solution was allowed to stand until organic layer survives. Then, the organic layer is merged and transferred. Anhydrous sodium sulfate is added into CH_2Cl_2 layer for drying. CH_2Cl_2 layer is concentrated at low temperature in the rotary evaporator; highly pure nitrogen is bubbled into the said layer until only 1 mL of the said solution is left. GC-MS analysis is applied.

Gas chromatography-mass spectrometry, Agilent 6890 Net GC-Agilent 5973 Net MS series, is used; chromatographic column for HP-5 MS quartz capillary column (25 m \times 0.25 mm \times 0.25 μm). The pattern of input sample is branch-stream-free system, carrier gas is helium gas, and the flow rate is 1.0 mL/min. Temperature raising procedure is 40~290°C (10°C/min). Ionization mass spectrometry conditions are as follows: voltage is 70 eV and the scanning range is of 30~400 m/z .

Fourier transformed infrared spectrometer and ultraviolet-visible spectrometer are used to qualitatively characterize potassium ferrate.

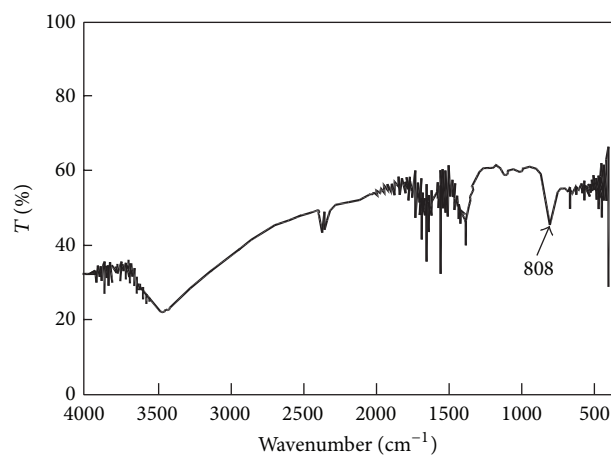
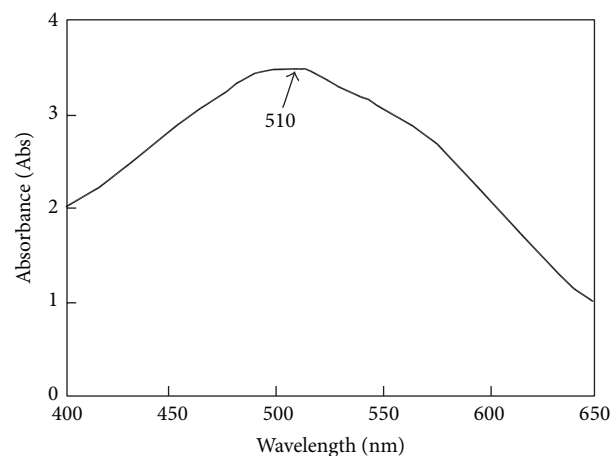
3. The Results and Discussion

3.1. The Characterization of Potassium Ferrate Crystal. Fourier infrared spectrometer determined the purple crystal infrared spectrum at experimental conditions, as shown in Figure 1.

As can be seen in the figure, there is an absorption peak at 808 cm^{-1} , which is potassium ferrate crystal Fe-O bond stretching vibration characteristic peak. The peak is considered as the infrared characteristic peak of potassium ferrate. Other impurity peaks in the infrared spectrogram should be water vapor occurring in the instrument and the characteristics of absorption peak of the organic solvent used in the purification elution [15, 16].

Potassium Ferrate Ultraviolet-Visible Absorption Spectrum Characteristics. 0.0934 g purple crystal is weighed to prepare 100 mL of potassium ferrate solution in volumetric flask. Ultraviolet-visible spectrometer is used to test the ultraviolet-visible absorption spectrum, as shown in Figure 2.

As can be seen in the figure, there is an obvious characteristic absorption peak at 510 nm, which is ultraviolet-visible

FIGURE 1: FTIR spectra of K_2FeO_4 .FIGURE 2: UV-Vis DRS of K_2FeO_4 .

characteristic absorption peak of potassium ferrate. The peak is also considered as the quantitative analysis wavelength.

3.2. The Influence of Reaction Time on Aromatic Hydrocarbon Removal. When the oxidant concentration of potassium ferrate is at 6 mg/L, the removal percentage of three kinds of aromatic hydrocarbon along with the change of time is shown in Figure 3. As can be seen in the figure, the transformation oxidation process of potassium ferrate for three kinds of aromatic hydrocarbon mainly occurred in the initial 5–10 minutes when the removal percentage of

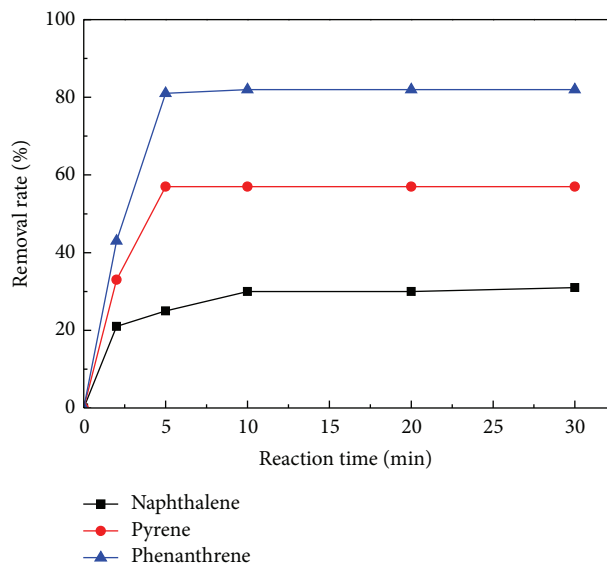


FIGURE 3: Influence of reaction time on aromatic hydrocarbons conversion and removal.

aromatic hydrocarbon increased rapidly as time increased. In five minutes later, the removal percentage of aromatic hydrocarbon only increased slightly. The result is consistent with the degradation rule of potassium ferrate oxidation degrading BPA [17] and arsenic [18]. Furthermore, it can be seen that over 80% final removal percentage of phenanthrene, 37% that of naphthalene, and 58% that of pyrene are developed, respectively. This shows that potassium ferrate can effectively transform phenanthrene in a relatively short time. These results are consistent with potassium ferrate high activity and instability. By comparison of three kinds of aromatic hydrocarbon removal percentage it is found that potassium ferrate has high oxidation, but to different samples its oxidation ability is not the same. Relatively, phenanthrene is most likely to be transformed, and naphthalene is more stable. The experiment results consisted of the three substances' delocalization. According to the experimental results, the oxidation reaction time of potassium ferrate to the three substances is preliminarily identified to be 20 min.

3.3. The Influence of the Amount on Aromatic Hydrocarbon Removal Effect. The influence of potassium ferrate amount on aromatic hydrocarbon removal ability is shown in Figure 4, derived from measurement of samples in 20 min. As can be seen in Figure 4, as potassium ferrate amount increases, three kinds of aromatic hydrocarbon removal percentage gradually increased. Relatively, at the same reagent amount, phenanthrene has the highest removal percentage. When the potassium ferrate concentration is 10 mg/L, phenanthrene has the highest removal percentage, reaching 98%; pyrene and naphthalene were 84% and 61%, respectively. Further improvement of amount of oxidant potassium ferrate cannot obviously improve the removal percentage for the three substances. Removal of the aromatic hydrocarbons in micropolluted source water, therefore, has the most appropriate 10 mg/L potassium ferrate amount.

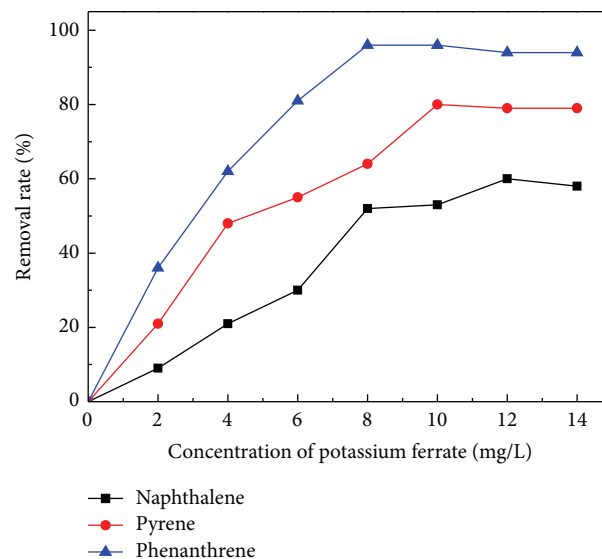


FIGURE 4: Influence of K_2FeO_4 concentration on aromatic hydrocarbons conversion and removal.

Potassium ferrate has strong oxidation, regardless of being in acidic medium or alkaline medium. The electrode potential is significantly higher than potassium permanganate and potassium dichromate; it can oxidize most organic substances. In hydrolysis process potassium ferrate produces strong oxidation hydroxyl free radicals [19]; at the same time, the unstable intermediate pentavalent iron and tetravalent iron also have a strong oxidizing ability [20]. The final reduction product is ferric iron. Potassium ferrate removal of aromatic hydrocarbon is the outcome of concerted action of these strong oxidizing substances. Low concentration potassium ferrate can transform removal of aromatic hydrocarbon. When the reaction time is 20 min, potassium ferrate concentrations are 12, 8, and 10 mg/L; naphthalene, phenanthrene, and pyrene removal percentage reached the maximum value, that is, 67%, 98%, and 84%, respectively.

3.4. Analysis of the Intermediate of Removing Phenanthrene. Due to the special stability of benzene ring structure, intermediate products can be generated during the oxidation process of aromatic substances. Thus, the removal process of aromatic substances has a potential environmental risk. Therefore, we studied the concrete structure of intermediate by GC-MS analysis.

Following are the GC of potassium ferrate system and mass spectrogram of some intermediates to transform phenanthrene.

Figure 5 is the GC of potassium ferrate system to transform phenanthrene.

As can be seen in the figure, the retention time of phenanthrene and main potassium ferrate reaction products was 12.443, 13.375, 13.575, and 18.139 min, respectively. In terms of corresponding mass spectrum, the peak retention time at 12.453 min is the undegraded phenanthrene peak. Compared

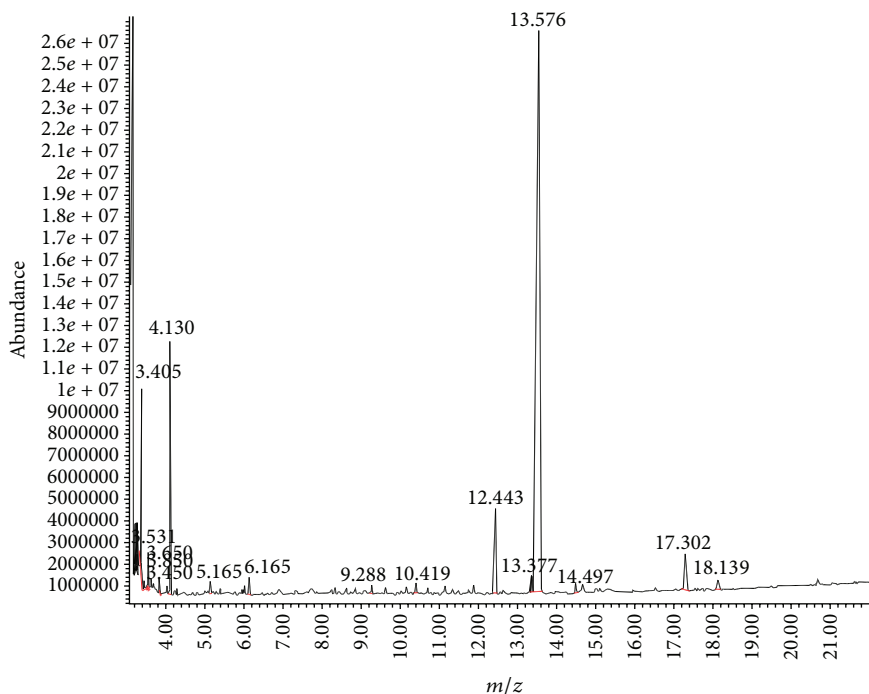


FIGURE 5: The GC map of phenanthrene conversion and removal by potassium ferrate system.

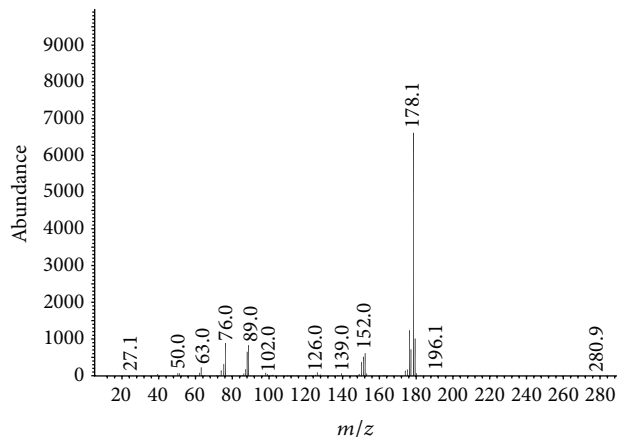


FIGURE 6: The mass spectrogram of 12.443 min.

with mass spectrometry retrieve library standard spectrogram, other intermediates mainly include butyl phthalate, 9,10-phenanthraquinone, and diphenyl-2,2'-biformaldehyde. In addition, there are some significant intermediates, such as 9-fluorenone and dimethylbenzal. And the peak of the main production prepared by phenanthrene reaction with potassium ferrate is at 13.575 min; the component area percentage accounted for 82.66%. Specific mass spectrum and structural formula of main products are as follows.

- (1) The mass spectrum peak diagram in GC of retention time at 12.443 min is as shown in Figure 6.

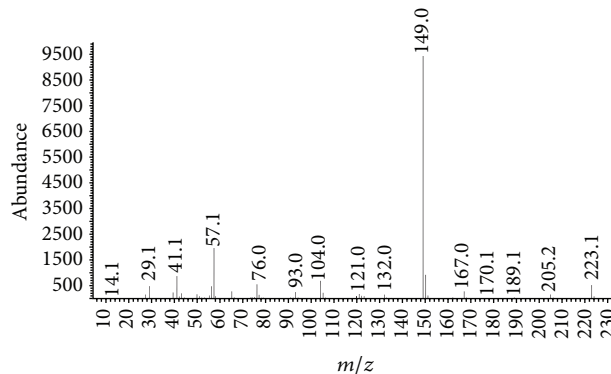
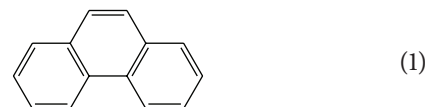


FIGURE 7: The mass spectrogram of 13.375 min.

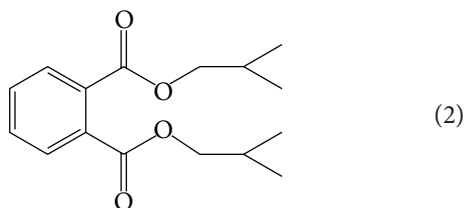
According to comparison with the spectral library spectrum standard substance, phenanthrene residue is identified in original solution, with 96% matching degree with the literatures, as the following structural formula:



- (2) The peak mass spectrum diagram in GC as of retention time at 13.375 min is as shown in Figure 7.

According to comparison with the spectral library spectrum standard substance, this material is identified as butyl

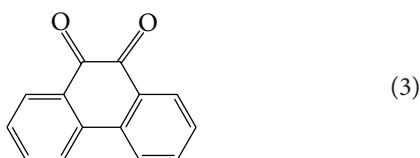
phthalate, with 86% matching degree, and its formula is as follows:



This material area percentage is only 1.32%, to show that this material accounts for a very small proportion in the product. This kind of material can be the intermediate produced by complex reaction of oxidation.

(3) The peak mass spectrum diagram in GC of retention time at 13.575 min is as shown in Figure 8.

According to comparison with the spectral library spectrum standard substance, this material is identified as 9,10-phenanthraquinone, with 92% matching degree, and its formula is as follows:



This material area percentage is 82.66%, to show that this material accounts for a very high proportion in the product. It is the main product of potassium ferrate in transformation of phenanthrene. Phenanthrene is made up of three benzene rings, where 9,10-position has strong chemical reactivity, prone to oxidation. In potassium ferrate oxidation system, phenanthrene gives Fe (VI) electron to be oxidized. In addition, phenanthrene can get 98% transformation in ferrate oxidation system, but it cannot completely inorganic, but is turned into 9,10-phenanthrenequinone. According to the research results by Lawton et al. [21], quinone structure is a kind of functional group more biophile than benzene ring. Its relatively weak biological resistance is advantageous over the biochemical conversion process. It changes aromatic hydrocarbon environmental durability characteristics and, to some extent, reduces the environmental risk.

(4) The peak mass spectrum diagram in GC of retention time at 18.139 min is as shown in Figure 9.

According to comparison with the spectral library spectrum standard substance, this material is identified as diphenyl-2,2'-biformaldehyde, with 70% matching degree, and its formula is as follows:

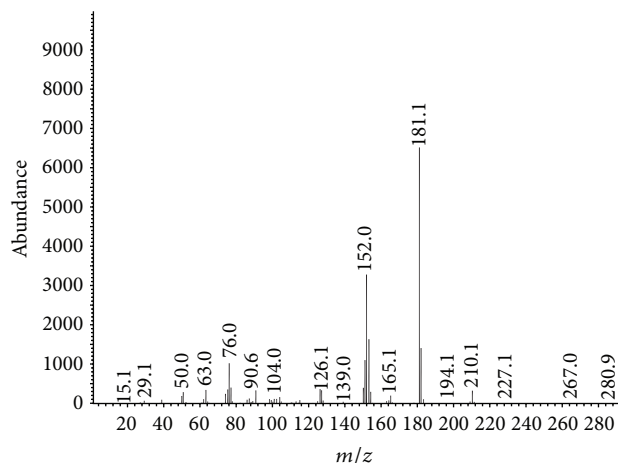
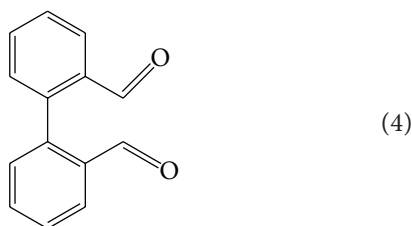


FIGURE 8: The mass spectrum of 13.575 min.

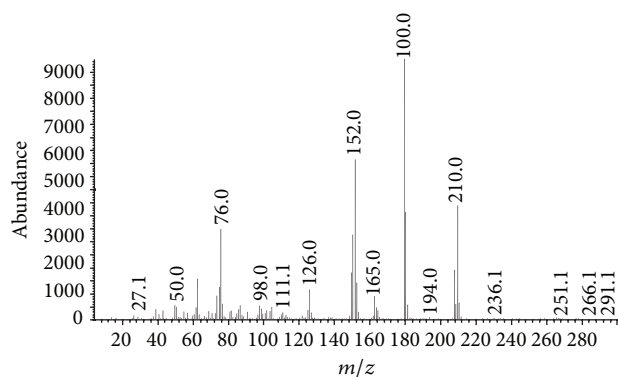


FIGURE 9: The mass spectrum of 18.139 min.

This material area percentage is only 1.05%, showing that this material accounts for a very small proportion in the product. In the process of potassium ferrate oxidation of phenanthrene, Fe (VI) to be reduced generates Fe (V), Fe (IV), and Fe (III) [22, 23] through single electron transfer steps. Phenanthrene 9,10-position has strong chemical reactivity, prone to oxidation. In potassium ferrate oxidation system, phenanthrene gives Fe (VI) electron to be oxidized. Since this is an oxidation system, diphenyl-2,2'-biformaldehyde is easy to be oxidized by potassium ferrate, so its proportion in products accounted for quite a few.

3.5. Primary Analysis of Oxidation System Mechanism to Transform Phenanthrene. In the process of potassium ferrate to oxidize phenanthrene, Fe (VI) to be reduced generates Fe (V), Fe (IV), and Fe (III) [24, 25] through single electron transfer steps. Phenanthrene is made up of three benzene rings, of which 9,10-position has strong chemical reactivity prone to oxidation. In potassium ferrate oxidation system, phenanthrene gives Fe (VI) electron to be oxidized. According to the single electron transfer mechanism, the possible reaction of potassium ferrate and phenanthrene is shown in Figure 10.

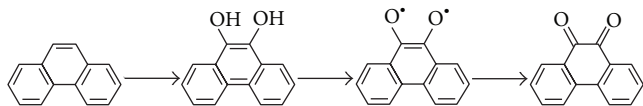


FIGURE 10: The possible way of reaction of potassium ferrate with phenanthrene.

4. Conclusions

This experiment adopts the hypochlorite oxidation approach to constantly synthesize potassium ferrate. The transformation oxidation process of potassium ferrate for aromatic hydrocarbons mainly occurred in the initial 5–10 minutes. Compared with aromatic hydrocarbon transformation removal percentage, it was found that potassium ferrate has high oxidation, but to different samples its transformation oxidation ability is not the same. Relatively, phenanthrene is most likely to be transformed, and naphthalene is more stable. In potassium ferrate, to remove phenanthrene, in GC and in the intermediate mass spectrum analysis, phenanthrene gives electron to Fe (VI) of potassium ferrate oxidation system, so that phenanthrene oxidation occurs. Thus possible reaction path is proposed: the quinone structure is a kind of functional group more biophile than benzene ring. Because of its biologically weak resistance, it is advantageous to the biochemical conversion process, to conversion of aromatic hydrocarbon's environmental durability characteristics, and, to some extent, to reduction of the environmental risk.

Conflict of Interests

The authors declare that there is no conflict of interests regarding the publication of this paper.

References

- [1] N. F. Y. Tam, L. Ke, X. H. Wang, and Y. S. Wong, "Contamination of polycyclic aromatic hydrocarbons in surface sediments of mangrove swamps," *Environmental Pollution*, vol. 114, no. 2, pp. 255–263, 2001.
- [2] M. Sanders, S. Sivertsen, and G. Scott, "Origin and distribution of polycyclic aromatic hydrocarbons in surficial sediments from the Savannah River," *Archives of Environmental Contamination and Toxicology*, vol. 43, no. 4, pp. 438–448, 2002.
- [3] R.-A. Doong and Y.-T. Lin, "Characterization and distribution of polycyclic aromatic hydrocarbon contaminations in surface sediment and water from Gao-ping River, Taiwan," *Water Research*, vol. 38, no. 7, pp. 1733–1744, 2004.
- [4] F. Lin, H. Ye, and Y. Song, "Preparation and electrochemical properties of Li-doped BaFeO₄ as electrode material for lithium-ion batteries," *Electrochemistry Communications*, vol. 2, no. 6, pp. 531–534, 2001.
- [5] V. K. Sharma, "Potassium ferrate(VI): an environmentally friendly oxidant," *Advances in Environmental Research*, vol. 6, no. 2, pp. 143–156, 2002.
- [6] M. Alsheyab, J.-Q. Jiang, and C. Stanford, "On-line production of ferrate with an electrochemical method and its potential application for wastewater treatment—a review," *Journal of Environmental Management*, vol. 90, no. 3, pp. 1350–1356, 2009.
- [7] J. Q. Jiang, S. Wang, and A. Panagouloupoulos, "The exploration of potassium ferrate(VI) as a disinfectant/coagulant in water and wastewater treatment," *Chemosphere*, vol. 63, no. 2, pp. 212–219, 2006.
- [8] Y. Y. Eng, V. K. Sharma, and A. K. Ray, "Ferrate(VI): green chemistry oxidant for degradation of cationic surfactant," *Chemosphere*, vol. 63, no. 10, pp. 1785–1790, 2006.
- [9] B. L. Yuan, Y. B. Li, X. D. Huang, H. Liu, and J. Qu, "Fe(VI)-assisted photocatalytic degradation of microcystin-LR using titanium dioxide," *Journal of Photochemistry and Photobiology A: Chemistry*, vol. 178, no. 1, pp. 106–111, 2006.
- [10] D. Tiwari, H.-U. Kim, B.-J. Choi et al., "Ferrate(VI): a green chemical for the oxidation of cyanide in aqueous/waste solutions," *Journal of Environmental Science and Health A: Toxic/Hazardous Substances & Environmental Engineering*, vol. 42, no. 6, pp. 803–810, 2007.
- [11] V. K. Sharma, "Use of iron(VI) and iron(V) in water and wastewater treatment," *Water Science and Technology*, vol. 49, no. 4, pp. 69–74, 2004.
- [12] J. Q. Jiang, "Research progress in the use of ferrate(VI) for the environmental remediation," *Journal of Hazardous Materials*, vol. 146, no. 3, pp. 617–623, 2007.
- [13] C. Li, Z. X. Li, N. Graham et al., "The aqueous degradation of bisphenol A and steroid estrogens by ferrate," *Water Research*, vol. 42, no. 1-2, pp. 109–120, 2008.
- [14] V. K. Sharma, S. K. Misra, and A. K. Ray, "Kinetic assessment of the potassium ferrate(VI) oxidation of antibacterial drug sulfamethoxazole," *Chemosphere*, vol. 62, no. 1, pp. 128–134, 2006.
- [15] F. Dong, Y. Sun, M. Fu, Z. Wu, and S. C. Lee, "Room temperature synthesis and highly enhanced visible light photocatalytic activity of porous BiOI/BiOCl composites nanoplates microflowers," *Journal of Hazardous Materials*, vol. 219–220, pp. 26–34, 2012.
- [16] F. Dong, Y. Sun, M. Fu, W.-K. Ho, S. C. Lee, and Z. Wu, "Novel in situ N-doped (BiO)₂CO₃ hierarchical microspheres self-assembled by nanosheets as efficient and durable visible light driven photocatalyst," *Langmuir*, vol. 28, no. 1, pp. 766–773, 2012.
- [17] X. L. Zhu and C. W. Yuan, "Photocatalytic degradation of pesticide pyridaben on TiO₂ particles," *Journal of Molecular Catalysis*, vol. 229, no. 1-2, pp. 95–105, 2005.
- [18] M. A. Rahman and M. Qamar, "Semiconductor mediated photocatalysed degradation of a pesticide derivative, acephate in aqueous suspensions of titanium dioxide," *Journal of Advanced Oxidation Technologies*, vol. 9, no. 1, pp. 103–109, 2006.
- [19] M. Iwasaki, M. Hara, H. Kawada et al., "State of arts for bleach plant effluent closure," *Journal of Colloid and Interface Science*, vol. 224, no. 1, pp. 202–204, 2000.
- [20] D. C. Hurum, A. G. Agrios, K. A. Gray, T. Rajh, and M. C. Thurnauer, "Explaining the enhanced photocatalytic activity of Degussa P25 mixed-phase TiO₂ using EPR," *Journal of Physical Chemistry B*, vol. 107, no. 19, pp. 4545–4549, 2003.
- [21] L. A. Lawton, P. K. J. Robertson, B. J. P. A. Cornish, I. L. Marr, and M. Jaspars, "Processes influencing surface interaction and photocatalytic destruction of microcystins on titanium dioxide photocatalysts," *Journal of Catalysis*, vol. 213, no. 1, pp. 109–113, 2003.
- [22] S. Malato, J. Blanco, A. Vidal, and C. Richter, "Photocatalysis with solar energy at a pilot-plant scale: an overview," *Applied Catalysis B: Environmental*, vol. 37, no. 1, pp. 1–15, 2002.

- [23] A. G. Rincón, C. Pulgarin, N. Adler, and P. Peringer, "Interaction between *E. coli* inactivation and DBP-precursors—dihydroxybenzene isomers—in the photocatalytic process of drinking-water disinfection with TiO_2 ," *Journal of Photochemistry and Photobiology A Chemistry*, vol. 139, no. 2-3, pp. 233–241, 2001.
- [24] W. He, J. Wang, H. Shao, J. Zhang, and C.-N. Cao, "Novel KOH electrolyte for one-step electrochemical synthesis of high purity solid K_2FeO_4 : comparison with NaOH," *Electrochemistry Communications*, vol. 7, no. 6, pp. 607–611, 2005.
- [25] B.-L. Yuan, X.-Z. Li, and N. Graham, "Aqueous oxidation of dimethyl phthalate in a Fe(VI)- TiO_2 -UV reaction system," *Water Research*, vol. 42, no. 6-7, pp. 1413–1420, 2008.

Research Article

Influence of Zn/Fe Molar Ratio on Optical and Magnetic Properties of ZnO and ZnFe₂O₄ Nanocrystal as Calcined Products of Layered Double Hydroxides

Abdullah Ahmed Ali Ahmed,¹ Zainal Abidin Talib,² Mohd Zobir Hussein,³
Moayad Husein Flaifel,⁴ and Naif Mohammed Al-Hada²

¹ Department of Physics, Faculty of Applied Science, Thamar University, P.O. Box 87246, Dhamar, Yemen

² Department of Physics, Faculty of Science, Universiti Putra Malaysia (UPM), 43400 Serdang, Selangor, Malaysia

³ Advanced Materials and Nanotechnology Laboratory, Institute of Advanced Technology (ITMA), Universiti Putra Malaysia (UPM), 43400 Serdang, Selangor, Malaysia

⁴ School of Applied Physics, Faculty of Science and Technology, Universiti Kebangsaan Malaysia, 43600 Bangi, Selangor, Malaysia

Correspondence should be addressed to Abdullah Ahmed Ali Ahmed; abdullah2803@gmail.com

Received 25 April 2014; Revised 2 June 2014; Accepted 23 June 2014; Published 10 July 2014

Academic Editor: Jie-Fang Zhu

Copyright © 2014 Abdullah Ahmed Ali Ahmed et al. This is an open access article distributed under the Creative Commons Attribution License, which permits unrestricted use, distribution, and reproduction in any medium, provided the original work is properly cited.

The coprecipitation method has been used to synthesize layered double hydroxide (Zn-Fe-LDH) nanostructure at different Zn²⁺/Fe³⁺ molar ratios. The structural properties of samples were studied using powder X-ray diffraction (PXRD). LDH samples were calcined at 600°C to produce mixed oxides (ZnO and ZnFe₂O₄). The crystallite size of mixed oxide was found in the nanometer scale (18.1 nm for ZnFe₂O₄ and 43.3 nm for ZnO). The photocatalytic activity of the calcination products was investigated using ultraviolet-visible-near infrared (UV-VIS-NIR) diffuse reflectance spectroscopy. The magnetic properties of calcined LDHs were investigated using a vibrating sample magnetometer (VSM). The calcined samples showed a paramagnetic behavior for all Zn²⁺/Fe³⁺ molar ratios. The effect of molar ratio on magnetic susceptibility of the calcined samples was also studied.

1. Introduction

Layered double hydroxides (LDHs) are one of the popular inorganic hosts to form an organic-inorganic hybrid type nanocomposite or so-called nanolayered composite materials [1]. LDHs, also known as hydrotalcite-like structure and anionic clay compounds, belong to a special class of synthetic two-dimensional inorganic compounds with lamellar structures. The chemical composition of LDHs can be described by the general formula $[M_{1-x}^{2+}M_x^{3+}(\text{OH})_2]^{x+}[(A^{n-})_{x/n} \cdot m\text{H}_2\text{O}]^{x-}$, where M²⁺ = divalent metals, M³⁺ is trivalent metals, and Aⁿ⁻ is an anion with charge *n*. Molar fraction number mol of water in LDH interlayer per formula weight of compounds and $x = M^{3+}/(M^{3+} + M^{2+})$ molar fraction (normally, it is between 0.2 and 0.33) [2].

An important use of LDH precursors is to get mixed nanometal oxides by calcination at temperature above 600°C [3, 4]. This method has been used to address the problem of the fast recombination of photogenerated electron-hole pairs in the mixed semiconductors to enhance the photocatalytic efficiency of semiconductor. Nano-zinc oxide (ZnO) with its excellent features has been used as photocatalysts [5]. At the same time, ZnFe₂O₄ spinel, which is a semiconductor with narrow band gap, exhibits characteristics of excellent visible-light response, as well as favorable magnetism and good photochemical stability [6]. In the current paper, Zn-Fe-CO₃-LDH has been synthesized by the coprecipitation method with Zn²⁺/Fe³⁺ molar ratios of 1, 2, 3, and 4 at the final pH value of 8. The mixed metal oxides were formed by the calcination process of LDH at 600°C. The structural,

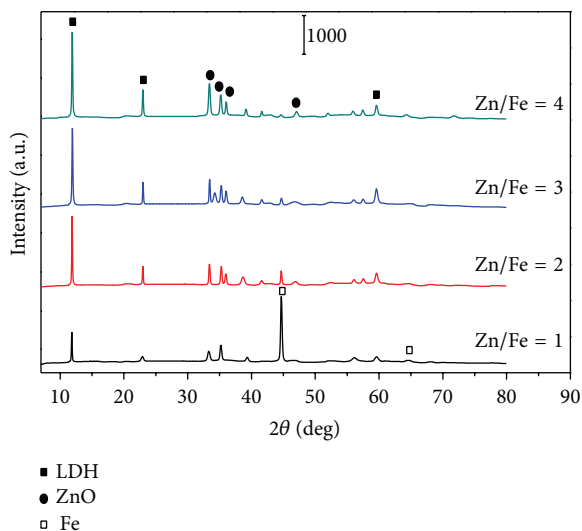


FIGURE 1: PXRD patterns of Zn-Fe-LDH samples synthesized at different $\text{Zn}^{2+}/\text{Fe}^{3+}$ molar ratios.

optical, and magnetic properties of calcination products were studied.

2. Experimental

2.1. Synthesis of Zn-Fe-LDH and Its Calcination Products. LDH precursors (Zn-Fe-LDH) were synthesized using coprecipitation method at pH 8 with $\text{Zn}^{2+}/\text{Fe}^{3+}$ molar ratios of 1, 2, 3, and 4. $\text{Zn}^{2+}/\text{Fe}^{3+}$ molar ratio was changed to evaluate its effect on the properties of the calcination products of LDH.

The synthesis was carried out by a slow addition of two metal nitrates solutions which were $\text{Zn}(\text{NO}_3)_2 \cdot 6\text{H}_2\text{O}$ and $\text{Fe}(\text{NO}_3)_3 \cdot 9\text{H}_2\text{O}$. The concentrations of $\text{Zn}(\text{NO}_3)_2 \cdot 6\text{H}_2\text{O}$ solution were 0.025, 0.050, 0.075, and 0.1 M for $\text{Zn}^{2+}/\text{Fe}^{3+}$ molar ratios of 1, 2, 3, and 4, respectively, while the concentration of $\text{Fe}(\text{NO}_3)_3 \cdot 9\text{H}_2\text{O}$ solution was fixed at 0.025 M for all samples. The solution that contained 0.1 M of Na_2CO_3 was added slowly (dropwise addition) to the metal nitrates solutions with constant stirring. The pH value for all samples was controlled by addition of aqueous NaOH (0.5 M). The resulting slurry was aged at 70°C for 18 h in an oil bath shaker (50 rpm). The precipitate was washed with deionized water many times with centrifugation. Finally, the precipitate was dried in an oven at 70°C for two days. The resultant Zn-Fe- CO_3 -LDH was ground into fine powder.

Heat-treated samples of Zn-Fe- CO_3 -LDH were prepared by heating LDH at 600°C . The samples were labeled ZrF, where r represents the $\text{Zn}^{2+}/\text{Fe}^{3+}$ molar ratio. Heating was performed in an electric tubular furnace at atmospheric pressure in a ceramic boat holder for 3 h at a rate of $3^\circ\text{C}/\text{min}$ (heating and cooling rate). The annealing process was performed in the ambient air. After the heat treatment was completed, the sample was left to cool to room temperature and stored in a sample bottle for further characterization.

2.2. Characterizations. Powder X-ray diffraction (PXRD) patterns of the samples were recorded on an X-ray diffractometer (X'PERT-PRO PANALYTICAL) using $\text{CuK}\alpha$ ($\lambda = 1.54060 \text{ \AA}$) at 40 kV and 40 mA. The slit configuration includes the fixing type of the divergence slit with slit size of 0.25° . The goniometer radius is 240 mm and distance of the focus-divergence slit is 100 mm. The scan configuration includes the continuous scan type with step size of $0.0330 [2\theta]$ and scan step time of 19.685 s. The optical properties were studied using a UV-VIS-NIR diffuse reflectance spectrophotometer (Shimadzu, UV-3600). This spectrophotometer is equipped with an integrating-sphere detector. The magnetic properties of calcined samples were measured using a vibrating sample magnetometer (VSM Model Lakeshore 7404).

3. Results and Discussion

3.1. Powder X-Ray Diffraction (PXRD) Study. Figure 1 shows XRD patterns of Zn-Fe- CO_3 -LDH prepared at different $\text{Zn}^{2+}/\text{Fe}^{3+}$ molar ratios of 1, 2, 3, and 4. XRD patterns exhibit two characteristic intense peaks of basal reflection of Zn-Fe- CO_3 -LDH which were located near 2θ of 11.9° and 23.1° corresponding to diffraction by (003) and (006) planes, respectively. As seen in Figure 1, Zn-Fe- CO_3 -LDH phase is observed with ZnO phase which was formed during the aging of the coprecipitated products or during the titration process [7, 8]. At $\text{Zn}^{2+}/\text{Fe}^{3+}$ molar ratio of 1, the Fe metal also was clearly observed. This may be attributed to the presence of a residual of the Fe ions which could not precipitate into prepared Zn-Fe- CO_3 -LDH layer. At $\text{Zn}^{2+}/\text{Fe}^{3+}$ molar ratio values of 2, 3, and 4, the high crystallinity of (003) and (006) peaks was observed which indicated the presence of a well-ordered layered structure [7].

XRD patterns exhibit ZnO/ ZnFe_2O_4 nanocomposite as the calcination products of Zn-Fe- CO_3 -LDH samples at different $\text{Zn}^{2+}/\text{Fe}^{3+}$ molar ratios (Z1F, Z2F, Z3F, and Z4F) as shown in Figure 2. X'Pert-High-Score Plus software has been used to analyze the XRD data. The peaks of hexagonal wurtzite structure of ZnO were observed near 2θ of $31.8, 34.5, 36.3, 47.7, 56.6, 62.9, 66.5, 68.1, 69.1, \text{ and } 77^\circ$ which correspond to diffraction by (100), (002), (101), (102), (110), (103), (200), (112), (201), and (202) planes, respectively, (reference code: 01-079-0206). For ZnFe_2O_4 nanocrystal, the peaks were located at 2θ of $18.2, 29.9, 35.2, 42.8, 53.2, 56.6, 62.1, \text{ and } 66.4^\circ$ which corresponds to diffraction by (111), (220), (311), (400), (422), (511), (440), and (442) planes, respectively (reference code: 01-089-4926). This is identified as face-centered-cubic (FCC) franklinite ZnFe_2O_4 with space group Fd-3m (227) and lattice parameters of $a = b = c = 8.443 \text{ \AA}$.

The crystallinity of ZnO phase increased with the increase in $\text{Zn}^{2+}/\text{Fe}^{3+}$ molar ratio, while ZnFe_2O_4 nanocrystal was observed with almost the same crystallinity due to the fixing of Fe^{3+} content during the preparation of Zn-Fe- CO_3 -LDH samples. This observation is in good agreement with the literature [7]. The average crystallite size of ZnFe_2O_4 in the (111) crystal plane is 18.1 nm [9] and for ZnO in the (002)

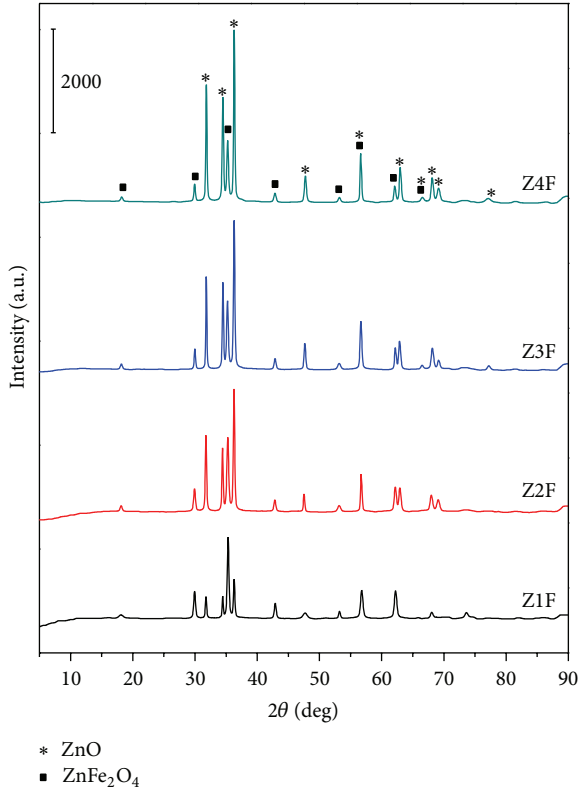


FIGURE 2: PXRD patterns of calcined Zn-Fe-LDH nanostructure.

crystal plane it is 43.3 nm [3, 10, 11] as estimated using Scherrer's equation.

3.2. UV-Visible Spectra. The fundamental absorption of light, which corresponds to an electronic excitation from the valance band to the conduction band, can be applied to calculate the optical band-gap energy (E_g). In this study, the optical band-gap energy can be calculated using the Kubelka-Munk equation in terms of reflectance (R):

$$F(R_{\infty}) = \frac{(1 - R_{\infty})^2}{2R_{\infty}}, \quad (1)$$

where R_{∞} is the diffuse reflectance of the examined samples ($R_{\infty} = R_{\text{sample}}/R_{\text{standard}}$) and $F(R_{\infty})$ is called the remission or Kubelka-Munk function [12, 13]. Thus, the band gap is obtained using the following equation:

$$(F(R_{\infty}) \cdot h\nu)^2 = A(h\nu - E_g). \quad (2)$$

The variation of $(F(R_{\infty}) \cdot h\nu)^2$ versus $(h\nu)$ is plotted and the straight line range of these plots is extended on $(h\nu)$ axis to obtain the values of optical band gap (E_g).

Figure 3(a) shows the recorded reflectance of calcined Zn-Fe-LDH samples and Figure 3(b) exhibits the band-gap energies of ZnO phase which is found at around 3.19 eV. The average band gap of ZnO/ZnFe₂O₄ nanocomposite annealed at 600°C is found at ~2.30 eV as shown in Figure 3(c). The band-gap value of pure ZnFe₂O₄ is 1.9 eV [14], while the band gap for whole nanocomposite (ZnO/ZnFe₂O₄) increased to

2.32 eV as seen in the recent study [15]. This is in good agreement with our results. On the other hand, the ZnO band-gap energy decreases from ~3.37 eV (for pure ZnO phase) [16] to around 3.19 eV in this work. This phenomenon occurs due to the presence of ZnO with another metal oxide (ZnFe₂O₄) which indicates the photocatalytic activity [17]. As seen in Figure 3(c), another band gap also is observed at ~2.70 eV which may be attributed to the presence of ZnO/ZnFe₂O₄ nanocomposite.

Table 1 exhibits the effect of Zn²⁺/Fe³⁺ molar ratio on the crystallite size of mixed metal oxide (ZnO and ZnFe₂O₄) and ZnO band-gap energy. As Zn²⁺/Fe³⁺ molar ratio value increases from 1 to 4, the crystallite size of ZnO phase decreases from 51.2 to 36.6 nm; thus, the ZnO band gap increases from 3.188 to 3.198 eV. The fluctuation in band-gap value of ZnO in Table 1 may be attributed to the additional ZnO phase which formed during the preparation of Zn-Fe-LDH as shown in Figure 1.

As seen in Figure 3(d), the absorbance of LDH calcination products has shown an edge at 360 nm which indicates the free exciton absorption of the lower particle size of ZnO [18]. The broad band at around 295 nm may suggest charge transfer transition from O²⁻ to Fe³⁺ in ZnFe₂O₄ spinel [19]. The threshold of the absorption band of ZnFe₂O₄ spinel occurs at around 685 nm. The blue shift absorption of ZnFe₂O₄ spinel and ZnO compared with the ZnFe₂O₄ (700 nm) may be attributed to the quantum-size effect.

Under visible-light irradiation, photogenerated electrons (e) and holes (h) are produced in mixed oxides (ZnO and ZnFe₂O₄) via electron excitation from valence band (VB) to conduction band (CB) of ZnFe₂O₄ nanocrystal. Due to the differences in the positions of band gap in these oxides, the photogenerated electrons transferred from CB of ZnFe₂O₄ to CB of ZnO as illustrated schematically in Figure 4. At the same time, the number of holes with positive charge left (VB) of ZnAl₂O₄ to (VB) of ZnO. The difference in the energy levels of ZnO and ZnFe₂O₄ semiconductors is important in achieving such charge separation which gives rise to the improvement of the photocatalytic activity of ZnO [17].

3.3. Magnetic Spectroscopy. The magnetic behavior of mixed oxides (ZnO and ZnFe₂O₄) as a function of Zn²⁺/Fe³⁺ molar ratio incorporated is quite different. All calcined samples exhibit a paramagnetic behavior as shown in Figure 5. The typical curves for paramagnetic systems can be defined as

$$M = \chi \cdot H, \quad (3)$$

where M is the magnetization, H is the applied magnetic field, and χ is the magnetic susceptibility.

Normally, the magnetic contribution of pure ZnFe₂O₄ nanocrystal below a critical value of particle size 10 nm for [9] is superparamagnetic behavior, while this behavior changed to paramagnetic when ZnFe₂O₄ nanocrystal was calcined at temperature of 650°C [9]. This is due to the oxygen vacancies of ZnFe₂O₄ fully occupied during the heat treatment in air, which is responsible for the reduction in magnetic moment. In this study, the room temperature magnetic hysteresis loop of the calcined products of LDH (ZnO and ZnFe₂O₄) shows

TABLE 1: Crystallite size and optical band-gap energy (E_g) for Z1F, Z2F, Z3F and Z4F samples.

Samples	ZnO size ^a (nm)	ZnFe ₂ O ₄ size ^a (nm)	E_g of ZnO phase (eV)
Z1F	51.2	10.3	3.188 ± 0.014
Z2F	42.7	20.6	3.196 ± 0.015
Z3F	42.7	20.6	3.187 ± 0.020
Z4F	36.6	20.7	3.198 ± 0.018

^aCrystallite size: calculated using Scherrer's equation.

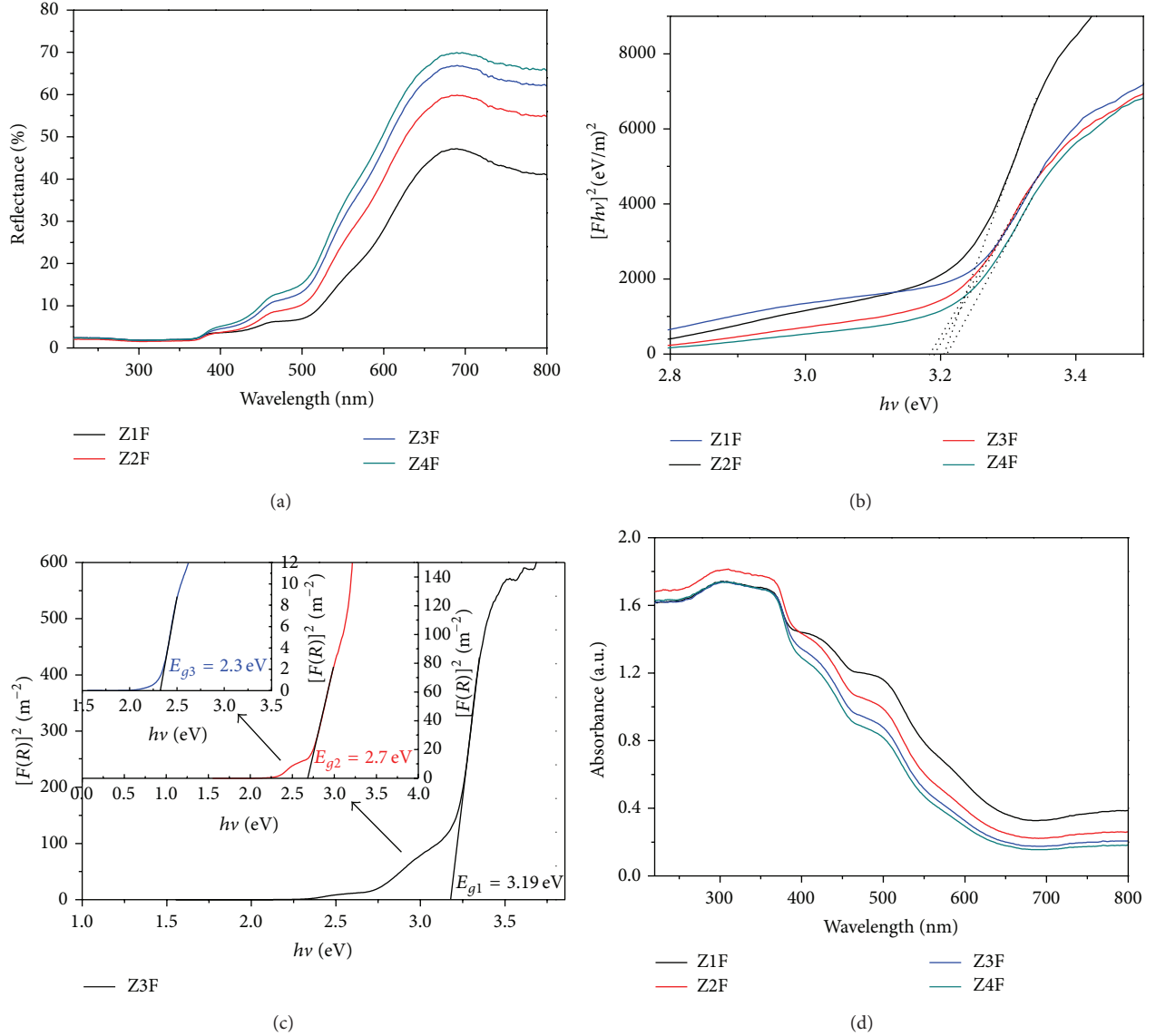


FIGURE 3: Kubelka-Munk transformed reflectance spectra of (a) reflectance spectra of ZnO/ZnFe₂O₄ nanocomposite, (b) band-gap energy of ZnO, (c) Kubelka-Munk plot ZnO/ZnFe₂O₄ nanocomposite (for sample Z3F as an example), and (d) diffuse reflectance UV-visible absorption spectra of calcined Zn-Fe-LDH nanostructure.

a paramagnetic behavior as shown in Figure 5. The final magnetization value (there is no saturation magnetization) decreases as Zn content (Zn²⁺/Fe³⁺ molar ratio) increases due to the presence of high crystalline ZnO. Figure 6 shows the

magnetic susceptibility as function of the Zn²⁺/Fe³⁺ molar ratio in the samples. The value of paramagnetic response (χ) decreases with the increase in Zn²⁺/Fe³⁺ molar ratio according to the observed formation of ZnO [7].

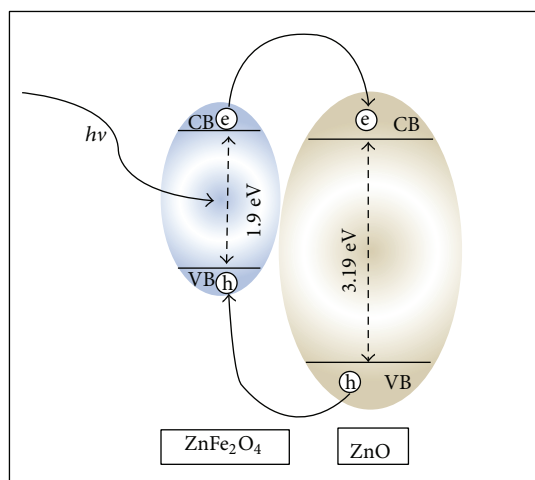


FIGURE 4: Scheme of the coupling action of different energy bands between ZnO and ZnFe_2O_4 [17].

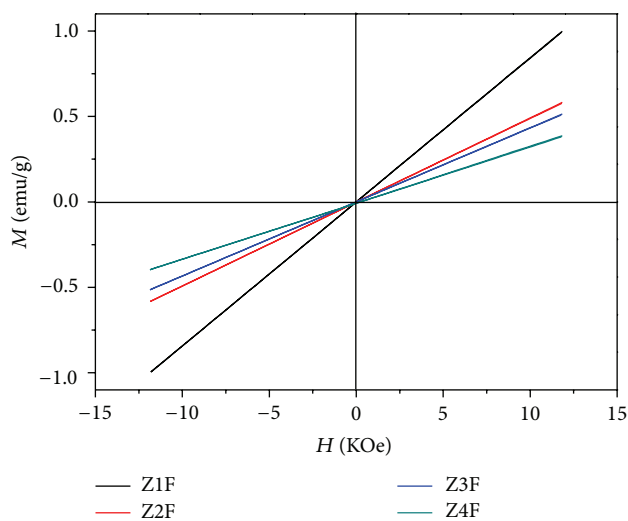


FIGURE 5: Paramagnetic contribution of the hysteresis loop after the calcination.

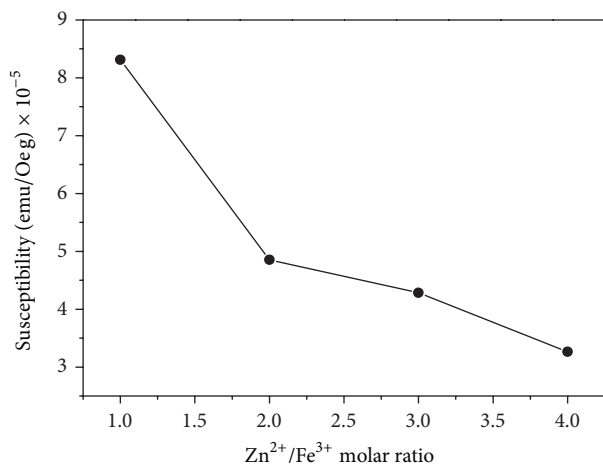


FIGURE 6: Susceptibility as function of $\text{Zn}^{2+}/\text{Fe}^{3+}$ molar ratio for calcined samples.

4. Conclusions

The coprecipitation method was used to synthesize Zn-Fe-LDH at the $\text{Zn}^{2+}/\text{Fe}^{3+}$ molar ratios of 1, 2, 3, and 4. XRD patterns of the calcined LDH showed ZnO and ZnFe_2O_4 phases. XRD confirmed that ZnFe_2O_4 is composed of franklinite. The crystallite sizes of both phases in nanocrystal range were found as 18.1 nm for ZnFe_2O_4 and 43.3 nm for ZnO. The optical band-gap value of ZnO was improved to around 3.19 eV due to the photocatalytic activity, while the optical band-gap energy of $\text{ZnO}/\text{ZnFe}_2\text{O}_4$ nanocomposite was found at around two values of 2.30 and 2.70 eV. The magnetic behavior of mixed oxides (ZnO and ZnFe_2O_4) phases showed a paramagnetic behavior due to the oxygen vacancies of ZnFe_2O_4 fully occupied during the heat treatment in air, which resulted in the reduction in magnetic moment. The magnetic susceptibility decreased as $\text{Zn}^{2+}/\text{Fe}^{3+}$ molar ratio increased due to the increase in the crystallinity of formed ZnO.

Conflict of Interests

The authors declare that there is no conflict of interests regarding the publication of this paper.

Acknowledgments

The authors would like to thank Universiti Putra Malaysia (UPM) for supporting this work. A. A. A. Ahmed thanks RMC-UPM for the support.

References

- [1] F. Kovanda, E. Jindová, K. Lang, P. Kubát, and Z. Sedláková, "Preparation of layered double hydroxides intercalated with organic anions and their application in LDH/poly (butyl methacrylate) nanocomposites," *Applied Clay Science*, vol. 48, no. 1, pp. 260–270, 2010.
- [2] F. Cavani, F. Trifirò, and A. Vaccari, "Hydrotalcite-type anionic clays: preparation, properties and applications," *Catalysis Today*, vol. 11, no. 2, pp. 173–301, 1991.
- [3] A. A. A. Ahmed, Z. A. Talib, M. Z. B. Hussein, and A. Zakaria, "Improvement of the crystallinity and photocatalytic property of zinc oxide as calcination product of ZnAl layered double hydroxide," *Journal of Alloys and Compounds*, vol. 539, pp. 154–160, 2012.
- [4] M.-Y. Guan, D.-M. Xu, Y.-F. Song, and Y. Guo, " $\text{ZnO}/\text{ZnAl}_2\text{O}_4$ prepared by calcination of ZnAl layered double hydroxides for ethanol sensing," *Sensors and Actuators B: Chemical*, vol. 188, pp. 1148–1154, 2013.
- [5] L. Xu, Y.-L. Hu, C. Pelligra et al., "ZnO with different morphologies synthesized by solvothermal methods for enhanced photocatalytic activity," *Chemistry of Materials*, vol. 21, no. 13, pp. 2875–2885, 2009.
- [6] X. Li, Y. Hou, Q. Zhao, W. Teng, X. Hu, and G. Chen, "Capability of novel ZnFe_2O_4 nanotube arrays for visible-light induced degradation of 4-chlorophenol," *Chemosphere*, vol. 82, no. 4, pp. 581–586, 2011.
- [7] A. I. C. Heredia, M. I. Oliva, C. I. Zandalazini et al., "Synthesis, characterization, and catalytic behavior of MgAlZnFe mixed

- oxides from precursors layered double hydroxide," *Industrial & Engineering Chemistry Research*, vol. 50, no. 11, pp. 6695–6703, 2011.
- [8] A. A. A. Ahmed, Z. A. Talib, and M. Z. bin Hussein, "Thermal, optical and dielectric properties of Zn-Al layered double hydroxide," *Applied Clay Science*, vol. 56, pp. 68–76, 2012.
- [9] Y. Sun, W. Wang, L. Zhang, S. Sun, and E. Gao, "Magnetic ZnFe₂O₄ octahedra: Synthesis and visible light induced photocatalytic activities," *Materials Letters*, vol. 98, pp. 124–127, 2013.
- [10] E. M. Seftel, E. Popovici, M. Mertens et al., "Zn-Al layered double hydroxides: synthesis, characterization and photocatalytic application," *Microporous and Mesoporous Materials*, vol. 113, no. 1–3, pp. 296–304, 2008.
- [11] S. Yuan, Y. Li, Q. Zhang, and H. Wang, "ZnO nanorods decorated calcined Mg-Al layered double hydroxides as photocatalysts with a high adsorptive capacity," *Colloids and Surfaces A: Physicochemical and Engineering Aspects*, vol. 348, no. 1–3, pp. 76–81, 2009.
- [12] J. Torrent and V. Barron, *Encyclopedia of Surface and Colloid Science*, Marcel Dekker, New York, NY, USA, 2002.
- [13] P. F. Wang, Z. H. Li, and Y. M. Zhu, "Research on the direct doping effect of silicon on cubic boron nitride ceramics by UV-VIS diffuse reflectance," *Materials Chemistry and Physics*, vol. 123, no. 2–3, pp. 356–359, 2010.
- [14] J. S. Jang, P. H. Borse, J. S. Lee et al., "Synthesis of nanocrystalline ZnFe₂O₄ by polymerized complex method for its visible light photocatalytic application: an efficient photo-oxidant," *Bulletin of the Korean Chemical Society*, vol. 30, pp. 1738–1742, 2009.
- [15] M. H. Habibi and A. H. Habibi, "Nanostructure composite ZnFe₂O₄/FeFe₂O₄/ZnO immobilized on glass: photocatalytic activity for degradation of an azo textile dye F3B," *Journal of Industrial and Engineering Chemistry*, vol. 20, no. 1, pp. 68–73, 2013.
- [16] Z. L. Wang, "Zinc oxide nanostructures: growth, properties and applications," *Journal of Physics: Condensed Matter*, vol. 16, pp. R829–R858, 2004.
- [17] L. Sun, R. Shao, L. Tang, and Z. Chen, "Synthesis of ZnFe₂O₄/ZnO nanocomposites immobilized on graphene with enhanced photocatalytic activity under solar light irradiation," *Journal of Alloys and Compounds*, vol. 564, pp. 55–62, 2013.
- [18] D. Sridev and K. Rajendran, "Synthesis and optical characteristics of ZnO nanocrystals," *Bulletin of Materials Science*, vol. 32, no. 2, pp. 165–168, 2009.
- [19] T. Xie, L. Xu, C. Liu, and Y. Wang, "Magnetic composite ZnFe₂O₄/SrFe₁₂O₁₉: preparation, characterization, and photocatalytic activity under visible light," *Applied Surface Science*, vol. 273, pp. 684–691, 2013.

Research Article

Structural Characterization of Carbon Nanomaterial Film *In Situ* Synthesized on Various Bulk Metals

J. Y. Xu, R. Yang, Z. Z. Fan, and X. C. Lei

College of Materials Science and Engineering, Chongqing University, Chongqing 400030, China

Correspondence should be addressed to J. Y. Xu; junyaoxu@cqu.edu.cn

Received 7 May 2014; Accepted 28 May 2014; Published 19 June 2014

Academic Editor: Wen Zeng

Copyright © 2014 J. Y. Xu et al. This is an open access article distributed under the Creative Commons Attribution License, which permits unrestricted use, distribution, and reproduction in any medium, provided the original work is properly cited.

Carbon nanofiber films were prepared via a simple chemical vapor deposition (CVD) method on various bulk metal substrates including bulk 316 L stainless steel, pure cobalt, and pure nickel treated by surface mechanical attrition treatment (SMAT). The microstructures of the carbon nanomaterial film were studied by SEM, TEM, XRD, and Raman spectroscopy. In this paper, bulk metallic materials treated by SMAT served as substrates as well as catalysts for carbon nanomaterial film formation. The results indicate that the carbon nanofiber films are formed concerning the catalytic effects of the refined metallic particles during CVD on the surface of SMAT-treated bulk metal substrates. However, distinguished morphologies of carbon nanomaterial film are displayed in the case of the diverse bulk metal substrates.

1. Introduction

Surface mechanical attrition treatment (SMAT) is proved to be an effective technique to achieve nanocrystallization in the surface layer of the bulk materials by means of severe plastic deformation (SPD). It has been successfully applied in a variety of materials including pure metals, alloys, and steels [1, 2]. With this kind of surface modification, the surface properties, for example, diffusivities, can be greatly enhanced [3–5]. Carbon nanomaterials, on the other hand, have attracted much attention due to their excellent properties and the inspiring applications [6]. Carbon nanomaterial film with rational structural design synthesized directly on the surface of bulk substrate displays wide potential applications [7, 8]. Thus, various templates or new techniques are developed [9–11]. However, few of them are facile and of low cost. Recently, using hybrid SMAT, that is, SMAT followed by chemical vapor deposition (CVD), carbon nanomaterials have been successfully synthesized *in situ* on the surface of bulk transition metals [12, 13]. It is a new way to obtain functional carbon nanomaterial film *in situ* on bulk metals, which shows many prospective potential applications.

To get more details about the synthesized carbon products, in current work, scanning electron microscopy (SEM), transmission electron microscopy (TEM), X-ray diffraction

(XRD), and Raman spectroscopy were used to characterize the resulting carbon nanomaterials.

2. Experimental Details

Three metallic plates including stainless steel (AISI 316 L), pure cobalt (purity 99.9%), and pure nickel (purity 99.9%) were chosen as substrates to *in situ* synthesize carbon nanomaterial films by method of SMAT followed by CVD. The size of plates was 20 mm in diameter and 1 mm in thickness.

Surface modification was firstly applied on the bulk metallic samples by the SMAT process to achieve nanostructured surface layer. The details of the SMAT were described in the literature [2]. Figure 1 displays the schematic illustration of the SMAT setup. Due to the severe plastic deformation introduced on the sample surface by numerous repeated multidirectional impacts, the metallic grains in the surface were refined into the nanometer regime. The key operation parameters of the SMAT process were outlined as the following: the vibration frequency of the ultrasonic system was 20 kHz, the shot diameter was 2 mm, and the perpetual treatment time was 30 min.

Subsequently, a one-step CVD process was adopted for the synthesis of the nanostructured carbon films. The SMAT samples were inserted into the center of a quartz tube furnace,

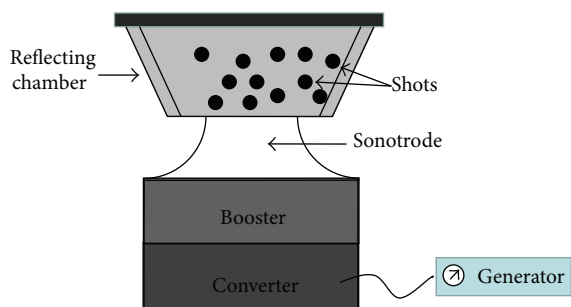


FIGURE 1: Schematic illustration of the experimental SMAT setup.

which was heated to 550°C. A mixture of $C_2H_2/H_2/N_2$ (50/100/300, v/v/v) was introduced into the tube at a flow rate of 450 sccm (mL/min) and kept for 30 min. After that, the samples were cooled down to room temperature in the furnace with the protection of N_2 atmosphere to obtain the final products.

For the microstructural analysis of carbon nanomaterial films, SEM was carried out on a Sirion, FEI working at 3 kV accelerated voltage. TEM observations were performed using a Philips CM30 microscope working under 300 kV accelerated voltage. XRD analysis was carried out with $Cu K\alpha$ radiation. Scans were performed at a rate of 0.05°/s, in the range of $2\theta = 20-85^\circ$. Raman scattering measurements were performed with Jobin Yvon Horiba HR 800 micro-Raman system. Scans were in the range 1000–2000 cm^{-1} , 10 s, 3 to 5 acquisitions per point, using an Ar^+ laser with wavelength of 488 nm.

3. Results and Discussions

After CVD process, black thin films have been obviously formed on the surface of the SMAT areas. SEM and TEM characterizations were performed to estimate the nature of the products and to get more detailed information of the morphology. The films were carefully scratched from the substrates and were dispersed in distilled water using ultrasonication to prepare the specimens for TEM observations. The representative SEM and TEM images of the samples were shown in Figure 2. As can be seen from Figure 2(a), a mixture composed of amorphous carbon, carbon nanofibers, and metallic particles was synthesized on SMAT 316 L stainless steel substrate. Many metallic particles embedded in amorphous carbon are observed (Figure 2(b)). In contrast, residual metal particles are rarely observed on the surface of SMAT Co, and the film mainly composed of carbon nanofibers is formed, as shown in Figures 2(c) and 2(d). The nanofibers have a relatively uniform diameter of about 25 nm despite several much thicker fibers. Most of the carbon nanofibers are curly and entangled with each other. Some metal particles are maintained at the top ends of the fibers, as can be seen from Figure 2(d), which implies that the growth of the carbon nanofibers on SMAT Co might follow the “deposition-diffusion-nucleation-growth” mechanism. Differing from the morphologies of carbon films on SMAT 316 L stainless and SMAT Co, a thick black film composed of carbon products

with the appearance as dust clusters was formed on SMAT Ni. Figures 2(e) and 2(f) show the typical SEM and TEM images of the carbon nanomaterials synthesized on SMAT Ni, indicating long and straight thick fibers with a diameter of over 100 nm. Also, there are relatively thin curly fibers around the straight thick fibers.

The phase composition of SMAT metals after CVD process was studied by XRD. Figure 3 collects the XRD data of the obtained products. For the SMAT 316 L stainless steel (Figure 3(a)), it is observed that the XRD patterns contain the diffraction peaks of both the γ austenite phase and the α' martensite phase, indicating that a martensite transformation has taken place during the SMAT process and led to a mixed structure of martensite and austenite. The noncrystal broad peak reveals the presence of the amorphous carbon. The diffraction peak at $2\theta =$ (about 26°) can be indexed as the (002) graphite reflection. The intensity of the diffraction peaks relates to the graphitization degree of the carbon nanofibers. Result deduced from the XRD patterns suggests that graphite products have formed on the SMAT 316 L stainless steel. For the SMAT Co, as shown in Figure 3(b), the diffraction peaks of Co are evidently broadened due to the grain refinement. No obvious noncrystal broad peak is observed, indicating that there is hardly amorphous carbon among the products. The representative peak of graphite C (002) is sharp and smooth, which represents the high degree of long-range order of the carbon products. XRD patterns shown in Figure 3(c) display the peaks of Ni and carbon nanofibers. The representative peak of graphite C (002) ($2\theta = 26^\circ$) is smooth but broader than that of the carbon nanofibers synthesized on SMAT Co, indicating a lower degree of long-range order of the carbon products. Nevertheless, no obvious noncrystal broad peak representing the amorphous carbon is observed. The broadening peaks of Ni may be attributed to nanocrystallization of the metallic surface layer.

Although using the SEM and TEM can directly observe the microstructure of the carbon nanomaterial, the comprehensive graphitization quality cannot be represented. Raman spectroscopy is one of the most valuable techniques for characterizing the deposited carbon by providing the information about the surface molecular vibration [14]. The carbon bond nature of the deposited carbon products over SMAT 316 L stainless steel, Co, and Ni was characterized by Raman spectroscopy and the obtained results are presented in Figure 4. As shown in Figure 4(a), the products synthesized on SMAT 316 L stainless steel exhibit two distinct Raman bands located at around 1359 cm^{-1} and at around 1597 cm^{-1} . The peak at 1597 cm^{-1} is the graphite band (G-band), which implies the high degree of symmetry and order of carbon materials, generally used to identify well-ordered carbon, while the peak at 1359 cm^{-1} is the disorder-induced phonon mode (D-band), which is attributed either to structural imperfection of graphite or to the presence of nanoparticles as well as to the in-plane carbon-carbon stretching vibrations arising. Its shifts and line-width variations are indications of the defects of the crystal lattice. The ratio of the G-band to the D-band represents the amount of sp^2 (graphite) clusters in the sample. High G/D ratio represents high graphitization quality.

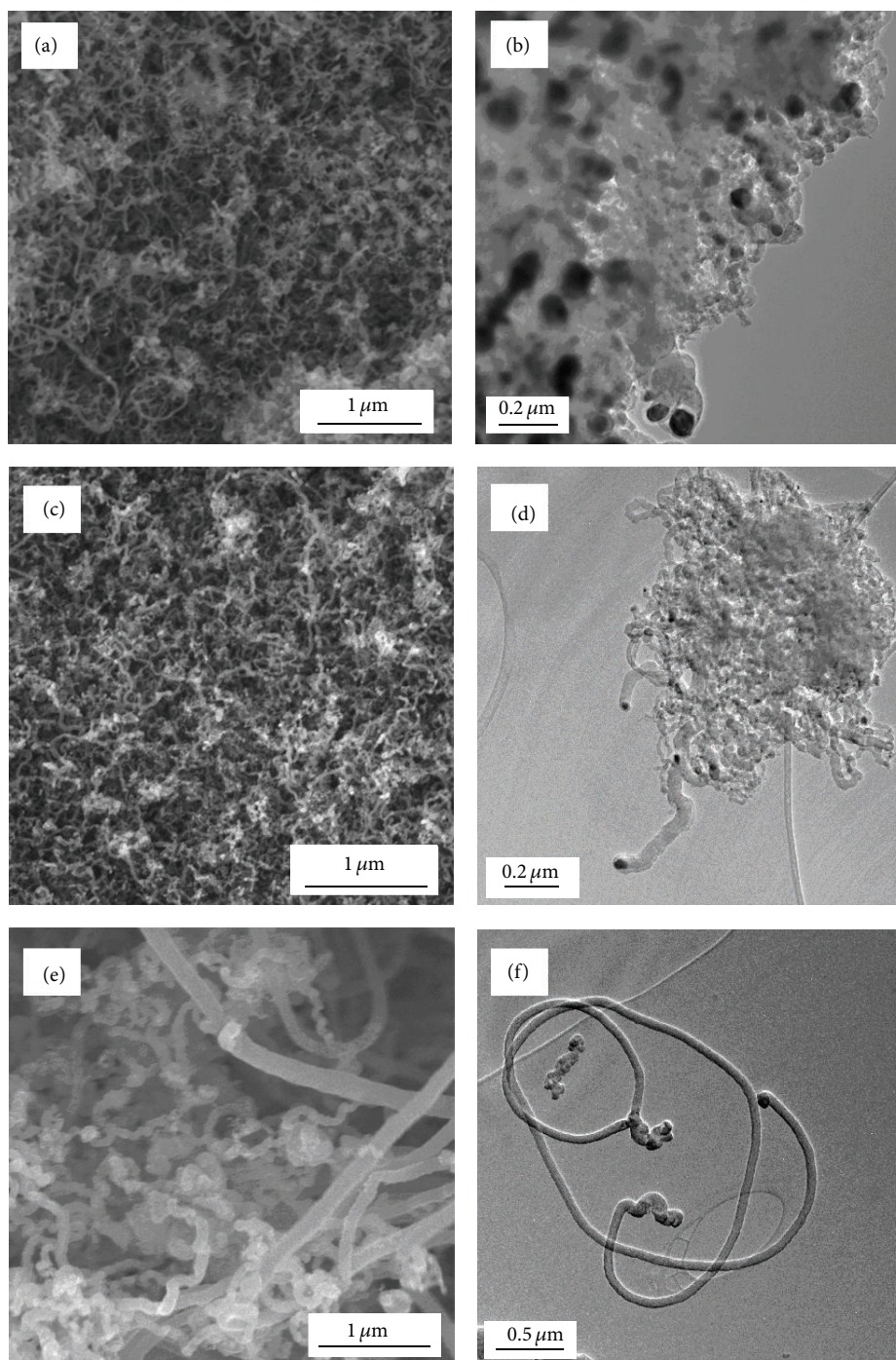


FIGURE 2: SEM (a, c, and e) and TEM (b, d, and f) images of the carbon nanofibers synthesized on different SMAT metals: (a, b) on SMAT 316 L stainless steel; (c, d) on SMAT Co; and (e, f) on SMAT Ni.

In Figure 4(a), the intensity of peak D is a little lower than that of peak G, which indicates that the products over SMAT 316 L stainless steel have relatively higher graphitization. The products formed on SMAT Co were also characterized by Raman spectroscopy, as shown in Figure 4(b). The figure displays two distinct bands located at 1394 cm^{-1} (D peak) and 1590 cm^{-1} (G peak). Peak G corresponds to sp^2 bonding (due to the graphitic structure) and peak D corresponds to

sp^3 bonding (due to the disordered structure in carbon). In this case, the intensity of peak G is much higher than that of peak D, which indicates the carbon with high graphitization. Figure 4(c) displays the Raman spectrum of the carbon nanofibers formed on SMAT Ni, showing two peaks assigned to carbon located at 1342 cm^{-1} (D-band peak) and 1578 cm^{-1} (G-band peak). It is noted that in this case the intensity of D-band peak is comparative with that of G-band peak.

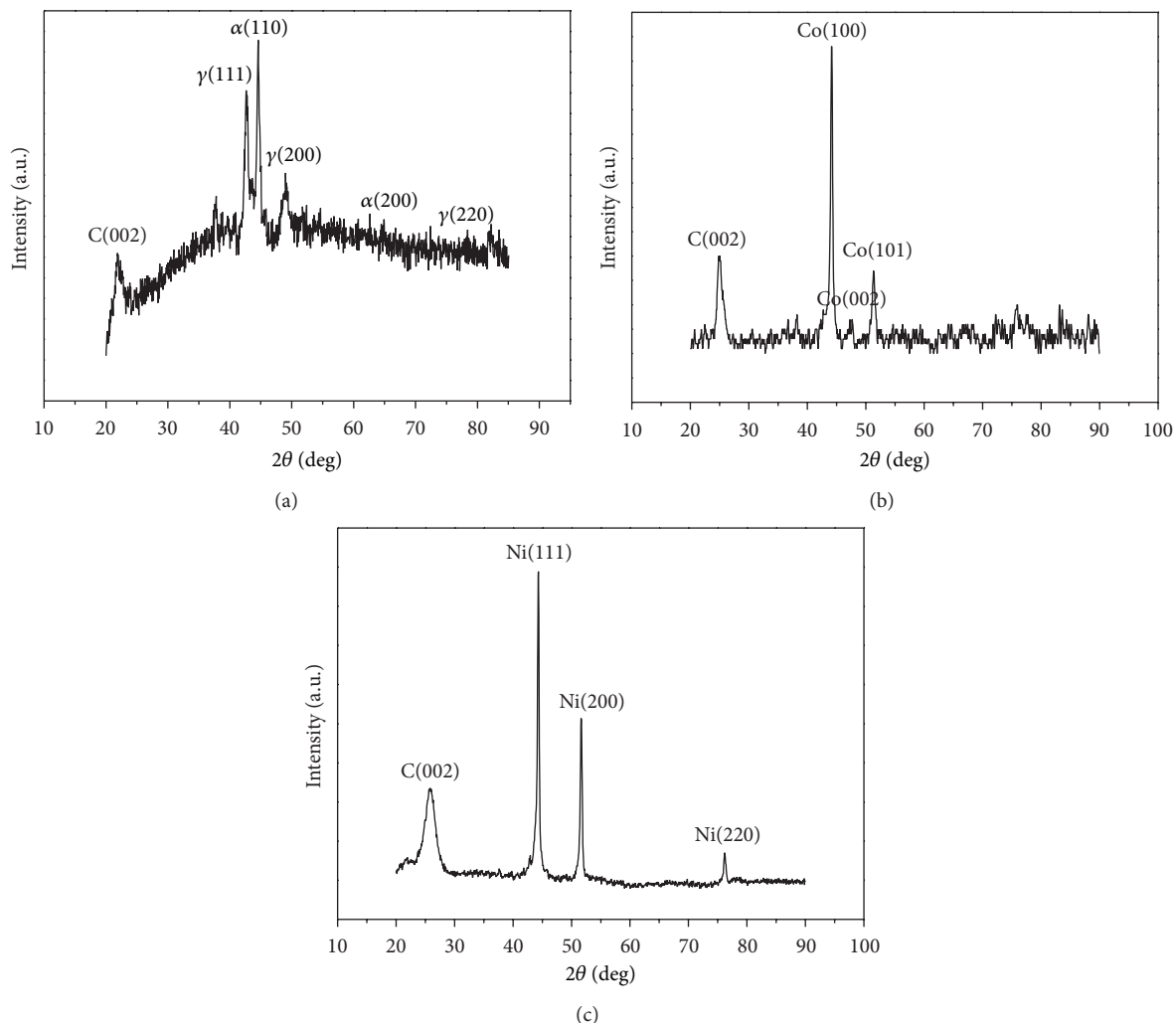


FIGURE 3: XRD patterns of carbon nanofibers synthesized on (a) SMAT 316 L stainless steel, (b) SMAT Co, and (c) SMAT Ni.

This indicates that two-dimensional disorders existed in the basal plane, which is quite common in pyrolytic carbon materials synthesized by CVD. The existence of a carbon sheet turbostratic structure in the carbon nanomaterial can also result in a significant D-band peak.

The catalytic ability of the transition metals to prepare carbon nanomaterial is thought to be related to the complicated factors including their catalytic activity for the decomposition of volatile carbon compounds, the formation of metastable carbides, and the diffusion of carbon through the metal particles [15]. It was reported in the literatures [16, 17] that the high chemical reactivity of the nanocrystalline metal particles (because of numerous grain boundaries) and a large excess energy in form of nonequilibrium defects bring an extra driving force stored in the SMAT metals. The high concentration of the nonequilibrium defects (dislocations and subgrain boundaries) that are induced by plastic deformation may decrease the activation energy of diffusion and act as fast atomic transfer channels as well.

4. Conclusions

In summary, carbon material films were synthesized on the surface of the SMAT 316 L stainless steel, SMAT Co, and SMAT Ni by means of CVD process. Bulk metallic materials by SMAT surface modification served as substrates as well as catalysts for carbon nanomaterial film formation. Different metallic materials result in carbon nanomaterial film with various morphologies. Carbon nanofibers synthesized on SMAT 316 L stainless steel are not uniform or dense, along with amorphous carbon and many embedded inactive metallic particles. SMAT Co results in rather thin, uniform, and curly carbon nanofibers. These two kinds of carbon nanofibers show significant G-band peak in Raman characterizations, indicating high graphitization in the samples while carbon nanofibers formed on SMAT Ni are straighter, longer, and thicker, showing significant D-band peak in Raman characterization.

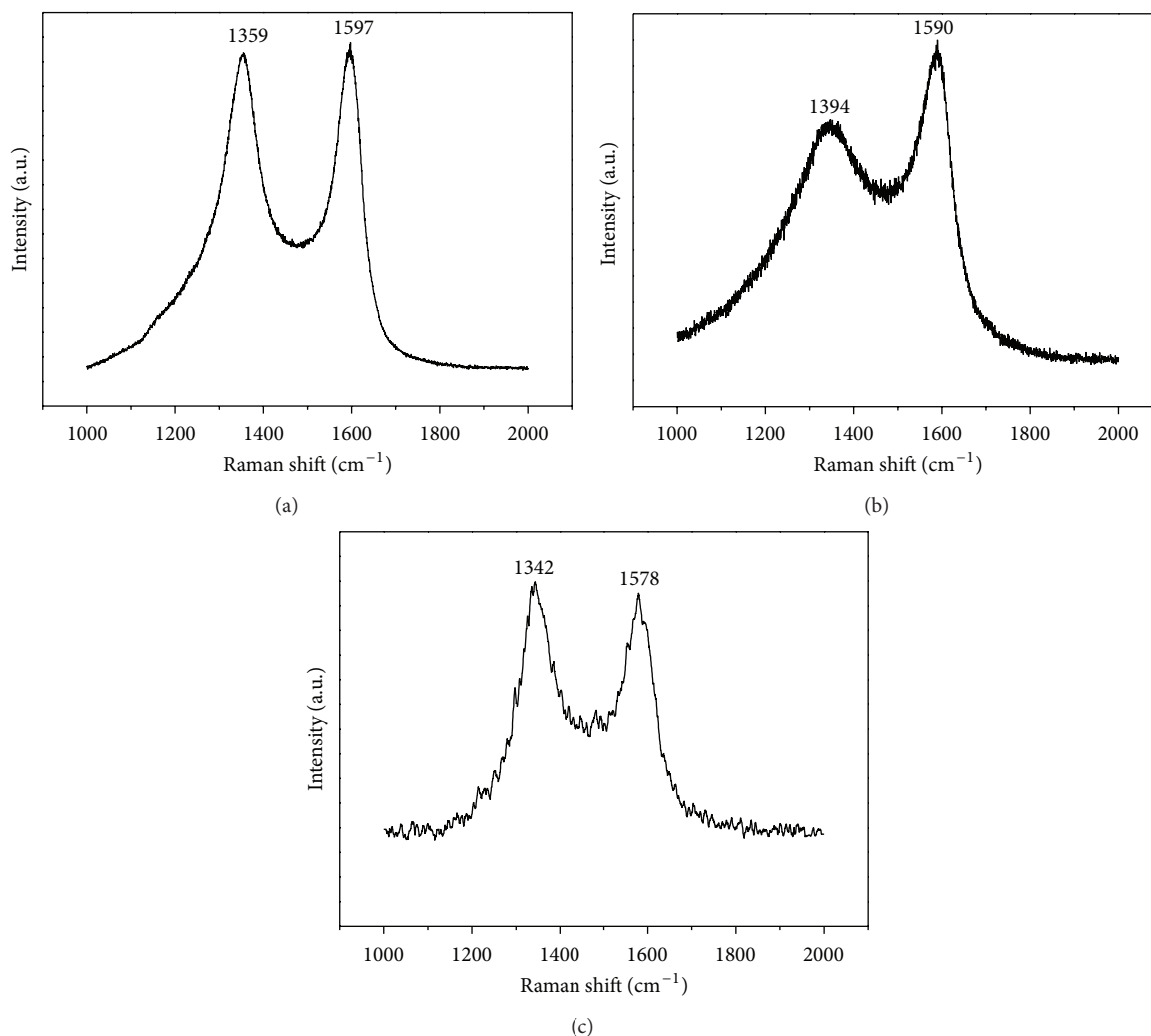


FIGURE 4: Raman spectrum of carbon nanofibers synthesized on (a) SMAT 316 L stainless steel, (b) SMAT Co, and (c) SMAT Ni.

Conflict of Interests

The authors declare that there is no conflict of interests regarding the publication of this paper.

Acknowledgments

This work was supported by the National Natural Science Foundation of China (Grant no. 51201190), Natural Science Foundation of Chongqing, China (CSTC 2011BB4080), and Fundamental Research Funds for the Central Universities (no. CDJZR12130043).

References

- [1] K. Lu and J. Lu, "Surface nanocrystallization (SNC) of metallic materials-presentation of the concept behind a new approach," *Journal of Materials Science and Technology*, vol. 15, no. 3, pp. 193–197, 1999.
- [2] K. Lu and J. Lu, "Nanostructured surface layer on metallic materials induced by surface mechanical attrition treatment," *Materials Science and Engineering A*, vol. 375–377, no. 1-2, pp. 38–45, 2004.
- [3] W. P. Tong, N. R. Tao, Z. B. Wang, J. Lu, and K. Lu, "Nitriding iron at lower temperatures," *Science*, vol. 299, no. 5607, pp. 686–688, 2003.
- [4] Z. B. Wang, K. Lu, G. Wilde, and S. V. Divinski, "Interfacial diffusion in Cu with a gradient nanostructured surface layer," *Acta Materialia*, vol. 58, no. 7, pp. 2376–2386, 2010.
- [5] X. Si, B. N. Lu, and Z. B. Wang, "Aluminizing low carbon steel at lower temperatures," *Journal of Materials Science and Technology*, vol. 25, no. 4, pp. 433–436, 2009.
- [6] Y. Gogotsi and V. Presser, Eds., *Carbon Nanomaterials*, CRC Press, 2013.
- [7] H. C. Chang, C. C. Li, S. F. Jen et al., "All-carbon field emission device by direct synthesis of graphene and carbon nanotube," *Diamond and Related Materials*, vol. 31, pp. 42–46, 2013.
- [8] S. Claramunt, O. Monereo, M. Boix et al., "Flexible gas sensor array with an embedded heater based on metal decorated carbon nanofibres," *Sensors and Actuators B: Chemical*, vol. 187, pp. 401–406, 2013.
- [9] S. S. Fan, M. G. Chapline, N. R. Franklin, T. W. Tomblor, A. M. Cassell, and H. J. Dai, "Self-oriented regular arrays of carbon

- nanotubes and their field emission properties,” *Science*, vol. 283, no. 5401, pp. 512–514, 1999.
- [10] C. Bower, W. Zhu, S. H. Jin, and O. Zhou, “Plasma-induced alignment of carbon nanotubes,” *Applied Physics Letters*, vol. 77, no. 6, pp. 830–832, 2000.
- [11] R. L. Vander Wal and L. J. Hall, “Carbon nanotube synthesis upon stainless steel meshes,” *Carbon*, vol. 41, no. 4, pp. 659–672, 2003.
- [12] X. F. Yang and J. Lu, “A new way to synthesize carbon nanofiber film on bulk titanium via hybrid surface mechanical attrition treatment,” *Applied Surface Science*, vol. 264, pp. 191–196, 2013.
- [13] J. Y. Xu, X. C. Lei, R. Yang, and Z. Z. Fan, “In situ formation of carbon nanomaterials on bulk metallic materials,” *Journal of Nanomaterials*, vol. 2014, Article ID 690630, 9 pages, 2014.
- [14] M. S. Dresselhaus, G. Dresselhaus, R. Saito, and A. Jorio, “Raman spectroscopy of carbon nanotubes,” *Physics Reports*, vol. 409, no. 2, pp. 47–99, 2005.
- [15] S. B. Sinnott, R. Andrews, D. Qian et al., “Model of carbon nanotube growth through chemical vapor deposition,” *Chemical Physics Letters*, vol. 315, no. 1-2, pp. 25–30, 1999.
- [16] Z. B. Wang, N. R. Tao, W. P. Tong, J. Lu, and K. Lu, “Diffusion of chromium in nanocrystalline iron produced by means of surface mechanical attrition treatment,” *Acta Materialia*, vol. 51, no. 14, pp. 4319–4329, 2003.
- [17] Z. B. Wang, J. Lu, and K. Lu, “Chromizing behaviors of a low carbon steel processed by means of surface mechanical attrition treatment,” *Acta Materialia*, vol. 53, no. 7, pp. 2081–2089, 2005.

Research Article

Fabrication and Characterization of Regenerated Cellulose Films Using Different Ionic Liquids

Jin-Hui Pang,¹ Xin Liu,¹ Miao Wu,¹ Yu-Ying Wu,² Xue-Ming Zhang,^{1,2} and Run-Cang Sun^{2,3}

¹ MOE Key Laboratory of Wooden Material Science and Application, Beijing Forestry University, Beijing 100083, China

² Institute of Biomass Chemistry and Technology, Beijing Forestry University, Beijing 100083, China

³ State Key Laboratory of Pulp and Paper Engineering, South China University of Technology, Guangzhou, China

Correspondence should be addressed to Yu-Ying Wu; wuyuying-1980@163.com and Xue-Ming Zhang; xm.zhang@bjfu.edu.cn

Received 21 April 2014; Accepted 7 May 2014; Published 9 June 2014

Academic Editor: Shao-Wen Cao

Copyright © 2014 Jin-Hui Pang et al. This is an open access article distributed under the Creative Commons Attribution License, which permits unrestricted use, distribution, and reproduction in any medium, provided the original work is properly cited.

The demand for substitution of fossil-based materials by renewable bio-based materials is increasing with the fossil resources reduction and its negative impacts on the environment. In this study, environmentally friendly regenerated cellulose films were successfully prepared using 1-allyl-3-methylimidazolium chloride (AmimCl), 1-butyl-3-methylimidazolium chloride (BmimCl), 1-ethyl-3-methylimidazolium chloride (EmimCl), and 1-ethyl-3-methylimidazolium acetate (EmimAc) as solvents, respectively. The results of morphology from scanning electron microscopy (SEM) and atomic force microscopy (AFM) showed that all the cellulose films possessed smooth, highly uniform, and dense surface. The solid-state cross-polarization/magic angle spinning (CP/MAS) ¹³C NMR spectra and X-ray diffraction (XRD) corroborated that the transition from cellulose I to II had occurred after preparation. Moreover, it was shown that the ionic liquid EmimAc possessed much stronger dissolubility for cellulose as compared with other ionic liquids and the cellulose film regenerated from EmimCl exhibited the most excellent tensile strength (119 Mpa). The notable properties of regenerated cellulose films are promising for applications in transparent biodegradable packaging and agricultural purpose as a substitute for PP and PE.

1. Introduction

With the development of modern society and industry, there is growing demand for development of renewable and biodegradable materials as substitutes for petroleum-derived synthetic polymers [1]. Cellulose is the most abundant natural polymer in nature and it will become one of the most promising polymeric resources, which is renewable, biodegradable, and biocompatible [2, 3]. However, chemical processing of cellulose is extremely difficult in general because it is neither meltable nor soluble in water or common solvents due to its partially crystalline structure and close chain packing via numerous inter- and intramolecular hydrogen bonds [4, 5].

Over the past decades, several cellulose solvent systems have been available for dissolving cellulose, such as viscose process (CS₂) [6, 7], LiCl/N,N-dimethylacetamide (DMAc) [8], DMSO/paraformaldehyde (PF) [9], and some aqueous solutions of metal complexes [10]. However, these conventional cellulose solvent systems have disadvantages,

such as limited dissolving capability, toxicity, high cost, solvents recovery, uncontrollable side reaction, and instability during cellulose processing and/or derivatization. The recently developed Lyocell process [11], which uses N-methylmorpholine N-oxide (NMMO) to dissolve cellulose directly, also has some disadvantages including the formation of byproducts, the degradation of cellulose, and high cost [12]. In recent years, Zhang et al. [13, 14] have developed a green and efficient method for dissolution of cellulose in NaOH/urea aqueous solution, in which the cellulose can be rapidly dissolved as precooled to -12°C within 2 min. However, the dissolution process is limited in terms of cellulose concentration and degree polymerization (DP). More recently, ionic liquids (ILs) have attracted much attention due to their high electrochemical and thermal stability, non-flammability, and tunable solubility properties [15]. Ionic liquids are often fluid at room temperature and consist entirely of ionic species and represent a new class of solvents

with high polarity. Since no toxic or explosive gases are formed due to their low vapor pressure, ionic liquids are considered as “green solvents.” Moreover, ionic liquids exhibited outstanding dissolving capability for cellulose [16], which will broaden the comprehensive utilization for cellulose. It has been shown that the ability to dissolve cellulose is not an inherent property of this broad class of compounds [17]. Among the vast number of ILs reported so far, only a minority dissolve cellulose. In order to compare the dissolubility and processability of different ionic liquids on cellulose, four ILs including 1-allyl-3-methylimidazolium chloride (AmimCl), 1-ethyl-3-methylimidazolium chloride (EmimCl), 1-butyl-3-methylimidazolium chloride (BmimCl), and 1-ethyl-3-methylimidazolium acetate (EmimAc) were chosen as solvents to dissolve cellulose and elaborate regenerated cellulose films. The morphology, chemical structure, and mechanical properties of cellulose films were investigated to evaluate the desirability of their applications in the packaging and functional materials fields.

2. Materials and Methods

2.1. Materials. Cotton linter, supplied by Silver Hawk Fiber Corporation (Shandong province, China), was used as cellulose sample with the degree of polymerization (DP) 920. The degree of polymerization was measured by TAPPI test method using cupriethylenediamine (CED) as a solvent and a capillary viscometer, to give an indication of the average degree of polymerization of the cellulose materials. The viscosities determined as centipoises (cP) were converted to degree of polymerization (DP) based on the following formula:

$$DP^{0.905} = 0.75 \times [954 \times \log(X) - 325], \quad (1)$$

where X = TAPPI viscosity in cP.

The cellulose sample used was dried in vacuum at 105°C for 24 h before using. The ILs 1-ethyl-3-methylimidazolium acetate (EmimAc), 1-allyl-3-methylimidazolium chloride (AmimCl), 1-ethyl-3-methylimidazolium chloride (EmimCl), and 1-butyl-3-methylimidazolium chloride (BmimCl), used as solvents for dissolution of the cellulose, were purchased from Chengjie Chemistry Corporation.

2.2. Preparation of Regenerated Cellulose Films. In a typical procedure for preparation of regenerated cellulose film, 5 g cotton linter sample was dispersed in 100 g ILs of EmimAc, AmimCl, EmimCl, and BmimCl, respectively. The mixture was heated at different temperatures in the range of 80°C–120°C under magnetic stirring until cellulose dissolved in ILs completely. After dissolution, the resulting transparent solution was cast on a glass plate and then immediately coagulated in the water to obtain transparent regenerated cellulose gel. The regenerated cellulose gel was washed with running distilled water and then air dried. All films were kept in a conditioning cabinet at 50% relative humidity (RH) and 25°C to ensure the stabilization of their water content before characterization.

2.3. Thickness Measurements. A micrometer (Lorentzen & Wettre, precision 1 μm) was used to measure film thickness. Measurement was taken at six different locations on each film, and the mean value was used in the calculations of the mechanical test.

2.4. Scanning Electron Microscopy Analysis. Scanning electron micrographs (SEM) were taken on a HITACHI S-3400N scanning electron microscope with 10 kV acceleration voltage and at a magnification of 2000. The free surface and the fracture surface of the films were sputtered with gold-palladium on a HITACHI E-1010 and then observed and photographed.

2.5. Atomic Force Microscopy Analysis. Atomic force microscopy (AFM) (SPM-9600, Shimadzu) was used to study the morphology of film surface. In AFM scanning, two to four interest locations on each sample were tested. Small pieces of films were glued onto metal disks and attached to a magnetic sample holder located on the top of the scanner tube. Phase images were recorded under ambient air conditions. All of the images were recorded in contact mode using silicon cantilevers.

2.6. X-Ray Diffraction. Crystallinity of the regenerated cellulose film samples was determined by X-ray diffraction patterns using XRD-6000 instrument (Shimadzu, Japan). The method was the same as that at literature [13].

2.7. Thermal Analysis. Thermal analysis was determined by using thermogravimetric analysis (TGA) and differential thermal analysis (DTA) on a simultaneous thermal analyzer (SDT Q600 TGA/DSC, TA Instrument). The samples weighed around 10 mg were heated from room temperature to 600°C at a heating rate of 10°C/min under an inert atmosphere of N₂.

2.8. Fourier Transform Infrared Spectra Analysis. Infrared spectra of cellulose film samples were recorded with a Fourier transform IR spectrometer (FT-IR TENSOR27, Germany) in ATR mode. The specimens were measured directly with a scan range from 400 cm⁻¹ to 4000 cm⁻¹.

2.9. CP/MAS ¹³C NMR Spectra. Solid-state cross-polarization/magic angle spinning (CP/MAS) ¹³C NMR spectra of the regenerated cellulose film samples were recorded on a Bruker AV-III 400 M spectrometer (Germany) operated at a ¹³C frequency of 100.6 MHz. A 4 mm zirconia (ZrO₂) rotor was used to pack cellulose films, and the measurement was performed using a CP pulse program with a 2 ms contact time and a 2 s delay between transitions. The spinning speed was set at 5 kHz for all samples.

2.10. Contact Angle Measurements. Contact angles of the cellulose films were measured to calculate the surface free energies of the cellulose films. The measurements were performed at room temperature by the sessile drop method using

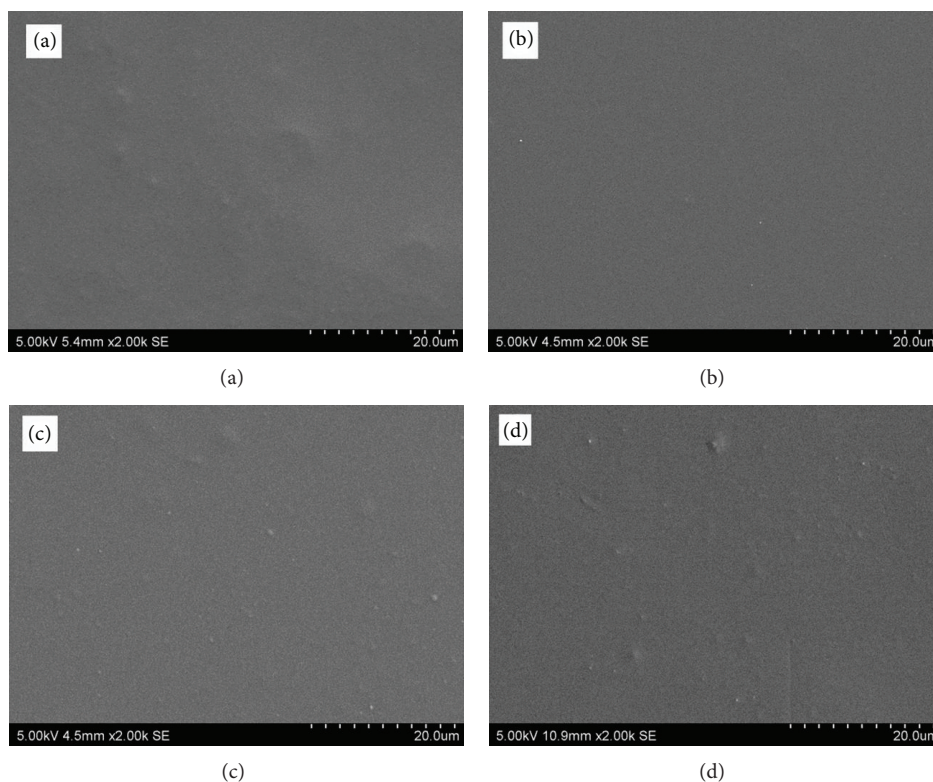


FIGURE 1: SEM images of regenerated films, (a) AmimCl, (b) BmimCl, (c) EmimCl, and (d) EmimAc.

TABLE 1: Crystallinity, peak positions in X-ray diffractograms, and contact angle of cellulose films.

Sample	Crystallinity (%)	Diffraction angle 2θ				Contact angle/ θ°
		(-110)	(110)	(200)	(020)	
Cotton linter	54.01	15.0	16.4	22.6	—	—
AmimCl	38.41	12.8	20.2	—	21.2	38.48
BmimCl	39.25	12.6	20.2	—	21.2	40.08
EmimCl	39.24	12.8	20.6	—	21.2	54.12
EmimAc	34.04	12.8	20.2	—	21.2	34.18

a goniometer equipped with a high-speed camera (OCA 20, Data physics Ltd., Germany).

2.11. Tensile Strength Testing. The tensile strength of the regenerated cellulose films was measured by using a tensile testing machine (Zwick Universal testing machine Z005) at a speed of 5 mm/min. The samples were cut in the rectangular specimens with a width of 20 mm and length of 60 mm, and eight replicate specimens were tested from each film type. A grip distance of 20 mm was maintained. The measurements were performed at 25°C and relative humidity of 50%.

3. Results and Discussion

3.1. Topography of Films. The topography of produced films was analyzed by SEM and AFM. SEM and AFM micrographs of the regenerated films are shown in Figures 1 and 2. The SEM images indicated that all the regenerated films displayed

smooth, highly uniform, and dense surface, indicating a complete regeneration of cellulose. The small nodules especially in the cellulose film obtained from ionic liquid EmimAc (sample d) were possibly caused by the presence of bubbles in processes of casting and coagulation. AFM images with higher resolution were recorded to determine the surface structural information of the films, whereas the height images were generated for the additional morphology and surface roughness of the films. AFM images (Figure 2) revealed that the surface of the regenerated cellulose films displayed typical granular morphology.

3.2. Crystallinity. The X-ray diffraction patterns of cotton linter and cellulose films regenerated from AmimCl, BmimCl, EmimCl, and EmimAc are shown in Figure 3. The value of crystallinity and diffraction planes of cellulose films are presented in Table 1. It was shown that the XRD profiles of cotton linter exhibited typical diffraction cellulose I angles

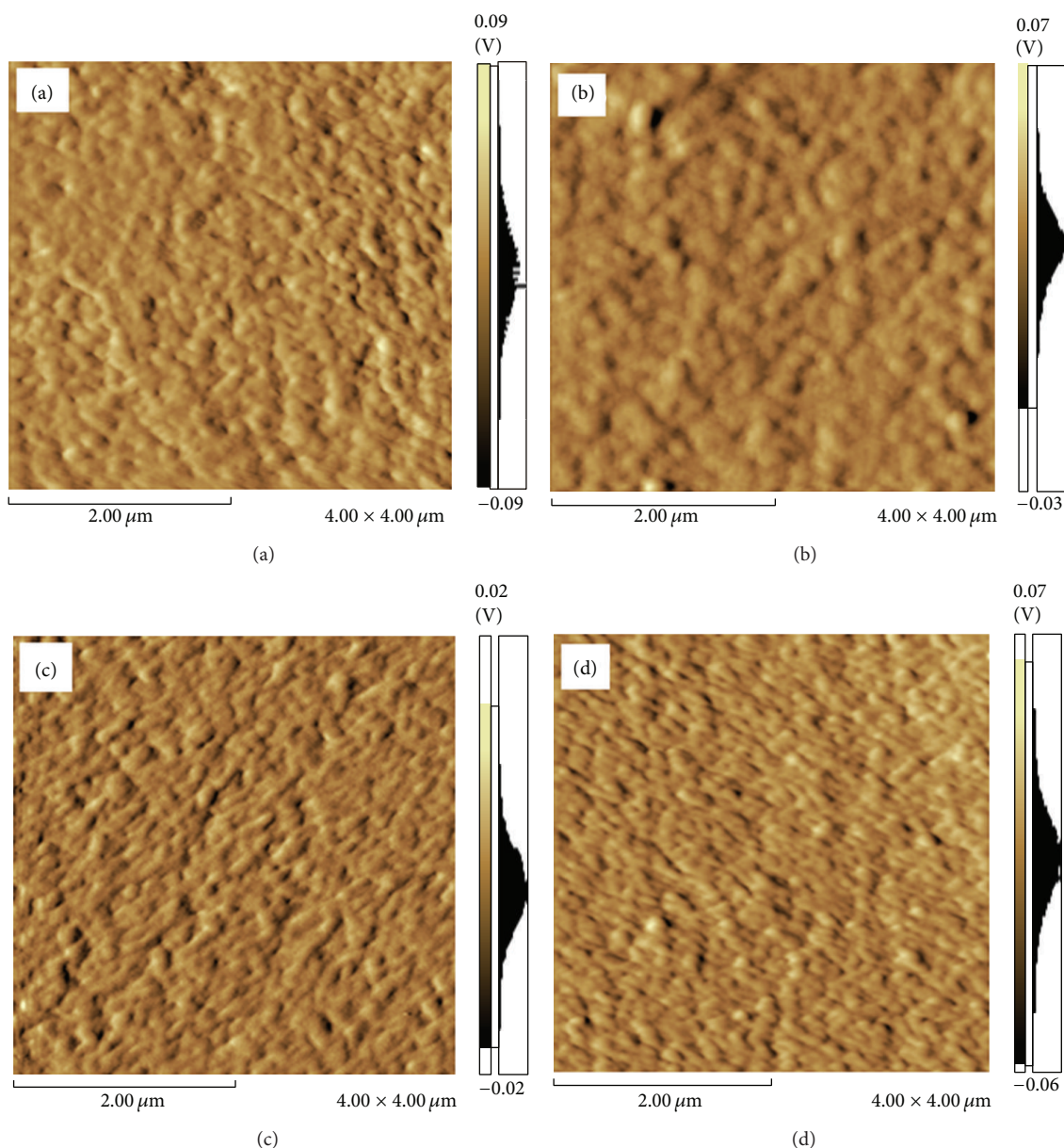


FIGURE 2: AFM images of regenerated films, (a) AmimCl, (b) BmimCl, (c) EmimCl, and (d) EmimAc.

(2θ) around at 15.0° , 16.4° , and 22.6° , which corresponded to the diffraction planes of (-110) , (110) , and (200) , respectively [18]. The diffraction patterns of the regenerated films (spectra b, c, d, and e) from the four ILs showed a broad peak at $2\theta = 20.2^\circ$ (110), 21.2° (020) and a small broad peak at $2\theta = 12.8^\circ$ (-110), which correspond to the crystalline form of cellulose II [19–21]. These results indicate that the transformation from cellulose I to cellulose II occurred after the dissolution and regeneration process in ILs. Compared to the original cellulose, the crystallinity of the regenerated cellulose films was lower than that of the cotton linter (Table 1). These results meant that the inter- and intramolecular hydrogen bonds between cellulose molecule were rapidly broken during the dissolution process, thus destroying the original crystalline

form [22, 23]. Moreover, the coagulation process was unfavorable to the cellulose crystallization [24]. In addition, it was noteworthy that the regenerated film fabricated with EmimAc had relatively higher hydrophilicity as the contact angle was the lowest (34.18°) as well as crystallinity (34.04%), which demonstrated that EmimAc exhibited much stronger dissolubility for cellulose as compared with other ILs.

3.3. FT-IR. FT-IR spectroscopy was used to obtain direct information on chemical changes in cellulose during dissolution and regeneration. Figure 4 illustrates the FT-IR spectra of the regenerated films prepared from AmimCl (spectrum a), BmimCl (spectrum b), EmimCl (spectrum c), and EmimAc (spectrum d). The peak at 3331 cm^{-1} is originated from

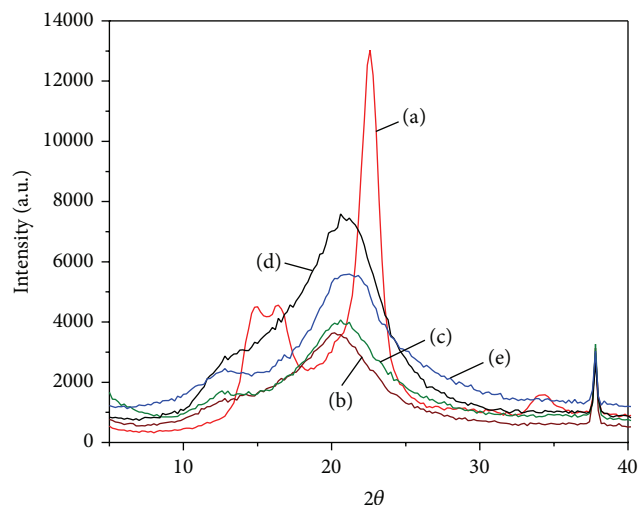


FIGURE 3: XRD images of films, (a) cotton linter, (b) AmimCl, (c) BmimCl, (d) EmimCl, and (e) EmimAc.

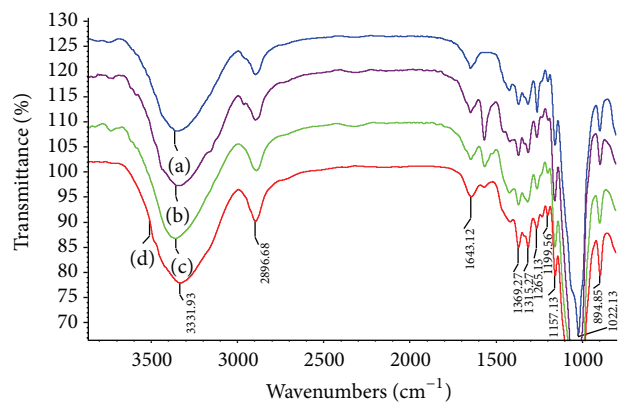


FIGURE 4: FT-IR images of films, (a) AmimCl, (b) BmimCl, (c) EmimCl, and (d) EmimAc.

the stretching of -OH groups and the signal at 2896 cm^{-1} is assigned to CH- stretching [25]. The band at 1643 cm^{-1} could be due to water in the amorphous region [26]. The peak at 1369 cm^{-1} is attributed to the O-H bending vibration and the strong band at 1022 cm^{-1} is attributed to the characteristic C-O-C stretching. The band at 1430 cm^{-1} in all spectra indicated that all samples contained a mixture of crystallized cellulose II and amorphous cellulose [27]. The bands due to C-O antisymmetric bridge stretching and C-O-C pyranose ring skeletal vibration were detected at 1157 cm^{-1} . A small sharp band at 894 cm^{-1} corresponds to the glycosidic C-H deformation with ring vibration contribution and O-H bending, which is characteristic of β -glycosidic linkages between glucose in cellulose [28]. Moreover, the intensity of this band is relatively higher as compared with cellulose I, which corroborated the transition from cellulose I to II [29]. The bands at 1375 , 1315 , and 1156 cm^{-1} are assigned to CH -stretching, CH_2 wagging, and C-O stretching in cellulose II, respectively [30]. Furthermore, it could be observed that these spectra were

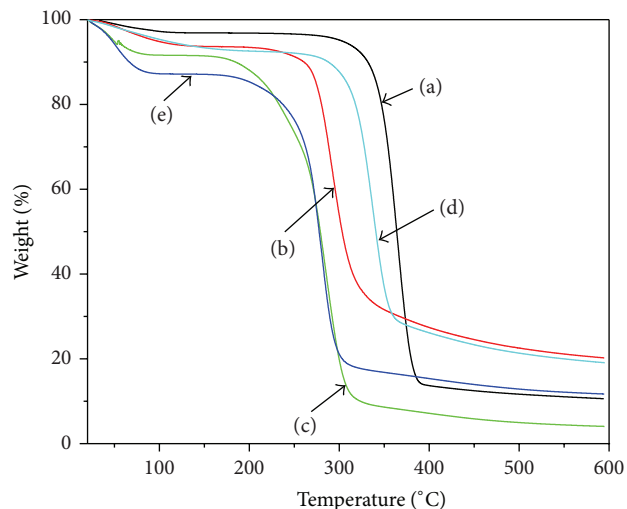


FIGURE 5: TGA of films, (a) virgin fibers, (b) AmimCl, (c) BmimCl, (d) EmimCl, and (e) EmimAc.

quite similar and no new peaks appeared in the regenerated samples, which indicated that no chemical reaction between the ILs and the cellulose had occurred during the dissolution and regeneration process. In other words, AmimCl, BmimCl, EmimCl, and EmimAc were nonderivatizing solvents for cellulose, which was consistent with the literature [7, 27].

3.4. Thermal Properties. Thermal degradability is affected by the chemical composition of the material. The typical TGA and DSC curves of the regenerated cellulose films are shown in Figures 5 and 6. As shown in Figure 5, the thermal decomposition of the original cellulose and the regenerated cellulose was divided into two weight loss stages, corresponding to the slow pyrolysis and fast pyrolysis stages, respectively. At the first stage, the mass loss was associated with the volatilization of water. At the fast pyrolysis stage, the onset decomposition temperatures of the regenerated cellulose films were all lower than that of the original cellulose, especially the cellulose films regenerated from BmimCl (sample c) and EmimCl (sample d). The maximum decomposition rate (T_{max} , the decomposition temperature corresponding to the maximum weight loss rate) is shown in Figure 6. It was noted that thermal stabilities of the regenerated cellulose films were lower than that from original cellulose, which was probably caused by the lower crystallinity of regenerated cellulose as the previous work has shown that lower crystallinity and lower cellulose crystallite size can accelerate the degradation process and reduce the wood thermal stability [31].

3.5. ^{13}C CP/MAS NMR Spectra. The ^{13}C CP/MAS NMR spectra of cotton linter and different film samples are shown in Figure 7. The major signals at 105.8, 89.2, 75.3, 72.9, 71.7, and 65.4 ppm in the spectrum of cotton linter are attributed to the C-1, C-4, C-5, C-3, C-2, and C-6, respectively, which correspond to the cellulose I structure [32]. Compared with native cellulose, the C-6 signal of the regenerated cellulose film shifted from 65.4 to 62.8 ppm as a single peak, suggesting

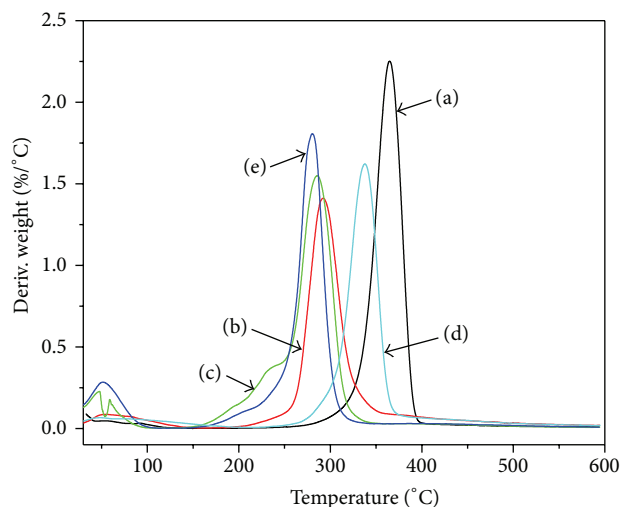


FIGURE 6: DSC of films, (a) virgin fibers, (b) AmimCl, (c) BmimCl, (d) EmimCl, and (e) EmimAc.

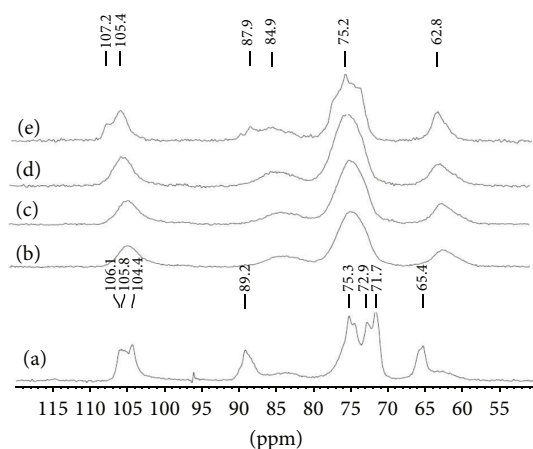


FIGURE 7: ^{13}C CP-MAS spectra of films, (a) virgin fibers, (b) AmimCl, (c) BmimCl, (d) EmimCl, and (e) EmimAc.

that the “*t-g*” conformation (ca. 66 ppm for C-6) of the C6-OH group for the crystalline parts of cellulose I had changed into a “*g-t*” conformation (ca. 61–63 ppm for C-6) of cellulose II [33]. For the regenerated cellulose films, the C-4 peaks located at 87.9 ppm shifted to higher magnetic field than the native cellulose (89.2 ppm), and the intensity was significantly lower, which suggested the dramatic decrease in the crystallinity due to the dissolution and regeneration process.

3.6. Mechanical Properties. To examine the suitability of the cellulose films for industry applications, the mechanical properties of the regenerated cellulose films were determined. The typical stress-strain curves of regenerated films prepared in AmimCl (a), BmimCl (b), EmimCl (c), and EmimAc (d) are shown in Figure 8. It can be seen from Figure 8 that the cellulose film regenerated from EmimCl caused the most excellent tensile strength, which was suggested by the highest

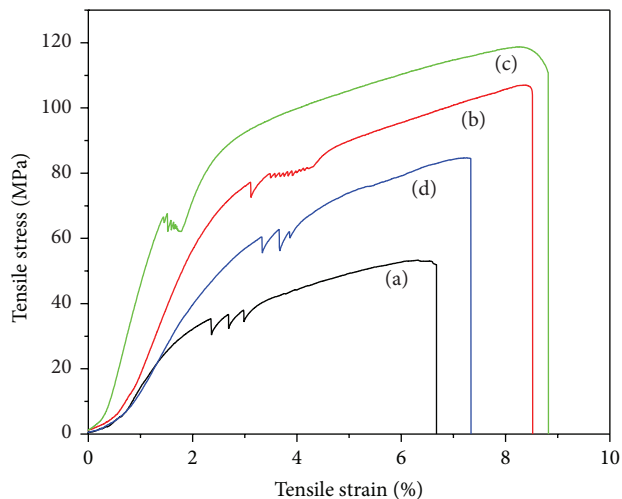


FIGURE 8: Strength of films, (a) AmimCl, (b) BmimCl, (c) EmimCl, and (d) EmimAc.

tensile stress (119 Mpa). Moreover, it was noted that the tensile strain of regenerated film prepared by EmimCl was the highest (8.8%). In addition, all the samples showed thermoplastic like behavior with stress increasing rapidly at small strains and more slowly after a yield point. In comparison, although the tensile strength value for the regenerated cellulose films obtained from AmimCl was lowest, it was still slightly higher than those of the largely used commercial polyolefin films, such as polyethylene (PE) and polypropylene (PP) with tensile strength in the range of 20–40 Mpa [34]. Therefore, these results indicated that the environmentally friendly regenerated cellulose films had the potential to replace both nonbiodegradable PE and PP for packaging and agricultural purpose.

4. Conclusion

The regenerated cellulose films were successfully prepared using different ionic liquids including AmimCl, BmimCl, EmimCl, and EmimAc as solvents. It was shown that the regenerated cellulose films displayed smooth, highly uniform, and dense morphology properties. ^{13}C CP/MAS NMR spectra and XRD corroborated that the transition from cellulose I to II had occurred after preparation. In comparison, the ionic liquid EmimAc possessed much stronger dissolubility for cellulose and the cellulose film regenerated from ionic liquid EmimCl exhibited the most excellent tensile strength. The notable properties of the regenerated cellulose films are promising for applications in transparent, biodegradable packaging and agricultural purpose as a substitute for PP and PE.

Conflict of Interests

The authors declare that there is no conflict of interests regarding the publication of this paper.

Acknowledgments

The authors are grateful for the financial support of this research from the Beijing Higher Education Young Elite Teacher Project (YETP0766), Program for New Century Excellent Talents in University (NCET-12-0782), Natural Science Foundation of China (no. 31170557), Major State Basic Research Projects of China (973-2010CB732203), and China Ministry of Education (no. 111).

References

- [1] R. A. Gross and B. Kalra, "Biodegradable polymers for the environment," *Science*, vol. 297, no. 5582, pp. 803–807, 2002.
- [2] L. Zhang, D. Ruan, and J. Zhou, "Structure and properties of regenerated cellulose films prepared from cotton linters in NaOH/urea aqueous solution," *Industrial and Engineering Chemistry Research*, vol. 40, no. 25, pp. 5923–5928, 2001.
- [3] J. Schurz, "Trends in polymer science. A bright future for cellulose," *Progress in Polymer Science*, vol. 24, no. 4, pp. 481–483, 1999.
- [4] K. Bredereck and F. Hermanutz, "Man-made celluloses," *Review of Progress in Coloration and Related Topics*, vol. 35, pp. 59–75, 2005.
- [5] S. Mahmoudian, M. U. Wahit, A. F. Ismail, and A. A. Yussuf, "Preparation of regenerated cellulose/montmorillonite nanocomposite films via ionic liquids," *Carbohydrate Polymers*, vol. 88, no. 4, pp. 1251–1257, 2012.
- [6] R. Li, L. Zhang, and M. Xu, "Novel regenerated cellulose films prepared by coagulating with water: structure and properties," *Carbohydrate Polymers*, vol. 87, no. 1, pp. 95–100, 2012.
- [7] Y. Cao, H. Li, Y. Zhang, J. Zhang, and J. He, "Structure and properties of novel regenerated cellulose films prepared from corn-husk cellulose in room temperature ionic liquids," *Journal of Applied Polymer Science*, vol. 116, no. 1, pp. 547–554, 2010.
- [8] S. L. Williamson, R. S. Armentrout, R. S. Porter, and C. L. McCormick, "Microstructural examination of semi-interpenetrating networks of poly(N,N-dimethylacrylamide) with cellulose or chitin synthesized in lithium chloride/N,N-dimethylacetamide," *Macromolecules*, vol. 31, no. 23, pp. 8134–8141, 1998.
- [9] J.-F. Masson and R. S. J. Manley, "Cellulose/poly(4-vinylpyridine) blends," *Macromolecules*, vol. 24, no. 22, pp. 5914–5921, 1991.
- [10] T. Heinze and T. Liebert, "Unconventional methods in cellulose functionalization," *Progress in Polymer Science*, vol. 26, no. 9, pp. 1689–1762, 2001.
- [11] K. Saalwächter and W. Burchard, "Cellulose in new metal-complexing solvents. 2. Semidilute behavior in Cd-tren," *Macromolecules*, vol. 34, no. 16, pp. 5587–5598, 2001.
- [12] Z. Liu, H. Wang, Z. Li et al., "Characterization of the regenerated cellulose films in ionic liquids and rheological properties of the solutions," *Materials Chemistry and Physics*, vol. 128, no. 1–2, pp. 220–227, 2011.
- [13] H. S. Qi, C. Y. Chang, and L. N. Zhang, "Preparation of chitin/cellulose composite gels and films with ionic liquids," *Green Chemistry*, vol. 11, pp. 177–184, 2009.
- [14] J. Cai and L. Zhang, "Rapid dissolution of cellulose in LiOH/urea and NaOH/urea aqueous solutions," *Macromolecular Bioscience*, vol. 5, no. 6, pp. 539–548, 2005.
- [15] R. D. Rogers and K. R. Seddon, "Ionic liquids—solvents of the future?" *Science*, vol. 302, no. 5646, pp. 792–793, 2003.
- [16] S. Shang, L. Zhu, and J. Fan, "Physical properties of silk fibroin/cellulose blend films regenerated from the hydrophilic ionic liquid," *Carbohydrate Polymers*, vol. 86, no. 2, pp. 462–468, 2011.
- [17] M. Gericke, P. Fardim, and T. Heinze, "Ionic liquids—promising but challenging solvents for homogeneous derivatization of cellulose," *Molecules*, vol. 17, no. 6, pp. 7458–7502, 2012.
- [18] A. Isogai, M. Usuda, T. Kato, T. Uryu, and R. H. Atalla, "Solid-state CP/MAS ¹³C NMR study of cellulose polymorphs," *Macromolecules*, vol. 22, no. 7, pp. 3168–3172, 1989.
- [19] D. Han and L. Yan, "Preparation of all-cellulose composite by selective dissolving of cellulose surface in PEG/NaOH aqueous solution," *Carbohydrate Polymers*, vol. 79, no. 3, pp. 614–619, 2010.
- [20] H. Qi, J. Cai, L. Zhang, and S. Kuga, "Properties of films composed of cellulose nanowhiskers and a cellulose matrix regenerated from alkali/urea solution," *Biomacromolecules*, vol. 10, no. 6, pp. 1597–1602, 2009.
- [21] S. S. Rahatekar, A. Rasheed, R. Jain et al., "Solution spinning of cellulose carbon nanotube composites using room temperature ionic liquids," *Polymer*, vol. 50, no. 19, pp. 4577–4583, 2009.
- [22] H.-Z. Chen, N. Wang, and L.-Y. Liu, "Regenerated cellulose membrane prepared with ionic liquid 1-butyl-3-methylimidazolium chloride as solvent using wheat straw," *Journal of Chemical Technology and Biotechnology*, vol. 87, no. 12, pp. 1634–1640, 2012.
- [23] S. H. Zeronian and H.-S. Ryu, "Properties of cotton fibers containing the cellulose IV crystal structure," *Journal of Applied Polymer Science*, vol. 33, no. 7, pp. 2587–2604, 1987.
- [24] H. Zhang, J. Wu, J. Zhang, and J. He, "1-allyl-3-methylimidazolium chloride room temperature ionic liquid: a new and powerful nonderivatizing solvent for cellulose," *Macromolecules*, vol. 38, no. 20, pp. 8272–8277, 2005.
- [25] H. Lateef, S. Grimes, P. Kewcharoenwong, and B. Feinberg, "Separation and recovery of cellulose and lignin using ionic liquids: a process for recovery from paper-based waste," *Journal of Chemical Technology and Biotechnology*, vol. 84, no. 12, pp. 1818–1827, 2009.
- [26] J. Yin, K. Luo, X. Chen, and V. V. Khutoryanskiy, "Miscibility studies of the blends of chitosan with some cellulose ethers," *Carbohydrate Polymers*, vol. 63, no. 2, pp. 238–244, 2006.
- [27] M. L. Nelson and R. T. O'Connor, "Relation of certain infrared bands to cellulose crystallinity and crystal lattice type, Part II. A new infrared ratio for estimation of crystallinity in celluloses I and II," *Journal of Applied Polymer Science*, vol. 8, no. 8, pp. 1325–1341, 1964.
- [28] A. X. Jin, J. L. Ren, F. Peng et al., "Comparative characterization of degraded and non-degradative hemicelluloses from barley straw and maize stems: composition, structure, and thermal properties," *Carbohydrate Polymers*, vol. 78, no. 3, pp. 609–619, 2009.
- [29] F. Carrillo, X. Colom, J. J. Suñol, and J. Saurina, "Structural FTIR analysis and thermal characterisation of lyocell and viscose-type fibres," *European Polymer Journal*, vol. 40, no. 9, pp. 2229–2234, 2004.
- [30] J. Široký, R. S. Blackburn, T. Bechtold, J. Taylor, and P. White, "Attenuated total reflectance Fourier-transform Infrared spectroscopy analysis of crystallinity changes in lyocell following continuous treatment with sodium hydroxide," *Cellulose*, vol. 17, no. 1, pp. 103–115, 2010.

- [31] M. Poletto, A. J. Zattera, M. M. C. Forte, and R. M. C. Santana, "Thermal decomposition of wood: influence of wood components and cellulose crystallite size," *Bioresource Technology*, vol. 109, pp. 148–153, 2012.
- [32] V. Castelvetro, M. Geppi, S. Giaiacopi, and G. Mollica, "Cotton fibers encapsulated with homo- and block copolymers: synthesis by the atom transfer radical polymerization grafting-from technique and solid-state NMR dynamic investigations," *Biomacromolecules*, vol. 8, no. 2, pp. 498–508, 2007.
- [33] K. Kamide, K. Okajima, and K. Kowsaka, "Dissolution of natural cellulose into aqueous alkali solution: role of supermolecular structure of cellulose," *Polymer Journal*, vol. 24, no. 1, pp. 71–86, 1992.
- [34] H. Ding, *Handbook of Plastic Industry*, Chemical Industry Press, Beijing, China, 1995.